Relative Space-Time Kinematics
of an Anchorless Network

Relative Space-Time Kinematics
of an Anchorless Network

Proefschrift

ter verkrijging van de graad van doctor
aan de Technische Universiteit Delft,
op gezag van de Rector Magnificus Prof. ir. K.C.A.M. Luyben,
voorzitter van het College voor Promoties,
in het openbaar te verdedigen
op vrijdag 28 oktober 2016 om 10:00 uur
door

Raj Thilak RAJAN

Master of Science, University of Pune,
Maharashtra, India

geboren te Madurai, India

This dissertation has been approved by the promotor:
Prof. dr. ir. A-. J. van der Veen

Composition of the doctoral committee:

Rector Magnificus	Chairman
Prof. dr. ir. A-. J. van der Veen	Delft University of Technology

Independent members:

Prof. dr. ir. G. J. T. Leus	Delft University of Technology
Prof. dr. ir. E. Gill	Delft University of Technology
Prof. dr. ir. P. Visser	Delft University of Technology
Prof. dr. A. Leshem	Bar-Ilan University, Israel
Prof. dr. ir. M. Moonen	KU Leuven, Belgium
Dr. ir. M. J. Bentum	University of Twente

To my teachers for their inspiration
& to my mentors for their guidance

Summary

Space and time awareness has been an integral quest of human evolution, and more so in the currently burgeoning era of wireless sensor networks (WSN), internet of things (IoT) and big data. The rapid advances in technology in recent times has led to affordable, miniaturized and low-power sensor nodes, enabling the feasibility of networks with numerous nodes. These nodes are typically equipped with diverse portfolio of sensors to measure various physical phenomenon, which are cooperatively communicated and processed for appropriate statistical inference. To ensure coherent sampling, efficient communication and prudent inference, the knowledge of position and time of the sampled data is imperative, and consequently accurate space-time estimation of the nodes is as valuable as the sampled data itself.

In this dissertation we address the space-time estimation of a specific class of WSNs, namely an *anchorless network of asynchronous mobile nodes*. As the terminology suggests, we consider a network of mobile nodes under non-relativistic motion, whose space-time kinematics are to be estimated. In addition, the term *anchorless* indicates no apriori information on the absolute position or time of any node within the network. This approach is a stark contrast to conventional anchored scenarios, e.g., GPS-based localization, where absolute space-time reference is known. Anchorless networks arise naturally when deployed in inaccessible regions, where an absolute space-time reference is non-existent or only intermittently available. Moreover, when a swarm of nodes is considered, imparting the absolute reference to all the nodes could be limited by communication resources. A few application scenarios include, for example, indoor localization, underwater networks, drone swarms and space-based satellite arrays. In such anchorless networks, it is paramount to understand the *relative* space-time kinematics, which is the primary theme of this dissertation.

Unfortunately, our understanding of relative kinematics in Euclidean space is inherently dependent on an absolute reference. For instance, consider the first-order relative spatial kinematics, i.e., relative velocity, which is rightly defined as the vec-

tor difference between absolute velocities of the respective nodes. However, in the absence of apriori information on any absolute velocities, a natural question arises if these relative velocities can be estimated using only pairwise distance measurements between the nodes. In addition to relative spatial estimation, the asynchronous clocks on-board each of these nodes must also be synchronized, in the absence of a known absolute time-reference. These are some of the fundamental challenges which are addressed in this dissertation.

A key motivation to investigate the relative space-time kinematics arises from radio astronomy. The information-rich radiation from cosmic sources impinging on Earth-based radio astronomy interferometers is severely limited at ultra-long wavelengths of larger than 10 meters, an impediment which can be overcome by deploying a satellite-array in outer-space. Due to the large number of satellites and potentially far-away deployment, the orbiting satellite array is an anchorless network of asynchronous mobile nodes, which must jointly synchronize and localize all the satellites in the cluster, with minimal support from Earth-based ground stations. We motivate the need for such a space-based array in Chapter 2 using a few science cases and give an overview of current trends and technologies towards the feasibility of such an array. In context of this dissertation, the following Chapter 3 discusses the potential of-the-shelf clocks suitable for such a satellite array and argues that the first-order clock model is a sufficient approximation of the inherently non-linear clock.

The Chapters 4-6 form the main contributions of this dissertation, where we go beyond the scope of space-based arrays and address the broader class of anchorless networks of asynchronous mobile nodes. In Chapter 4, given two-way communication between the nodes, we show that the clock discrepancies of the respective nodes in a network and the pairwise time-varying distance can be jointly estimated under non-relativistic scenarios. In the absence of a predefined time-reference, we propose a few statistically optimal clock references, and the performance of these blind-clock references are discussed. In Chapter 5, under independent linear velocity assumption, we show that the relative velocity of the nodes can be estimated given only time-varying pairwise distances. The data model developed in this chapter is generalized and extended in Chapter 6 to estimate higher-order relative kinematics, such as relative acceleration. For the sake of completeness, we show that the absolute kinematics of the nodes can also be obtained using the proposed data model, provided the absolute kinematics of a few nodes are known. We derive theoretical lower bounds for the developed data models to verify the performance of the proposed algorithms. Finally, although the focus of this dissertation is on relative localization and synchronization, the techniques identified can be possibly extended to broader application areas in unsupervised learning and exploratory data analysis.

Samenvatting

Kennis over ruimte en tijd is altijd een thema geweest in de menselijke evolutie. Dit is momenteel sterk aan de orde in het bruisende tijdperk van draadloze communicatie, het internet der dingen, en "big data". De recente snelle ontwikkeling in technologie heeft geleid tot betaalbare, kleine en laag-vermogen sensoren, waarmee het mogelijk is grote netwerken te bouwen. De knooppunten in dit netwerk bestaan typisch uit een reeks van sensoren die diverse fysische parameters kunnen meten, die gedeeld worden met de buren om statistische schattingen op uit te voeren. Om de sensoren coherent te samplen, data te communiceren en de schattingen betrouwbaar uit te voeren, is het nodig om de positie en het tijdstip van samplen te weten, en daardoor is nauwkeurige ruimte-tijd informatie van de knooppunten van even groot belang als de sensordata zelf.

In dit proefschrift behandelen we de ruimte-tijd schatting voor een specifiek sensor netwerk, namelijk een *ankerloos netwerk van asynchrone mobiele knooppunten*. Hiermee bedoelen we een netwerk van mobiele knooppunten in niet-relativistische beweging, waarvan de ruimte-tijd kinematica geschat moeten worden. De term *ankerloos* betekent dat er van geen enkel knooppunt in het netwerk a-priori informatie is over absolute positie of tijd. Dit is in sterk contrast met conventionele technieken, bijvoorbeeld GPS localisatie, waar een absolute ruimte-tijd referentie bekend is. Ankerloze netwerken komen op een natuurlijke manier voor wanneer een netwerk uitgerold wordt in onherbergzame gebieden, waar een absolute ruimte-tijd referentie niet beschikbaar is (of slechts tijdelijk beschikbaar). Bovendien is, voor een zwerm knooppunten, het distribueren van de absolute ruimte-tijd referentie naar alle knooppunten vaak lastig door beperkingen in de communicatie. Toepassingen zijn bijvoorbeeld localisatie binnenshuis, onderwater netwerken, zwermen van drones, en zwermen van satellieten. In deze ankerloze netwerken is het van essentieel belang om de *relatieve* ruimte-tijd kinematica te begrijpen, wat het primaire thema is van dit proefschrift.

Samenvatting

Helaas is ons begrip van relatieve kinematica in de Euclidische ruimte inherent afhankelijk van een absolute referentie. Beschouw bijvoorbeeld de eerste-orde relatieve ruimtelijke kinematica, dat wil zeggen relatieve snelheid, gedefinieerd als het verschil tussen de absolute snelheidsvectoren tussen tween knooppunten. Echter, zonder a-priori informatie over absolute snelheden is het de vraag of deze relatieve snelheden geschat kunnen worden door enkel paarsgewijze metingen van de afstanden tussen knooppunten. Verder moeten de asynchrone klokken van ieder knooppunt gesynchroniseerd worden, zonder gebruik te maken van een absolute tijd-referentie. Dit zijn een paar van de fundamentele uitdagingen die we in dit proefschrift behandelen.

Een belangrijke motivatie om de relatieve ruimte-tijd kinematica te onderzoeken komt voort uit de radioastronomie. De straling van kosmische bronnen die door de ionosfeer op de aarde valt wordt sterk gefilterd voor de lange golflengtes (groter dan 10 meter). Dit kan worden overkomen door gebruik te maken van een zwerm satellieten buiten de dampkring. Vanwege het grote aantal satellieten en de mogelijk grote afstand tot de aarde is deze zwerm een ankerloos netwerk van asynchrone mobiele knooppunten, die onderling gesynchroniseerd en gelocaliseerd moeten worden, met minimale interactie met grondstations op aarde. We motiveren de noodzaak van een ruimte-gebaseerde zwerm in hoofdstuk 2 aan de hand van een aantal wetenschappelijke vragen, en geven een overzicht van trends en technologie die de realisatie van zo een zwerm mogelijk maken. Hoofdstuk 3 behandelt mogelijke standaard klokken die geschikt zouden kunnen zijn voor een satellietzwerm; we beargumenteren dat een eerste-orde klokmodel een voldoende goede benadering is voor het inherent niet-lineaire gedrag van de klok.

Hoofdstukken 4-6 vormen de belangrijkste bijdragen in dit proefschrift. Hierin gaan we verder dan ruimte-gebaseerde zwermen en kijken we naar de bredere klasse van ankerloze netwerken met mobiele knooppunten.

Gegeven twee-weg communicatie tussen knooppunten laten we in hoofdstuk 4 zien dat de klokparameters tussen de knooppunten gemeenschappelijk geschat kunnen worden (onder niet-relativistische aannames). Bij gebrek aan een voorgedefinieerde tijdreferentie stellen we een aantal statistisch optimale referenties voor, en behandelen we de prestaties van deze blinde klok-referenties.

Onder aannames van onafhankelijke lineaire snelheden laten we in hoofdstuk 5 zien dat de relatieve snelheid van de knooppunten geschat kan worden, gegeven enkel de tijdvariërende paarsgewijze afstanden. Het datamodel in dit hoofdstuk wordt vervolgens veralgemeend en uitgebreid in hoofdstuk 6, waarin we de hogere-orde relatieve kinematica ontwikkelen, zoals relatieve versnellingen. Ter completering laten we zien dat de absolute kinematica van de knooppunten ook verkregen kan worden uit het voorgestelde datamodel, als de absolute kinematica van enkele knooppunten

bekend is. We leiden theoretische ondergrenzen af voor deze modellen om de prestatie van de voorgestelde algoritmes te testen.

Hoewel de nadruk van dit proefschrift ligt op relatieve localisatie en synchronisatie, zijn een aantal van de voorgestelde technieken geschikt voor bredere toepassingsgebieden rond zelfstandig leren en exploratieve data-analyse.

Alle-Jan van der Veen
Delft, The Netherlands

List of Figures

List of Tables

Contents

Contents

1

Introduction

1.1   Motivation

This dissertation aims to understand the relative space-time kinematics of an anchorless network of asynchronous mobile nodes under non-relativistic motion.[1] Kinematics is the study of mobile nodes, without considering the forces that caused the motion or the masses of those nodes. In this work, a cluster of mobile nodes is considered, where the relative time-varying positions have to be estimated. We pursue this challenge by modeling and estimating the relative spatial kinematics of the mobile nodes, given two-way communication. In addition, all the nodes are equipped with clocks on-board, which must also be synchronized. These mobile nodes reside in an Euclidean space with no absolute reference for position or time, and thus the cluster of asynchronous nodes form an anchorless network. Such anchorless networks are often described in literature as GPS-free networks [Čapkun, Hamdi and Hubaux 2002] or anchor-free networks [Priyantha et al. 2003].

A key motivation to pursue this topic stems from the application of space-based ultra-long wavelength radio astronomy, which is briefly discussed in Section 1.2. The challenges of estimating relative space-time kinematics in the context of classical anchored localization and synchronization is laid out in Section 1.4. In Section 1.6, the goal of this dissertation along with key research questions are presented. A brief outline of this dissertation is given, highlighting the main contributions. The results of this dissertation have been disseminated in various peer-reviewed journals and conferences in diverse fields, which are listed in Section 1.7.

1.2   Radio astronomy

Astronomy is the study of our cosmos, the celestial objects within, and the related phenomena that govern their existence and evolution. The oldest form of astronomy is optical astronomy, which describes the observations in the visible spectrum of ≈ 400nm to ≈ 700nm. Until the late nineteenth century, observational astronomy was only limited to this narrow band of visible wavelengths. This limitation was primarily due to the atmospheric blockage of other wavelengths and also due to lack of high quality detectors. The discovery of infrared radiation (wavelengths longer than red light) in 1800 was a landmark event, which marked the beginning of our understanding of the universe beyond the known visible spectrum.

---

[1]The terminology 'space-time' should not be misinterpreted as the 'spacetime continuum', which is a mathematical model considered in relativistic scenarios. Throughout this dissertation we only consider non-relativistic scenarios, and limit our discussion to the Euclidean space.
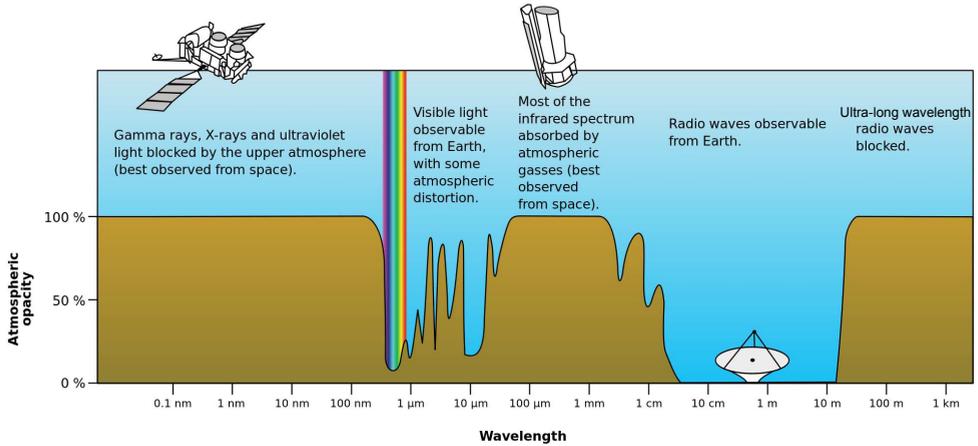
Figure 1.1: ***Atmospheric opacity:*** The opacity (or transparency) of the Earths' atmospheric at various wavelengths across the electromagnetic spectrum [Wikipedia 2008].

Over the last century, baring a few frequency windows, almost the entire electromagnetic spectrum has been explored by either improved ground based detectors, or by going to outer-space beyond the atmospheric barrier, or both. The technological advancements in the aerospace industry and key policy decisions played a major role in this success. As seen in the Figure 1.1, in the spectral regions of atmospheric opacity, space-based detectors such as International ultraviolet explorer, Chandra X-ray Observatory [Weisskopf et al. 2000], XMM-Newton [Jansen et al. 2001] and Fermi gamma-ray space telescope [Atwood et al. 2009] opened the observational windows of ultraviolet spectra, x-rays and gamma-rays. In the visible, near-infrared and near-ultraviolet spectra, the Hubble telescope not only achieved higher resolution, but also led to groundbreaking discoveries, such as the observational validation of the accelerating universe [Riess et al. 1998]. The emissions at these various wavelengths are governed by diverse physical mechanisms and thus offer new insights about the cosmic processes under study, which otherwise would not be possible only with observations in the optical spectrum.

Unlike the wavelengths below a few centimeters, radio astronomy enjoys a transparent atmosphere for a significantly large spectral window. Radio astronomy explores the cosmos in the radio frequencies of 10MHz-3GHz (i.e., $\approx$ 30m up to $\approx$ 1cm). Despite this natural advantage, the advent of radio astronomy was much recent, and arrived only after the inception of infrared astronomy. All along the nineteenth century, although physicists speculated the possibility of observing radio

ways from cosmic objects, progress was hindered due to technical limitations of the instruments of that era. It was not until early 20th century, when the dawn of radio astronomy appeared serendipitously. In 1931, a Bell labs engineer named Karl Jansky, was investigating long-distance ship to-shore communications at the wavelength of 14.6m. During one of his experiments, he fortuitously detected an extraterrestrial radiation from the center of our Milky Way galaxy. Since this historical event, radio astronomy has enabled numerous groundbreaking discoveries in the last few decades. These include, radio galaxies in 1948, the observation of the 21cm hydrogen line in 1951, quasars in 1963, cosmic wave background (CMB) in 1965, and pulsars in 1968, to name a few. For an excellent review on the evolution of radio astronomy see [Arnold 2014], and for an overview of radio astronomy instrumentation refer to [Wilson, Rohlfs and Hüttemeister 2009].

The development of Earth-based radio astronomy has historically been toward higher angular resolution, higher sensitivity and shorter wavelength. More recently however, interesting and fundamental scientific drivers have rekindled the interest in long wavelength radio astronomy of > 3m [Weiler 2000; Jester and Falcke 2009]. For example, to better understand the orgins of our universe, astronomers observe the highly red-shifted 21cm line emission from the epoch of re-ionization era [Zaroubi et al. 2012]. The radiation emitted during the Dark Ages is Doppler shifted to longer wavelengths, which is typically more than few meters. Consequentially, the past decade has seen the rise of various radio astronomy arrays, particularly for low-frequency observations below 100MHz, e.g., low frequency array (LOFAR) [van Haarlem et al. 2013]. However, towards the lower end of this spectrum, Earth-based radio astronomy below frequencies of 30MHz (> 10m) is severely restricted due to man-made interference, ionospheric distortion and almost complete non-transparency of the ionosphere below 10MHz (> 30m), as illutrated in Figure 1.1. Therefore, this narrow spectral band remains possibly the last unexplored frequency range in (radio) astronomy. A straightforward solution to investigate these ultra-long wavelengths is to deploy a space-based antenna array far away from Earths' ionosphere. This proposition is no different to what has been successfully achieved in other astronomical spectra.

1.3 Ultra-long wavelength astronomy

The promise of space-based ultra-long wavelength radio astronomy has lured radio astronomers for over half a century, almost since the inception of radio astronomy itself [Gorgolewski 1965]. At these wavelengths, the sky noise dominates the system
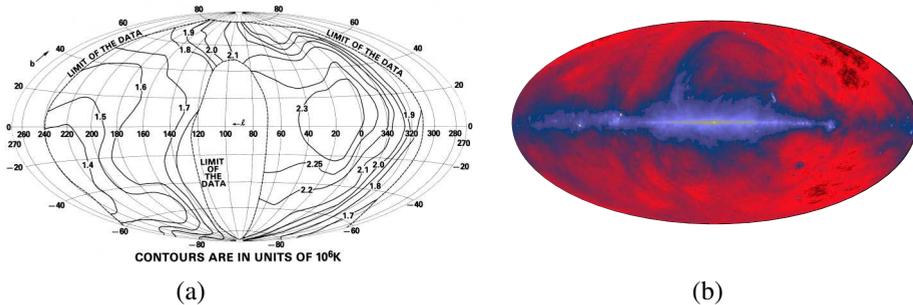
Figure 1.2: ***Status of ultra-long wavelength radio astronomy:*** The all sky map as observed by (a) Lunar orbiter radio astronomy explorer 2 (RAE-2) at 4.7 MHz [Novaco and Brown 1978] and by (b) Jordell Bank + Parks + Effelsberg at 408MHz [Haslam et al. 1982].

performance and subsequently its sensitivity. Therefore, successful missions which mapped the sky in this frequency regime, such as the lunar orbiter RAE-2, were restricted by very poor spatial resolution ($> 30°$). Figure 1.2(a) shows the contour map of non-thermal emission at 4.7MHz, as observed by the RAE-2 in 1973. In comparison, earth based observatories have achieved far higher quality images at 470MHz as shown in Figure 1.2(b). To overcome this impediment, a large number of antennas need to be deployed, with higher bandwidth and longer integration times. To this end, various investigations were conducted in the past, but these attempts were unfortunately limited by technology and computing resources [Weiler 2000]. However current processing and communication trends show promise for ultra-long wavelength astronomy.

Recently concluded projects, such as the ESA funded FIRST (Formation-flying sub-ionospheric radio astronomy science and technology) [Bergman et al. 2009] and DARIS (Distributed aperture array for radio astronomy in space) [Boonstra et al. 2011] , have shown the feasibility of a small cluster of < 10 satellites using off the shelf components. The FIRST study proposed a constellation of 7 satellites deployed at the second Earth-Moon Lagrange (L2) point, sufficiently far enough from Earth to avert interference and allowed for a low-drift orbit. On the other hand, the DARIS study primarily investigated the feasible ULW science cases and showed ready feasibility of 9 satellites using existing off the shelf technologies. The benefits of both these studies were combined in the SURO-LC concept, which proposed a mission at Sun-Earth L2. In all these aforementioned studies, due to the small number of satellites, a centralized architecture was proposed with a dedicated mothership for processing and communication of the observed data. However, for a larger cluster of satellites

catering to multiple science cases, more fundamental technological challenges arise, which were investigated in the OLFAR (Orbiting Low Frequency Antennas for Radio Astronomy) project [Rajan et al. 2011]. These challenges include, for instance, deployment of a large number of satellites with multiple observational antennas, inter-satellite communication, distributed signal processing, imaging at ultra-long wavelengths, down-linking science data to Earth and radio frequency interference (RFI) mitigation. These challenges and the current status of ultra-long wavelength radio astronomy are discussed in Chapter 2 of this dissertation.

In addition to the above issues, a fundamental challenge is to jointly localize and synchronize all the satellites in the network [2]. The space-based ultra-long wavelength array will be deployed far away from Earth based interference, and thus may be beyond the range of our GPS guidance systems. Furthermore, the sheer number of possible satellites (> 10) makes it challenging for our ground based stations to constantly monitor and track the space-time of these satellites. In case the satellite array is Lunar orbiting, then Earth occultation of the satellite array behind the Moon may completely obstruct Earth based communication and guidance for a period of few hours. Hence the satellite array will be an anchorless network, cooperatively estimating the time varying relative position, and correct for their respective on-board clock errors. Incidentally, the estimation of relative positions and time are sufficient for on-board processing of astronomical data, for inter-satellite communication and for collision avoidance.

The estimation of the relative time-varying positions and clock errors is the central theme of this dissertation. However, the discussion is not limited to satellite arrays, instead a much broader category of wireless mobile networks will be addressed. In the following section, we briefly discuss the challenge of estimating relative time-varying positions and clock errors in the absence of anchors and in the context of prevalent localization and synchronization solutions.

1.4 Localization and synchronization

In recent years, tremendous advances in MEMS and semiconductor technology have propelled the development of low-cost sensor nodes, which are capable of efficient wireless communication and data processing. In wireless networks comprising of

---

[2]Incidentally, the quest for accurate time keeping and precise position awareness is intricately woven with the origins of astronomy and the needs of ancient voyagers. For an excellent review on the evolution of time keeping and navigation, refer to [Allan, Ashby and Hodge 1997] and [Samama 2007] respectively.

such sensor nodes, localization and synchronization are quintessential for communication, data processing, prudent statistical inference and in general coherent functioning of the network. In the burgeoning era of big data and internet of things (IoT), accurate time stamping of the given data and the spatial information of the sensor nodes is almost indispensable. Localization and synchronization enabled wireless sensor networks pervade numerous applications areas of the modern age society, e.g, defense, healthcare, scientific, industrial, civilian , home networks, and in the context of this dissertation, space-based satellite networks [Mautz 2012; Wang, Ghosh and Das 2010].

1.4.1 Synchronization

Accurate positioning of nodes in a network is almost always related to accuracies of clocks on-board the nodes. Wireless networks consisting of numerous nodes are typically equipped with cheap and light-weight clocks, such as crystal oscillators, which offer portability and economic feasibility. However, crystal oscillators are highly non-linear in nature, with timing errors of few tens of parts per million (ppm), and thus have to be corrected frequently for numerous applications [Elson and Römer 2003]. An alternative is to use an atomic clock, such as Cesium beams, Rubidium, Hydrogen masers, which offer orders of magnitude higher accuracy. However, a major drawback of such clocks are that they are typically bulky, expensive and power hungry devices. Nonetheless, these atomic clocks can be used to improve the long-term stability of the cheaper clocks, such as crystal oscillators. Thus, the calibration of less accurate clocks against a higher quality clock reference via communication i.e., clock synchronization, is a crucial aspect of all wireless (sensor) networks. A detailed overview of various standards, classifications, time (and frequency) characterizations and popular metrics to evaluate clocks can be found in [Riley 2008].

1.4.2 Localization

Localization i.e., position estimation of nodes, can be broadly categorized under numerous categories, for e.g., as indoor vs outdoor localization, anchored vs anchorless, the radios employed for measurements and more importantly, the type of measurement techniques employed [Patwari et al. 2005; Mao, Fidan and Anderson 2007; Sayed, Tarighat and Khajehnouri 2005b]. These measurement techniques typically fall under three subgroups, namely range-based (lateration), angle-based (angulation) and proximity-based. In proximity-based scenarios, a dense grid of known anchors are deployed and the position of the unknown node is estimated by identifying its'

collocations w.r.t the known anchor positions. The angle-based solutions, measure the angle of arrival (AoA) and the desired target can be localized by the intersection of several pairs of angle direction lines, each formed by a cone from an anchor (or base station). Along similar lines, range-based solutions measure directly the distance between the node and the anchor via signal strength or time propagation delay over the channel of communication.

The prevalent range-based techniques are the round trip time of flight (RTOF), time of arrival (TOA), time difference of arrival (TDOA) and received signal strength (RSS). The RSS directly measures the power of the received signal and is typically insensitive timing discrepancies, however offers poor accuracy and needs models specific to the application case and environment. Alternatively, the TDOA scheme provides improved accuracies and eliminates the timing errors of the node to be localized. The anchors of a TDOA network must still be synchronized. Unlike the angle-based, proximity-based, TDOA and RSS techniques, if modeled correctly, TOA captures both the clock discrepancies of the nodes and the pair distances [Rajan and van der Veen 2011]. Since the pursuit in this work is to understand both time-varying positions and clock errors, the focus throughout this dissertation is on TOA measurements. Traditionally, the problem of localization and synchronization has been resolved independently. However, due to the overwhelming demands for self-governing networks, the problem of joint localization and synchronization has been recently explored [Wang, Ma and Leus 2011b; Ahmad et al. 2013].

1.5   Relative space-time kinematics

In contrast to anchored networks, joint synchronization and localization solutions for anchorless networks have received considerably less attention. Such anchorless networks naturally arise when nodes in the network are deployed in inaccessible locations or only can only be intermittently monitored. For instance, RF signals are heavily attenuated in underwater communication and hence employing GPS based solutions are challenging [Akyildiz, Pompili and Melodia 2005; Chandrasekhar et al. 2006]. In indoor wireless sensor networks when anchor nodes are sparsely deployed, access to a spatial reference frame is only sporadically available [Yang, Wu and Liu 2012]. As discussed in earlier sections, a space-based array deployed on the lunar far-side or lunar orbiting may be devoid of anchors, and therefore must cooperatively estimate the time-varying satellite positions.

For immobile networks, the relative positions of a network of N nodes in P dimensional space can be estimated using Multidimensional scaling (MDS) like al-

gorithms [Shang and Ruml 2004]. The origins of MDS stem from the field of psychometrics [Kruskal 1964] and later matured under multivariate analysis [Borg and Groenen 2005]. Furthermore, when the nodes are mobile but the pairwise distances are fixed, then we consider the study of rigid body kinematics ["Dynamics of Multibody Systems" 2008]. However, the broader challenge of estimating relative positions of mobile nodes from time-varying distance measurements has not been not sufficiently investigated. When the nodes are mobile, then subspace tracking based algorithms yield relative time-varying positions, however this is valid only under small perturbations and does not give sufficient insight into the kinematics of motion [Jamali-Rad and Leus 2012]. To truly understand the relative positions over time, one must estimate the relative kinematics of the mobile nodes, which include the relative position, relative velocity and other higher order derivatives.

A fundamental bottleneck towards this challenge is that our understanding of relative kinematics is inherently in terms of an absolute reference. For instance, relative velocity (the first order relative kinematics) is rightly defined as the subtraction of two absolute velocity vectors. In the absence of anchors, i.e., an absolute reference frame, a natural question arises, if the relative kinematics of the mobile nodes can be estimated given only time-varying distances. Secondly, in addition to the spatial kinematics, the clocks on-board these nodes are also time-varying. Therefore the clock errors and time-varying distance must be efficiently decoupled. This dissertation addresses these unique challenge of understanding and estimating relative space-time kinematics, which to the best of the author's knowledge has never been addressed before.

1.6   Scope of this dissertation

In this section, the scope, goals and the research challenges of this dissertation are presented, in addition to a brief summary of key results from each chapter.

1.6.1   OLFAR

The research work presented in this dissertation was funded under the STW OLFAR project, within the ASSYS perspectief program. OLFAR is orbiting low frequency antennas for radio astronomy, a project that aims to design and develop a detailed system concept for a swarm (> 50) of scalable autonomous satellites in space (well above the Ionosphere) to be used as a scientific instrument for ultra-long wavelength observations. The large number of such spatially distributed satellites will collect-

ively synthesize an aperture dish of diameter 100 km. To ensure coherent communication between the satellites, collision avoidance, time-stamping of observation data and for radio astronomy imaging, all the satellites must be tightly synchronized and localized in the absence of anchors, which is the primary focus of this dissertation.

1.6.2   Problem statement

Consider an anchorless network of N asynchronous mobile nodes in a P dimensional Euclidean space, with no absolute information on time and spatial reference frame. Given two-way communication between the nodes, estimate the clock discrepancies and the relative kinematics of the mobile nodes.

1.6.3   Research questions

The problem statement can be further broken down into smaller questions, which will be addressed in this dissertation. Given an anchorless network of N asynchronous mobile nodes in a P dimensional Euclidean space, each of which is capable of two-way communication, we pose the following research questions.

(R1) **Synchronization and ranging:** How can the time-varying pairwise distances and clock discrepancies be estimated simultaneously ?

(R2) **Choice of clock reference:** How does the choice of clock reference impact the accuarcy of the estimates? What is the most optimal clock reference ?

(R3) **Relative position and relative velocity:** How can the relative positions and relative velocities of the nodes be jointly estimated using only time-varying pairwise distance measurements ?

(R4) **Relative kinematics:** In addition to relative position and relative velocity, how can the higher order kinematics of motion such as relative acceleration be estimated ?

For the sake of a better understanding, we illustrate these research questions in Figure 1.3, which is discussed in the following section. These illustrations will be used consistently in appropriate chapters of this dissertation.
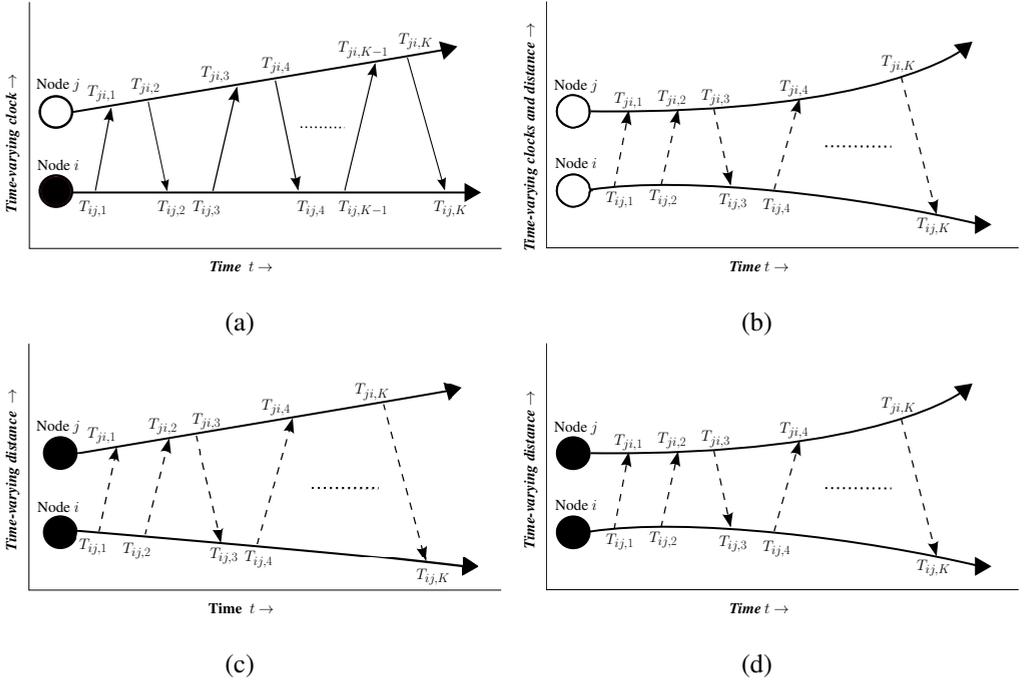
Figure 1.3: ***Generalization of two-way ranging to mobile nodes:*** (a) Classical two-way ranging between a pair of fixed asynchronous nodes, (b) Generalized two-way ranging (GTWR) between a pair of asynchronous mobile nodes (Chapter 4), (c) A pair of mobile nodes with linear independent velocities (Chapter 5), (d) A pair of mobile nodes with non-linear motion (Chapter 6). The shaded nodes indicate ideal clocks.

1.6.4 Generalized two-way ranging (GTWR)

An underlying contribution in this dissertation is the generalization of the classical two-way ranging (TWR) framework. Figure 1.3(a) shows the TOA based TWR between a pair of asynchronous nodes which is commonly applied in wireless sensor networks for both synchronization and ranging [IEEE Working Group 802.15.4 2007; Sundararaman, Buy and Kshemkalyani 2005]. The node pair $\{i, j\}$ transmit and receive alternatingly, during which K timestamps are recorded at each node. The transmission (or reception) recorded at node i and node j are denoted by $T_{ij,k}$ and $T_{ji,k}$ respectively. Under the assumption that node i (shaded in black) is the clock reference, node j appears to drift linearly w.r.t. node i despite the fixed distance between the

nodes. This framework can be readily extended to sender-receiver, receiver-receiver, pairwise listening, broadcasting and other prevalent communication schemes (see [Wu, Chaudhari and Serpedin 2011] and references therein). However, in these scenarios the pairwise distance between the nodes is assumed fixed and the clock model is almost always linear. More recent studies have also considered solutions using non-linear clock models for fixed networks [Xie, Janssen and van der Veen 2016].

In this dissertation, we propose an extension of the classical TWR to a mobile scenario. The generalized two-way ranging (GTWR) is illustrated in Figure 1.3 (b), which in comparison to TWR, offers distinct additional features. Firstly, although the two-way communication is essential, we levy no constraints on the sequence, direction or number of communications. Secondly, we now consider both time-varying clocks and time-varying distances simultaneously which is illustrated by the curved lines. This enables us to solve the joint synchronization and ranging problem for mobile nodes, which is the research question posed as (R1) in the previous section. Finally, in search of an optimal clock reference (R2), both the nodes are considered asynchronous at the outset, unlike in Figure 1.3(a).

In the later part of this dissertation, the focus is solely on the spatial kinematics of the nodes, where we assume the mobile nodes are synchronized. In particular, we consider two scenarios. Firstly, to jointly understand relative position and relative velocity (R3), we consider that the nodes are in independent linear motion, which is shown in Figure 1.3 (c). Secondly, to address (R4), we investigate the more general case, where the node positions are non-linear functions of time, which is illustrated in Figure 1.3 (d). In comparison to Figure 1.3 (b), in Figure 1.3 (d) we consider only the time-varying distance and assume synchronized nodes, as indicated by the shaded nodes.

1.6.5   Outline and main results

The outline of this dissertation is now presented, along with the main results from each chapter.

Chapter 2 is an overview of the current status of space-based radio astronomy for ultra-long wavelength observations.

- *Previous studies:* An extensive survey of previous space-based radio astronomy studies and missions are summarized.

- *System design:* The achievable science cases supported by an ultra-long wavelength array are briefly discussed, along with the design requirements

for a specific science case, namely extra-galactic surveys. A concise study on various subsystems is presented, including radio astronomy antenna design, processing and communication architectures. The navigation challenges and the need for joint space-time estimation of the satellites are studied. A list of potential deployment locations are discussed, in addition to the technological challenges for future space-based arrays.

Chapter 3 discusses the clock requirements for a wireless sensor network, with a particular spotlight on space-based radio astronomy arrays.

- *Clock model:* The phase errors of a clock is modeled as a polynomial in time. The short term and long term accuracies of the clock are discussed in terms of clock jitter and Allan deviation respectively.

- *Clock requirements:* For a space-based array, given a sufficiently low Allan deviation for a certain coherence time, we show that it suffices to assume the clock as a linear model. The clock requirements of a satellite array for ultra-long wavelength observations are presented, and a list of commercially available clocks are discussed.

Chapter 4 presents a framework to jointly synchronize and estimate the pairwise-distances of an anchorless network of mobile nodes (Figure 1.3 (b)), and subsequently addresses the research questions (R1) and (R2). The key contributions of this chapter are as follows

- *Time-range model:* A novel time-range model is presented which combines a first-order clock model with a polynomial approximation of the time-varying pairwise distance.

- *Algorithms:* For a pair of asynchronous nodes, we present a Least squares based solution to jointly estimate clock errors and the time-varying pairwise distance. The proposed solution is extended to enable network-wide ranging and synchronization, using a constrained Least squares approach.

- *Choice of clock reference:* The effect of the clock reference(s) on the accuracy of the clock estimates is discussed, particularly in pursuit of an optimal clock reference (see research question (R2)).

- *Cramér-Rao bounds:* To validate the performance of the proposed estimators, theoretical lower bounds are derived for Gaussian noise assumption on the

measurements. The Cramér-Rao lower bound is the lowest achievable variance by any unbiased estimator.

Chapter 5 deals with the joint relative position and relative velocity estimation of an anchorless network of mobile nodes, and therefore addresses the question (R3). In contrast to the previous chapter, we assume that the nodes are synchronized as illustrated in Figure 1.3 (c). The key results of this chapter are as follows

- *First-order relative kinematics:* A novel data model is developed, which relates the time-varying distance measurements to the first-order relative kinematics of the nodes. The term relative velocity is defined along similar lines to the well known relative position.

- *Algorithms:* Closed-form algorithms are proposed for jointly estimating the relative positions and relative velocities of the nodes. Given these estimates, a framework to estimate the time-varying relative positions of the nodes is also presented.

- *Cramér-Rao bounds:* For a network of N nodes in P dimensional Euclidean space, Cramér-Rao bounds are derived for unbiased estimators of relative position and relative velocity.

Chapter 6 extends the first-order kinematic model to estimate the Mth order relative kinematics, and searches for solutions to the research question (R4). The contributions of this chapter are as follows

- *Relative kinematics:* A generalized data model is derived, which relates the time-varying distances to the relative positions of the nodes over time. In particular, the goal is to estimate the relative position, relative velocity and higher order derivatives. The new data model is inherently ill-posed, which can be solved using relative immobility constraints.

- *Algorithms:* We propose a constrained optimization problem, and subsequent estimators for both the absolute and relative kinematics of the mobile nodes.

- *Cramér-Rao bounds:* Constrained and unconstrained lower bounds are derived for the proposed relative and absolute kinematics estimators, based on the novel data model.

Chapter 7 reports the final conclusions of this dissertation and provides suggestions for future work.

1.7 List of publications

The work presented in this dissertation has led to the numerous peer-reviewed journals and conferences, which span across the fields of signal processing, aerospace and astronomy. The principal article leading to each chapter of this dissertation is mentioned at the beginning of the appropriate chapter. A list of selected publications are as follows.

Journals

[J1] **R. T. Rajan**, G. Leus, and A. -J. van der Veen. "Relative Kinematics Of An Anchorless Network". In: Submitted to *Elsevier* Signal Processing.

[J2] **R. T. Rajan** et al. "Space-based Aperture Array For Ultra-Long Wavelength Radio Astronomy". In: *Springer* Experimental Astronomy (2016).

[J3] **R. T. Rajan**, G. Leus, and A. -J. van der Veen. "Joint relative position and velocity estimation for an anchorless network of mobile nodes". In: *Elsevier* Signal Processing 115 (2015), pp. 66–78.

[J4] **R. T. Rajan** and A. -J. van der Veen. "Joint Ranging and Synchronization for an Anchorless Network of Mobile Nodes". In: *IEEE* Transactions on Signal Processing, 63.8 (Apr. 2015), pp. 1925–1940.

[J5] S. Chepuri, **R. T. Rajan**, G. Leus, and A. -J. van der Veen. "Joint Clock Synchronization and Ranging: Asymmetrical Time-Stamping and Passive Listening". In: *IEEE* Signal Processing Letters 20.1 (Jan. 2013), pp. 51 –54.

Selected Conferences

[C1] H. Ramezani, **R. T. Rajan**, and G. Leus. "Cramér Rao Lower Bound for Underwater Range Estimation with Noisy Sound Speed Profile". In: *IEEE* 48th Asilomar Conference on Signals, Systems and Computers, 2014, pp. 44–48.

[C2] **R. T. Rajan**, G. Leus, and A. -J. van der Veen. "Relative Velocity Estimation Using Multidimensional Scaling". In: *IEEE* International Workshop on Computational Advances in Multi-Sensor Adaptive Processing (CAMSAP), Dec. 2013, pp. 125–128. [3]

---

[3][C2] was nominated for the best paper award at the *IEEE* CAMSAP 2013 conference.

[C3] **R. T. Rajan**, M. Bentum, and A. -J. Boonstra. "Synchronization for space based ultra low frequency interferometry". In: *IEEE* Aerospace Conference. Mar. 2013, pp. 1–8.

[C4] **R. T. Rajan**, M. Bentum, A. Gunst, and A. -J. Boonstra. "Distributed correlators for interferometry in space". In: *IEEE* Aerospace Conference, Mar. 2013, pp. 1–9.

[C5] **R. T. Rajan** and A. -J. van der Veen. "Joint non-linear ranging and affine synchronization basis for a network of mobile nodes". In: European Signal Processing Conference (EUSPICO). Sept. 2013, pp. 1–5.

[C6] **R. T. Rajan** and A. -J. van der Veen. "Joint motion estimation and clock synchronization for a wireless network of mobile nodes". In: *IEEE* International Conference on Acoustics, Speech and Signal Processing (ICASSP). Mar. 2012, pp. 2845–2848.

[C7] **R. T. Rajan** and A. -J. van der Veen. "Joint ranging and clock synchronization for a wireless network". In: *IEEE* International Workshop on Computational Advances in Multi-Sensor Adaptive Processing (CAMSAP). Dec. 2011, pp. 297 –300.

[C8] A. Budianu, **R. T. Rajan** et al. "OLFAR: Adaptive topology for satellite swarms". In: International Astronautical Congress (IAC). Republic of South Africa, Oct. 2011, pp. 1–9.

[C9] **R. T. Rajan**, S. Engelen et al. "Orbiting Low Frequency Array for Radio astronomy". In: *IEEE* Aerospace Conference. Mar. 2011, pp. 1 –11.

[C10] N. Saks, A. -J. Boonstra, **R. T. Rajan** et al. "DARIS, A Fleet of Passive Formation Flying Small Satellites for Low Frequency Radio Astronomy". In: Small Satellites Systems and Services - The 4S Symposium. 2010.

Selected Technical Reports

[T1] **R. T. Rajan** Signal processing estimates for DARIS. Technical Report:ASTRON-RP-388. Netherlands Institute for Radio Astronomy (ASTRON), Jun. 2010.

[T2] **R. T. Rajan** Clock requirements for radio astronomy in space. Technical Report:ASTRON-RP-385. Netherlands Institute for Radio Astronomy (ASTRON), Jun. 2010.

Other contribution

[M1] M. J. Bentum, C. J. M. Verhoeven, S. Engelen, **R. T. Rajan** and A. Budianu, "Radiotelescoop zwermt uit rond de maan". In: *Bits&Chips*, Mar.2013

Space-based radio astronomy

The aim of this chapter is to discuss the current trends and technologies towards the feasibility of a space-based aperture array for astronomical observations in the Ultra-Long Wavelength (ULW) regime of greater than 10m i.e., below 30MHz. The achievable science cases are discussed, and the system design for selected scenarios such as extra-galactic surveys is presented. A discussion is presented on various sub-systems of the potential satellite array, such as radio astronomical antenna design, the on-board signal processing, communication architectures and joint space-time estimation of the satellite network. In light of a scalable array and to avert single point of failure, we propose both centralized and distributed solutions for the ULW space-based array. The benefits of various deployment locations discussed and the technological challenges for future space-based radio arrays are summarized.

2.1 Introduction

The success of Earth-based radio astronomy in the frequencies between 30MHz and 3GHz is jointly credited to Earth's transparent ionosphere and the steady technological advancements during the past few decades. In recent times, radio astronomy has seen the advent of a large suite of radio telescopes, particularly towards the longer observational wavelengths, i.e., $\geq$ 3m. These arrays include the Murchison widefield array (MWA) [Lonsdale et al. 2009], low frequency array (LOFAR) [van Haarlem et al. 2013] and the long wavelength array (LWA) [Ellingson et al. 2009] to name a few. These developments have been motivated by new and interesting science drivers such as the detection of highly red-shifted 21cm line emission from the epoch of re-ionization [Zaroubi et al. 2012], deep surveys of the sky in search for high redshift radio sources [Röttgering et al. 2011], surveys of pulsars and cosmic radio transients [Stappers et al. 2011] and study of ultrahigh-energy cosmic rays [Falcke et al. 2005]. The frequencies below 30MHz are well suited for studying the global dark ages signal, extragalactic surveys, (extra) solar planetary bursts and high energy particle physics [Weiler 2000; Jester and Falcke 2009].

However, Earth-based astronomical observations at these ultra-long wavelengths are severely restricted [Kaiser and Weiler 2000]. Firstly, due to ionospheric distortion, especially during the solar maximum period, scintillation occurs and the celestial signals suffer from de-correlation among the elements of a ground based telescope array [Kassim et al. 1993]. Advanced calibration and mitigation techniques which are currently employed in LOFAR can be used to remove these distortions, provided the time scale of disturbances is much longer than the time needed for calibration process [Wijnholds et al. 2010]. Furthermore, at frequencies below 10MHz the iono-

sphere is completely non-transparent which impede observations by ground-based instruments. In addition to ionospheric interference, man-made transmitter signals below 30MHz also impede astronomical observations. This terrestrial interference was even observed as far as ~400,000km away from Earth by the RAE-2 lunar orbiter, which was limited by very poor spatial resolution at these wavelengths, e.g., $37°$ at 9.18MHz [Alexander et al. 1974]. Due to the above mentioned reasons, the very low frequency range of $0.3 - 30$ MHz remains one of the last unexplored frontiers in astronomy. *A straightforward solution to observe the radio sky at ULW with the desired resolution and sensitivity is to deploy a dedicated satellite array in outer-space.* Such a space-based array must be deployed sufficiently far away from Earth's ionosphere, to avoid terrestrial interference and offer stable conditions for calibration during scientific observations.

2.1.1 Previous studies

The proposition for a space-based radio astronomy instrument is not novel [Weiler et al. 1988; Basart et al. 1997a; Basart et al. 1997b; Kaiser and Weiler 2000]. One of the first such proposals was made by Gorgolewski [1965], who discussed the benefits of a moon-based radio interferometer. In 1968 and 1973, the RAE-1 [Weber, Alexander and Stone 1971] and RAE-2 [Alexander et al. 1974] satelliets were launched respectively. The RAE-1 covered a frequency range of 0.2MHz to 9.2MHz using two 229 meter V-antennas and one 37 meter electric dipole, while the RAE-2 mapped the non-thermal galactic emission in the frequency range of 25kHz to 13MHz using a single 37m dipole antenna, achieving a resolution of $37°$. These explorers were the first dedicated missions exclusively for ULW radio astronomy. Science at the ultra-long wavelengths was revived in the 1990s with a particular focus on Lunar based arrays [Burke 1990; Burns et al. 1990]. The Lunar surface on the far-side presents a large and stable platform for antennas and shields unwanted interference from Earth and the Sun [Woan 1999; Kuiper and Jones 2000; Takahashi 2003; Aminaei et al. 2014], which motivated studies such as VLFA [Smith 1990], MERIT [Jones et al. 2007] and more recently DEX [Klein-Wolt M. et al. 2013]. Along similar lines, Lunar orbiting single-satellite missions dedicated for radio astronomy such as LORAE [Burns 1990] and DARE [Burns et al. 2012] were also investigated to map bright sources and to facilitate relatively easier Earth-based down-link of science data. Furthermore, the pursuit of higher angular resolutions has led to Earth-orbiting single-satellite missions such as HALCA [Hirabayashi et al. 2000] and Radio Astron [Kardashev et al. 2013] which enable Earth-space very long baseline interferometry [Gurvits 2012].

However, the concept of space-based ULW array for radio astronomy has re-

ceived considerably less attention and has been explored inadequately, which is our primary focus in this chapter. The successful single-satellite RAE missions motivated the first space-based array proposal to NASA i.e., the low frequency space array (LFSA) [Weiler et al. 1988]. Another notable NASA funded study in this regard was the ALFA concept, which proposed an array of $10 - 16$ satellites in a distant retrograde orbit [Jones et al. 2000]. More recently, two ESA funded studies namely FIRST [Bergman et al. 2009] and DARIS [Boonstra et al. 2010] investigated passive-formation flying missions for space-based satellite arrays (see Table 2.1). The FIRST study proposed a constellation of 7 satellites deployed at the second Earth-Moon Lagrange (L2) point, sufficiently far enough from Earth to avert interference and allowed for a low-drift orbit. On the other hand, the DARIS study primarily investigated the feasible ULW science cases and showed ready feasibility of 9 satellites using existing off the shelf technologies. The benefits of both these studies were combined in the SURO-LC concept, which proposed a mission at Sun-Earth L2. In all these studies, a dedicated centralized mothership managed the processing and communication. However, futuristic arrays such as OLFAR [Bentum et al. 2009; Rajan et al. 2011] with ≥ 10 satellites will operate cooperatively and employ distributed architectures for both processing and communication.

2.1.2   Overview

The purpose of this chapter is to discuss the current technological advances towards the feasibility of space-based array for radio astronomy at ultra-long wavelengths. We justify the scientific need for such a space-based array and elaborate on the system design in Section 2.2. Various subsystems of the potential satellite array are discussed in the Sections 2.2 - 2.7, including the astronomy antenna design in Section 2.3. While current technologies limits us to ≤ 10 nodes, we foresee next generation arrays will contain larger number of satellites and operate as a co-operative wireless network. Hence, a dominant theme is the extension of the proposed centralized solutions to distributed scenarios, particularly for processing (Section 2.4), communication (Section 2.5) and joint space-time estimation of the satellites in the network (Section 2.7). We summarize the article with a brief overview of the potential deployment locations (Section 2.6) and the fundamental challenges ahead for a space-based ULW array (Section 2.8).

	FIRST	DARIS	SURO-LC	OLFAR
Timeline	$2009 - 2010$	$2009 - 2010$	$2011 - 2012$	$2010 - 2014$
No. of satellites (N)	$6^{\dagger} + 1^{\ddagger}$	$8^{\dagger} + 1^{\ddagger}$	$\geq 8^{\dagger} + 1^{\ddagger}$	≥ 10
No. of polarizations (N_{pol})	3	3	3	3
Obs. frequency (ν)	$0.3 - 50$ MHz	$0.3 - 10$ MHz	$0.5 - 60$ MHz	$0.3 - 30$ MHz
Instantaneous BW ($\Delta\nu$)	100KHz	1 MHz	1MHz	≥ 1 MHz
Obs. wavelength (λ)	$600 - 6$ m	$10^3 - 30$ m	$600 - 5$m	$10^3 - 10$m
Longest baseline	30 km	100 km	30 km	100 km
Spatial resolution	$0.6'$ at 50MHz	$1'$ at 10MHz	$0.5'$ at 60MHz	$0.3'$ at 30MHz
Array architecture	Centralized	Centralized	Centralized	Distributed
Estimated Mass	≈ 200Kg†, ≈ 10Kg‡	≈ 550Kg†, ≈ 100Kg‡	≈ 500Kg†, ≈ 10Kg‡	≤ 5Kg
Deployment location(s)	Sun-Earth L2	Dynamic solar orbit, Moon far side, Sun-Earth L2	Sun-Earth L2	Earth/Moon orbit

Table 2.1: **Recent space-based aperture array studies:** An overview of system requirements for ultra-long wavelength observations, as specified by various space-based aperture array studies, namely FIRST [Bergman et al. 2009], DARIS [Saks et al. 2010; Boonstra et al. 2010], SURO-LC [Baan 2012] and OLFAR [Bentum et al. 2009; Rajan et al. 2011], where † and ‡ denote mothership and daughter node respectively.

2.2 Ultra-long wavelength interferometry

2.2.1 Aperture synthesis

Radio astronomy imaging is achieved by aperture synthesis, where in the cosmic signals received at a large number of time-varying antenna positions, are coherently combined to produce high quality sky maps. For a $N-$antenna array, each antenna pair forms a *baseline* of an aperture synthesis interferometer, contributing $\bar{N} \triangleq 0.5N(N-1)$ unique sampling points at a given time instant. Let $\mathbf{x}_i(t)$ and $\mathbf{x}_j(t)$ be two arbitrary antenna position vectors at time t forming a baseline, then the corresponding uvw point is defined as

$$[u_{ij}(t), v_{ij}(t), w_{ij}(t)]^T \triangleq (\mathbf{x}_i(t) - \mathbf{x}_j(t))/\lambda, \qquad (2.1)$$

where u_{ij}, v_{ij}, w_{ij} are the spatial frequencies in terms of the observed wavelength λ. Figure 2.1(a) shows (in blue) the uvw points for a $N = 9$ satellite cluster which is arbitrarily deployed with a maximum distance separation of $d = 50$km and an observational frequency of 10MHz. The effective synthesized aperture is then obtained by projecting the uvw points onto a 2-D plane which is orthogonal to the source direction. As an illustration, Figure 2.1(a) shows 3 such projections (in black) for sources orthogonal to the uv, uw and wv planes. The minimum distance between the satellites is only constrained by practical safety requirements and the maximum distance d between the satellites defines the resolution of the interferometric array as

$$\theta = \lambda/d. \qquad (2.2)$$

The Van Cittert-Zernike theorem relates the spatial correlation of these antenna pairs directly to the source brightness distribution by a Fourier transform [Thompson, Moran and Swenson Jr 2008]. Hence for radio imaging, each antenna pair output is cross-correlated to measure the coherence function which is subsequently converted to a sky map, conventionally by an inverse Fourier transform. Figure 2.1(b) shows the normalized Point Spread Function (PSF) corresponding to the aperture coverage in Figure 2.1(a), for a single point source along the w direction. A densely sampled aperture plane lowers the spatial side-lobes of the sky image. The filling factor of the synthesized aperture can be increased by either using bandwidth synthesis or by populating sufficient baselines. In bandwidth synthesis, different frequency channels can be used to scale λ. As shown in Figure 2.1(c) and Figure 2.1(d), using only 10 frequency bins uniformly distributed across $1 - 10$MHz, the aperture filling and the PSF is significantly improved as compared to Figure 2.1(b). A first-order simulation of an array of $N = 9$ satellites in Earth-leading orbit around the Sun yields

orbit
Snapshot

(a) uvw: Snapshot

(d) PSF: Snapshot

(b) uvw: Bandwidth synthesis

(e) PSF: Bandwidth synthesis

(c) uvw: Complete orbit

(f) PSF: Complete orbit
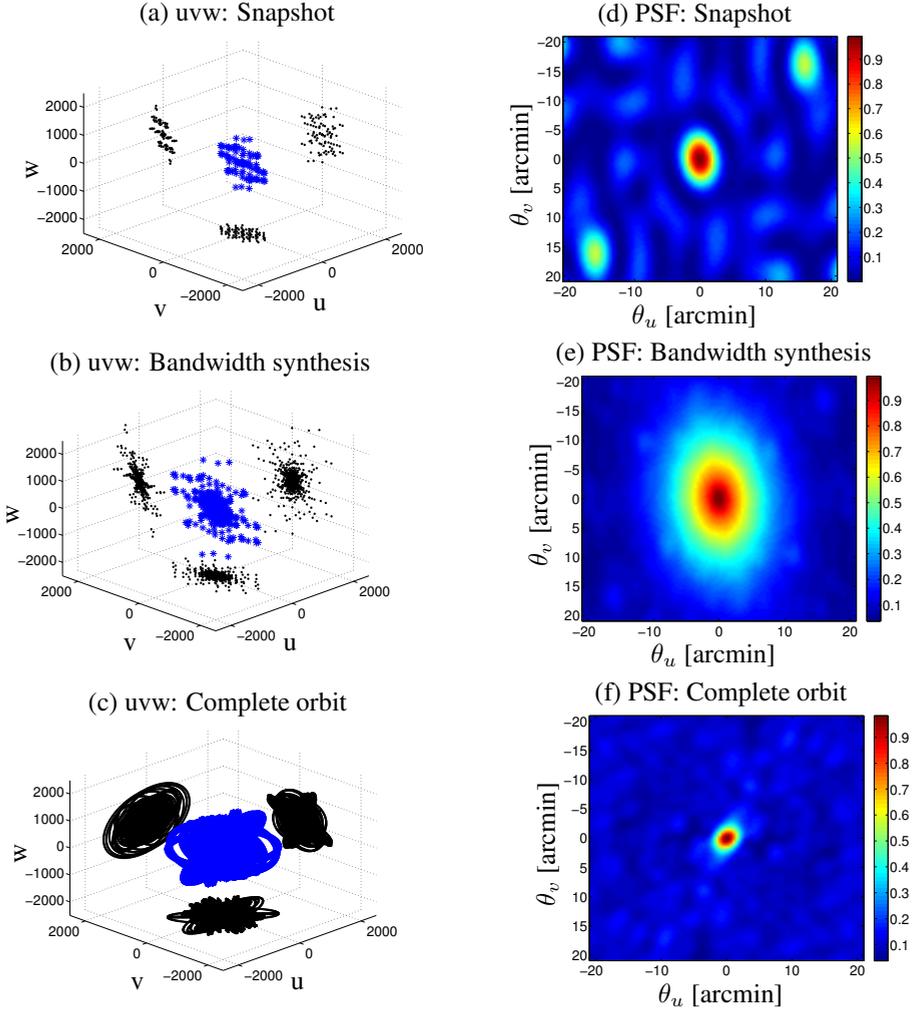
Figure 2.1: ***Baseline and PSF simulations:*** The aperture filling of a 9-satellite ULW array for an Earth leading orbit around the Sun (a)-(c), to illustrate the effect of the sampling space on the normalized Point Spread Function (PSF) (d)-(f). The uvw coverage for the 3-D array of satellites at $\nu = 10$MHz (a) for a single snapshot $N_t = 1$ along with (d) the corresponding PSF. Bandwidth synthesis is illustrated in (b) which shows the uvw coverage of single snapshot using 10 frequency bins uniformly distributed in the range 1 - 10 MHz with (e) the resultant PSF. The subfigures (c) and (f) show the uvw and the corresponding PSF, for an entire orbit around the sun at 10MHz with a single observation each day, i.e., 365 snapshots.

Figure 2.1(e) and the corresponding PSF in Figure 2.1(f), where one snapshot each day is assumed at a single observation frequency of 10MHz. The number of uvw points are directly related to the unique number of baselines and the observational frequency. To achieve the confusion limit and resolve the sources individually, the total number of unique uvw points over the observational time period must be larger than the total number of detected sources.

2.2.2   Ultra-long wavelength sky

The dominant foreground in the low frequency radio sky is the galactic synchrotron radiation, which is due to synchrotron emission from electrons moving in the Galactic magnetic field. This emission causes the brightness temperature to rise from $\sim 10^4$K at 30MHz, to as high as $\sim 10^7$K around 2MHz [Oberoi and Pincon 2005]. At frequencies below 2MHz, the Galactic plane is nearly completely opaque and the extra-galactic sources cannot be observed. More explicitly, for frequencies above 2MHz, the sky temperature can be approximated as [Jester and Falcke 2009]

$$T_{sky} = 16.3 \times 10^6 \text{K} \left(\frac{\nu}{2\text{MHz}}\right)^{-2.53} \quad \text{at } \nu > 2\text{MHz}, \tag{2.3}$$

where ν is the observation frequency. For Earth-based observations at higher frequencies (> 100MHz), the overall system noise temperature T_{sys} plaguing the cosmic signal is typically dominated by the noise from receiver electronics T_{rec}. However, at lower frequencies (≤ 30 MHz), the intense galactic background implies that T_{sky} will be at least an order in magnitude larger than T_{rec}, and hence the overall noise temperature $T_{sky} \gg T_{sys}$. The immediate effect of this extremely high sky noise is the poor sensitivity of the interferometric array. The 1-σ RMS sensitivity for an antenna array of N nodes is [Cohen 2004]

$$S_\sigma = \frac{235.6 \, T_{sys}}{\lambda^2 \sqrt{N(N-1)(t_{obs}/1\text{hour})(\Delta\nu/1\text{MHz})}} \quad \text{mJy/beam}, \tag{2.4}$$

where $\Delta\nu$ is the bandwidth, t_{obs} is the observation time period over which the signal is integrated and the total number of estimated sources above this sensitivity is given by

$$N_>(S) = 1800 \big(S/10\text{mJy}\big)^{-0.3} \big(\nu/10\text{MHz}\big)^{-0.7}. \tag{2.5}$$

Furthermore, the scattering in the interplanetary media (IPM) and interstellar media (ISM) also hinder observational frequencies less than 30MHz, which limit the maximum baseline between the satellites to

$$d_{ISM} = 47\text{km} \times (\nu/1\text{MHz})^{1.2} \quad \text{and} \quad d_{IPM} \approx 10\text{km} \times (\nu/1\text{MHz}). \tag{2.6}$$

For very long baseline interferometry, Linfield et al. [1996] noted that angular broadening of radio sources due to interstellar scattering will cause interplanetary scattering to be greatly reduced. Finally, the lower limit of the achievable noise is not the RMS sensitivity of the array, but the confusion limit. The presence of unresolved sources with individual flux densities below the detection limit leads to a constant noise floor, that is reached after a certain observation time t_{obs} [Jester and Falcke 2009]. For extra-galactic observations, under certain nominal assumptions, this anticipated confusion limit due to background sources is

$$S_{conf}(\theta, \nu) = 16\text{mJy} \times (\theta/1')^{1.54}(\nu/74\text{MHz})^{-0.7}, \qquad (2.7)$$

where θ is the effective resolution for which the flux is below the confusion limit. The confusion limit is the lower limit to the achievable noise floor and thus is an upper limit to the useful collective area of the array. In other words, adding more antennas only decreases the time in which the confusion limit is reached, but not the overall array sensitivity (2.4). The time necessary for an array to achieve this confusion limited sensitivity is given by the "survey equation"

$$t_{survey} = 3.3(N/100)^{-2}(10\nu/\Delta\nu)(\nu/1\text{MHz})^{-0.66}(\theta/1')^{-3.08}. \qquad (2.8)$$

Using these elementary and yet fundamental equations, a preliminary design for a space-based array can be proposed for desired science cases. For a more detailed study, refer to [Jester and Falcke 2009].

2.2.3   System definition

The science cases for an ULW array broadly span cosmology, galactic surveys, transients from solar and planetary bursts and even the study of Ultra-High Energy particles. Although a single satellite mission would suffice to detect the global dark-ages signal, over 10^4 antennas are required to investigate the radio emission from Extrasolar planets [see 2009, Table 1]. For the first space-based ULW array however, with possibly only a few satellite nodes, extra-galactic surveys and study of transients are among the best suited science cases [Boonstra et al. 2011], which we present as case studies. The proposed space-based array design can be readily extended to cater to other science cases, such as detection of the global dark-ages signal.

Parameter	Notation	Units	Equation	Extra-galactic survey					
Sensitivity	S_σ	Jy	Input	6.5E-02	6.5E-02	6.5E-02	6.5E-02	6.5E-02	6.5E-02
Baseline	d	km	Input	100	100	100	100	100	100
Obs. Time	t_{obs}	hours	Input	24	720	8760	720	8760	8760
Obs. frequency	ν	MHz	Input	10	10	10	10	10	30
Bandwidth	$\delta\nu$	MHz	Input	1	1	1	3	3	3
Resolution	θ	arcmin	(2.2)	1.03	1.03	1.03	1.03	1.03	0.34
System temperature[†]	T_{sys}	K	(2.3)	2.8E+05	2.8E+05	2.8E+05	2.8E+05	2.8E+05	1.7E+04
No. of Antennas	N		(2.4)	229	42	12	25	7	4
ISM Max. Baseline	d_{ISM}	km	(2.6)	7.4E+02	7.4E+05	7.4E+05	7.4E+05	7.4E+05	2.8E+06
IPM Max. Baseline	d_{IPM}	km	(2.6)	100.0	100.0	100.0	100.0	100.0	300.0
Confusion limit	S_{conf}	Jy	(2.7)	0.07	0.07	0.07	0.07	0.07	0.01
Resolution (Conf. lim.)		arcmin	(2.4), (2.7)	1.00	1.00	1.00	1.00	1.00	1.65
Max. Baseline (Conf. lim.)		km	(2.2), (2.7)	103.09	103.09	103.09	103.09	103.09	20.86
Time to Conf. lim.		hours	(2.8),(2.7)	0.14	4.05	46.39	3.98	43.64	38.94

Table 2.2: *System requirements for extra-galactic surveys:* The estimated system parameters to achieve the desired resolution of $1'$ and sensitivity of 65mJy for Extra-galactic surveys, for varying observation time, observation frequency and instantaneous bandwidth ([†] indicates sky noise dominated).

The expected signal strength for the extra-galactic surveys is in the order of 65mJy with a desired spatial resolution of ~1′. In Table 2.2, we present different scenarios to investigate the effects of varying observational frequencies, bandwidth and observation time, on the number of antennas to achieve 65mJy. It is evident that increasing the observation time (1 day, 1 month, 1 year) steadily reduces the required number of antennas. Secondly, increasing the bandwidth (1MHz to 3 MHz) is also an alternative to achieve the desired resolution for a small array. However, the increase in bandwidth has little effect on the confusion limit. We note that the confusion limit is a bottleneck for shorter integration times and lower observing frequencies. The maximum baseline is in general confusion limited for frequencies $\geq$ 10MHz, however at $<$ 10MHz, the ISM and IPM scattering limits the maximum baseline and subsequently the resolution. At 10MHz, we require at least one year of observation time with more than 7 antennas for an observational bandwidth of 3MHz to achieve the 65mJy sensitivity. However, in the last column of the Table 2.2, we see that at 30MHz, only 4 antennas sufficient. Such a configuration is estimated to detect over a million sources using (2.5).

A similar investigation was conducted for Jupiter-like flares and Giant crab-like pulses, which are bright events in the order of MJy and kJy respectively, with typical time scales of milliseconds. The desired resolution for these transient radio systems is ~1′ at $\leq$ 30MHz. Since these events are extremely bright, even a single antenna with a nominal bandwidth of 10% of observational frequency would meet the desired requirements. However, unlike the extragalactic surveys the observations are not confusion limited but possibly by the number of baselines for short integration timescales of milliseconds. The number of unique uvw points will depend inadvertently on the deployment location and pairwise distance variations between of the antennas. However, in general this limitation can be overcome by increasing the integration times in both these cases by over a minute.

In general, higher bandwidth, higher observing frequencies and longer integration times require less antennas to reach the same sensitivity level. In this chapter we choose the DARIS mission specifications as a reference to illustrate various subsystems. To this end, we particularly focus on an array of $N = 9$ satellites, with a maximum satellite separation of 100km and capable of observing the skies at $0.1 - 10$MHz. This particular setup meets the requirements for the extra-galactic survey and transient radio system science cases. However, all the proposed techniques and technologies can be readily extended to a larger array, for observation frequencies up to 30MHz.
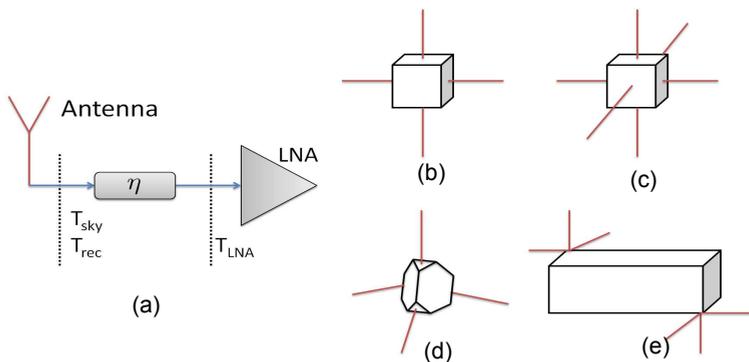
Figure 2.2: ***Space-based antenna model and potential configurations:*** (a) System model of the observation Antenna connected to an LNA (b) Configuration of a dipole antenna on a cubesat (c) Configuration of a tripole antenna in a cubesat (d) Configuration of an antenna with four monopoles (e) A dipole antenna placed on the opposite ends of a 3-cubesat.

2.3 Radio astronomy antenna design

A critical component for the space-based array is the design of the observational antenna. Figure 2.2(a) shows the system model of the observation antenna connected to a LNA, wherein the antenna is modeled as an *ideal* lossless antenna, followed by an attenuator representative of the antenna losses. For the observation frequencies of $0.3 - 30$MHz, this front end must be sky noise limited i.e., $T_{rec} < 0.1T_{sky}$, where T_{rec} is the receiver noise and T_{sky} is the sky noise temperatures which are defined at the interface between the lossless antenna and attenuator. The LNA noise temperature T_{LNA} defined at the input of the LNA is equal to $(1 - \eta)T_0$, where η is the radiation efficiency and T_0 is the physical temperature of the antenna. Without loss of generality, we assume that the LNA noise is dominant over the noise contribution of subsequent electronics of the receiver. Under these assumptions, the prerequisite on the LNA noise temperature is derived as

$$T_{LNA} < (1 - |\Gamma|^2)(0.1\eta T_{sky} - (1 - \eta)T_0), \tag{2.9}$$

where Γ is the reflection coefficient of the antenna [Arts, van der Wal and Boonstra 2010]. A straightforward candidate for the observation antenna is a dipole (e.g., Figure 2.2(b)), which can be realized by rolling out metallic strips from the satellite [Manning 2000]. The observational wavelengths are much larger compared to the dimensions of the satellites and hence due to practical limitations, the realized dipole
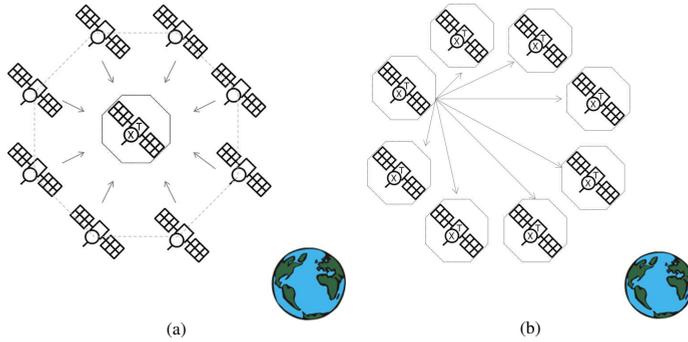
Figure 2.3: ***Correlator architectures:*** An illustration of two potential correlator architectures for space-based radio interferometric array, where the tags 'X' and 'T' on the nodes indicate correlation and transmission to Earth capabilities respectively. In the **(a) centralized correlator** architecture a centralized mother ship receives data from all observational satellites, correlates and down-links data to Earth. On the contrary, in the **(b) distributed correlator** framework, the observed data is evenly distributed among all nodes. After correlation, all satellite nodes down-link their respective correlated data to Earth.

will be short compared to the wavelength. A classic half-wave dipole for 10MHz and 30MHz observation frequencies yields a dipole length of 15m and 10m respectively. For lower frequencies, a similar dipole lengths begets a short-dipole with a directional pattern similar but less directional as compared to the half-wave dipole. Consequentially, the radiation resistance of the small antenna would be low and the thermal noise will significantly dominate the total antenna noise.

Two orthogonal dipoles (Figure 2.2(b)) are in principle sufficient to get all the polarization information of the cosmic signal [Arts, van der Wal and Boonstra 2010], however a tripole (i.e., three dipoles, see Figure 2.2(c)) can be used to obtain information of all 3 components. The third dipole improves the directivity of the antenna system, thereby increasing the field of view. Along similar reasoning, an equiangular spaced four monopole configuration can also be considered, as shown in Figure 2.2(d). However, the number of correlations is much higher and consequentially demanding more signal processing hardware for each antenna. In the OLFAR study where a 3U-cubesat ($30 \times 10 \times 10$ cm) is utilized, the monopoles are deployed in groups of three at the opposite ends of the satellite, as seen in Figure 2.2(e). The asymmetric design changes the properties of the monopoles and reduces the purity of the gain patterns of the independent components, which is studied by Smith and Arts [2013] and experimentally evaluated on a smaller scale by Quillien et al. [2013].

Data rates and processing	Notation/Equation	Value	Units/Remark
No. of satellites (or antennas)	N	9	(scalable)
No. of polarizations	N_{pol}	3	
No. of channels/signals	$N_{sig} = N_{pol}N$	27	
No. of bits	N_{bits}	1	bits
Observation frequency	ν	≤ 10	MHz
Instantaneous bandwidth	$\Delta\nu$	1	MHz
Spectral resolution	$\Delta\nu_{res}$	1	kHz
No. of bins	$N_{bins} = \Delta\nu/\Delta\nu_{res}$	1000	
Snapshot integration time	τ	1	second
Observed data rate	$D_{obs} = 2\Delta\nu N_{pol}N_{bits}$	6	Mbps/satellite
Centralized			
Mothership data reception	$D_{in}^c = D_{obs}(N-1)$	48	Mbps
Earth down link data rate	$D_{out}^c = 2N_{sig}^2 N_{bits}N_{bins}/\tau$	1.46	Mbps
Distributed			
No. of sub-bands	$N_{sb} = N$	9	
Sub-band bandwidth	$\Delta\nu_{sb} = \Delta\nu/N_{sb}$	111.11	kHz
Inter-satellite reception	$D_{in}^d = D_{in}^c/N$	5.34	Mbps/satellite
Earth down link data rate	$D_{out}^d = D_{out}^c/N$	162.2	kbps/satellite

Table 2.3: *Digital signal processing estimates:* Data rate estimates for a centralized correlator and a frequency distributed FX correlator for the DARIS mission of 9-satellites.

2.4 Digital signal processing

Sky images in radio astronomy are made by calculating the Fourier transform of the measured coherence function [Taylor, Carilli and Perley 1999]. The coherence function is the cross correlation product between two antenna signals located at the two spatial positions, averaged over a period of the integration time τ_{int}. One way to implement such a system is using the traditional XF correlator *i.e.,* cross correlation first and Fourier transform later, and the more recent FX correlator which measures directly the cross-power spectrum between the two antenna signals [Bunton 2004]. Although the XF architecture is beneficial because bandwidth can be traded for spectral resolution, the FX architecture offers computational efficiency [Rajan et al. 2013]. The ratio of the number of multipliers required for XF correlator to the FX correlator is given by

$$N_X^{xf/fx} = \left(\frac{N_{sig}N_{bins}}{N_{sig} + \log_2 N_{bins}}\right), \tag{2.10}$$
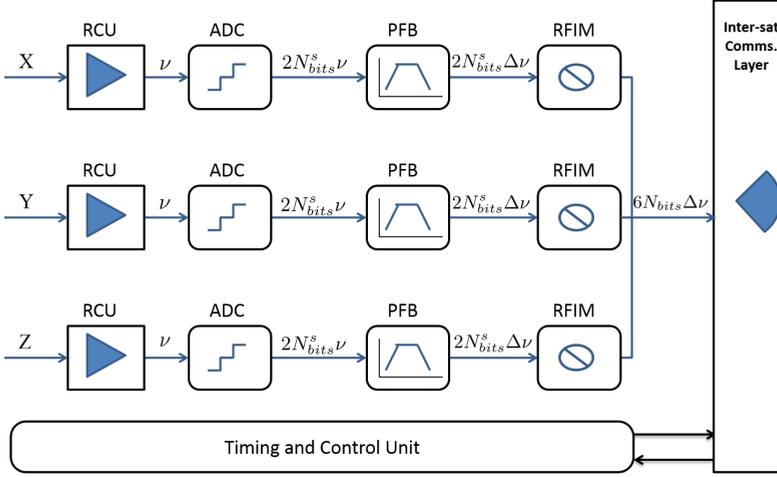
Figure 2.4: ***Node level signal processing:*** Given the low observational bandwidth, the $N_{pol} = 3$ polarized astronomical signals received by each antenna will be signal conditioned and Nyquist sampled with a 14-bit (or more) analog to digital converter (ADC). A coarse poly-phase filter bank (PFB) is used to selectively choose the desired instantaneous bandwidth of $\Delta\nu = 1$MHz. After successful RFI mitigation (RFIM), only $N_{bits} = 1 - 2$bits will be used in further processing stages [Altunin 2001]. The total data generated for N_{pol} signal paths in each satellite is $D_{obs} = 6\Delta\nu N_{bits}$bps, which is transported to the inter-satellite communication layer.

where $N_{sig} = N_{pol}N$, $N_{bins} = \Delta\nu/\Delta\nu_{res}$, $\Delta\nu$ is the instantaneous bandwidth and $\Delta\nu_{res}$ the spectral resolution (See Appendix 2.A). Observe that the multiplicands in the XF mode are additive in the FX mode, besides the $\log_2$ reduction on the number of frequency bins. Thus, although for lower number of nodes the XF is comparable to FX mode, for large scalable architectures the FX mode is computationally cost effective. Since we prefer a scalable space-based array the FX architecture is chosen as the preferred architecture . Table 2.3 shows data rates for a cluster of $N = 9$ nodes, with an instantaneous bandwidth of $\Delta\nu = 1$MHz and $\tau = 1$ second integration time.

A typical pre-processing unit at each satellite node is shown in Figure 2.4, where each satellite generates $D_{obs} = 2\Delta\nu N_{pol}N_{bits}$bps. Observe that with $N_{pol} = 3$, for a signal with nominal instantaneous bandwidth of $\Delta\nu = 1$MHz sampled with $N_{bit} = 1$bit resolution, the output data rate is 6Mbps. Given a far away deployment location, such as Lunar orbit (~400,000 km) or Earth leading/trailing (~2×10^6 to ~4×10^6 km), this down-link data rate levies heavy prerequisites on the limited resources of a small satellite using current techonology. Hence, the satellite cluster must not only employ on-board pre-processing of astronomical signals, but also on-

board correlation to minimize down-link data rate back to Earth. To this end, either a centralized or a distributed correlator can be employed as illustrated in Figure 2.3.

2.4.1   Centralized architecture

In the centralized FX correlator framework each satellite node transmits $D_{obs} = 2\Delta\nu N_{pol}N_{bits}$bps to the centralized mothership, which in turn receives $D_{in}^c = D_{obs}(N-1)$bps in total, excluding the data collected from the antenna on the mothership itself. The input data from all satellites is then correlated and the output is then transmitted down to Earth at the rate $D_{out}^c = (2N_{sig}^2 N_{bins}/\tau)$bps, where $N_{bins} = \Delta\nu/\Delta\nu_{res}$. A significant drawback of the centralized correlation is that it depends heavily on the healthy operation of a single correlation station, which introduces a Single point Of failure (SPOF) for large array of satellites in space.

2.4.2   Distributed architecture

To alleviate SPOF, a Frequency distributed correlator is proposed where each node is assigned a specific sub-band $\Delta\nu_{sb}$ of the observed instantaneous bandwidth $\Delta\nu_{sb}$ for cross correlations [Rajan et al. 2013]. Hence, in addition to the node pre-processing (Figure 2.4), a secondary fine Polyphase Filter Bank (PFB) is implemented to further split the instantaneous bandwidth $\Delta\nu$ into N_{sb} sub bands, each of bandwidth $\Delta\nu_{sb} = \Delta\nu/N_{sb}$. Each satellite is assigned a specific sub-band for processing and the other $(N_{sb} - 1)$ sub-bands are transmitted to corresponding satellites via the intra-satellite communication layer. Furthermore, for even distribution of data and to ensure scalability, we enforce the number of sub-bands equal to the number of satellite nodes, *i.e.*, $N_{sb} = N$. Subsequently, in the distributed framework, each node receives a specific sub-band of the observed data, i.e., (D_{obs}/N_{sb}) from $N-1$ other satellites in the network which yields a total input of $D_{in}^d = (D_{obs}/N_{sb})(N-1) = (D_{in}^c/N)$bps, and down-links $D_{out}^d = (D_{out}^c/N)$bps respectively. More generally, these sub-bands can also be dynamically allocated, depending on the availability of resources on each satellite.

Thus, the Frequency distributed correlator reduces the inter-satellite communication by a factor N. Furthermore, at the cost of equipping all observational satellite nodes with communication capability (both inter-satellite and down-link to Earth), SPOF is averted and scalability is ensured. In the context of the projects discussed earlier, DARIS, FIRST and SURO-LC implement a centralized architecture, whereas OLFAR employed the distributed architecture. Given that the system frequency is typically an order of magnitude or more than the processing instantaneous bandwidth,
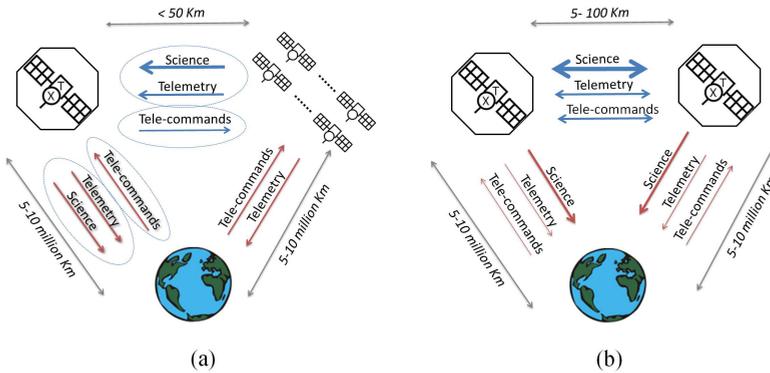
Figure 2.5: ***Communication architectures:*** An illustration of a **(a) centralized communic-ation architecture** and **(b)** single pairwise-link of a **distributed communication architec-ture** for a space-based radio interferometric array, where the inter-satellite link is indicated in blue and the Earth-downlink by red. Telemetry and tele-commands are exchanged between the satellites and with Earth in both scenarios.

computing requirements are negligibly small, which has been duly noted by all these studies.

2.5   Communications

The potential communication scenarios for the envisioned space-based array are shown in Figure 2.5, which follow directly from the correlator architectures discussed in the previous section. As shown in Figure 2.5 (a), the centralized architecture comprises of a mothership collecting raw observed data from a cluster of daughter satellites and, down-links the processed data to an Earth-based ground station. Alternatively, in case of the distributed scenario shown in Figure 2.5 (b), all satellites are capable of both exchanging data and correlating them, before down-linking back to Earth. In addition to the science data, housekeeping information is also exchanged between the satellites via tele-commands and telemetry, which is expected to be relatively small ($\lesssim$ 100kbps) in comparison to the astronomical data of 6Mbps. The housekeeping information is critical for control, timing and synchronization of the satellite, and to maintain coherence within the satellite network.

2.5.1   Inter-Satellite Link (ISL)

Implementing the ISL using high-frequency optical communication [Sodnik, Furch and Lutz 2006; Toyoshima 2005] has many advantages as compared to radio communication, such as reduced mass and volume of equipment, higher data rates and no regulatory restrictions as experienced for radio frequency (RF) bands. However, this would also require extremely accurate alignment of the satellites, robust synchronization and more power than what could potentially be available for a small satellite. In the RF domain, OFDM is an efficient modulation scheme for the ISL, in particular for a scalable antenna array with limited available bandwidth [Nee and Prasad 2000]. OFDM is well suited to frequency selective channels and it potentially offers a good spectral efficiency. With OFDM, the separation between each channel is equal to the bandwidth of each channel, which is the minimum distance by which the channels can be separated. The signals from each satellite node which form individual channels will be modulated using a form of Phased Shift Keying (PSK), Amplitude Shift Keying (ASK), or a combination Quadrature Amplitude Modulation (QAM). In this study, we consider an ISL transmission frequency of 2.45GHz, although other frequency bands can also be used. One of the possible solutions to implement the ISL is to use patch antennas on each face of a satellite node, such that the combined implementation yields a full coverage of the sky. All the satellites will have patch antennas on all six faces for both uplink and downlink.

   In the centralized scenario, under nominal assumptions, the link margin for the 100kbps uplink (from Mothership to Node) and 6.01Mbps downlink is estimated to be 13.2dB and 2.3dB respectively, assuming a transmission power of 5W and 1W for the Mothership and node [Boonstra et al. 2011]. However, extending these link margin estimates of the centralized ISL architecture to a distributed scenario poses two fundamental challenges. Firstly, the transmission data rate between every satellite pair is now 5.44Mbps, which includes 5.34Mbps of science data (see Table 2.3) and 100kbps of housekeeping data. Secondly, in the absence of a centralized correlator, the maximum distance between the satellites is 100km, a factor 2 compared to the centralized scenario. Hence, to achieve the same link margin of 2.3dB as the node to mothership downlink, the transmission power of each satellite in the distributed architecture must be 4 times that of the centralized scenario, i.e., 20W [Rajan et al. 2016]. This requirement is a bottle neck for scalable array of small satellites with limited transmission power. One possibility is to use clustering schemes and multi-hop approaches to reduce the communication distances between the satellites, which is a research area currently being explored [Budianu et al. 2011; Naghshvar, Zhuang and Javidi 2012].

2.5.2   Space to Earth Downlink

The total downlink data rate D_{out}^c after correlation quadratically increases with the number of nodes in the cluster and reduces linearly with the integration time (see Table 2.3). In the DARIS study, for a cluster of 9 satellites with 1 second integration interval, the downlink of ≥ 1.46Mbps was achieved using an off-the-shelf X-band downlink unit. For arrays larger than 50 satellites with minimal power, it is difficult to establish Earth-based downlink with current off the shelf technology. However, these challenges and possible distributed downlink scenarios are currently being investigated [Budianu, Meijerink and Bentum 2015]. An additional constraint is the number of limited ground stations on Earth. For instance, the core ESA network has two deep space networks of 35m antennas along with several antennas in the $13 - 15$m class [Vassallo et al. 2007]. The DARIS study concluded that a single ESAs 35m ground station for 8hours/day suffices the need for the data generated cluster of 9 satellites with a centralized mothership [Boonstra et al. 2011].

2.6   Deployment locations

The deployment location of the space-based array must be chosen to ensure the following conditions.

1. Minimize RFI during scientific observation cycles.

2. Offer maximum possible down-link data rate.

3. Provide sufficient positional stability during integration time τ.

4. Must remain within a sphere of ~100km.

In addition, each satellite must offer low noise conditions with minimal EMC and stable temperature (and gain) conditions to easen calibration. To alleviate the high complexity of active control to keep all the satellites within a cluster, passive formation flying could be employed. In passive formation flying paradigm for a satellite array, the satellites are allowed to drift, and only minimal maneuvers are employed to ensure safety and spatial coherence. The relative positions, orientations and the time aboard all the satellites are constantly monitored. This approach eliminates the need for excess propulsion and heavy orbital maintenance equipment fon all satellites. Additionally, the naturally varying position vectors of the satellites produce unique uvw sampling points, which consequently improve the PSF. The following

section discusses the quest to find an optimum balance between down-link data rates and maximizing observation time, emphasizing the challenges in various deployment locations.

2.6.1 Lagrange points

The relative velocities of the satellites are minimal at Lagrangian points and hence these locations offer increased positional stability for longer time intervals. Therefore, the Lagrange points are an optimal choice to increase the integration time τ_{int} of the observations and also the mission lifetime. The Earth-Moon L4 and L5 are much closer for Earth based communication, but are suspected to be less radio quiet relative to the Earth-Moon L2. Although the Earth-Moon L2 point located at ~61347km away from the Moon is in the cone of radio-silence and is sufficiently shielded from RFI, this Lagrange point may not be a favorable deployment location since electromagnetic transmission in this radio quiet zone may pollute the environment and affect future missions in this location [Maccone 2005]. The Sun-Earth L4 and L5 points are too far and subsequently limit downlink rates. In contrast, the Sun-Earth L2 libration point at ~1.5 Million km away from Earth, is a tradeoff between downlink data rate, RFI avoidance and increasing τ_{int}. Although this is a stationary point, in practice a satellite operating at L2 will experience a gravity gradient with a slow and steady outward drift. Such a scenario is preferred by the FIRST [Bergman et al. 2009] and SURO-LC [Baan 2012] studies. The SURO-LC proposed an array of 8 daughter satellites drifting slowly in Lissajous orbit and a mothership at a fixed distance of 10km from the cluster. While such a mission will provide enhanced imaging performance with improved uvw coverage and longer integration times, the downlink data rate (using current technology) is estimated to be $2 - 3$ orders of magnitude less than an array deployed in the Moon orbit [Rajan et al. 2011].

2.6.2 Orbiting the Moon

An equatorial orbit around the Moon presents a relatively easier down-link to Earth and sufficiently long eclipse times behind the Moon w.r.t. Earth. The RAE-2 showed that interference at very low frequencies is reduced by 2 orders of magnitude behind the moon, making it an ideal location for radio astronomy observations [Alexander et al. 1974]. However, during the eclipse behind the moon the cluster has no communication with Earth. The long eclipse time periods shield against radio noise from Earth and enable the science observations. The Eclipse time period can be increased by decreasing the orbital altitude, however consequently the percentage of the orbit

in the shade increases. In addition, by decreasing the orbital altitude, the relative range rates of the satellites also increase, which in turn affects the baseline stability during scientific observations. Hence, a balance between the relative velocity and the eclipse time must be found [Rajan et al. 2011].

2.6.3   Orbiting the Sun

A potential reference orbit for formation flying around the Sun is the Earth orbit itself [Saks et al. 2010]. However, if the satellites are too close to Earth, then the terrestrial interference is a major disturbance to science observations. Alternatively, an orbit around the Sun with a different eccentricity than the Earth orbit keeps the satellite array at 4 to 10 million km from Earth, which is far enough to offer both stability and also reduce radio noise from Earth. The large distance separation severely limits the available down-link bandwidth upto at least an order of magnitude compared to the Lunar orbits. In view of an optimal balance between increased data-downlink and RFI free science observations, the DARIS study used the Earth orbit as a reference orbit with the satellite nodes orbiting at a distance of 4 to 10 million km from Earth. Hence, even though the constellation orbits the Sun as a central body, the reference orbit does go around the Earth, from leading to trailing. The particular orbit is relatively stable with low relative range rates and thus allows continuous scientific observations, however is sensitive to minor perturbations in the injection velocities of the satellites [Boonstra et al. 2011; Saks et al. 2010].

2.7   Synchronization and navigation

To maintain coherence, all the satellites must be synchronized, and their relative positions known up to sub-meter accuracies. These requirements on space-time accuracies at ULWs are considerably lower in comparison to other space-based array missions, such as LISA [Bik, Visser and Jennrich 2007]. Almost all Earth-based antenna arrays synchronize using GPS-aided atomic clocks, where fixed antenna positions are known up to millimeter accuracies, cf. e.g., LOFAR [van Haarlem et al. 2013]. However, the envisioned space-based array will be deployed far-away from Earth-based GPS satellites and unlike Earth-based antennas, these satellites will be mobile. In addition, given the large number of satellites and limited ground-segment capability, tracking each satellite independently is infeasible. Moreover, in certain deployment locations such as the Lunar orbit, the satellite array will be partially or even completely disconnected from Earth-based ground stations during eclipse
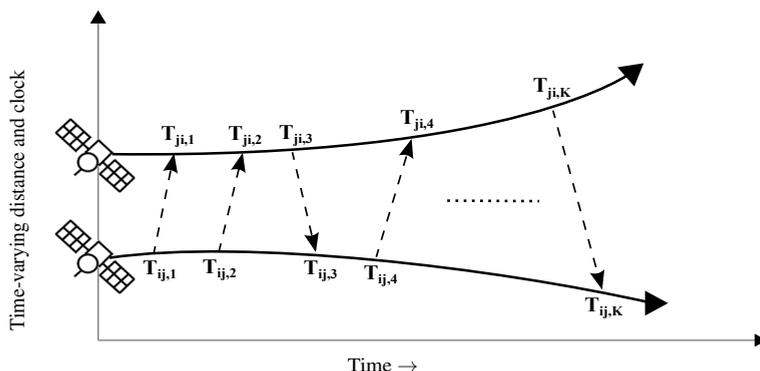
Figure 2.6: ***Dynamic ranging:*** A generalized two-way ranging (GTWR) scenario between a pair of *asynchronous mobile satellite nodes* where the nodes transmit and receive asymmetrically [Rajan and van der Veen 2015]. See Chapter 4.

periods. Thus, the satellite array must be an anchorless network, cooperatively synchronizing the clocks and estimating time-varying relative positions, in the absence of absolute reference on time and position. The estimated relative positions, which are identical to the absolute positions upto a rotation and translation, are sufficient for inter-satellite communication, collision avoidance and on-board correlation of astronomical data. For radio astronomy imaging however, to ensure the desired orientation of the projected baselines (see Figure 2.1), an external reference may be required occasionally to map the relative spacecraft positions on an inertial reference frame. Such an absolute reference can be obtained by tracking a few satellites, during intermittent Earth-based communication.

2.7.1   Dynamic ranging

The satellites of a space-based radio astronomy array will be equipped with space-qualified and light-weight atomic clock oscillators, which offer long-term stability [Rajan, Bentum and Boonstra 2013]. See Chapter 3 . All clocks are inherently non-linear w.r.t. the ideal time t and for a *mobile network*, the distance is also time-varying. In case of an anchorless network of mobile asynchronous nodes, estimating both the clock discrepancies and time-varying distances (and subsequently time-varying positions) is a bootstrap problem.

Figure 2.6 illustrates this challenge via the generalized two-way ranging (GTWR) scenario between a pair of *asynchronous mobile satellite nodes* [Rajan and van der Veen 2015]. The asynchronous nodes transmit and receive asymmetrically, dur-

ing which K time stamps are recorded at respective nodes. Unlike classical TWR where the transmission and reception is alternating, this particular framework imposes no pre-requisites on the sequence or number of two-way communications. Consequently, this framework can be readily extended to a plethora of TWR ranging protocols, including broadcasting and passive listening [Serpedin and Chaudhari 2009]. Furthermore, we also consider the time-varying distance between the satellites during the asymmetric two-way communication. Let $T_{ij,k}$ and $T_{ji,k}$ be the kth local time-markers recorded at the ith and jth satellite nodes, whose deviation from the *true* time is represented by $\mathcal{C}_i(T_{ij,k})$ and $\mathcal{C}_j(T_{ji,k})$ respectively. If $d_{ij}(t)$ is the time-varying pairwise distance between the nodes, then for the kth transmission, the GTWR equation is

$$\mathcal{C}_i(T_{ij,k}) - \mathcal{C}_j(T_{ji,k}) = \pm d_{ij}\Big(\mathcal{C}_i(T_{ij,k})\Big), \tag{2.11}$$

where $\pm$ indicates the direction of the transmission between the nodes and without loss of generality the *true* time distance $d_{ij}(t)$ is replaced with the clock model at satellite i. We will use this framework in the following chapters, to tackle the challenge of relative localization and synchronization.

In Chapter 4, given the time measurements, both the clock discrepancies and the time-varying distances are estimated using classical least squares based solutions [Rajan and van der Veen 2015]. Given these pairwise distances, the relative satellite positions can be estimated using MDS-like algorithms [Borg and Groenen 2005]. In addition to the relative positions, the relative velocities can also be estimated using the coefficients of the approximated distance polynomial [Rajan, Leus and van der Veen 2015], which is presented in Chapter 5. A more generalized extension to estimate higher-order kinematics in Euclidean space such as relative acceleration, is discussed in Chapter 6. These solutions are particularly suited for *cold start* scenarios when no apriori information is readily available, for instance during arbitrary satellite network deployment. For longer time scales, when the orbital dynamics of the deployment location is well known, the estimated space-time parameters can be tracked and improved using recursive filters e.g., Kalman Filter [Kay 1993].

An added advantage of using dynamic ranging is that the timestamps can potentially piggyback on the housekeeping data exchanged between the satellite nodes, which mitigates the need for a dedicated ranging system. However, if a ranging system is employed, then the achievable lower bound on the standard deviation for Time Of Arrival in multipath-free channels is given by

$$\sigma \geq \big(8\pi^2 F_c^2 BT \, \mathrm{SNR}\big)^{-1/2}, \tag{2.12}$$

where F_c denotes the carrier frequency, $B \ll F_c$ is the bandwidth of the signal, T is the signal duration in seconds [Patwari et al. 2005]. A typical noise variance on the time-markers of $\sigma = 3.3 \times 10^{-8}$ seconds (i.e., 1 meter) can be adequately achieved by a wireless node communicating at $F_c = 2.4$GHz with a nominal bandwidth of 1kHz transmitting and SNR=10dB for a signal duration of T~1ms.

2.7.2 Attitude determination

In addition to localization and synchronization, attitude determination is critical for both navigation and radio astronomy imaging. For estimating spacecraft orientation, two-vector attitude determination can be employed by the spacecrafts, where these vectors are either (a) the unit-vectors to the Sun and the Earths' magnetic field vector or (b) unit vectors to two stars. The pointing direction for the satellites can be provided by commercially available sun and star trackers, which form an integral part of the Attitude and orbit control system (AOCS) in the satellites. Using these measurements, methods such as TRIAD or a solution to Wahbas' problem yield the on-board attitude determination [Markley and Crassidis 2014].

2.8 Summary and discussion

A satellite cluster of less than 10 nodes is scientifically very interesting and meets the requirements for the extra-galactic survey science cases in terms of resolution and sensitivity. At least 4 antennas observing at 30 MHz for more than a year is sufficient to achieve the confusion limit of 65 mJy with $1'$ resolution and allows the detection of over a million sources (Section 2.2.3). Moreover, even with fewer antennas, transient science cases such as bright Jupiter-like flares and Crab-like pulses can be addressed. In the OLFAR design, all the satellites will be equipped with 2 (or 3) 5m dipole antennas (or two 2.5 monopoles) to observe the ≤ 30MHz spectrum (Section 2.3).

For a nominal observational bandwidth of ≥ 1MHz, each satellite is estimated to generate ≥ 6 Mbits/s, which must be correlated in space to minimize downlink data rate to Earth. In both centralized and distributed scenarios, the processing requirements for filtering and correlation is negligibly small for up to ~50 satellites and can be readily incorporated into the On Board Computer (OBC) (Section 2.4). To establish the inter-satellite link, satellites will be equipped with patch antennas to transmit the desired ≥ 6Mbps data rate. The communication between the satellites is a fundamental bottleneck, which limits the bandwidth of observation and possibly the achievable baseline for radio astronomy imaging (see Section 2.5.1). In the cent-

ralized scenario, the Node to Mothership link can be established with 5W over 50km distance with a positive link margin. However, in the distributed scenario upto 15W is desired to establish a link over 100km, which could be improved using clustering schemes and multi-hop communication (Section 2.5). Nonetheless, the proposed distributed framework remains indispensable for large and scalable array of ≥ 10 satellites, where SPOF must be avoided.

In inaccessible (e.g., Moon-farside) or far-away deployment scenarios (e.g., Lagrange points), the satellites must be synchronized and localized cooperatively, to minimized the dependence on Earth-based ground stations (Section 2.7). In addition, the orientation of the satellites can be estimated using the sensors in the Attitude and Orbit Control System (AOCS) which include the sun sensor and star trackers. All the satellites need to be equipped with sufficient propulsion to ensure precise deployment and to maintain the maximum baseline separation of 100km.

2.8.1   Technological challenges for ULW arrays

The actual satellite implementation is intricately connected to specific mission requirements, the number of satellites, the active choices in network architecture and the deployment location. However, recently concluded studies give insights into the current state-of-the-art space technology for ULW radio astronomy arrays. Figure 2.7 shows the mass and power breakdown for the DARIS mission, where all subsystems use only off the shelf components [Boonstra et al. 2011]. The power consumption for the daughter node and the mothership was estimated at 160W and 502W respectively. Reliable and highly efficient solar panels based on triple junction GaAs cells were employed on both the mothership and Daughter nodes to meet the power requirements. Furthermore, the dry mass of each daughter node was estimated at ~100kg and the Mothership at ~550kg.

In comparison to DARIS, futuristic missions such as OLFAR are expected to be lighter by two orders of magnitude and consume at least an order of magnitude less in power consumption (see Table 2.1). The reduced mass and power requirements will not only enable a larger array of antennas for radio astronomy, but can potentially enable the system to piggy-back on other missions, without the need for a dedicated launch vehicle. Thus, future missions will possibly consist of relatively cheaper nano-satellites with miniaturized and power-efficient subsystems.

Further potential research areas identified during the OLFAR study include the antenna design for observation frequencies of $0.3 - 30$MHz, development of efficient imaging techniques for radio astronomy, high speed and robust RF inter-satellite communications techniques [Budianu et al. 2013] and investigating control and reliability

Daughter Node Mass Budget
- Link to Mothership (14kg)
- Harness (7kg)
- Payload (1kg)
- Structure/Mechanisms (18kg)
- AOCS (8kg)
- Propulsion (20kg)
- Power+ODBH (23kg)
- Solar Array (5kg)
- Thermal (4kg)

Mothership Mass Budget
- Link to Daughters (11kg)
- Link to Earth (49.5kg)
- Harness (49.5kg)
- Payload (5.5kg)
- Structure/Mechanisms (215kg)
- AOCS (27.5kg)
- Propulsion (82.5kg)
- Power (55kg)
- ODBH (22kg)
- Solar Array (16.5kg)
- Thermal (16.5kg)

Daughter Node Power Budget
- Link to Mothership (45.2W)
- Harness (8.1W)
- Payload (21.1W)
- Power+ODBH (46.5W)
- Thermal (14.1W)
- AOCS (24.9W)

Mothership Power Budget
- Link to Earth (155.6W)
- Link to Daughters (60.2W)
- Harness (25.1W)
- Payload (85.3W)
- OBDH (35.1W)
- AOCS (60.2W)
- Thermal (40.2W)
- Power (40.2W)

Figure 2.7: ***Mass and power budget analysis of the DARIS mission:*** The DARIS mission consists of 8 Daughter nodes and 1 centralized mothership. The mass (and power) of each Daughter satellite and Mothership was estimated to be 100kg (160W) and 550kg (502W) respectively [Boonstra et al. 2011].

of large satellite arrays [Engelen, Gill and Verhoeven 2014]. In addition, observability challenges such as the unknown RFI environment at the desired deployment location must also be investigated, possibly by a ≥ 2 satellite interferometer via a precursor mission.

2.8.2   Conclusion

The frequency window of ≤ 30 MHz remains one of the last unexplored frequency regimes in astronomy, which opens a new realm of interesting science cases. To achieve the science objectives at these wavelengths with desired resolution and sensitivity, a dedicated space-based ULW array is necessary. Recent advances in technology and computing resources have improved both the feasibility and scientific desirability of such a space-based array. In this chapter, we justified the need for a space-based antenna array for ultra-long wavelength radio astronomy and discussed various subsystems needed to achieve the desired science cases. More recently con-

cluded studies such as DARIS, FIRST, SURO have shown feasibility of such an array. In particular, the DARIS project showed that a cluster of less than 10 satellites can be launched using current off the shelf technology. An expanded set of science cases can be targeted by scaling the number of satellite nodes, extending the frequency range of observation and increasing the instantaneous bandwidth. However, this would significantly increase the mass, power consumption and eventually the cost of the mission. Some of these technological challenges have been tackled under the OLFAR study. More generally, the on-going work on miniaturized nano-satellites may pave the way for feasible and affordable missions in the future.

In the rest of this dissertation, the focus is explicitly on relative localization and synchronization, which is one of the key challenges identified in this chapter. A step towards tackling this challenge is to understand the clock requirements for ultra-long wavelength radio astronomy, and then list a handful of suitable clocks which cater to these specifications. These steps are discussed in the following chapter.

Appendix 2.A   Computational requirements

The goal of this section is to calculate the computational requirements of each satellite for on-board radio astronomy signal processing. In particular, we focus on correlation which is a fundamental task of a radio interferometer. All the satellites in the potential space-based array will perform on-board correlation, primarily to reduce the data downlink rate. A first order processing model is presented, which estimates the processing for correlation as the number of real N_{bit} multipliers required for each mode, neglecting addition as a second order computation [1]. Memory is another crucial factor, but is dependent on the implementation style on the hardware and hence will be ignored in this work. The signal processing system in all scenarios is assumed to run at rate f_{sys} and all the satellites are completely synchronized. The complete list of conventions used is given in Table 2.3.

In our estimation, we presume N satellite nodes with N_{pol} polarizations and subsequently the total number of signal paths N_{sig} is given as $N_{sig} = N_{stat}N_{pol}$. In the pre-processing block, each of these signals are conditioned, discretized and quantized at the Nyquist rate of 2ν (see Figure 2.4). An instantaneous bandwidth of $\Delta\nu_i < \nu$ is then filtered for further processing. Thus each channel comprises of a single polarization with base bandwidth of $\Delta\nu_i$ which is coded with N_{bits} post quantization. In addition, in all the cases presented, it is assumed that the electrical, front end and geometrical delays have been compensated.

2.A.1   Signal processing blocks

Prior to investigating the types of correlators for radio interferometry and their computational costs, the number of real multiplications required for fundamental signal processing blocks are discussed. These include complex multiplications, Fast Fourier transform (FFT) and the Poly-phase filterbank.

Complex Multiplications

The product of any 2 complex numbers; say $(a_1 + ib_1)$ and $(a_2 + ib_2)$ is given as $(a_1a_2 - b_1b_2) + i(a_1b_2 + a_2b_1)$, which involves 4 real multipliers per second. Thus cross correlating N_{sig} complex channels, produces a $N_{sig} \times N_{sig}$ Hermitian matrix consuming $4N_{sig}^2$ real multipliers. However, note that the diagonal terms containing the auto correlations only consume half the number of multipliers. In

---

[1] This work is partly based on the conference proceeding, "*Distributed correlators for interferometry in space*" by R.T.Rajan et al. in *IEEE* Aerospace Conference, Mar. 2013, pp. 1–9

addition, exploiting the symmetric nature of the Hermitian matrix, the total number of real N_{bit} multipliers required for correlating N_{sig} channels is

$$N_X = 4(0.5N_{sig}(N_{sig} - 1) + 2N_{sig} = 2N_{sig}^2, \tag{2.13}$$

where $0.5N_{sig}(N_{sig} - 1)$ is the number of off-diagonal terms and $2N_{sig}$ is the total number of auto correlations.

Discrete Fourier transform (DFT)

Given a discrete set of complex data sequence $\mathbf{x} = [x_0, x_1, \ldots, x_{N-1}]^T \in \mathbb{C}^{M \times 1}$, the output of the DFT $\mathbf{y} = [y_0, y_1, \ldots, y_{N-1}]^T \in \mathbb{C}^{M \times 1}$ is given by

$$y_k = \sum_{n=0}^{N-1} x_n W_N^{nk} \quad \text{for } \{n, k\} = \{0, 1, \ldots, N - 1\}, \tag{2.14}$$

where $W_N = \exp(-j2\pi/N)$, is the Nth complex root of unity. N is the length of the data vector and also indicates the spectral resolution of the Fourier transform. The above equation is a linear isomorphic transformation, which is of the form $\mathbf{y} = \mathbf{W}_N \mathbf{x}$ where $\mathbf{W}_N \in \mathbb{C}^{M \times M}$ is a twiddle matrix containing all the twiddles. For an N-point DFT the number of multiplications is $\mathcal{O}(N^2)$. A computationally efficient algorithm to evaluate the DFT is the Fast Fourier Transform or FFT, which reduces the multiplications to $\mathcal{O}(N \log N)$. Using a straight forward pipelined Radix-2 implementation, the FFT equation can be further broken down to $(N/2)(\log_2 N)$ butterfly stages of 4 multipliers each. For a given input signal of bandwidth $\Delta\nu$, the FFT provides N_{bins} coefficients at the rate $\Delta\nu/N_{bins}$. Hence the total number of real $N_{bit} \times N_{bit}$ multiplications per second required is given as

$$N_X^{fft} = 4(\Delta\nu/N_{bins})(N_{bins}/2)\log_2 N_{bins} = 2\Delta\nu \log_2 N_{bins}. \tag{2.15}$$

Poly-phase Filter Bank (PFB)

A poly phase filter bank for a single node, single polarization consists of a FIR filter and a FFT module. The number of multiplications for a single FIR filter equals the number of taps N_{taps}. For an input bandwidth $\Delta\nu$, the total number of real multiplications for a complex signal is $4\Delta\nu N_{taps}$. In combination with the FFT (2.15), we have the total number of real multiplications required for a PFB as

$$\begin{aligned} N_X^{pfb} &= 4\Delta\nu N_{taps} + 2\Delta\nu(\log_2 N_{bins}) \\ &= 2\Delta\nu(2N_{taps} + (\log_2 N_{bins})). \end{aligned} \tag{2.16}$$

2.A.2 Correlation

Radio astronomers calculate the Fourier transform of the measured coherence function to make maps of the sky. Let $x_i(t)$ and $x_j(t)$ be two time varying signals received at spatial positions labeled i and j, then the coherence function is the cross correlation product between and is given as

$$\zeta_{ij}(\tau) = \langle\, x_i(t)x_j^*(t - \tau_{ij})\,\rangle_{\tau_{int}}, \qquad (2.17)$$

where $\langle . \rangle$ is the expectation operator, the superscript $(*)$ indicates conjugation and τ_{ij} geometric delay between the two antenna pair. The number of cross-correlation products increase as $O(N^2)$ for N antennas and the expectation operator is applied over a period of integration time τ_{int}. There are 3 ways to implement a correlator. The first option is using the traditional correlator model XF i.e. cross correlation first and Fourier transform later. The second alternative is the more recent FX correlator which measures the cross-power spectrum between two antenna signals. While XF architecture is beneficial because bandwidth can be traded for spectral resolution, FX architecture reduces processing requirements and offers scalability when the number of antennas is large. Before describing the computational requirements for XF and the FX architectures, we briefly present the number of multiplications for essential signal processing blocks in the following section.

XF Correlator

The conventional method to directly measure the cross-correlation function forms the basis for the XF or 'Lag' correlator [Romney.J.D 1999]. The signal $x_j(t)$ is delayed and correlated with $x_i(t)$ to produce ζ_{ij} as a function of lags (τ), which is later Fourier transformed to produce the baseline cross power spectra. The cross correlation operation is a function of lags, which could be varied in quantization of $n\Delta\tau$ where $-N_{lags}/2 \leq n < N_{lags}/2$, where for a given observation bandwidth $\Delta\nu$, $\Delta\tau$ is limited by $\Delta\tau_{min} = 1/2\Delta\nu$. The signal x_j is delayed by $\Delta\tau$, multiplied and accumulated at every sample clock before propagating to the next segment. For N_{sig} such slices, the total number of real multiplications per second is given from (2.17) and (2.13)

$$N_X^{xf} = N_X N_{lags} \Delta\nu_i = 2N_{sig}^2 N_{lags}\left(\frac{\Delta\nu_i}{f_{sys}}\right), \qquad (2.18)$$

where we $N_{sig} = N_{stat}N_{pol}$ and f_{sys} is the system processing frequency.

An advantage of XF architecture is that the Fourier transform (FFT) operation can either be an online or an off-line process. This means that the correlator operates on the entire bandwidth for all nodes N_{stat} and the data generated can be transmitted/stored without the immediate need to Fourier transform.

FX Correlator

An alternative to the XF correlator is to directly measure the cross-power spectrum. The term FX correlator was coined by Chikada [Chikada et al. 1987] who built the first such correlator, implementing the reversal of the order of operations compared to the XF architecture. If $X_i(\nu)$ and $X_j(\nu)$ are the real time Fourier transforms of the delay compensated waveform $x_i(t)$ and $x_j(t)$ then using convolution theorem , the correlation function $\zeta_{ij}(\tau)$ in (2.17) can be written as a multiplication in the Fourier spectrum [Richard Thompson.A 1994]

$$\begin{aligned} \zeta_{ij}(\tau) &\;\leftrightharpoons\; X_i(\nu)X_j^*(\nu) \\ &\;\leftrightharpoons\; X_{ij}(\nu). \end{aligned} \tag{2.19}$$

Note that the cross-power spectrum to the right is a function of frequency and its Fourier transform to the left is a function of lags (τ). From implementation perspective, the essence is to transform each input signal x_i into frequency domain F and then multiply-accumulate X over each spectral bin for all the nodes, to produce the cross-power spectrum and later the visibility function off-line. Unlike the XF correlator, the FX correlator must do a node based Fourier transform on-line. The number of points N, is given by the spectral resolution intended for the application i.e N_{bins}. A shift register loads N_{bins} samples which is Fourier transformed to produce N_{bins} points. The number of points N_{bins} can be interpreted as the spectral translation of N_{lags} from XF correlator in the time domain. The total number of multiplications (N_X^{fx}) required is the sum of multiplications for node-based FFT (N_X^{fft}) and multiplications for Correlations (N_X^{corr}).

Consider N_{sig} signals inputted to the correlator block, then using a N_{bins} - point FFT processor for each signal and referring to eq(2.15) we have the total number of multiplications required as

$$N_X^{fft} = 2\,N_{sig}\left(\frac{\Delta\nu_i}{f_{sys}}\right)\log_2 N_{bins}. \tag{2.20}$$

In contrast to the XF mode, where each sample is cross-multiplied at input rate, in FX mode each spectral bin is cross-multiplied and accumulated only once for N_{bins}

samples, thereby reducing the number of computations by a factor N_{bins}. In other words, the multipliers operate at a rate $(\Delta\nu_i / N_{bins})$ instead of $\Delta\nu_i$. From (2.13) we have , the number of multiplications required for correlation as

$$N_X^{corr} = 2N_{sig}^2 \left(\frac{\Delta\nu_i}{f_{sys}} \right).$$ (2.21)

The total number of multiplications for a N_{sig} channel and N_{bins} FX correlator is then

$$
\begin{aligned}
N_X^{fx} &= N_X^{fft} + N_X^{corr} \\
&= 2N_{sig} \left(\frac{\Delta\nu_i}{f_{sys}} \right) [N_{sig} + \log_2 N_{bins}].
\end{aligned}
$$ (2.22)

XF vs FX

The computational requirements of XF are much higher than FX mode for large number of nodes and higher spectral resolution. Comparing (2.18) and (2.22) we have the processing factor given as

$$N_X^{xf/fx} = \left(\frac{N_{sig} N_{bins}}{N_{sig} + \log_2 N_{bins}} \right).$$ (2.23)

As can be seen, the multiplicands in the XF mode are additive in the FX mode , besides the $\log_2$ reduction on the number of frequency bins. Thus, although for lower number of nodes the XF is comparable to FX mode, for large number of nodes and scalable architectures, the FX mode is computationally cost effective.

3

Clocks

In this chapter, we present first order clock requirements for an anchorless network of mobile nodes, with applications to space-based interferometry at ultra-long wavelengths. Space-based interferometers, such as the OLFAR cluster will be an anchorless network deployed far from Earth, with occasional communication with Earth, which presents new challenges in synchronization and localization of the satellites. The primary focus of this chapter is on clock synchronization, in particular the specifications of the oscillator on-board each of the satellite nodes. We begin by modeling the phase error of a general oscillator as a polynomial in time. The bounds on the short term and long term clock requirements are defined in terms of jitter and Allan deviation respectively. Given a robust clock, which is stable for a certain coherence time, we show that it suffices to assume the clock as a first order model. We discuss the particular use case of OLFAR, and present clock requirements for an OLFAR satellite. A list of commercially available clocks which meet these requirements are discussed.

3.1 Introduction

Recently, new and interesting science drivers have emerged in the spectrum of ultra long wavelength (ULW) of > 3m, which are driving the need for a distributed array of radio telescopes in space, far from Earth's atmosphere and terrestrial interference. Until now, such a system in space was financially and technically constrained. However, more recent studies [Saks et al. 2010] have shown that with extrapolation of current signal processing and satellite technologies, a low frequency radio telescope in space could be feasible in the coming years. In this chapter, we particularly focus on the OLFAR [Rajan et al. 2011] feasibility study, which aims to develop a detailed system concept and to design and build scalable autonomous satellite flight units to be used as an astronomical instrument for low frequencies. The OLFAR cluster will employ Distributed correlation- Distributed Down-link architecture for processing and communication, where in, within the network, all the satellites are capable of two-way communication with one other. The observed data is accurately time stamped by the local oscillator before transmitting to another satellite for correlation. All the satellites are independently capable of down-linking correlated data to Earth. In certain deployment locations, e.g., Moon-orbit, the OLFAR network maybe completely disconnected from Earth-based communication, particularly when the satellites traverse over the dark side of the Moon. See Chapter 2 for a detailed explanation of these challenges.

Furthermore, unlike terrestrial radio astronomy arrays, the OLFAR nodes are mo-

bile and asynchronized, which presents a unique challenge to jointly synchronize and locate the nodes up to desired accuracies. To maintain *coherence*, during observation, for processing and during communication, the OLFAR network must be synchronized. The OLFAR cluster will be a cooperative network of satellites, which will correct for clock errors cooperatively with minimal help from Earth based ground stations. Furthermore, in addition to synchronization, the OLFAR satellites must also find pairwise distances to estimate relative positions for radio interferometry, to avoid collision and for passive formation flying. The proposed localization and synchronization solutions must use limited resources to ensure minimal mass and power budget.

In this chapter, our focus is on the fundamental clock requirements for space-based interferometry. A generic clock model is presented in Section 3.2, where the clock error is approximated as a polynomial in the presence of random noise. For short term stability, we emphasize the need to minimize clock jitter and its tolerance levels for a given node in the network. The long term deviation of clock from its nominal frequency is described using Allan deviation, which is shown to be a measure of non linear components in a given clock (in Section 3.3). In Section 3.4, the short term and long term clock stability requirements are discussed, in addition to desired position accuracies for interferometry. A few commercially available clocks which meet OLFAR requirements are presented. In addition, joint localization and synchronization algorithms are recommended, which suit OLFAR needs and use minimal overhead on the entire system.

3.2 Clock model

Let A and ν denote the nominal amplitude and frequency of a practical clock oscillator residing in a node, then the corresponding clock output is modelled as [Barnes et al. 1971]

$$a(t) = (A + \delta A(t))\sin(2\pi\nu\bar{\mathcal{C}}(t)), \tag{3.1}$$

where t represents the *true* time and $\delta A(t)$ is the amplitude error modulated on the ideal amplitude of the signal. The clock output is often hard limited using differential comparison techniques which minimizes this amplitude error. Hence, the time varying amplitude $\delta A(t)$ can generally be eliminated, but not ignored. The argument to the sinusoid $2\pi\nu\bar{\mathcal{C}}(t)$ is the total accumulated phase in radians, where $\bar{\mathcal{C}}(t) = t + \delta\bar{\mathcal{C}}(t)$ is the corresponding frequency normalized phase with units of time. For an ideal clock source $\bar{\mathcal{C}}(t) = t$, however in reality, time varying errors $\delta\bar{\mathcal{C}}(t)$ exists and the

fundamental challenge is to minimize it within acceptable limits depending on system requirements.

The phase error of the clock source can be understood by expanding $\delta\bar{\mathcal{C}}(t)$ as a polynomial of *true* time t and consequentially $\bar{\mathcal{C}}(t)$ is

$$
\begin{aligned}
\bar{\mathcal{C}}(t) &= t + \delta\bar{\mathcal{C}}(t), \\
&= \phi + [1 + \dot{\phi}]t + 0.5\ddot{\phi}t^2 + \ldots + \eta(t), \\
&= \phi + \omega t + 0.5\ddot{\phi}t^2 + \ldots + \eta(t),
\end{aligned} \tag{3.2}
$$

where ϕ indicates the time or phase offset of node i. The rate of change of phase i.e., the frequency offset is denoted by $\dot{\phi}$ and we define the clock skew of node as $\omega = 1 + \dot{\phi}$. The second-order coefficient $\ddot{\phi}$ is the rate of change of frequency offset, i.e., the frequency drift and $\eta(t)$ is the stochastic noise. In reality, there are other systematic deviations which affect the clock performance, which include modulation sidebands, shock, vibrations, humidity, temperature and radiation. These environmental effects have been ignored and thus not explicitly incorporated into the model. However, more generally, these errors can be assumed to be contained within $\eta(t)$. The phase parameter ϕ and its higher order derivatives are real valued and deterministic, whose slow variations with *true* time t are neglected in the above model. For an ideal clock with no phase errors, we have $\bar{\mathcal{C}}(t) = t$ and subsequently $[\phi, \dot{\phi}, \ddot{\phi}] = [0, 0, 0]$.

3.3   Clock stability

In approximating the phase error as a function of *true* time, we inherently assume the coefficients are time-invariant for a small period of time. This assumption relies heavily on the ability of the oscillator to reproduce these coefficients consistently with minimal fluctuations. A statistical measure of the fluctuations of the phase error $\delta\bar{\mathcal{C}}(t)$ over a given time duration is defined by the chosen *stability* criterion. In this chapter, we discuss both the short-term ($t \ll 1$ second) and long-term ($t \gg 1$ second) stability of a clock, both of which are dependent on the data rate of the input signal. In particular, the short-term stability severely limits the input sampling and quantization data, which is briefly discussed in Appendix 3.A.

To investigate the long-term deviation of the phase error, we use *Allan variance* as the clock measure. The normal standard deviation of the phase error $\delta\bar{\mathcal{C}}(t)$ in (3.1) does not converge, due to the accumulation of phase errors which increase in time t. However, since the Allan variance converges as compared to the normal standard deviation, it is a recognized clock specification parameter to estimate the long term

clock stability i.e., $t \gg 1$ second. In addition to Allan variance, there are also other estimators to characterize the fluctuations of the clock source, such as Overlapping Allan, Modified Allan and Hadamard variance to name a few [Riley 2008]. However, we use the Allan variance since it is an IEEE standard and more widely accepted as a measure when reporting performance of commercially available clocks. For the sake of completeness and to illustrate its relation with the phase error $\delta\bar{\mathcal{C}}(t)$, the Allan variance [Allan 1987] is briefly derived for time domain measurements of the clock source.

3.3.1   Continuous time

We begin by determining the instantaneous frequency deviation of the clock signal $a(t)$ from its ideal frequency ν, which is obtained by differentiating the total accumulated phase $2\pi\nu\bar{\mathcal{C}}(t)$ and dividing by 2π, i.e.,

$$\nu(t) = \frac{1}{2\pi}\frac{d}{dt}2\pi\nu\bar{\mathcal{C}}(t) = \nu + \nu\frac{d}{dt}\delta\bar{\mathcal{C}}(t). \tag{3.3}$$

Rearranging the terms and dividing both sides by the nominal frequency ν we have

$$\zeta(t) \triangleq \frac{d}{dt}\delta\bar{\mathcal{C}}(t) = \frac{\nu(t) - \nu}{\nu} \tag{3.4}$$

where $\zeta(t)$ is the normalized fractional frequency deviation of $a(t)$ and $\delta\bar{\mathcal{C}}(t)$ is the phase error in seconds. Now, the average fractional frequency deviation over a period, say τ, is then

$$\bar{\zeta}(t,\tau) = \frac{1}{\tau}\int_t^{t+\tau}\zeta(t)dt. \tag{3.5}$$

Finally, the two-sample *Allan variance* is defined as one half of the time-averaged squares of the differences between adjacent fractional frequency deviations $\bar{\zeta}(t,\tau)$ i.e.,

$$\boxed{\sigma_\zeta^2(\tau) = 0.5\langle(\bar{\zeta}(t+\tau,\tau) - \bar{\zeta}(t,\tau))^2\rangle} \tag{3.6}$$

where $\langle.\rangle$ is the expectation over sufficiently large number samples and $\sigma_\zeta(\tau)$ is the Allan deviation for the time duration τ [1].

---

[1] The fractional frequency, average fractional frequency and the Allan variance are conventionally represented by y, $\bar{y}$ and σ_y respectively, instead of ζ, $\bar{\zeta}$, and σ_ζ. However, in the following chapters, we will use $\mathbf{y}$ to represent the velocity of mobile nodes, and therefore we employ ζ, $\bar{\zeta}$, and σ_ζ.

3.3.2 Discrete time

Let $\{\bar{\mathcal{C}}(T_k)\}_{k=1}^{K}$ be a discrete set of time measurements at *true* time instances T_k obtained from the oscillator. If the nominal spacing between adjacent measurements is $\tau = T_{k+1} - T_k$, then the average fractional frequency offset during the kth measurement interval of length τ is

$$\bar{\zeta}_{k,\tau} = \frac{\delta\bar{\mathcal{C}}(T_k + \tau) - \delta\bar{\mathcal{C}}(T_k)}{\tau}, \tag{3.7}$$

Now, substituting for $\delta\bar{\mathcal{C}}(T_k)$ from (3.2) and introducing $\eta_{i,k+1}$, we have

$$
\begin{aligned}
\bar{\zeta}_{k,\tau} &= \frac{\phi + \dot{\phi}[T_k + \tau] + 0.5\ddot{\phi}[T_k + \tau]^2 + \ldots + \eta_{k+1}}{\tau} \\
&\quad - \frac{\phi + \dot{\phi}T_k + 0.5\ddot{\phi}T_k^2 + \ldots + \eta_k}{\tau} \\
&= \dot{\phi} + \ddot{\phi}[T_{k+1} - 0.5\tau] + \ldots + \dot{\eta}_k,
\end{aligned}
\tag{3.8}
$$

where $\dot{\eta}_k = \tau^{-1}[\eta_{k+1} - \eta_k]$. Subsequently, the Allan variance in (3.6) is then

$$\sigma_\zeta^2(\tau) = 0.5\langle[\bar{\zeta}_{k+1,\tau} - \bar{\zeta}_{k,\tau}]^2\rangle = 0.5\langle[\ddot{\phi}\tau + \ldots + \ddot{\eta}_k]^2\rangle, \tag{3.9}$$

where $\ddot{\eta}_k = \tau^{-1}[\dot{\eta}_{k+1} - \dot{\eta}_k]$. Note that $\ddot{\phi}$ is the frequency drift, η_k is the random deviation and more generally, contains other higher order terms of the polynomial in (3.2). Thus, in essence, the Allan deviation alleviates the linear trend of the phase error $\delta\bar{\mathcal{C}}(t)$ in (3.2) by eliminating $\{\phi, \dot{\phi}\}$ and gives a measure of noise contributed by the higher order non linear components of the clock for an integration time τ. In other words, for a sufficiently low Allan deviation, the inherently non-linear clock model can be approximated as an *affine clock model*

$$\bar{\mathcal{C}}(t) \approx \omega t + \phi. \tag{3.10}$$

This linearized clock model will be employed in the context of joint ranging and synchronization in Chapter 4.

3.3.3 Stability requirements

The approximated linear clock model is valid, provided the Allan deviation is negligible over a certain time period called the coherence time τ_c. We pose a rough stability requirement on the clock, following [Thompson, James.M.Moran and Swenson
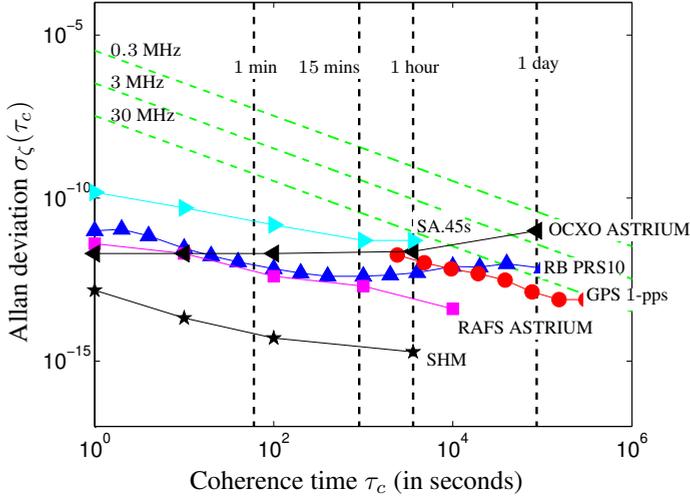
Figure 3.1: ***Long-term clock stability:*** Allan deviations of free running clocks are plotted versus the coherence time (in green) for various input frequencies ν_i. The map is overlayed with Allan deviations of potential clocks for potential space-based low frequency arrays namely PRS-10 Rubidium [Stanford 2006] , RAFS ASTRIUM [Droz et al. 2007], GPS 1pps [Lombardi et al. 2001], OCXO ASTRIUM [Airbus Defense and Space 2012], SA.45s CSAC and Space Hydrogen Maser (SHM) [Goujon et al. 2010].

1994; Ulvestad, Edwards and Linfield 1986] and define the *coherence time* τ_c, such that the RMS phase error of the clock remains less than 1 radian

$$2\pi\nu_o\sigma_\zeta(\tau_c)\tau_c \lessgtr 1, \tag{3.11}$$

where ν_o is the observational frequency and $\sigma_\zeta(\tau_c)$ is the Allan deviation as a function of τ_c. The product $\sigma_\zeta(\tau_c)\tau_c$ can be visualized as the time drift due to non-linear components of the clock after τ_c seconds. The clocks should be stable at least for the integration time τ_c, during which it suffices to estimate and correct (ω, ϕ) for synchronization.

3.4   Space-based radio astronomy

In an OLFAR node the maximum input frequency is 30MHz and the minimum integration time desired is 1 second [Rajan et al. 2011]. Thus for the minimum *coherence time* $\tau_c^{min} = 1s$, the Allan deviation must satisfy $\sigma_\zeta^{max}(\tau_c^{min} = 1s) \leq 10^{-8}$. Ideally,

the maximum coherence time τ_c^{max} must be as large as possible since it defines the calibration interval available to correct for the phase error. Figure 3.1 shows Allan deviations of the clock versus the coherence time as per (3.11) for various input frequencies ν and the performance of various atomic clocks. We use the OLFAR observational frequencies of $0.3 - 30$MHz, for which almost all the proposed clocks give a coherence time of 15 minutes to 1 hour, during which time period the clocks can be approximated as a linear model (3.10). Secondly, as mentioned in the earlier section, the short-term stability of the chosen clock hampers the input sampling and quantization of the data stream. The figure of merit for short-term clock stability is typically given by the sampling jitter of the clock, in terms of the desired SNR of the observation signal. See Appendix 3.A for a brief overview on short-term clock stability requirements.

For interferometry at wavelengths $10 - 10^3$ meters, the positions of the satellites must be known accurately up to a fraction of the smallest observational wavelength. This implies that the distance between the OLFAR satellites must be known with an accuracy < 1 meter. Relative positions of the satellites are sufficient for both radio astronomy and to avoid collision, which in turn can be estimated by measuring pairwise ranges between the satellites. In conjunction with the clock accuracies discussed in the previous section, the requirements on position and time of an OLFAR satellite can be briefly summarized as follows.

1. Allan deviation $\sigma_\zeta(\tau_c)$: Section 3.3 (3.11)

    a) $\sigma_\zeta(\tau_c) \leq 10^{-8}$ for $\tau_c = 1$ second
    b) $\sigma_\zeta(\tau_c) \leq 10^{-11}$ for $\tau_c = 1000$ seconds

2. Sampling jitter Δt_{jitter} : Appendix 3.A (3.13)

    a) $\Delta t_{\text{jitter}} < 10$ps for 8 bit sampling of observation signal
    b) $\Delta t_{\text{jitter}} < 1$ps for 12 bit sampling of observation signal

3. Range: < 1m accuracy

The time-position requirements of OLFAR scale with the needs of the ground based low frequency radio telescope LOFAR (low frequency antenna array) which observes the sky at $30 - 120$MHz. The LOFAR stations are equipped with Rubidium standard PRS-10 and long term stability is ensured by correcting rubidium clocks using the 1 pulse per second (1pps) output of a GPS receiver [Gunst and Schoonderbeek 2007]. For longer antenna separations at lower frequencies, it is observed

Clock	Manufacturer	Technology	Mass (grams)	Power (watts)	Space qualified ?
PRS-10	SRS	Rubidium	600	14	No
RAFS	EADS Astrium	Rubidium	3300	30	Yes
OCXO-F	EADS Astrium	OCXO	220	2	Yes
SA.45s	Symmetricom	Rubidium	< 35	< 0.125	No

Table 3.1: List of potential clocks for an OLFAR satellite which are commercially available. All the clocks output a 10MHz reference frequency and power indicates steady state consumption. The long term stability of these clocks are plotted in Figure 3.1.

that the phase errors are dominated by ionospheric disturbances instead of clock errors. Furthermore, the LOFAR antennas are fixed and their positions are measured up centimeter accuracies on each dimension.

3.5 Potential clocks

To achieve Allan deviations of order $10^{-8} - 10^{-11}$, Rubidium oscillators and Oven controlled crystal oscillators (OCXO) are considered. Although cesium and maser families can offer orders of magnitude lower Allan deviations, they are also very expensive both in terms of mass and power for an OLFAR satellite and are therefore not considered in this survey. The Allan-deviations σ_ζ of potential (currently available) clocks are plotted in Figure 3.1 against the coherence time τ_c. For the sake of reference, the plot is overlayed with the desired Allan-deviation (3.11) for various input frequencies ν_{in} (in green). Table 3.1 shows additional features of these clocks such as mass and power consumption.

Rubidium standards

RB-PRS10 is a rubidium based frequency standard with Allan deviations of $\sigma_{\zeta,prs} \leq 10^{-11}$ for 1-100 seconds [Stanford 2006] which is currently employed in LOFAR radio telescope [De Vos, Gunst and Nijboer 2009], but not space qualified. A secondary solution is the Astrium RAFS (Rubidium atomic frequency standard) which is a space qualified robust clock system, used in the Galileo satellite navigation [Droz et al. 2007] with $\sigma_{\zeta,rafs} \leq 10^{-11}$ for $1 < \tau_c < 1000$ seconds. Both these systems

have low clock jitters < 0.1 picosecond for input frequencies of $\nu_{in} = 30\text{MHz}$. The RAFS is marginally equivalent to the PRS10-RB in terms of Allan deviations however achieves a far better noise floor at 3×10^{-14} for ($t > 10^3$ seconds). However, refering to Table 3.1, RAFS is not a practical solution due to limitation of space and mass in an OLFAR satellite.

Oven controlled crystal oscillator (OCXO) standards

An alternative to Rubidium standard is the oven controlled crystal oscillator or OCXO. More specifically a space qualified variant is offered by Airbus OCXO-F [Airbus Defense and Space 2012], which weighs 220 grams, consumes 2 Watts during steady state operation and which can be easily incorporated in the OBC module [Saks et al. 2010]. The Allan variances of OCXO are better than its Rubidium counterparts for only up to τ_c=10 seconds, beyond which the Rubidium standards fair better.

Vertical cavity surface emitting laser (VCSEL) based Rubidium

In addition to the above mentioned clocks, there has been consistent research in developing chip scale atomic clocks in the past decade [Serkland et al. 2006][Knappe et al. 2004] based on Vertical Cavity Surface Emitting Lasers, which enable orders of magnitude reduction in size and power. SA.45s is a Rubidium Chip Scale Atomic Clock (CSAC) which is based on VCSEL and meets the Allan deviation requirements of OLFAR upto 1000 seconds, as shown in Figure 3.1. This CSAC weighs < 35 grams and has a steady power consumption of 125 mW, which suit the needs of an OLFAR satellite. Although the SA.45s is not space qualified, more recently similar CSACs are available for space-based applications e.g., Airbus OCXO-H [Airbus Defense and Space 2015].

3.6   Conclusions

The clock requirements of an OLFAR satellite have been investigated, by modeling the clock errors as polynomial in time. Each observation satellite needs to maintain a short term clock stability ($t \gg 1$s) of ≤ 1 ps to ensure sampling with 12 bits. Long term stability ($t \geq 1$) of clocks are given by Allan deviations $\sigma_\zeta(\tau_c)$ as a function of the coherence time τ_c. It is shown, using a simple derivation, that the Allan deviation indicates the noise contributed by the non linear components of the clock. Furthermore, given a space qualified clock which meets the Allan deviation requirements of $\sigma_\zeta(1) \leq 10^{-8}$ and $\sigma_\zeta(1000) \leq 10^{-11}$, the clock error can be approximated

as a linear function of *true* time, during the coherence period. The VCSEL based Rubidium SA.45s is a non-space qualified clock with low mass and minimal power consumption, which meets the long term stability requirements of OLFAR but only for coherence time up to 1000 seconds. This limits the maximum calibration time for each satellite to re-synchronize, i.e., estimate and correct for their respective clock offset (ϕ) and clock drift ($\dot{\phi}$).

In the next chapter, the approximated linear clock model (3.10) is used to propose a novel data model for joint synchronization and ranging for a network of mobile nodes. Furthermore, in the following chapters we do not limit our discussion to space-based radio astronomy networks, but instead address the broader application area of wireless networks.

Appendix 3.A   Dynamic range and sampling jitter

This section investigates the effect of short term ($t \ll 1$ second) clock discrepancies on the signal processing system. Traditionally, the first stage comprises of two processes, i.e., sampling and quantization. The Sample and Hold (S/H) block decimates the input signal periodically along the time axis and the analog to digital Converter (ADC) quantizes the input signal along the amplitude scale. The fluctuations in the sampling time causes the phase modulation of the incoming analog signal and results in an additional noise component in the signal. These unwanted variations in time, called jitter, lead to uncertainty as to when the analog input is actually sampled. The Signal to Noise Ratio (SNR) of the S/H block with sampling jitter Δt_{jitter} is given as [Kester 2004]

$$\text{SNR}(dB) = -20 \log_{10}(2\pi\nu_{in}\Delta t_{\text{jitter}}), \tag{3.12}$$

where ν_{in} is the frequency of a pure sinusoid input signal. The Δt_{jitter} is the total RMS jitter from the clock source and the ADC circuitry, i.e.,

$$\Delta t_{\text{jitter}} = \sqrt{\Delta t_{ADC}^2 + \Delta t_{\text{CLK}}^2},$$

where Δt_{ADC} and Δt_{CLK} are RMS jitters due to ADC and clock source respectively. Now, since the ADC follows the S/H, the best achievable SNR post quantization is limited by the SNR of the S/H. Hence considering an ADC with significantly high SNR i.e., $\Delta t_{ADC} \ll \Delta t_{\text{CLK}}$, we can approximate the total jitter (3.12) as

$$\Delta t_{\text{jitter}} \approx \Delta t_{\text{CLK}} = \frac{10^{\frac{-\text{SNR}}{20}}}{2\pi\nu_{in}}, \tag{3.13}$$

Thus, given the desired dynamic range, (3.13) solves for the tolerable clock jitter. Observe that the jitter sampling error is not a function of the clock frequency, but instead only dependent on the desired dynamic range and the frequency of the input signal. Figure 3.2 shows limiting cases of the SNR versus input frequencies, which illustrates the fact that the dynamic range of system deteriorates with increase in frequency due to jitter error. Further more, assuming a best performance scenario (i.e., with a distortion-less High-SNR ADC), the SNR from (3.13) can be represented as the Effective Number Of Bits (ENOB) i.e.,

$$\text{ENOB} = \frac{\text{SNR} - 1.76}{6.02}, \tag{3.14}$$

The satellites of the potential space-based cluster will employ direct sampling of
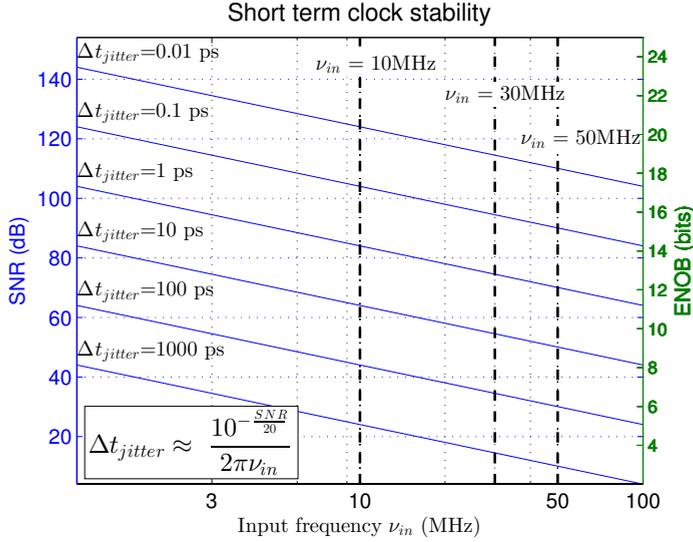
Figure 3.2: ***Short-term clock stability:*** Limiting cases of the SNR and corresponding ENOB due to jitter t_{jitter} versus input frequency ν_{in} . The demarkation lines at 10MHz, 30MHz and 50MHz show the maximum input frequencies of the DARIS, OLFAR and FIRST systems at $\nu_{in} = 30$MHz.

the entire observation bandwidth (0.3MHz- 30MHz) [Rajan et al. 2011]. Furthermore, the required dynamic range will depend on the radio frequency interference (RFI) level at the deployment locations. Some of the potential deployment locations include, moon orbit, Earth-moon L2 point and Earth- leading/trailing, where the interference levels at these wavelengths are little understood [Bentum and Boonstra 2011]. Hence, although only 1-2 bits are sufficient for radio astronomy imaging, the OLFAR system will sample at >8 bits and the remaining bits will be discarded by a RFI mitigation stage. Referring to Figure 3.2, to achieve quantization resolution of 16 bits at $\nu_{in} = 30$MHz, the required sampling jitter must be < 0.1ps and for 12 bits/cycle sampling, we must ensure $\Delta t_{\text{jitter}} < 1$ps.

4

Synchronization and ranging

Synchronization and localization are critical challenges for the coherent functioning of a wireless network, which are conventionally solved independently. Recently, various estimators have been proposed for pairwise synchronization between immobile nodes, based on time stamp exchanges via two-way communication. In chapter 3, we showed that the phase error of a clock oscillator, with sufficiently low Allan deviation, can be approximated as a linear function in time. In this chapter, we consider an *anchorless network of asynchronous mobile nodes*, where each node has an independent clock oscillator and the inter-nodal pairwise distance is also time-varying. We present a novel joint time-range model, treating both asynchronized clocks and the pairwise distances as a polynomial function of *true* time. For a pair of nodes, a least squares solution is proposed for estimating the pairwise range parameters between the nodes, in addition to estimating the clock offsets and clock skews. Extending these pairwise solutions to network-wide ranging and clock synchronization, we present a central data fusion based global least squares algorithm. A unique solution is non-existent without a constraint on the cost function e.g., a clock reference node. Ergo, a constrained framework is proposed and a new Constrained Cramér-Rao Bound (CCRB) is derived for the joint time-range model. In addition, to alleviate the need for a single clock reference, various clock constraints are presented and their benefits are investigated using the proposed solutions. Simulations are conducted and the algorithms are shown to approach the theoretical limits.

4.1   Introduction

The coherent functioning of wireless networks relies heavily on time synchronization among nodes [Zhang, Liu and Honghui Xia 2002; Elson and Estrin 2003; Sundararaman, Buy and Kshemkalyani 2005; IEEE Working Group 802.15.4 2007]. All nodes in a network are equipped with independent clock oscillators, which must be synchronized to a global reference, to facilitate accurate time stamping of data and synchronized communication of processed information. Clock oscillators in these nodes are inherently non-linear [Barnes et al. 1971; Lindsey et al. 1985; Allan 1987], however, if calibrated astutely, can be approximated as a linear function for a small measurement time period. The unknown regression coefficients of such an affine clock model will be the clock offset and clock skew. Global time synchronization within the network is then achieved by estimating all clock offsets and clock skews of the nodes and compensating the respective clocks aptly. Furthermore, when nodes are arbitrarily deployed in the field, then position estimation is often equally crit-

ical as time synchronization [Sayed, Tarighat and Khajehnouri 2005a; Patwari et al. 2005]. The intermediate distances between all the nodes in the network (obtained via ranging) is one of the key inputs for almost all localization techniques e.g., time of arrival (TOA) [Cheung et al. 2004], time difference of arrival (TDOA) [Chan and Ho 1994], multidimensional scaling (MDS) [Borg and Groenen 2005]. Moreover, when the nodes are mobile, distance estimation using ranging is a challenge, particularly when the clocks of the nodes are asynchronous.

In this chapter, we consider an *anchorless network of asynchronous mobile nodes*, capable of two-way communication. All the nodes are in motion, i.e., *mobile* during the two-way communication and hence the pairwise distances are unique at each time instant. In addition, all the nodes are equipped with independent clocks, which are *asynchronous* w.r.t. some reference time, i.e., *true* time, during the two-way communication. Finally, by the term *anchorless*, we consider an autonomous and co-operative network with no external (reference) information on either time, distance or position. Hence we assume no a priori knowledge on the nodes initial positions and/or on their respective motion. Thus, our fundamental challenge is to understand the joint variation of local time at each node and time-varying pairwise distances between the cluster of nodes. After obtaining the pairwise distances at discrete intervals of time, the relative positions of the nodes at respective time instances can be obtained via MDS [Borg and Groenen 2005]. We assume the need for bi-directional communication between the nodes, but a full mesh network is not always necessary.

4.1.1 Applications

Our motivation for this work are *inaccessible* mobile wireless networks, which have partial or no information of absolute co-ordinates and/or clock references. Such scenarios are prevalent in under-water communication [Chandrasekhar et al. 2006], indoor positioning systems [Liu et al. 2007], autonomous swarm networks [Bürkle, Segor and Kollmann 2011] and envisioned space based satellite networks with minimal ground segment capability, such as OLFAR i.e., orbiting low frequency antennas for radio astronomy [Rajan et al. 2016]. The OLFAR network is an interferometric array of ≥ 10 identical, scalable and autonomous satellites in space to be used as a scientific instrument for ultra long wavelength observations. The OLFAR cluster will be deployed far from the earth orbiting global positioning systems. If the interferometric array is deployed on the Moon far-side, or orbits the Moon such that the Moon eclipses the array against Earth, then Earth-based communication will be completely cut-off. In the absence of apriori reference on position and time, cooperative synchronization and localization is one of the fundamental challenges for OLFAR

like *anchorless networks*. See Chapter 2 for a detailed description. In this chapter, we focus particularly on the joint ranging and synchronization of such an anchorless network.

4.1.2   Previous work

The joint estimation of clock parameters (upto a first order) and the pairwise distances via two-way ranging is a well studied topic for a network of stationary nodes [Sundararaman, Buy and Kshemkalyani 2005; IEEE Working Group 802.15.4 2007]. For a pair of fixed nodes capable of bi-directional communication, the classical two-way ranging (TWR) model involves 2 clock offsets, 2 clock skews and the pairwise distance between the nodes, which results in an unsolvable five dimensional problem. However, traditionally, one clock is assumed to be the reference clock which reduces the cardinality to 3 and given sufficient measurements, the absolute clock skew and clock offset of the second node, and its pairwise distance from the first node can be estimated. For estimating the clock errors, maximum likelihood estimates and Low Complexity Least Square (LCLS) estimates are proposed in [Noh et al. 2007] and [Leng and Wu 2010] respectively, and distributed solutions are presented in [Etzlinger, Wymeersch and Springer 2014]. A step further, joint estimation of clock parameters and the fixed distances for the entire network of nodes was proposed in [Rajan and van der Veen 2011]. An overview of estimators for a plethora of two-way ranging protocols and approaches are presented in [Serpedin and Chaudhari 2009] and, joint localization and synchronization for an anchored network is addressed in [Zheng and Wu 2010][Etzlinger et al. 2013]. Furthermore, the connectivity, capacity, clocks, and function computation required for synchronizing large network of nodes is discussed in [Freris, Graham and Kumar 2010].

However, all these propositions are based on the classical two-way ranging data model [IEEE Working Group 802.15.4 2007], where the node positions are fixed and consequently the pairwise ranges are independent of time. In case of an *anchorless network of mobile nodes*, the nodes are in motion during the time-of-flight measurement window. As a result, the pairwise distances are a non-linear function of time and our proposition is to approximate this continuous function as a polynomial function in time, for a small measurement period. Under this context, the unknown coefficients of this monomial approximation (called range parameters) need to be estimated, which beget the pairwise distances at discrete time intervals. Furthermore, for an unsynchronized network, these range parameters are plagued with clock errors, which must be estimated and the respective clocks calibrated. Along these lines, for a network of mobile nodes, we had previously proposed a joint first-order time-range

model in [Rajan and van der Veen 2012], where clock parameters were estimated along with range parameters upto the first order. We further extended this model to a joint second-order ranging and affine synchronization basis for a network of mobile nodes in [Rajan and van der Veen 2013], where second-order range parameters were also estimated. However, in reality, the order of the time-varying distance approximation is typically unknown, as it depends on the initial position, the nature of node mobility and the measurement time window. This motivates the need for a unified time-range basis which can estimate both the clock parameters and pairwise distances without any a priori information on the motion of the nodes.

4.1.3 Contributions

In this chapter, we propose a generic joint time-range basis (Section 4.2), which combines the affine clock model (Section 4.2.1) with a generalized $(L-1)$th order non-linear range model for an *anchorless network of mobile nodes*. In the presence of clock errors, the time-varying distance measurements are corrupted with clock skews and clock offsets and the relation is addressed in Section 4.2.2. The proposed joint basis is applied in a TWR framework (Section 4.3.1) and a *Mobile Pairwise Least Squares (MPLS)* solution (Section 4.3.2) is proposed for a pair of mobile nodes, to estimate the clock skews, offsets and the range parameters of the pairwise distance between the nodes. Furthermore, for the entire network, all the clock skews, offsets and range parameters can be estimated using the proposed *Mobile Global Pairwise Least Squares (MGLS)* algorithm (Section 4.4.1). More generally, when the order of distance approximation L is unknown, iterative solutions are proposed for both the pairwise and global solutions. A unique solution is non-existent without a constraint on the cost function (e.g., clock reference node) and hence, a constrained framework is proposed. A new Constrained Cramér-Rao Bound (CCRB) is derived in Section 4.5 for the estimated clock and range parameters. In addition, instead of the classic constraint of using a single clock reference, alternative *sum constraint* and *nullspace constraint* are proposed (Section 4.6) which are shown to yield about a factor of magnitude better performance on the clock skew and offset estimation. The performance of the proposed algorithms and choice of constraints are analyzed using simulations in Section 4.7.

4.2   Joint time-range basis

4.2.1   Affine time model

Consider a network of N nodes equipped with independent clock oscillators which, under ideal conditions, are synchronized to the global time. However, in reality, due to various oscillator imperfections and environment conditions the clocks vary independently and are inherently non-linear. Nonetheless, the local time at a given node can be approximated to a linear function, provided the Allan deviation of the respective clock is negligible for a small time period, as discussed in the previous chapter (*See Chapter 3*). Let t_i be the local time at node i, then its divergence from the ideal *true* time t is to first order given by the affine clock model,

$$t_i = \omega_i t + \phi_i \quad \Leftrightarrow \quad \mathcal{C}_i(t_i) \triangleq t = \alpha_i t_i + \beta_i, \tag{4.1}$$

where $\omega_i \in \mathbb{R}_+$ and $\phi_i \in \mathbb{R}$ are the clock skew and clock offset of node i and the function $\mathcal{C}_i(t_i)$ relates the local time t_i to the *true* time $t \triangleq \mathcal{C}_i(t_i)$. In actuality, the clock skew (ω_i) and clock offset (ϕ_i) are time-varying, but we assume they remain constant for small measurement time period (say ΔT), which is often a reasonable assumption [Freris, Graham and Kumar 2010]. Alternatively, the 2nd part of (4.1) shows the translation from local time t_i to the global time t, where $[\alpha_i, \beta_i] \triangleq [\omega_i^{-1}, -\phi_i \omega_i^{-1}]$ are the calibration parameters needed to correct the local clock at node i. The clock skew and clock offset parameters for all N nodes are represented by $\boldsymbol{\omega} = [\omega_1, \omega_2, \ldots, \omega_N]^T \in \mathbb{R}_+^{N \times 1}$ and $\boldsymbol{\phi} = [\phi_1, \phi_2, \ldots, \phi_N]^T \in \mathbb{R}^{N \times 1}$ respectively, and similarly the clock calibration parameters of the network are $\boldsymbol{\alpha} \in \mathbb{R}_+^{N \times 1}$ and $\boldsymbol{\beta} \in \mathbb{R}^{N \times 1}$. The unique relation between all the clock parameters is given by

$$\boldsymbol{\alpha} \triangleq \mathbf{1}_N \oslash \boldsymbol{\omega} \quad \Leftrightarrow \quad \boldsymbol{\omega} \triangleq \mathbf{1}_N \oslash \boldsymbol{\alpha}, \tag{4.2a}$$

$$\boldsymbol{\beta} \triangleq -\boldsymbol{\phi} \oslash \boldsymbol{\omega} \quad \Leftrightarrow \quad \boldsymbol{\phi} \triangleq -\boldsymbol{\beta} \oslash \boldsymbol{\alpha}. \tag{4.2b}$$

Observe that for an ideal clock, $[\omega_i, \phi_i] = [1, 0]$ immediately implies $[\alpha_i, \beta_i] = [1, 0]$ and vice versa.

4.2.2   Non-linear range model

In addition to clock variations, the nodes are also in motion with respect to each other. Traditionally, when the nodes are fixed, the pairwise propagation delay τ_{ij} between a node pair (i, j) is $\tau_{ij} = c^{-1} d_{ij}$, where d_{ij} is the fixed distance between the node

pair and c is the speed of the electromagnetic wave in the medium. [1] However, when the nodes are mobile, then the relative distances between the nodes are a non-linear function of time. For a small measurement time period ΔT, the propagation delay $\tau_{ij}(t)$ between a node pair (i, j) is then, classically a Taylor series, given by

$$\begin{aligned} \tau_{ij}(t) &\triangleq c^{-1}\mathcal{R}_{ij}(t) \\ &\approx c^{-1}(r_{ij}^{(0)} + r_{ij}^{(1)}t + r_{ij}^{(2)}t^2 + \ldots + r_{ij}^{(L-1)}t^{L-1}), \end{aligned} \tag{4.3}$$

where $\mathcal{R}_{ij}(t)$ is the time-varying pairwise distance between node pair (i, j) and $\mathbf{r}_{ij} = \left[r_{ij}^{(0)}, r_{ij}^{(1)}, r_{ij}^{(2)}, \ldots, r_{ij}^{(L-1)}\right]^T \in \mathbb{R}^{L \times 1}$ contains all the range coefficients of the corresponding Taylor approximation. The order of approximation and the range of these L coefficients depend on the initial position and the type of motion of the respective nodes. However, the propagation delay between the node pair is not measured at true time, instead by a local node clock, say node i. Hence, substituting the equation of ideal *true* time t from (4.1), we have the propagation delay $\tau_{ij}(t_i)$ in terms of the local time t_i, i.e.,

$$\begin{aligned} \tau_{ij}(t_i) &= \mathcal{G}_{ij}(t_i) \triangleq c^{-1}\mathcal{R}_{ij}(\mathcal{C}_i(t_i)) \\ &\approx \gamma_{ij}^{(0)} + \gamma_{ij}^{(1)}t_i + \gamma_{ij}^{(2)}t_i^2 + \ldots + \gamma_{ij}^{(L-1)}t_i^{L-1}, \end{aligned} \tag{4.4}$$

where $\mathcal{G}_{ij}(t_i)$ describes the pairwise propagation delay w.r.t. the local time at t_i. The coefficients $\boldsymbol{\gamma}_{ij} = \left[\gamma_{ij}^{(0)}, \gamma_{ij}^{(1)}, \gamma_{ij}^{(2)}, \ldots, \gamma_{ij}^{(L-1)}\right]^T \in \mathbb{R}^{L \times 1}$ are translated range parameters, which can be expressed in terms of $\mathbf{r}_{ij}$, α_i and β_i.

For the entire network, comprising of $\bar{N} = \binom{N}{2}$ *unique* pairwise links for N nodes, all the unique range coefficients are given by

$$\begin{aligned} \mathbf{R} &= \left[\mathbf{r}_{12}, \mathbf{r}_{13}, \ldots, \mathbf{r}_{(N-1)N}\right]^T \in \mathbb{R}^{\bar{N} \times L} \\ &= \begin{bmatrix} r_{12}^{(0)} & r_{12}^{(1)} & \cdots & r_{12}^{(L-1)} \\ r_{13}^{(0)} & r_{13}^{(1)} & \cdots & r_{13}^{(L-1)} \\ \vdots & & \ddots & \vdots \\ r_{(N-1)N}^{(0)} & r_{(N-1)N}^{(1)} & \cdots & r_{(N-1)N}^{(L-1)} \end{bmatrix}, \end{aligned} \tag{4.5}$$

---

[1] Without the loss of generality, we assume line of sight communication and hence all physical layer effects such as multi-path and shadowing are beyond the scope of this work. These scenarios can be addressed using existing techniques in literature e.g., [Bellusci et al. 2008].

and along similar lines, we have the translated range coefficients

$$
\begin{aligned}
\boldsymbol{\Gamma} &= \left[\boldsymbol{\gamma}_{12}, \boldsymbol{\gamma}_{13}, \ldots, \boldsymbol{\gamma}_{(N-1)N}\right]^T \in \mathbb{R}^{\bar{N} \times L} \\
&= \begin{bmatrix}
\gamma_{12}^{(0)} & \gamma_{12}^{(1)} & \cdots & \gamma_{12}^{(L-1)} \\
\gamma_{13}^{(0)} & \gamma_{13}^{(1)} & \cdots & \gamma_{13}^{(L-1)} \\
\vdots & & \ddots & \vdots \\
\gamma_{(N-1)N}^{(0)} & \gamma_{(N-1)N}^{(1)} & \cdots & \gamma_{(N-1)N}^{(L-1)}
\end{bmatrix},
\end{aligned}
\tag{4.6}
$$

where $r_{ij}^{(l)}$ and $\gamma_{ij}^{(l)}$ represent the unique lth order range coefficient for ($0 \leq l \leq L-1$) of the node pair (i, j) respectively. Furthermore, vectorizing these coefficient matrices, we have

$$
\boldsymbol{\gamma} = \text{vec}(\boldsymbol{\Gamma}) \in \mathbb{R}^{\bar{N}L \times 1}, \quad \mathbf{r} = \text{vec}(\mathbf{R}) \in \mathbb{R}^{\bar{N}L \times 1}.
\tag{4.7}
$$

Observe that although $\mathcal{G}(\cdot)$ and $\mathcal{R}(\cdot)$ are non-linear functions, $\mathcal{C}_i(t_i) \ \forall \ 1 \leq i \leq N$ is an affine translation and thus there exists a linear transformation matrix $\mathbf{G} \in \mathbb{R}^{\bar{N}L \times \bar{N}L}$ containing $\begin{bmatrix} \boldsymbol{\alpha} & \boldsymbol{\beta} \end{bmatrix}$ such that

$$
\mathbf{r} = \mathbf{G}\boldsymbol{\gamma} \quad \Leftrightarrow \quad \boldsymbol{\gamma} = \mathbf{G}^{-1}\mathbf{r}.
\tag{4.8}
$$

The expression for $\mathbf{G}$ is derived in Appendix 4.A.

4.2.3   Time-range interrelation

In the following section we present a generalized TWR scenario where the joint time-range basis is applied. Furthermore, an estimation process is described to obtain the network parameters $\boldsymbol{\theta} = [\boldsymbol{\alpha}, \boldsymbol{\beta}, \boldsymbol{\gamma}]^T \in \mathbb{R}^{M \times 1}$ where $M = 2N + \bar{N}L$, that are uniquely related to the desired unknown clock and range parameters $\boldsymbol{\zeta} = [\boldsymbol{\omega}, \boldsymbol{\phi}, \mathbf{r}]^T \in \mathbb{R}^{M \times 1}$ by (4.2) and (4.8) respectively. Finally the distance at discrete time intervals is obtained using (4.4).

4.3   Pairwise synchronization and ranging

4.3.1   Data Model

Consider a pair of mobile nodes (i, j) with $i < j$, which are capable of two-way communication with each other as shown in Figure 4.1. The two nodes communicate
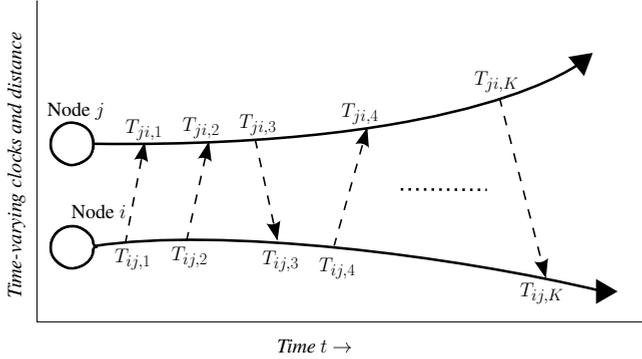
Figure 4.1: *Asynchronous pair of mobile nodes:* A generalized two-way ranging (TWR) scenario between a pair of asynchronous nodes in motion, where the nodes exchange K time stamps each. The curved lines symbolize the time-varying motion of the nodes, in addition to the independent clock drifts. *See Remark 1.*

messages back and forth, and the time markers of transmission and reception are registered independently at respective nodes in respective local time coordinates. The kth time stamp recorded at node i when communicating with node j is denoted by $T_{ij,k}$ and similarly at node j the time stamp is $T_{ji,k}$. Note that the total measurement period in this framework is $\Delta T = T_{ij,K} - T_{ij,1}$ seconds. The direction of the communication is indicated by $E_{ij,k}$, where $E_{ij,k} = +1$ for transmission from node i to node j and $E_{ij,k} = -1$ for transmission from node j to node i. Furthermore, the propagation delay between the nodes at each time instant $1 \leq k \leq K$ is given by $\tau_{ij,k} = c^{-1}d_{ij,k}$, where K is the total number of time stamps recorded at each node and $d_{ij,k}$ is the distance between the nodes at time instant k.

Under ideal circumstances, when the nodes are completely synchronized the noise free kth communication time markers are related as

$$T_{ji,k} = \begin{cases} T_{ij,k} + c^{-1}d_{ij,k} & \text{for } i \to j \tag{4.9a} \\ T_{ij,k} - c^{-1}d_{ij,k} & \text{for } i \leftarrow j \tag{4.9b} \end{cases}$$

which can be combined as

$$\begin{aligned} T_{ji,k} &= T_{ij,k} + c^{-1}E_{ij,k}d_{ij,k} & \text{for } i \leftrightarrow j \tag{4.10} \\ &= T_{ij,k} + c^{-1}E_{ij,k}\mathcal{R}_{ij}(T_{ij,k}), \tag{4.11} \end{aligned}$$

where the distance between the nodes $d_{ij,k} = c\tau_{ij,k}$ at time instant k is $\mathcal{R}_{ij}(T_{ij,k})$ defined in (4.3). However, due to clock uncertainties modeled in (4.2), and its sub-

sequent influence on distance (4.4), (4.11) translates to

$$\boxed{\mathcal{C}_i(T_{ij,k}) - \mathcal{C}_j(T_{ji,k}) + E_{ij,k}\mathcal{G}_{ij}(T_{ij,k}) = 0,} \qquad (4.12)$$

where without loss of generality, the time-varying pairwise distance is expressed as a function of time at node i.

Furthermore, in reality due to measurement noise on the time markers, (4.12) is

$$\mathcal{C}_i(T_{ij,k} + \eta_{i,k}) - \mathcal{C}_j(T_{ji,k} + \eta_{j,k}) + E_{ij,k}\mathcal{G}_{ij}(T_{ij,k} + \eta_{i,k}) = 0, \qquad (4.13)$$

where $\{\eta_{i,k}, \eta_{j,k}\}$ are noise variables plaguing the timing measurements at respective nodes. Rearranging the terms and incorporating the approximate range model for $\tau_{ij}(t_i)$ from (4.4) as a function of local time at node i we have,

$$\underbrace{\alpha_i T_{ij,k} - \alpha_j T_{ji,k} + \beta_i - \beta_j}_{\text{Clock parameters + Measurements}} + \underbrace{E_{ij,k}}_{\text{Direction}} \underbrace{(\gamma_{ij}^{(0)} + \gamma_{ij}^{(1)} T_{ij,k} + \dots)}_{\text{Range parameters + Measurements}} = \underbrace{\eta_{ij,k}}_{\text{noise}} \qquad (4.14)$$

which includes the error due to Taylor series expansion and where $\eta_{ij,k}$ is the stochastic noise between the node pair (i, j) at the kth instant, which is discussed in Section 4.5.

Remark 1: (**Mobile nodes during communication**): In Figure 4.1, the curved lines symbolize the independent clock drifts in addition to the time-varying distance between the nodes. In traditional TWR, for a fixed pair of nodes (i.e., $L = 1$), the pairwise distance $d_{ij,k}$ is assumed to be invariant for the total measurement period $\Delta T = T_{ij,K} - T_{ij,1}$. However, when the nodes are mobile, the distance at each time instance k is dissimilar. Hence, instead of the classical assertion that the nodes are relatively stable over a time period ΔT [IEEE Working Group 802.15.4 2007; Noh et al. 2007; Leng and Wu 2010], we suppose that the nodes are relatively stable over a much smaller time period of $\delta t = |T_{ij,k} - T_{ji,k}|$ i.e., the propagation time of the message. Furthermore, unlike previous cases [IEEE Working Group 802.15.4 2007; Noh et al. 2007; Leng and Wu 2010] where the transmission and reception was alternating, the proposed setup imposes no pre-requisites on the sequence or number of two-way communications [Rajan and van der Veen 2011; Rajan and van der Veen 2012; Rajan and van der Veen 2013]. However, at least a single communication in the opposite direction is required for a feasible solution.

4.3.2   Mobile Pairwise Least Squares (MPLS)

Extending (4.14) for all K communications, a generalized joint clock and $(L-1)$th order range model for a pair of nodes is

$$
\begin{bmatrix} \mathbf{A}_{ij,1} & \mathbf{A}_{ij,2} \end{bmatrix}
\begin{bmatrix}
\alpha_i \\
\alpha_j \\
\beta_i \\
\beta_j \\
\gamma_{ij}^{(0)} \\
\gamma_{ij}^{(1)} \\
\gamma_{ij}^{(2)} \\
\vdots \\
\gamma_{ij}^{(L-1)}
\end{bmatrix}
= \boldsymbol{\eta}_{ij},
\tag{4.15}
$$

where

$$
\mathbf{A}_{ij,1} = \begin{bmatrix} \mathbf{t}_{ij} & -\mathbf{t}_{ji} & \mathbf{1}_K & -\mathbf{1}_K \end{bmatrix},
\tag{4.16}
$$

$$
\mathbf{A}_{ij,2} = \mathbf{E}_{ij}\mathbf{V}_{ij},
\tag{4.17}
$$

$$
\mathbf{V}_{ij} = \begin{bmatrix} \mathbf{t}_{ij}^{\odot 0} & \mathbf{t}_{ij}^{\odot 1} & \cdots & ,\mathbf{t}_{ij}^{\odot L-1} \end{bmatrix},
\tag{4.18}
$$

contain the observation vectors

$$
\mathbf{t}_{ij} = [T_{ij,1}, T_{ij,2}, \ldots, T_{ij,K}]^T \in \mathbb{R}^{K \times 1},
\tag{4.19}
$$

$$
\mathbf{E}_{ij} = \mathrm{diag}(\mathbf{e}_{ij}) \in \mathbb{R}^{K \times K},
\tag{4.20}
$$

$$
\mathbf{e}_{ij} = [E_{ij,1}, E_{ij,2}, \ldots, E_{ij,K}]^T \in \mathbb{R}^{K \times 1}.
\tag{4.21}
$$

The time markers recorded at node i and node j while communicating with each other are stored in $\mathbf{t}_{ij}$ and $\mathbf{t}_{ji}$ respectively, $\mathbf{e}_{ij}$ is a known vector indicating the transmission direction for each data packet and the noise vector $\boldsymbol{\eta}_{ij} \in \mathbb{R}^{K \times 1}$ is

$$
\boldsymbol{\eta}_{ij} = [\eta_{ij,1}, \eta_{ij,2}, \ldots, \eta_{ij,K}]^T \in \mathbb{R}^{K \times 1}.
\tag{4.22}
$$

Given a sufficiently large number of communications K between the two nodes, the homogeneous system (4.15) has a non-trivial solution spanning the null space of $[\mathbf{A}_{ij,1} \; \mathbf{A}_{ij,2}]$. The known Vandermonde matrix $\mathbf{V}_{ij}$ is full rank for K sufficiently large. Secondly, in $\mathbf{A}_{ij,1}$ the column vectors $\mathbf{1}_K$ and $-\mathbf{1}_K$ are completely dependent

and although $[\mathbf{t}_{ij} \ - \ \mathbf{t}_{ji}]$ is full rank, it is observed that the matrix $\mathbf{A}_{ij,1}$ is rank deficient by 2 and the corresponding null space is data dependent [Rajan and van der Veen 2011].

A unique solution can be obtained by assuming either one of $\{\alpha_i, \alpha_j\}$ and either one of $\{\beta_i, \beta_j\}$ is known and thus eliminating respective columns in $\mathbf{A}_{ij,1}$, which is in turn accomplished by choosing one of the two nodes as a clock reference[Rajan and van der Veen 2011]. More generally, we can translate the homogeneous equations into normal equations by asserting one of the two nodes as the reference node, say node i with $[\alpha_i, \beta_i] = [1, 0]$. This gives

$$\mathbf{A}_{ij}\boldsymbol{\theta}_{ij} \ = \ \mathbf{b}_{ij} + \boldsymbol{\eta}_{ij} \tag{4.23}$$

where

$$\mathbf{A}_{ij} \ = \ [-\mathbf{t}_{ji} \ \ -\mathbf{1}_K \ \ \mathbf{A}_{ij,2}] \in \mathbb{R}^{K \times (L+2)}, \tag{4.24}$$

$$\boldsymbol{\theta}_{ij} \ = \ [\alpha_j \ \ \beta_j \ \ \boldsymbol{\gamma}_{ij}^T]^T \in \mathbb{R}^{(L+2) \times 1}, \tag{4.25}$$

$$\mathbf{b}_{ij} \ = \ -\mathbf{t}_{ij}. \tag{4.26}$$

The Mobile Pairwise Least Squares (MPLS) solution is then obtained by minimizing the l_2 norm,

$$\hat{\boldsymbol{\theta}}_{ij} = \arg\min_{\boldsymbol{\theta}_{ij}} \|\mathbf{A}_{ij}\boldsymbol{\theta}_{ij} - \mathbf{b}_{ij}\|^2 = (\mathbf{A}_{ij}^T\mathbf{A}_{ij})^{-1}\mathbf{A}_{ij}^T\mathbf{b}_{ij}, \tag{4.27}$$

where $\hat{\boldsymbol{\theta}}_{ij} = [\hat{\alpha}_j \ \hat{\beta}_j \ \hat{\boldsymbol{\gamma}}_{ij}^T]^T$ is an estimate of $\boldsymbol{\theta}$. Following, an estimate of the desired clock and range parameters $[\hat{\omega}_j \ \hat{\phi}_j \ \hat{\mathbf{r}}_{ij}^T]^T$ can then be obtained using (4.2) and (4.8). An estimate of the approximated distance $d_{ij,k}$ between the nodes at the kth time instant is then from (4.4)

$$\hat{d}_{ij,k} = c\left(\hat{\gamma}_{ij}^{(0)} + \hat{\gamma}_{ij}^{(1)}T_{ij,k} + \hat{\gamma}_{ij}^{(2)}T_{ij,k}^2 + \ldots + \hat{\gamma}_{ij}^{(L)}T_{ij,k}^{L-1}\right), \tag{4.28}$$

and for all $1 \le k \le K$, we have

$$\widehat{\mathbf{d}}_{ij} = c\mathbf{V}_{ij}\widehat{\boldsymbol{\gamma}}_{ij}, \tag{4.29}$$

where $\mathbf{V}_{ij}$ is the Vandermonde matrix (4.18) and $\hat{\mathbf{d}}_{ij} = \left[\hat{d}_{ij,1}, \hat{d}_{ij,2}, \ldots, \hat{d}_{ij,K}\right]^T \in \mathbb{R}^{K \times 1}$ is the distance estimate between the node pair (i, j) at all K time instances.

More generally, when L is unknown, solutions for increasing L can be estimated using iterative MPLS (iMPLS) (based on order recursive least squares [Kay 1993]),
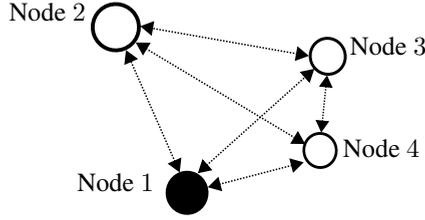
Figure 4.2: ***Illustration of a network of mobile nodes:*** A network with $N = 4$ nodes, each capable of two-way communication. The clock skews and clock offsets of node 2, 3 and 4 are unknown and are to be estimated, in addition to all unknown range parameters.

which we briefly describe in Appendix 4.B for the sake of completeness. This order recursive least squares not only implicitly estimates the unknown L by incrementing the number of columns of the Vandermonde structure $\mathbf{A}_{ij,2}$ iteratively, but also implements computationally economical updates of the inverse and solutions (4.27).

Although the MPLS solution is motivated for a mobile network of nodes, it is readily applicable for a network of immobile nodes. In that case, for a given node pair $\{i, j\}$ the estimated range parameter $r_{ij}^{(0)}$ indicates the fixed uncalibrated communication latency during the exchange of time stamps and the higher order range parameters indicate the latency fluctuations during communication.

Remark 2: (**Feasibility of the MPLS solution**): The solution (4.27) is feasible if $\mathbf{A}_{ij,L} \in \mathbb{R}^{K \times (L+2)}$ is a square or tall matrix i.e., the number of communications $K \geq (L + 2)$. Secondly, to ensure full column rank, we require $\mathbf{e}_{ij} \neq -\mathbf{1}_K$ and $\mathbf{e}_{ij} \neq +\mathbf{1}_K$. In other words, among the $K \geq (L + 2)$ data exchanges between the two nodes, there must be at least one transmission from i to j and j to i respectively.

Remark 3: (**Sub-optimality of the MPLS solution**): The proposed LS solution (4.27) is suboptimal if the linear model is heteroscedastic or when the noise plaguing the system (4.23) is correlated, which can be improved by employing a Weighted Least Squares (WLS). Alternatively, since both $\mathbf{A}$ and $\mathbf{b}$ contain noise, the corresponding cost function can be minimized using a Total Least Squares (TLS) estimator. [Lawson and Hanson 1974] .

4.4   Network synchronization and ranging

We now extend the pairwise model in (4.15) to the entire network, i.e., $N \geq 2$, and intend to find a global solution for joint ranging and synchronization. In the process, for the sake of notational simplicity we assume all nodes transmit K messages,

which is not mandatory. Secondly, we enforce the same approximation order on both time (first order) and distance ($(L-1)$th order) for all node pairs (during the small measurement period). Thus, the proposed solution may not be accurate when the magnitude of the estimation parameters of some nodes vary eccentrically from the rest of the cluster within the approximation time period. As an illustration, Figure 4.2 shows a network consisting of $N = 4$ nodes with $\bar{N} = 6$ pairwise communication links.

4.4.1   Mobile Global Least Squares (MGLS)

Aggregating (4.15) for all pairwise links in the network, we have a linear global model of the form

$$
\overbrace{[\mathbf{T} \quad \mathbf{H} \quad \bar{\mathbf{V}}]}^{\mathbf{A}} \overbrace{\begin{bmatrix} \boldsymbol{\alpha} \\ \boldsymbol{\beta} \\ \boldsymbol{\gamma} \end{bmatrix}}^{\boldsymbol{\theta}} = \boldsymbol{\eta},
\tag{4.30}
$$

where $\bar{\mathbf{V}} = \mathbf{E}\mathbf{V}$ and $\mathbf{V} \in \mathbb{R}^{\bar{N}K \times \bar{N}L}$ is a Vandermonde-like matrix given by

$$
\mathbf{V} = \begin{bmatrix} \mathbf{I}_{\bar{N}} \otimes \mathbf{1}_K & \bar{\mathbf{T}}^{\odot 1} & \dots & \bar{\mathbf{T}}^{\odot L-1} \end{bmatrix}.
\tag{4.31}
$$

$\mathbf{T} \in \mathbb{R}^{\bar{N}K \times N}, \bar{\mathbf{T}} \in \mathbb{R}^{\bar{N}K \times \bar{N}}$ are measurement matrices contain the timing vectors recorded at all N nodes. $\mathbf{H} \in \mathbb{R}^{\bar{N}K \times N}$ is a matrix of $\pm \mathbf{1}_K$ and $\mathbf{0}_K$, and $\mathbf{E} \in \mathbb{R}^{\bar{N}K \times \bar{N}L}$ contains all the vectors which indicate the direction of the two-way communication. The noise vector is represented as

$$
\boldsymbol{\eta} = [\boldsymbol{\eta}_{12}^T, \boldsymbol{\eta}_{13}^T, \dots, \boldsymbol{\eta}_{(N-1)(N)}^T]^T \in \mathbb{R}^{\bar{N}K \times 1},
\tag{4.32}
$$

where each $\boldsymbol{\eta}_{ij}$ is given by (4.22). We assume that the noise vectors for each pairwise communication $\boldsymbol{\eta}_{ij}$ are uncorrelated with one another, which may not be applicable for all communication schemes e.g., broadcasting.

For $N = 4$, $\mathbf{T}$, $\mathbf{H}$, $\bar{\mathbf{T}}$, $\mathbf{E}$ are of the form

$$
\mathbf{T} = \begin{bmatrix}
\mathbf{t}_{12} & -\mathbf{t}_{21} & & \\
\mathbf{t}_{13} & & -\mathbf{t}_{31} & \\
\mathbf{t}_{14} & & & -\mathbf{t}_{41} \\
& \mathbf{t}_{23} & -\mathbf{t}_{32} & \\
& \mathbf{t}_{24} & & -\mathbf{t}_{42} \\
& & \mathbf{t}_{34} & -\mathbf{t}_{43}
\end{bmatrix},
$$

$$
\mathbf{H} = \begin{bmatrix}
+\mathbf{1}_K & -\mathbf{1}_K & & \\
+\mathbf{1}_K & & -\mathbf{1}_K & \\
+\mathbf{1}_K & & & -\mathbf{1}_K \\
& +\mathbf{1}_K & -\mathbf{1}_K & \\
& +\mathbf{1}_K & & -\mathbf{1}_K \\
& & +\mathbf{1}_K & -\mathbf{1}_K
\end{bmatrix},
$$

$$
\bar{\mathbf{T}} = \mathrm{diag}(\mathbf{t}_{12}, \mathbf{t}_{13}, \mathbf{t}_{14}, \mathbf{t}_{23}, \mathbf{t}_{24}, \mathbf{t}_{34}),
$$
$$
\mathbf{E} = \mathrm{bdiag}(\mathbf{E}_{12}, \mathbf{E}_{13}, \mathbf{E}_{14}, \mathbf{E}_{23}, \mathbf{E}_{24}, \mathbf{E}_{34}), \tag{4.33}
$$

where the empty spaces in matrices $\mathbf{T}, \mathbf{H}$ are entries with 0. A similar structure can be obtained for $N \geq 4$. The vector $\mathbf{t}_{ij}$ contains the time stamps recorded at the ith node when communicating with the jth node in the network and is defined in (4.19). Similarly, $\mathbf{E}_{ij}$ contains the direction information of the corresponding pairwise communication and is defined in (4.20).

Let us analyze the submatrices of $\mathbf{A}$. We find $\bar{\mathbf{T}}$ and $\mathbf{E}$ are full column rank since they are block diagonal and subsequently, $\bar{\mathbf{V}} = \mathbf{E}\mathbf{V}$ is a full rank matrix. $\mathbf{H}$ is rank deficient by 1, with a null space spanning $\{\mathbf{1}_N\}$. The sparsely populated matrix $\mathbf{T}$ containing the time stamp vectors is full rank. However, augmenting $\mathbf{T}$ with the matrix $\mathbf{H}$ further reduces the rank of $\mathbf{A}$ by 1 and hence we require at least 2 constraints. This is expected, since a clock reference is needed to solve for unknown clock and range parameters of the network, as observed in Section 4.3.2.

4.4.2 Equality constrained least squares

Traditionally, a simple constraint would be to choose a random node as the clock reference and thereby eliminating the rank deficiency in $\mathbf{A}$. Following which, it is straightforward to formulate a global solution similar to (4.23), however in this section we will present a generic constrained least squares framework, the benefits of which will be discussed in Section 4.6.4. Thus, more generally, the unknown vector

$\boldsymbol{\theta} \in \mathbb{R}^{M \times 1}$, where $M = 2N + \bar{N}L$, can be estimated by minimizing the cost function

$$\min_{\boldsymbol{\theta}} \quad \|\mathbf{A}\boldsymbol{\theta}\|^2 \quad \text{s.t.} \quad \mathbf{C}\boldsymbol{\theta} = \mathbf{b}, \tag{4.34}$$

where $\mathbf{A}$ is the (rank-deficient) matrix defined in (4.30), $\mathbf{C} \in \mathbb{R}^{N_2 \times M}$ is a known constraint matrix and $\mathbf{b} \in \mathbb{R}^{N_2 \times 1}$, where N_2 is the number of constraints. The equation $\mathbf{C}\boldsymbol{\theta} = \mathbf{b}$ implements the feasibility conditions, enforcing $N_2 \geq 2$ linearly independent constraints on $\boldsymbol{\theta}$. Assuming the constraints are selected such that $\begin{bmatrix} \mathbf{A} \\ \mathbf{C} \end{bmatrix} \in \mathbb{R}^{(\bar{N}K + N_2) \times L}$ is non-singular and $\mathbf{b} \neq \mathbf{0}_{N_2}$ [Lawson and Hanson 1974], the solution to (4.34) is obtained by solving the Karush-Kuhn-Tucker (KKT) equations [Boyd and Vandenberghe 2004] and is given by

$$\begin{bmatrix} \hat{\boldsymbol{\theta}} \\ \hat{\boldsymbol{\lambda}} \end{bmatrix} = \begin{bmatrix} 2\mathbf{A}^T\mathbf{A} & \mathbf{C}^T \\ \mathbf{C} & \mathbf{0}_{N_2, N_2} \end{bmatrix}^{-1} \begin{bmatrix} \mathbf{0} \\ \mathbf{b} \end{bmatrix}, \tag{4.35}$$

where $\boldsymbol{\lambda} \in \mathbb{R}^{N_2 \times 1}$ is the Lagrange vector. A detailed discussion on the choice of the constraint matrix $\mathbf{C}$ is presented in Section 4.6.

Given the estimate $\hat{\boldsymbol{\theta}} = [\hat{\boldsymbol{\alpha}}^T, \hat{\boldsymbol{\beta}}^T, \hat{\boldsymbol{\gamma}}^T]^T$, an estimate of the clock parameters $\{\hat{\boldsymbol{\omega}}, \hat{\boldsymbol{\phi}}\}$ is estimated using (4.2) and the pairwise range parameters $\hat{\mathbf{r}}$ between the nodes using (4.8). Furthermore, all the *unique* $\bar{N}$ pairwise distances between the nodes $\hat{\mathbf{d}} = [\hat{\mathbf{d}}_{12}^T, \hat{\mathbf{d}}_{13}^T, \dots, \hat{\mathbf{d}}_{(N-1)N}^T]^T \in \mathbb{R}^{\bar{N}K \times 1}$ at all K time instances are given by

$$\hat{\mathbf{d}} = c\mathbf{V}\hat{\boldsymbol{\gamma}}, \tag{4.36}$$

where $\mathbf{V}$ is defined in (4.31). Similar to the iterative MPLS (iMPLS) solution (Appendix 4.B), we propose an iterative equality constrained least squares algorithm (iMGLS) in Appendix 4.C to estimate $\boldsymbol{\theta}$ in the presence of unknown L. Note that $\mathbf{d}$ is linearly dependent on the clock parameter estimates since $\hat{\mathbf{d}} = c\mathbf{V}\hat{\boldsymbol{\gamma}} = c\mathbf{V}\hat{\mathbf{G}}^{-1}\hat{\mathbf{r}}$ using (4.8), where $\hat{\mathbf{G}}$ is the transformation matrix containing the clock parameter estimates (4.6). While this 2-step optimization (of estimating the clocks first followed by distance) is suboptimal in theory, simulations point out the effectiveness of the method. *See Section 4.7.*

Remark 4: (**Extension to partially connected networks**): The closed form solution (4.35) is for a full mesh network. More generally, if some pairwise communications links are missing then the corresponding rows in the primary matrix $\mathbf{A}$ are dropped. Consequentially, the pairwise distances between those particular nodes cannot be estimated. However, despite missing links, network wide synchronization
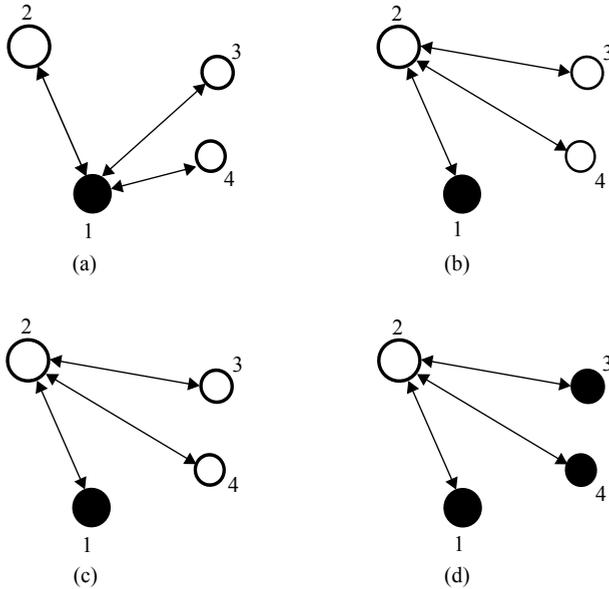
Figure 4.3: *Illustration of feasible networks for the proposed algorithms:* Four networks with $N = 4$ nodes each capable of two-way communication. The nodes shaded in black are the clock references. The 4 networks are illustrative examples where MGLS algorithm (and thus the constrained formulation) can be applied for network wide clock synchronization, despite missing communication links and multiple clock references.

is still feasible using the proposed algorithms if the primary matrix in (4.35) is full rank [Rajan and van der Veen 2011; Rajan and van der Veen 2012]. A few feasible topologies are illustrated in Figure 4.3. For global synchronization, the network must consist of at least $N - 1$ links, where every node has at least a single two-way communication link with one other node in the network.

Remark 5: (**Distributed MGLS**): It is worth noting that, for $N = 2$, the centralized MGLS is identical to the MPLS solution. However, the MGLS solution yields a better estimate for the clock parameters (when $\bar{N} > N$ *i.e.*, $N \geq 4$) due to an increase in number of *unique* pairwise links, which will be discussed in Section 4.7. Furthermore, although suboptimal, the MPLS is a distributed alternative to the centralized MGLS for estimating the clocks and range parameters. For large number of message exchanges and/or a large network of nodes i.e., $K\bar{N} \gg (L+2)$, the computational complexity of the MGLS algorithm is $\mathcal{O}(KN^2L^2)$, which can be distributed efficiently using prevalent techniques [Bertrand and Moonen 2011].

4.5 Cramér-Rao bounds

4.5.1 Noise modeling

In reality, the time markers in (4.13) are plagued with measurement noise, which for simplicity is here assumed to be Gaussian [Serpedin and Chaudhari 2009]. [2] Hence the noise on the nodes $\{i, j\}$ at the kth time instant in (4.13) are modeled as $\{\eta_{i,k}, \eta_{j,k}\} \sim \mathcal{N}(0, 0.5\sigma^2)$, where without loss of generality, we assume the same noise variance on both transmission and reception markers. Subsequently, the cumulative noise vector $\eta_{ij,k}$ for the pairwise link (4.14), after ignoring the higher order noise terms, is

$$\eta_{ij,k} = \alpha_j \eta_{j,k} - \left(\alpha_i + E_{ij,k}(\gamma_{ij}^{(1)} + 2\gamma_{ij}^{(2)} T_{ij,k} + \dots)\right)\eta_{i,k},$$

which is modeled as

$$\eta_{ij,k} \sim \mathcal{N}(0, 0.5\sigma^2(\alpha_j^2 + (\alpha_i + \gamma_{ij}^{(1)} + 2\gamma_{ij}^{(2)} T_{ij,k} + \dots)^2)).$$

Note that, for $c = 3 \times 10^8$ m/s the term $(\gamma_{ij}^{(1)} + 2\gamma_{ij}^{(2)} T_{ij,k} + \dots)$ is scaled by c^{-1} (by definition of $\boldsymbol{\gamma}$ in (4.68) and (4.67) and thus is negligibly small for small measurement periods. Hence the gaussian noise simplifies to

$$\eta_{ij,k} \quad \sim \quad \mathcal{N}(0, 0.5\sigma^2(\alpha_i^2 + \alpha_j^2)), \tag{4.37}$$

and for the entire network, we have

$$\boldsymbol{\eta} \sim \mathcal{N}(0, \boldsymbol{\Sigma}_\eta), \tag{4.38}$$

where $\boldsymbol{\Sigma}_\eta = \sigma^2(\tilde{\mathcal{A}} \otimes \mathbf{I}_K) \in \mathbb{R}^{K\bar{N} \times 1}$ and $\tilde{\mathcal{A}} \in \mathbb{R}^{\bar{N} \times 1}$ is of the form

$$\tilde{\mathcal{A}} = 0.5\text{diag}(\alpha_1^2 + \alpha_2^2, \ \alpha_1^2 + \alpha_3^2, \ \dots, \alpha_{N-1}^2 + \alpha_N^2). \tag{4.39}$$

Remark 6: (**Distance dependent noise**): In reality, the pairwise noise $\eta_{ij,k}$ is also dependent on the distance between the nodes and the physical communication medium [Jia and Buehrer 2008], in which case the noise is correlated with both channel effects and range parameters. The presented model can be readily extended to address these scenarios, where a weighted least squares solution would be appropriate in contrast to the proposed least squares solution.

---

[2]Elsewhere, the noise on the time markers is also modeled as uniformly random variable (rising from quantization errors) or an exponential distribution [Abdel-Ghaffar 2002; Serpedin and Chaudhari 2009].

4.5.2 Lower Bounds for joint time-range estimation

In order to verify the performance of the proposed algorithms, we derive a Constrained Cramér-Rao lower Bound (CCRB) for the joint affine clock and $L - 1$th order range model defined in (4.30). The error vector $\boldsymbol{\eta}$ in (4.30) is Gaussian by assumption and following immediately, the Constrained Cramér-Rao Bound (CCRB) on the error variance for an unbiased estimator is given by [Stoica and Ng 1998]

$$
\mathbb{E}\left\{(\hat{\boldsymbol{\theta}} - \boldsymbol{\theta})(\hat{\boldsymbol{\theta}} - \boldsymbol{\theta})^T\right\} \geq \boldsymbol{\Sigma}_\theta \triangleq \begin{bmatrix} \boldsymbol{\Sigma}_\alpha & * & * \\ * & \boldsymbol{\Sigma}_\beta & * \\ * & * & \boldsymbol{\Sigma}_\gamma \end{bmatrix} = \mathbf{U}(\mathbf{U}^T\mathbf{F}\mathbf{U})^{-1}\mathbf{U}^T, \quad (4.40)
$$

where $\boldsymbol{\Sigma}_\theta$ is the Cramér-Rao lower Bound on $\boldsymbol{\theta} = \begin{bmatrix} \boldsymbol{\alpha}^T, & \boldsymbol{\beta}^T, & \boldsymbol{\gamma}^T \end{bmatrix}^T$, $*$ represent entries not of interest, $\mathbf{U} \in \mathbb{R}^{M \times (M - N_2)}$ with $M = 2N + \bar{N}L$ is an orthonormal basis for the null space of the constraint matrix $\mathbf{C}$ with N_2 constraints

$$
\mathbf{F} = \mathbf{A}^T\boldsymbol{\Sigma}_\eta^{-1}\mathbf{A} \in \mathbb{R}^{M \times M}, \quad (4.41)
$$

is the Fisher Information Matrix (FIM) and $\boldsymbol{\Sigma}_\eta$ is the covariance of the noise on the time markers (4.38). Moreover, since the system parameters $\boldsymbol{\zeta} = \begin{bmatrix} \boldsymbol{\omega}^T, & \boldsymbol{\phi}^T, & \mathbf{r}^T \end{bmatrix}^T$ can be uniquely derived from $\boldsymbol{\theta}$, we have the CRB on the estimates of $\boldsymbol{\zeta}$ from standard error propagation formulas [Kay 1993] as

$$
\boldsymbol{\Sigma}_\zeta \triangleq \begin{bmatrix} \boldsymbol{\Sigma}_\omega & * & * \\ * & \boldsymbol{\Sigma}_\phi & * \\ * & * & \boldsymbol{\Sigma}_r \end{bmatrix} = \mathbf{J}_{\theta\zeta}\boldsymbol{\Sigma}_\theta\mathbf{J}_{\theta\zeta}^T, \quad (4.42)
$$

where $\boldsymbol{\Sigma}_\theta$ is given by (4.40) and $\mathbf{J}_{\theta\zeta} \in \mathbb{R}^{M \times M}$ is the Jacobian of the transformation of $\boldsymbol{\zeta}$ from $\boldsymbol{\theta}$ (Appendix 4.D). Following immediately, given the lower bound on the variance of $\boldsymbol{\gamma}$ as $\boldsymbol{\Sigma}_\gamma \in \mathbb{R}^{\bar{N}L \times \bar{N}L}$, the lower bound on the variance of the distance estimate (4.36) is

$$
\boldsymbol{\Sigma}_d = c^2\mathbf{V}\boldsymbol{\Sigma}_\gamma\mathbf{V}^T, \quad (4.43)
$$

where $\mathbf{V}$ is the Vandermonde-like matrix (4.31).

4.6 On the choice of clock reference

Observe that the solution to $\boldsymbol{\theta}$ in (4.35) and its corresponding performance (4.40), (4.42) is not only data dependent, but also depends on the choice of constraints. The

primary matrix $\mathbf{A}$ is rank deficient by 2 and hence, $N_2 \geq 2$ feasible constraints are needed on the clock parameters to ensure a unique solution in (4.35). In view of achieving an optimal solution, we discuss three potential constraints, namely (a) the *Classic constraint*, (b) a *Nullspace constraint* and (c) the *Sum constraint*.

4.6.1 Classic constraint

The minimum requirement for a feasible solution is to use an arbitrary node i as a clock reference, i.e., the constraint $\alpha_i = 1$ and $\beta_i = 0$, which yields the *classic constraint*,

$$\mathbf{C}_1 = \begin{bmatrix} \mathbf{c}_i^T & | & \mathbf{0}_N^T & | & \mathbf{0}_{\bar{N}L}^T \\ \mathbf{0}_N^T & | & \mathbf{c}_i^T & | & \mathbf{0}_{\bar{N}L}^T \end{bmatrix}, \quad \mathbf{b}_1 = \begin{bmatrix} 1 \\ 0 \end{bmatrix}, \tag{4.44}$$

where

$$\mathbf{c}_i = [\mathbf{0}_{i-1}^T, \ 1, \ \mathbf{0}_{N-i}^T]^T \quad \in \mathbb{R}^{N \times 1}. \tag{4.45}$$

Such a constraint is often utilized without further discussion for clock synchronization in a network of fixed nodes [IEEE Working Group 802.15.4 2007; Serpedin and Chaudhari 2009; Wu, Chaudhari and Serpedin 2011] and much of the literature on localization [Zheng and Wu 2010]. To alleviate the dependence on a single node for clock reference, we propose 2 virtual clocks via the *Nullspace constraint* and the *Sum constraint* in the following sections.

4.6.2 Nullspace constraint

Among the set of all feasible linearly independent constraints, the pseudo-inverse of the unconstrained FIM yields the lowest value for the total variance on all estimated parameters [Carvalho, Cioffi and Slock 2000]. Let the spectral decomposition of the rank deficient FIM be

$$\mathbf{F} = \begin{bmatrix} \mathbf{V}_1 & \mathbf{V}_2 \end{bmatrix} \begin{bmatrix} \mathbf{\Lambda}_1 & \mathbf{0} \\ \mathbf{0} & \mathbf{\Lambda}_2 \end{bmatrix} \begin{bmatrix} \mathbf{V}_1 & \mathbf{V}_2 \end{bmatrix}^T \approx \mathbf{V}_1 \mathbf{\Lambda}_1 \mathbf{V}_1^T, \tag{4.46}$$

where $\mathbf{\Lambda}_1$ is a diagonal matrix containing the non-zero eigenvalues and $\mathbf{V}_1$ the corresponding eigenvectors. Now, let $\mathbf{C}_2$ be the nullspace constraint matrix such that the range of $\mathbf{C}_2^T$ spans the null space of $\mathbf{F}$ (i.e., in the range of $\mathbf{V}_2$). Subsequently, the orthogonal basis for the null space of $\mathbf{C}_2$ i.e., $\mathbf{U}_2$ spans the range of $\mathbf{V}_1$, and the

trace of the CCRB (4.40) is

$$
\begin{aligned}
\mathrm{Tr}\left(\mathbf{\Sigma}_\theta\right) &= \mathrm{Tr}\left[\mathbf{U}_2(\mathbf{U}_2^T\mathbf{F}\mathbf{U}_2)^{-1}\mathbf{U}_2^T\right] \\
&= \mathrm{Tr}\left[\mathbf{V}_1(\mathbf{V}_1^T(\mathbf{V}_1\mathbf{\Lambda}_1\mathbf{V}_1^T)\mathbf{V}_1)^{-1}\mathbf{V}_1^T\right] \\
&= \mathrm{Tr}\left[\mathbf{\Lambda}_1^{-1}\right] = \mathrm{Tr}\left[\mathbf{F}^\dagger\right],
\end{aligned}
\tag{4.47}
$$

where we use the property $\mathbf{V}_1^T\mathbf{V}_1 = \mathbf{I}$ and exploit the cyclic nature of the trace operator. Hence, the nullspace constraint yields the pseudo-inverse of the unconstrained FIM, which is the lowest achievable total variance on all estimated parameters. This implies that any set of vectors which span the nullspace of the FIM form an optimal constraint for the system.

Observe that the Nullspace constraint offers little insight on the optimality of the independent parameters α, β, γ and subsequently on the translated parameters of interest ω, ϕ and $\mathbf{d}$. Furthermore, this constraint is data dependent and presents no physical intuition on the estimated parameters. However, the Nullspace constraint cannot be dismissed since it guarantees the lowest variance on the overall estimate θ.

4.6.3 Sum constraint

In the pursuit of a data independent constraint and inspired by [Wijnholds and van der Veen 2006], we propose a *sum constraint*, whereby we enforce *the sum of all α_i to be 1 and the sum of all β_i to be 0, i.e.,* $\sum_i^N \alpha_i = 1$ *and* $\sum_i^N \beta_i = 0$, which begets a new constraint matrix

$$
\mathbf{C}_2 = \left[\begin{array}{c|c|c} \mathbf{1}_N^T & \mathbf{0}_N^T & \mathbf{0}_{\bar{N}L}^T \\ \mathbf{0}_N^T & \mathbf{1}_N^T & \mathbf{0}_{\bar{N}L}^T \end{array}\right], \quad \mathbf{b}_2 = \begin{bmatrix} 1 \\ 0 \end{bmatrix}.
\tag{4.48}
$$

The sum constraint proposes a virtual "average" clock, which in turn is governed by the clock errors $\{\alpha, \beta\}$ of all the clocks in the network and thereby alleviates a single clock reference which maybe potentially unstable. In case of the classic constraint with a single clock reference, the variance of the reference clock parameters is artificially put to zero and thereby accruing its variance to all other clock parameter estimates. In comparison, the sum constraint computes the average β_i (and α_i) for all the nodes, which leads to about a factor 2 reduction in the variance of the estimate of β_i (and α_i), and subsequent improvement on ω and ϕ due to averaging, as observed in the simulations. *See Section 4.7.*

As shown in Section 4.6.2, any set of constraints that span the null space of the FIM yield an optimal estimate of the unknown parameter. Among the pair of

proposed sum constraints on $\boldsymbol{\alpha}, \boldsymbol{\beta}$, observe that the second constraint $[\mathbf{0}_N^T \ \mathbf{1}_N^T \ \mathbf{0}_{\bar{N}L}^T]^T$ indeed lies in the null space of the FIM (4.41), since $\mathbf{H}\mathbf{1}_N = \mathbf{0}_{\bar{N}}$. However, a similar argument cannot be made for the constraint on $\boldsymbol{\alpha}$, i.e., $[\mathbf{1}_N^T \ \mathbf{0}_N^T \ \mathbf{0}_{\bar{N}L}^T]^T$, thus the sum constraint is not yet optimal (unlike the case in [Wijnholds and van der Veen 2006]), although it is seen to be close to optimum in simulations.

4.6.4 Benefits of the constrained formulation

Contrary to the pairwise algorithm MPLS, which was formulated as a least square solution, the global algorithm is structured as a constrained least squares problem. Such a *generic framework* enables the user to incorporate additional *a priori* information into the constraint matrix $\mathbf{C}$ and thereby obtain a lower variance on the clock and range estimates. For example, if the network has three reference nodes, say node 1, 3, and 4, which is common in joint TOA localization and synchronization [Zheng and Wu 2010; Zhu and Ding 2010] (refer Figure 4.3(d)), then by increasing the number of rows M_2 of the constraint matrix $\mathbf{C}$, such as

$$\acute{\mathbf{C}} = \begin{bmatrix} \mathbf{c}_1^T & \mathbf{0}_N^T & \mathbf{0}_{\bar{N}L}^T \\ \mathbf{0}_N^T & \mathbf{c}_1^T & \mathbf{0}_{\bar{N}L}^T \\ \mathbf{c}_3^T & \mathbf{0}_N^T & \mathbf{0}_{\bar{N}L}^T \\ \mathbf{0}_N^T & \mathbf{c}_3^T & \mathbf{0}_{\bar{N}L}^T \\ \mathbf{c}_4^T & \mathbf{0}_N^T & \mathbf{0}_{\bar{N}L}^T \\ \mathbf{0}_N^T & \mathbf{c}_4^T & \mathbf{0}_{\bar{N}L}^T \end{bmatrix}, \quad \acute{\mathbf{b}} = \begin{bmatrix} \alpha_1 \\ \beta_1 \\ \alpha_3 \\ \beta_3 \\ \alpha_4 \\ \beta_4 \end{bmatrix}, \tag{4.49}$$

a better estimate can be obtained for the unknown clock parameters of node 2. As a special case, if there are one-way communication links from the reference nodes to node 2 and the reference nodes directly communicate their *true* time, then Figure 4.3(d) simplifies to the conventional GPS based synchronization and ranging [Kaplan and Hegarty 2006]. Likewise, for $L = 1$, in a network with adequate known node positions, one can incorporate known pairwise distances in the constraint matrix to yield higher accuracy in overall estimates. The formulation in (4.34) is thus a convenient framework to incorporate various prevalent scenarios.

4.7 Simulations

Simulations are conducted to evaluate the performance of the proposed estimators. We consider a network of $N = 5$ mobile nodes, each capable of two-way communication with each other. The nodes transmit and receive time stamps alternatively

and thus the direction matrix $\mathbf{E}$ is (4.33), where $\mathbf{e}_{ij} = [+1, -1]^T \otimes \mathbf{1}_{0.5K}$. The transmission time markers $\mathbf{t}_{ij}$ are linearly distributed within a small measurement time interval of $\Delta T = [-1.5, 1.5]$ seconds. All the nodes are equipped with independent clock oscillators, whose clock skews ($\boldsymbol{\omega}$) and clock offsets ($\boldsymbol{\phi}$) are uniform randomly distributed in the range $[1 - 10\text{ppm}, 1 + 10\text{ppm}]$ and $[-10, +10]$ seconds respectively, which are given by (4.50) and (4.51) respectively.

The metric used to evaluate the performance of the estimators is the Root Mean Square Error (RMSE) given by

$$\text{RMSE}(\hat{\mathbf{z}}, \mathbf{z}) = \sqrt{N_{\exp}^{-1} \sum_{n=1}^{N_{\exp}} ||\hat{\mathbf{z}}(n) - \mathbf{z}||^2}, \qquad (4.54)$$

where $\hat{\mathbf{z}}(n)$ is the nth estimate of the unknown vector $\mathbf{z} \in \mathbb{R}^{N \times 1}$ to be estimated and the number of experiments is $N_{\exp} = 1000$. Furthermore, along with the RMSE plots, the square Root of the constrained Cramér-Rao Bounds (RCRB) derived in Section 4.5 are also plotted for the three constraints discussed in Section 4.6. In case of the classic constraint, node 1 is assumed to be the reference node without loss of generality.

To verify the proposed algorithms, two simulation setups are considered: (a) a fixed network of asynchronous nodes, and (b) a mobile network of asynchronous nodes. Furthermore, both setups are evaluated for (1) varying number of pairwise communications K for fixed noise on the time markers with standard deviation $\sigma = 1\text{meter}$ and (2) varying σ in the range $[-10, +10]$ dBmeters for $K = 10$. The error of $\sigma = 1\text{meter}$ translates to a timing error of $\approx 3.3\text{ns}$ for a static network model, since $\text{var}(\tau_{ij}) = c^2 \times \text{var}(d_{ij})$ with $c = 3 \times 10^8$ m/s. Although such high SNR is not usually considered in clock synchronization literature [Wu, Chaudhari and Serpedin

$$\boldsymbol{\omega} \;=\; [1.0000, \, 0.9995, \, 1.0008, \, 1.0009, \, 0.9999]^T \qquad (4.50)$$

$$\boldsymbol{\phi} \;=\; [0, \, 1.8787, \, 8.1303, \, 4.5389, \, 1.9800]^T \qquad (4.51)$$

$$\mathbf{X} \;=\; \begin{bmatrix} -3446 & -748 & -4044 & -4566 & 1968 \\ -1424 & -1140 & 2712 & -4031 & 2111 \\ 4384 & -3376 & -4352 & -1198 & 1580 \end{bmatrix} \text{m} \qquad (4.52)$$

$$\mathbf{Y} \;=\; \begin{bmatrix} -35 & 36 & -13 & -47 & -20 \\ -43 & 40 & -42 & 8 & -8 \\ 23 & 19 & -23 & 4 & 41 \end{bmatrix} \text{m/s} \qquad (4.53)$$

2011], it is typical to achieve meter level accuracies for localization [Patwari et al. 2005; Patwari et al. 2003].

4.7.1   Immobile network

Let the locations of the N nodes be $\mathbf{X} = \begin{bmatrix} \mathbf{x}_1, \mathbf{x}_2, \ldots, \mathbf{x}_N \end{bmatrix} \in \mathbb{R}^{N \times 3}$ in a 3-dim. space, which are arbitrarily chosen to be (4.52), where $\mathbf{x}_i \in \mathbb{R}^{3 \times 1}$ is the position of the ith node. The time invariant propagation delay between the nodes is then

$$\tau_{ij} \triangleq c^{-1} d_{ij} = c^{-1} r_{ij}^{(0)} = c^{-1} \|\mathbf{x}_i - \mathbf{x}_j\|_2. \tag{4.55}$$

The proposed MPLS algorithm (Section 4.3.2) for $L = 1$ is independently applied, pairwise from node 1 to every other node as in Figure 4.3a to estimate all the unknown clock skews ($\boldsymbol{\omega}$), clock offsets ($\boldsymbol{\phi}$) and range parameters ($\mathbf{r}$). For the entire network, the proposed MGLS (Section 4.4.1) algorithm (with $L = 1$) is applied to estimate both the clock parameters $\{\boldsymbol{\omega}\ \boldsymbol{\phi}\}$ and the range parameters $\mathbf{r}$. Note that for a fixed network $\mathbf{d} \triangleq \mathbf{r} \in \mathbb{R}^{\bar{N} \times 1}$, where $\mathbf{d}$ contains all $\bar{N}$ *unique* pairwise distances within the network. Figure 4.4 show the RMSE plots for the clock skew ($\boldsymbol{\omega}$) and the clock offset ($\boldsymbol{\phi}$) and pairwise distances ($\mathbf{d}$). The RMSE of clock parameter estimates from the Low Complexity Least Squares (LCLS) solution [Leng and Wu 2010] ($L = 1$) is also presented for clock skew and offset, which not surprisingly performs similar to the MPLS solution for a fixed network [Rajan and van der Veen 2011].

The MGLS estimate outperforms the MPLS estimate, which is expected, since the total number of communication channels available for the MGLS estimate is greater than that for MPLS i.e., $\bar{N} > (N - 1)$ for $N \geq 2$. Furthermore, the MGLS is shown to achieve the CCRB bounds for $L = 1$ for both clock and range parameters since the least square solution is the Minimum Variance Unbiased estimate for the assumed Gaussian noise model. For the given experimental setup, with 10ns ($\approx$ 3.3meters) noise on the time measurements, distance accuracies improve by an order for $K = 100$ two-way communications (*see* Figure4.4(c)).

replacements
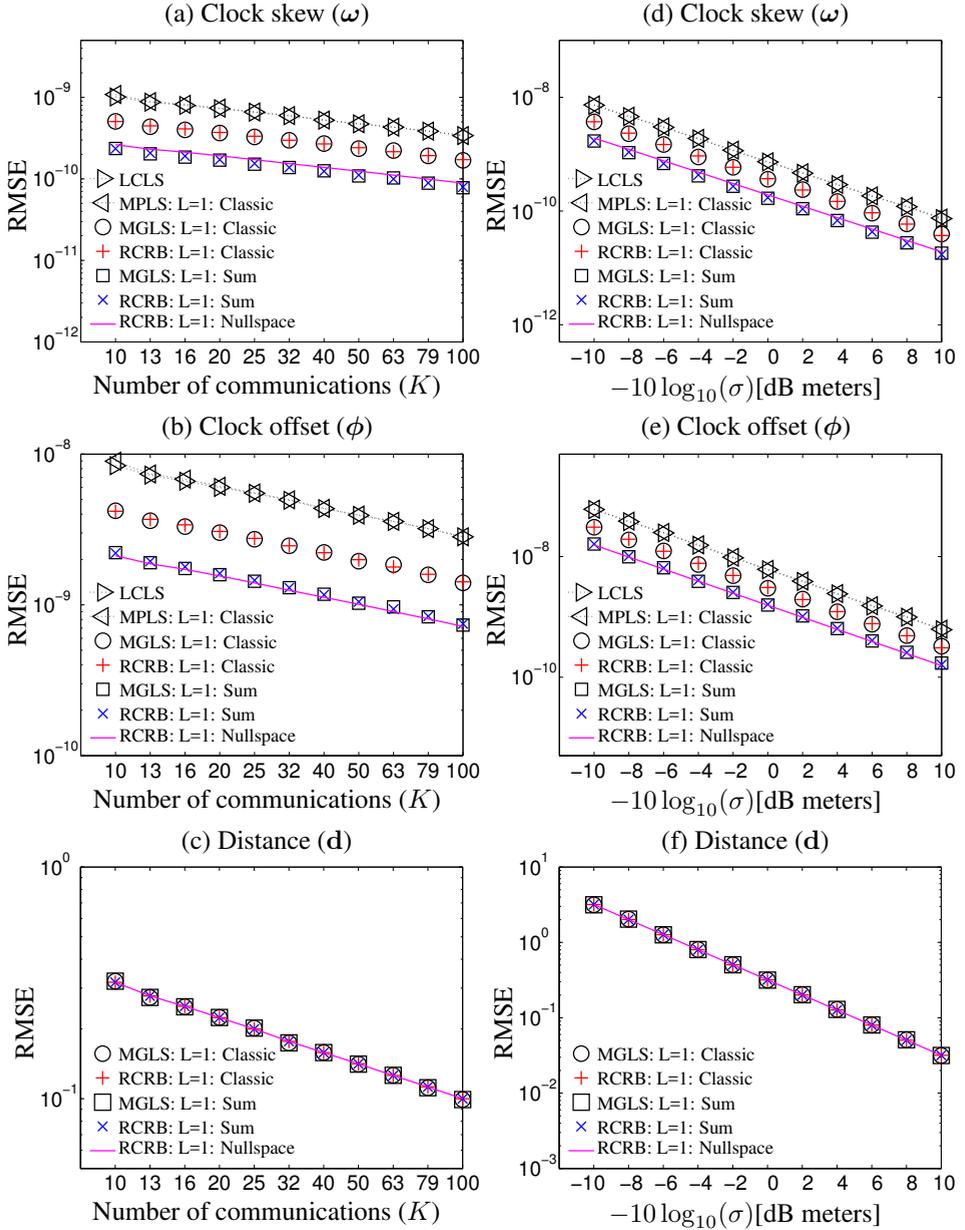
Figure 4.4: *Immobile network:* **(Left) Varying** K**:** RMSEs (and RCRBs) of (a) clock skew, (b) clock offset and (c) distances for varying number of communications (K) between the $N = 5$ *fixed* nodes for $\sigma = 3.3$nS (1 meter). **(Right) Varying** σ**:** RMSEs (and RCRBs) of (d) clock skew, (e) clock offset and (f) distances for a cluster of *fixed* nodes, for varying noise (σ) on the time measurements with $K = 10$ number of communications.

In addition, the nullspace and sum constraints are shown to improve the performance of the clock parameter estimates by about a factor 2. It is worth noting that, the RMSE (and RCRBs) of the clock parameters and distance for the sum constraint is nearly the same as the nullspace constraint. A discussion on the lower bound of the distance parameter is presented in Appendix 4.E.

4.7.2   Mobile network

To investigate the performance of the Least Square solutions for a cluster of mobile nodes, we consider a simple scenario where the nodes are mobile with constant independent velocities. [3] The independent constant velocities of the N nodes are given by $\mathbf{Y} = \begin{bmatrix} \mathbf{y}_1, \mathbf{y}_2, \ldots, \mathbf{y}_N \end{bmatrix} \in \mathbb{R}^{N \times 3}$, which similar to the initial positions, are also arbitrarily chosen as (4.53). Hence, the *true* time-varying propagation delay $\tau_{ij}(t)$ w.r.t. to the clock in node i, between the nodes at time instant k, is

$$\tau_{ij,k} \quad \triangleq \quad c^{-1}d_{ij,k} = c^{-1}\|\tilde{\mathbf{x}}_{i,k} - \tilde{\mathbf{x}}_{j,k}\|_2, \tag{4.56}$$

where

$$\tilde{\mathbf{x}}_{i,k} = \mathbf{x}_i + \mathbf{y}_i T_{ij,k} \quad \forall \, 1 \le i \le N. \tag{4.57}$$

Note that, even though the nodes are in linear motion, the pairwise distance between the nodes is always non-linear (4.56). In previous cases [Rajan and van der Veen 2011; Rajan and van der Veen 2012; Rajan and van der Veen 2013], fixed range parameters $\mathbf{r}_{ij} = \begin{bmatrix} r_{ij}^{(0)}, r_{ij}^{(1)}, r_{ij}^{(2)}, \ldots, r_{ij}^{(L-1)} \end{bmatrix}^T \forall i, j \le N$ *were used for simulation ensuring the linearity of the joint time-range model, which is unlike the current experimental setup where distance is inherently non-linear.*

Furthermore, since L is unknown the proposed iMPLS algorithm (Appendix 4.B) is independently applied, pairwise from node 1 to every other node as in Figure 4.3(a) to estimate all the unknown clock skews, clock offsets and range coefficients. For the given input parameters, the iterative algorithms are observed to converge for $L = 3$. For the entire network the iMGLS algorithm (Appendix 4.C) is applied to estimate the clock parameters $[\boldsymbol{\omega} \ \boldsymbol{\phi}]$ and the distances. Observe that unlike the fixed network (with $\bar{N}$ *unique* pairwise distances), the mobile scenario has $\bar{N}K$ *unique* pairwise distances to be estimated, i.e., $\bar{N}$ *unique* pairwise distances between the nodes, at all K discrete time instances during the measurement period ΔT. As before, we investigate the performance of the proposed algorithms for all the 3 constraints, i.e., the

---

[3]Note that the presented model is more general and readily applicable to any motion, as long as $\tau_{ij}(t)$ is a continuous function of time.

classic constraint, nullspace constraint and the sum constraint. All the corresponding RMSEs of the clock skew, offset and distance estimates are plotted in Figure 4.5 along with their respective RCRB derived in (4.42) and (4.43) for various constraints.

The proposed iMPLS algorithm outperforms the LCLS algorithm [Leng and Wu 2010] for clock skew and offset estimation of a mobile network, as shown in Figure 4.5(a), Figure 4.5(b), Figure 4.5(d) and Figure 4.5(e). Recall that the LCLS algorithm assumes a fixed network. In addition, numerous outliers are also observed in case of LCLS, since the approximation error of the time-varying distance dominates the Gaussian noise under consideration. *Secondly, it is perhaps not surprising that the iMGLS solution achieves the theoretical bounds asymptotically for the clock parameters* (α, β) *since the linearity of the clock model is ensured via exact parametrization. However, for the non-linear range model in conjunction with the affine clock model, given that the nodes are in independent linear motion (4.52, 4.53), the distance parameters achieving the CCRB at* $L = 3$ *validates the joint time-range model.*

Remark 7: (**Noise covariance**): We observed in (4.37) and (4.38) that the covariance of the noise on the time markers was coupled with the estimated parameter α. However, in spite of this dependency, the proposed least squares estimate achieves the CRB asymptotically. This is a consequence of the clock skews ω typically being close to 1, with errors of the order of 10^{-4} or so [IEEE Working Group 802.15.4 2007]. Therefore, $\alpha_i^2 \approx 1 \; \forall \; i \leq N$ in (4.37), which simplifies the scaling of the noise covariance (4.39) to $\tilde{\mathcal{A}} = \mathbf{I}_{\bar{N}}$ and subsequently (4.38) reduces to,

$$\boldsymbol{\eta} \quad \sim \quad \mathcal{N}(0, \sigma^2 \mathbf{I}_{K\bar{N}}). \tag{4.58}$$

Such an approximation is satisfactory and is implicitly employed in various literature [Noh et al. 2007; Leng and Wu 2010; Rajan and van der Veen 2011; Wu, Chaudhari and Serpedin 2011; Wang, Ma and Leus 2011a] for conventional fixed networks.

In Figure 4.5(d), Figure 4.5(e) and Figure 4.5(f), where the RMSE of the proposed algorithms are compared against varying noise variance, the iMPLS shows considerable improvement over LCLS for high SNR. For lower SNR however, particularly when $\sigma > 1$ meters, the difference between the performances of iMPLS and LCLS is negligible. This is because the noise variance exceeds the magnitude of the velocities (few meters/second in the current experimental setup) and hence, the effect of higher order approximation of the time-varying distance is ineffective.

replacements
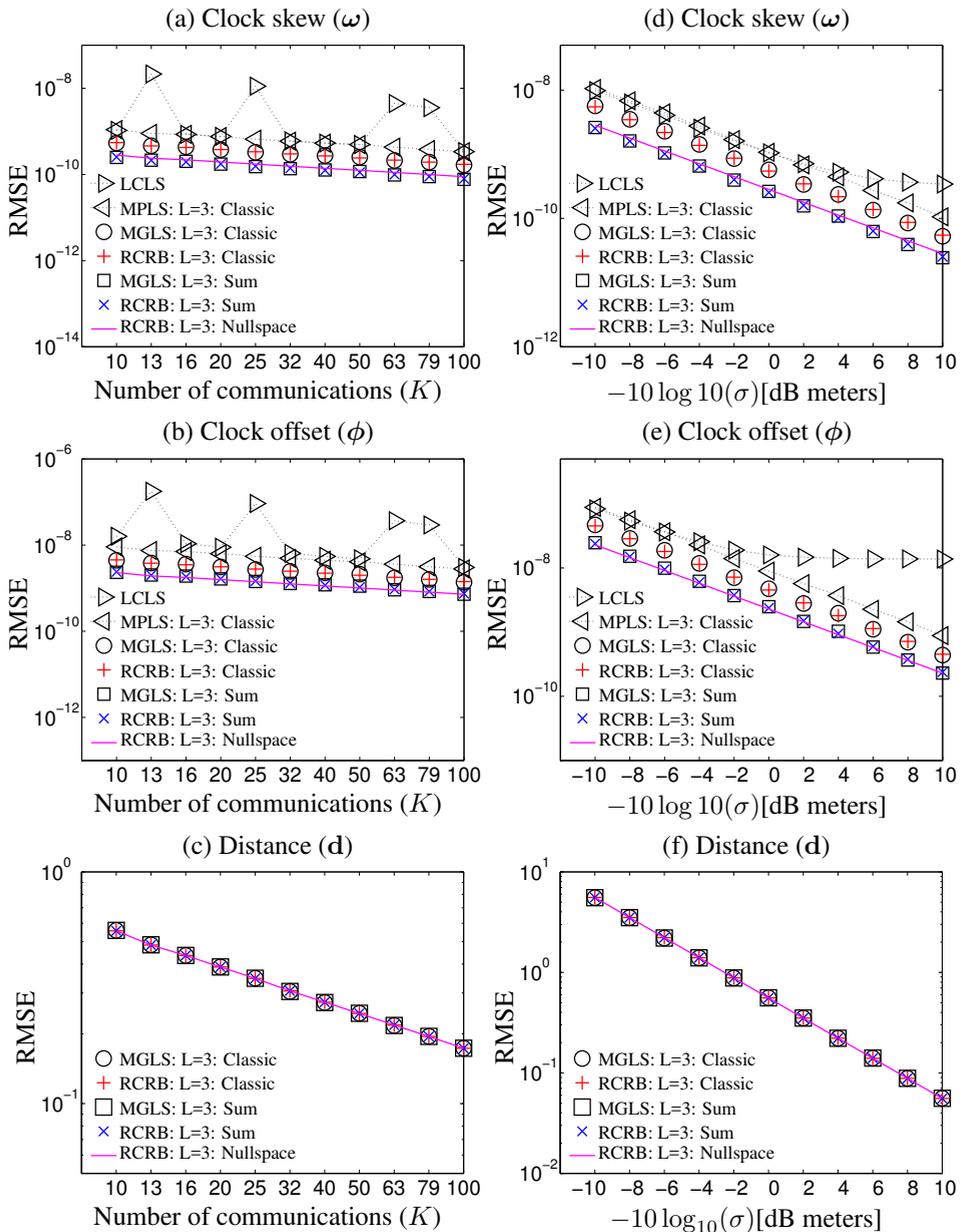
Figure 4.5: *Mobile network:* (**Left**) **Varying** K**:** RMSEs (and RCRBs) of (a) clock skew, (b) clock offset and (c) distance estimates, for varying number of communications (K) between the $N = 5$ *mobile* nodes for $\sigma = 3.3$nS (1 meter). (**Right**) **Varying** σ**:** RMSEs (and RCRBs) of (d) clock skew, (e) clock offset and (f) distance estimates for a cluster of *mobile* nodes, for varying noise (σ) on the time measurements with $K = 10$ number of communications.
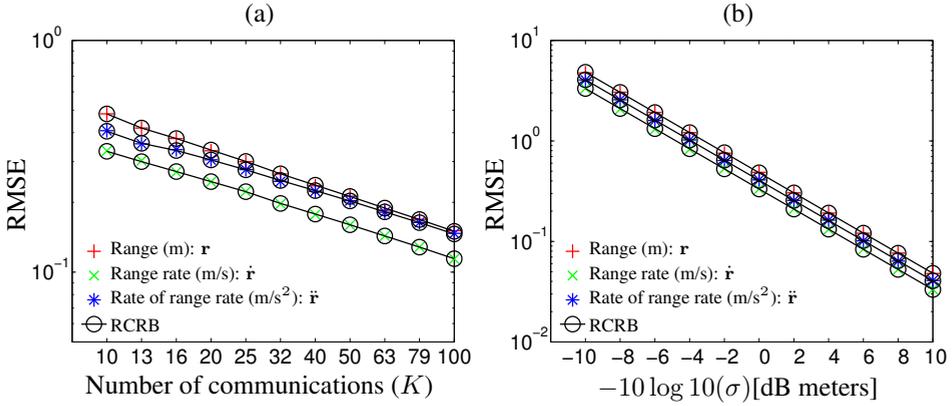
Figure 4.6: ***Mobile network: RMSEs of range parameters*** (a) for varying number of communications (K) between the nodes for $\sigma = 1$ meter and (b) for varying noise (σ) on the Time measurements with number of communication $K = 10$.

For the sake of completeness, the range coefficients along with their respective CRBs are also plotted in Figure 4.6, which are shown to achieve the derived CRB asymptotically. The purpose of these coefficients, beyond polynomial fitting of time-varying distance, will be discussed in the following chapters.

4.7.3 Effect of L on estimation error

The iterative algorithms (iMPLS, iMGLS) implicity choose the distance approximation order L which minimizes the Least Squares error. To understand the effect of choosing L on the RMSE of the clock and distance parameters, we investigate the performance of MPLS and MGLS algorithms for $L = 1, 2, 3$. Figure 4.7 shows the RMSE and RCRB plots of the proposed algorithm for varying K and varying SNR with a single clock reference, i.e., the classic constraint. [5]

For the given experimental setup, the RCRBs of the clock parameters are nearly indistinguishable for $L = 1, 2, 3$ (and thus overlay on the plots). However, Figure 4.7(a) and 4.7(b) show an order improvement in the performance of the MGLS algorithm for clock offset and skew. Furthermore, the disparity between $L = 1$ and the optimal $L = 3$ decreases steadily by an order of magnitude for higher SNR scenarios as presented in Figure 4.7(d) and 4.7(e). A significant advantage of utilizing the proper L is observed in RMSE of the distance parameter in Figure 4.7(c) and Figure 4.7(f). As the approximation order increases, the RCRB of the distance (dominated by the Vandermonde-like system) also increases, while the RMSE of the

distance estimate steadily decreases with incrementing L. An optimality is achieved at $L = 3$, when the RMSE of the distance estimate meets the RCRB. Similar to the performance of the clock parameters, for lower SNR the higher order approximation is redundant.

4.7.4 Extension to partially connected networks

The proposed MGLS algorithm caters to a full mesh network and can be extended to partial networks for clock synchronization as discussed in *Remark 3*. For the given mobile network of $N = 5$ nodes, the minimum requirement on the number of links is $N - 1 = 4$ and for a full mesh network we have $\bar{N} = 10$ links. We evaluate the performance of the MGLS algorithm for the synchronization in case of a partially connected network, by varying the number of connected links as $4, 6, 8$ and 10. The links are arbitrarily chosen such that each node has at least single two-way communication link with one other node in the network, to ensure network wide synchronization. Subsequently, the rows and columns of the corresponding non-existing links are eliminated from the primary matrix $\mathbf{A}$ (4.30). The MGLS algorithm is implemented for $L = 3$ with a single clock reference (i.e., classic constraint [5]) for $K = 10$ and $\sigma = 1$meter, and the performance of the clock parameters are presented in Figure 4.8, shown by blue colored markers. Not surprisingly, the RMSE of clock parameters deteriorate with the increase in missing links.

In addition, to emphasize the benefits of the constrained formulation (Section 4.6.4), we assume that first 3 clocks of the 5 node clocks are known in each of the partially connected networks under study. The constraint matrix is then accordingly designed (e.g., (4.49)) and the performance of the corresponding MGLS solution is presented in Figure 4.8, shown by red colored markers. The incorporation of 2 additional reference clocks improves the performance of the clock parameters. Furthermore, observe that a partially connected network with 8 links and 3 reference clocks outperforms the full mesh network of 10 with a single clock. Such observations can be directly interpreted from the CCRB and the proposed algorithm achieves this CCRB asymptotically, catering readily to such partially connected networks with (or without) apriori information.

---

[5]The classic constraint is arbitrarily chosen for investigating this scenario. Alternatively, these experiments can also be conducted using the proposed Nullspace and Sum constraints, which follow similar trends.
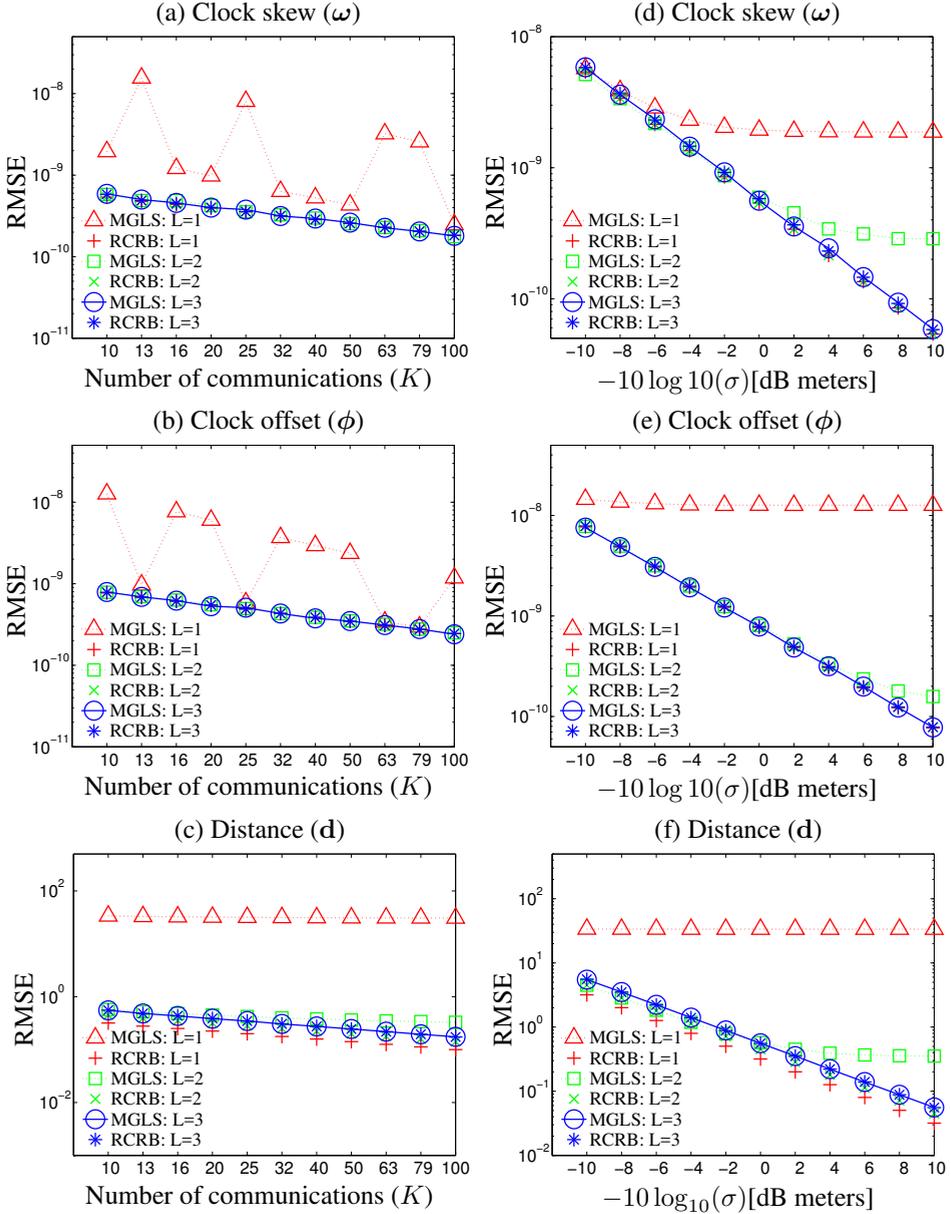
Figure 4.7: *Choice of L on estimator performance:* **(Left) Varying** K: RMSEs (and RCRBs) of (a) clock skew, (b) clock offset and (c) distances for varying number of communications (K) between the $N = 5$ *mobile* nodes with $\sigma = 3.3$nS (1 meter) and different orders of approximation L. **(Right) Varying** σ: RMSEs (and RCRBs) (a) clock skew, (b) clock offset and (c) distances, for varying noise (σ) on the time measurements with $K = 10$ and different orders of approximation L.
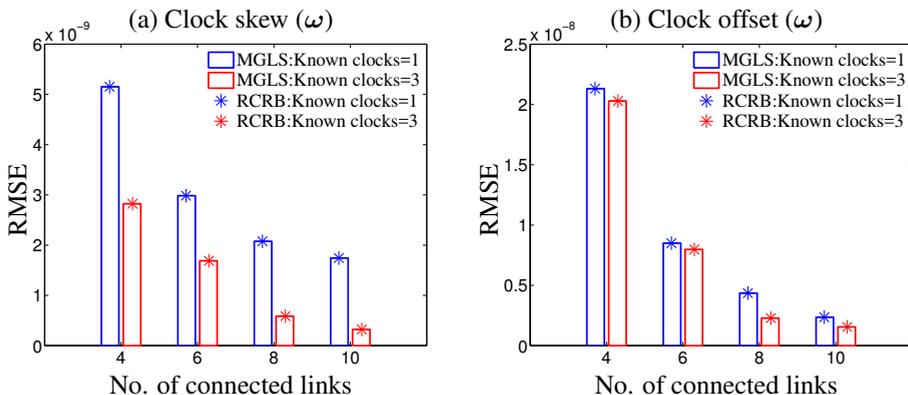
Figure 4.8: ***Effect of additional clocks on partially connected networks:*** RMSEs (and RCRBs) of (a) clock skew and (b) clock offset with $K = 10$, $L = 3, \sigma = 3.3$nS (1 meter) , for a mobile network with varying number of connected links.

4.7.5   Summary

We validate the joint time-range model by simulating an *asynchronous cluster of mobile nodes*, where the pairwise distances are time-varying, and the approximation order of distance L is unknown. The proposed MPLS and MGLS algorithms clearly outperform the prevalent solutions when the nodes are in motion, and in particular for relatively higher SNR on the time markers. More significantly, the variance of the estimated clock parameters and distance achieve the derived CCRB asymptotically. The proposed sum constraint shows an improvement of about factor 2 in contrast to the classic constraint, and is nearly identical to the performance of the "optimal" nullspace constraint. Furthermore, the extension of the proposed algorithms to a partially connected network is simulated for various number of missing links. In addition, the benefits of the constrained framework are shown by studying the effect of multiple clocks in partially connected networks.

4.8   Conclusions

The fundamental challenge has been to jointly estimate clock discrepancies and the time-varying distances between a cluster of asynchronous mobile nodes, which is addressed by proposing a novel joint time-range basis. The clock parameters are modeled up to the first order and the time-varying pairwise distances are approximated as a Lth order function of time. An elegant linear transformation decouples the

clock errors from the estimated range parameters. This joint time-range basis has been applied to the proposed generalized TWR scenario and is shown to be a linear system of unknown clock and range parameters. More generally, the joint basis can be applied to other two-way communication frameworks as well. Subsequently a global least squares solution (MGLS) is proposed, which is in turn an extension of the corresponding distributed pairwise algorithm (MPLS), to estimate all the clock parameters and the pairwise distances at discrete time intervals. Furthermore, when the order L of range approximation is unknown, iterative solutions (iMGLS, iMPLS) are proposed to estimate the apt approximation order for the distance measurement. A novel Constrained Cramér-Rao Bound is derived for the presented model and the proposed solutions meet this lower bound asymptotically, which is corroborated by the simulations. As an alternative to the classical single clock reference constraint, we propose the sum and the nullspace constraints which beget a lower variance for clock parameters.

The generalized constrained framework enables users to add more constraints if there is additional information available on the clock and range parameters from other systems, which would evidently increase overall estimation performance. The proposed framework is for a full mesh network with two-way communication capability, however robust synchronization is still feasible despite missing links, including one-way communication. More generally, these solutions can be easily extended to sender-receiver, receiver-receiver, pairwise listening, broadcasting and other prevalent communication schemes (see [Wu, Chaudhari and Serpedin 2011] and references therein).

The presented solutions are suited for autonomous networks with minimal a priori knowledge, where the clock and range parameters need to be estimated at *cold start*. Given the pairwise distances, the relative node positions of an anchorless network at every time instant can be estimated using Multidimensional scaling. In practice, over longer durations, a Kalman filter [Kay 1993] can be applied sequentially to track these network parameters, which would yield more efficient and optimal estimates with time. In addition, although the proposed model is targeted towards anchorless networks, it is readily applicable to anchored scenarios of time, distance and position.

In this chapter, the estimated range parameters are viewed merely as coefficients to fit the pairwise distances between the nodes. In the following chapters, we investigate the interpretation of the range parameters and their relationship to the relative kinematics of a mobile network.

Appendix 4.A   Range translation matrix **G**

To find an expression for $\mathbf{G}$, we begin by considering the classic case of a static network of immobile nodes i.e., $L = 1$. This is a special case of the dynamic range model in (4.3), which has been investigated extensively [IEEE Working Group 802.15.4 2007; Serpedin and Chaudhari 2009; Leng and Wu 2010; Freris, Graham and Kumar 2010; Rajan and van der Veen 2011]. When the nodes are fixed, the propagation delay $\tau_{ij}(t) \triangleq c^{-1}\mathcal{R}_{ij}(t) = c^{-1}r_{ij}^{(0)}$ is invariant with the *true* time t and following immediately we have

$$r_{ij}^{(0)} \quad \triangleq \quad c\gamma_{ij}^{(0)}. \tag{4.59}$$

A step further, in case of a mobile network, a first order range model is proposed in [Rajan and van der Veen 2012], where the translated range model (4.4) for $L = 2$ is given by

$$\mathcal{G}_{ij}(t_i) \quad = \quad \gamma_{ij}^{(0)} + \gamma_{ij}^{(1)}t_i. \tag{4.60}$$

Substituting the equation of ideal *true* time from (4.1) in (4.60), the translated range coefficients in terms of α_i, β_i and $r_{ij}^{(0)}$ are

$$\gamma_{ij}^{(1)} \quad \triangleq \quad c^{-1}\left(\alpha_i\, r_{ij}^{(1)}\right), \tag{4.61a}$$

$$\gamma_{ij}^{(0)} \quad \triangleq \quad c^{-1}\left(r_{ij}^{(0)} + r_{ij}^{(1)}\beta_i\right), \tag{4.61b}$$

and rearranging the terms,

$$r_{ij}^{(1)} \quad \triangleq \quad c\left(\alpha_i^{-1}\, \gamma_{ij}^{(1)}\right), \tag{4.62a}$$

$$r_{ij}^{(0)} \quad \triangleq \quad c\left(\gamma_{ij}^{(0)} - \alpha_i^{-1}\beta_i\gamma_{ij}\right). \tag{4.62b}$$

Along similar lines, extending the affine range model to a second order model [Rajan and van der Veen 2013] (i.e., $L = 2$), we have

$$\mathcal{G}_{ij}(t_i) \quad = \quad \gamma_{ij}^{(0)} + \gamma_{ij}^{(1)}t_i + \gamma_{ij}^{(2)}t_i^2, \tag{4.63}$$

where an expression for $\boldsymbol{\gamma}_{ij} = [\gamma_{ij}^{(0)}\ \gamma_{ij}^{(1)}\ \gamma_{ij}^{(2)}]$ in terms of the *true* range parameters $\mathbf{r}_{ij}$ and clock errors is obtained by substituting for ideal *true* time from (4.1) in (4.63),

which yields

$$\gamma_{ij}^{(2)} \triangleq c^{-1}\left(\alpha_i^2 \, r_{ij}^{(2)}\right), \tag{4.64a}$$

$$\gamma_{ij}^{(1)} \triangleq c^{-1}\left(\alpha_i r_{ij}^{(1)} + 2\alpha_i\beta_i r_{ij}^{(2)}\right), \tag{4.64b}$$

$$\gamma_{ij}^{(0)} \triangleq c^{-1}\left(r_{ij}^{(0)} + \beta_i r_{ij}^{(1)} + \beta_i^2, r_{ij}^{(2)}\right), \tag{4.64c}$$

or alternatively

$$r_{ij}^{(2)} \triangleq c\left(\alpha_i^{-2}\gamma_{ij}^{(2)}\right), \tag{4.65a}$$

$$r_{ij}^{(1)} \triangleq c\left(\alpha_i^{-1}\gamma_{ij}^{(1)} - 2\alpha_i^{-2}\beta_i\gamma_{ij}^{(2)}\right), \tag{4.65b}$$

$$r_{ij}^{(0)} \triangleq c\left(\gamma_{ij}^{(0)} + \alpha_i^{-1}\beta_i\gamma_{ij}^{(1)} - \alpha_i^{-2}\beta_i^2\gamma_{ij}^{(2)}\right). \tag{4.65c}$$

More generally, for any $L \geq 1$, the lth order translated range coefficient $\gamma_{ij}^{(l)}$ for the node pair $\{i,j\}$ is by symmetry

$$r_{ij}^{(l)} \triangleq c\sum_{\bar{l}=l}^{L-1} \binom{\bar{l}}{l} \alpha_i^{-\bar{l}}(-\beta_i)^{\bar{l}-l}\gamma_{ij}^{(\bar{l})} \quad \forall\, l = 0, 1, \ldots, L, \tag{4.66}$$

which for the sake of notational brevity can be written as

$$\mathbf{r}_{ij} = \tilde{\mathbf{G}}_i\boldsymbol{\gamma}_{ij} \quad \Leftrightarrow \quad \boldsymbol{\gamma}_{ij} = \tilde{\mathbf{G}}_i^{-1}\mathbf{r}_{ij}, \tag{4.67}$$

where $\tilde{\mathbf{G}}_i \in \mathbb{R}^{L\times L}, \forall\, l = 0, 1, \ldots L$ and $\bar{l} = l+1, l+2, \ldots L$ is a triangular matrix contains the clock discrepancies of node i and is given by

$$\{\tilde{\mathbf{G}}_i\}_{l+1,\bar{l}+1} = c\binom{\bar{l}}{l}\alpha_i^{-\bar{l}}(-\beta_i)^{\bar{l}-l}. \tag{4.68}$$

For the entire network of $\bar{N}$ *unique* pairwise links, we have

$$\tilde{\mathbf{r}} = \tilde{\mathbf{G}}\tilde{\boldsymbol{\gamma}} \quad \Leftrightarrow \quad \tilde{\boldsymbol{\gamma}} = \tilde{\mathbf{G}}^{-1}\tilde{\mathbf{r}}, \tag{4.69}$$

where $\tilde{\boldsymbol{\gamma}} = \mathrm{vec}(\boldsymbol{\Gamma}^T) = \mathbf{P}^T\boldsymbol{\gamma}$ and $\tilde{\mathbf{r}} = \mathrm{vec}(\mathbf{R}^T) = \mathbf{P}^T\mathbf{r}$, where $\mathbf{P} \in \mathbb{R}^{\bar{N}L\times\bar{N}L}$ is a permutation matrix. The transformation matrix $\tilde{\mathbf{G}} \in \mathbb{R}^{\bar{N}L\times\bar{N}L}$ is given by

$$\tilde{\mathbf{G}} = \mathrm{bdiag}\left(\mathbf{I}_{N-1}\otimes\tilde{\mathbf{G}}_1,\ \mathbf{I}_{N-2}\otimes\tilde{\mathbf{G}}_2,\ \ldots, \mathbf{I}\otimes\tilde{\mathbf{G}}_{N-1}\right), \tag{4.70}$$

which is only dependent on the clock calibration parameters $\{\boldsymbol{\alpha}, \boldsymbol{\beta}\}$ of the network. Finally, defining

$$\mathbf{G} = \mathbf{P}\tilde{\mathbf{G}}\mathbf{P}^T, \tag{4.71}$$

we have

$$\mathbf{r} = \mathbf{G}\boldsymbol{\gamma} \quad \Leftrightarrow \quad \boldsymbol{\gamma} = \mathbf{G}^{-1}\mathbf{r}, \tag{4.72}$$

which gives us a unique relation between the *true* range parameters and the translated range parameters, in the presence of clock errors. It is evident from (4.72) that the range parameters can be extracted uniquely from the modified range parameters despite clock discrepancies, provided $\mathbf{G}$ i.e., the clock calibration parameters $\begin{bmatrix} \boldsymbol{\alpha} & \boldsymbol{\beta} \end{bmatrix}$ are known. Furthermore, in the absence of clock errors, i.e., $\boldsymbol{\alpha} = \mathbf{1}_N$ and $\boldsymbol{\beta} = \mathbf{0}_N$, then $\mathbf{G} = c\mathbf{I}_{\bar{N}L}$ and following immediately $\mathbf{r} = c\boldsymbol{\gamma}$. Observe that, for a given node pair (i, j) although the translated parameters $(\boldsymbol{\gamma}_{ij})$ are dependent on the choice of clock reference i or j, the true range parameters $(\mathbf{r}_{ij})$ remain unique to a given node pair.

Appendix 4.B   iterative Mobile Pairwise Least Squares (iMPLS)

For a given distance approximation order l, the pairwise cost function (4.27) can be rewritten as

$$\hat{\boldsymbol{\theta}}_{ij,l} = \arg \min_{\boldsymbol{\theta}_{ij,l}} \epsilon_{ij,l} = (\mathbf{A}_{ij,l}^T \mathbf{A}_{ij,l})^{-1} \mathbf{A}_{ij,l} \mathbf{b}_{ij}, \tag{4.73}$$

where

$$\begin{aligned}
\epsilon_{ij,l} &= (\mathbf{A}_{ij,l}\boldsymbol{\theta}_{ij,l} - \mathbf{b}_{ij})^T (\mathbf{A}_{ij,l}\boldsymbol{\theta}_{ij,l} - \mathbf{b}_{ij}), &\tag{4.74}\\
\mathbf{A}_{ij,l} &= [-\mathbf{t}_{ji} \quad -\mathbf{1}_K \quad \mathbf{E}_{ij}\mathbf{V}_{ij,l}], &\tag{4.75}\\
\mathbf{V}_{ij,l} &= [\mathbf{t}_{ij}^{\odot 0} \quad \mathbf{t}_{ij}^{\odot 1} \dots, \quad \mathbf{t}_{ij}^{\odot l-1}], &\\
\boldsymbol{\theta}_{ij,l} &= [\alpha_j \quad \beta_j \quad \boldsymbol{\gamma}_{ij}^T]^T, &
\end{aligned}$$

and $\mathbf{b}_{ij} = -\mathbf{t}_{ij}$. More generally, when l is unknown, we briefly describe the iterative Mobile Pairwise Least Squares (iMPLS) algorithm for a pair of nodes, using the well known order recursive least squares [Kay 1993].

Algorithm 1 iterative Mobile Pairwise Least Squares (iMPLS)

Initialize:

1) For $l = 0$ define $\mathbf{A}_{ij,l} \triangleq \mathbf{A}_{ij,0}$ from (4.75)

2) Define $\bar{\mathbf{A}}_{ij,l} \triangleq \bar{\mathbf{A}}_{ij,0} = (\mathbf{A}_{ij,0}^T \mathbf{A}_{ij,0})^{-1}$

3) Estimate $\hat{\boldsymbol{\theta}}_{j,l} \triangleq \hat{\boldsymbol{\theta}}_{j,0}$ using (4.73)

4) Estimate LSE $\epsilon_{ij,l} \triangleq \epsilon_{ij,0}$ from (4.74)

3) Define $m = 3$ and $\delta_0 = \epsilon_{ij,0}/m$

while $\delta_l > \delta_{ij,tol}$ **do**

   4) Update inverse $\bar{\mathbf{A}}_{ij,l+1}$ using (4.76)

   5) Estimate $\hat{\boldsymbol{\theta}}_{ij,l+1}$ from (4.77)

   6) Update least squares error $\epsilon_{ij,l+1}$ using (4.78)

   7) Update $\delta_l \leftarrow (\epsilon_{ij,l+1} - \epsilon_{ij,l})/(m+1)$

   8) Update $l \leftarrow l+1$, $m \leftarrow m+1$, $\epsilon_{ij,l} \leftarrow \epsilon_{ij,l+1}$

end while

$$
\bar{\mathbf{A}}_{ij,l+1} = \begin{bmatrix} \bar{\mathbf{A}}_{ij,l} + \dfrac{\bar{\mathbf{A}}_{ij,l}\mathbf{A}_{ji,l}^T \mathbf{a}_{ij,l+1}\mathbf{a}_{ij,l+1}^T \mathbf{A}_{ij,l}\bar{\mathbf{A}}_{ij,l}}{\mathbf{a}_{l+1}^T \mathbf{P}_{ij,l}^{\perp} \mathbf{a}_{l+1}} & \dfrac{\bar{\mathbf{A}}_{ij,l}\mathbf{A}_{ji,l}^T \mathbf{a}_{ij,l+1}}{\mathbf{a}_{l+1}^T \mathbf{P}_{ij,l}^{\perp} \mathbf{a}_{l+1}} \\[3mm] \dfrac{\mathbf{a}_{ij,l+1}^T \mathbf{A}_{ij,l}\bar{\mathbf{A}}_{ij,l}}{\mathbf{a}_{l+1}^T \mathbf{P}_{ij,l}^{\perp} \mathbf{a}_{l+1}} & \dfrac{1}{\mathbf{a}_{ij,l+1}^T \mathbf{A}_{ij,l}\bar{\mathbf{A}}_{ij,l}} \end{bmatrix}, (4.76)
$$

$$
\boldsymbol{\theta}_{ij,l+1} = \begin{bmatrix} \boldsymbol{\theta}_{ij,l} - \dfrac{\bar{\mathbf{A}}_{ij,l}\mathbf{A}_{ji,l}^T \mathbf{a}_{ij,l+1}\mathbf{a}_{ij,l+1}^T \mathbf{P}_{ij,l}^{\perp} \mathbf{b}_{ij}}{\mathbf{a}_{l+1}^T \mathbf{P}_{ij,l}^{\perp} \mathbf{a}_{l+1}} \\[3mm] \dfrac{\mathbf{a}_{ij,l+1}^T \mathbf{P}_{ij,l}^{\perp} \mathbf{b}_{ij}}{\mathbf{a}_{ij,l+1}^T \mathbf{P}_{ij,l}^{\perp} \mathbf{a}_{ij,l+1}} \end{bmatrix}, \qquad (4.77)
$$

$$
\epsilon_{ij,l+1} = \epsilon_{ij,l} - \frac{(\mathbf{a}_{ij,l+1}^T \mathbf{P}_{ij,l}^{\perp} \mathbf{b}_{ij})^2}{\mathbf{a}_{ij,l+1}^T \mathbf{P}_{ij,l}^{\perp} \mathbf{a}_{ij,l+1}}, \qquad (4.78)
$$

where $\mathbf{a}_{ij,l+1} = \mathbf{e}_{ij} \odot \mathbf{t}_{ij}^{\odot\, l+1}$ and $\mathbf{P}_{ij,l}^{\perp} = \mathbf{I} - \mathbf{A}_{ij,l}\bar{\mathbf{A}}_{ij,l}\mathbf{A}_{ji,l}^T$.

Appendix 4.C   iterative Mobile Global Least Squares (iMGLS)

Similar to the pairwise model, we propose an iterative Mobile Global Least Squares solution to dynamically estimate all the clock and range parameters for a cluster of mobile nodes, when the range order is unknown. Note that for a given l, the KKT solution (4.35) is

$$\hat{\boldsymbol{\theta}}_l = \arg\min_{\boldsymbol{\theta}_l} \ \epsilon_l = \mathbf{B}_l^{-1}\underline{\mathbf{b}}, \tag{4.79}$$

where

$$
\begin{aligned}
\epsilon_l &= (\mathbf{B}_l\boldsymbol{\theta}_l - \underline{\mathbf{b}})^T(\mathbf{B}_l\boldsymbol{\theta}_l - \underline{\mathbf{b}}), & (4.80)\\
\mathbf{B}_l &= \begin{bmatrix} 2\mathbf{A}_l^T\mathbf{A}_l & \mathbf{C}_l^T \\ \mathbf{C}_l & \mathbf{0}_{N_2,N_2} \end{bmatrix}, & (4.81)\\
\mathbf{A}_l &= \begin{bmatrix} \mathbf{T} & \mathbf{H} & \mathbf{EV}_l \end{bmatrix}, \\
\mathbf{V}_l &= \begin{bmatrix} \mathbf{I}_{\bar{N}} \otimes \mathbf{1}_K & \bar{\mathbf{T}}^{\odot 1} & \dots & \bar{\mathbf{T}}^{\odot l-1} \end{bmatrix}, \\
\underline{\mathbf{b}} &= \begin{bmatrix} \mathbf{0}^T & \mathbf{b}^T \end{bmatrix}^T.
\end{aligned}
$$

Algorithm 2 iterative Mobile Global Least Squares (iMGLS)

Initialize:
1) For $l = 0$, define $\mathbf{B}_l \triangleq \mathbf{B}_0$ using (4.81)
2) Estimate $\widehat{\underline{\boldsymbol{\theta}}}_l \triangleq \widehat{\underline{\boldsymbol{\theta}}}_0$ using (4.79)
3) Estimate LSE $\epsilon_l \triangleq \epsilon_0$ from (4.80)
4) Define $m = 2N + \bar{N}$ and $\delta_l = \epsilon_0/m$.
while $\delta_l > \delta_{tol}$ **do**
   4) Estimate $\widehat{\underline{\boldsymbol{\theta}}}_{l+1}$ using (4.35)
   5) Obtain least squares error ϵ_{l+1} using (4.80)
   6) Update $\delta_l \leftarrow (\epsilon_{l+1} - \epsilon_l)/(m+1)$
   7) Update $l \leftarrow l+1, m \leftarrow m + \bar{N}, \epsilon_l \leftarrow \epsilon_{l+1}$
end while

Appendix 4.D   Jacobian $\mathbf{J}_{\theta\zeta}$

The Jacobian $\mathbf{J}_{\theta\eta}$ in (4.42) is given by

$$
\begin{aligned}
\mathbf{J}_{\theta\zeta} &\triangleq \left[\frac{\partial \zeta}{\partial \boldsymbol{\theta}^T}\right] \triangleq \left[\frac{\partial \zeta}{\partial \boldsymbol{\alpha}^T} \quad \frac{\partial \zeta}{\partial \boldsymbol{\beta}^T} \quad \frac{\partial \zeta}{\partial \boldsymbol{\gamma}^T}\right] \\[2mm]
&= \begin{bmatrix} \dfrac{\partial \boldsymbol{\omega}}{\partial \boldsymbol{\alpha}^T} & \dfrac{\partial \boldsymbol{\omega}}{\partial \boldsymbol{\beta}^T} & \dfrac{\partial \boldsymbol{\omega}}{\partial \boldsymbol{\gamma}^T} \\[2mm] \dfrac{\partial \boldsymbol{\phi}}{\partial \boldsymbol{\alpha}^T} & \dfrac{\partial \boldsymbol{\phi}}{\partial \boldsymbol{\beta}^T} & \dfrac{\partial \boldsymbol{\phi}}{\partial \boldsymbol{\gamma}^T} \\[2mm] \dfrac{\partial \mathbf{r}}{\partial \boldsymbol{\alpha}^T} & \dfrac{\partial \mathbf{r}}{\partial \boldsymbol{\beta}^T} & \dfrac{\partial \mathbf{r}}{\partial \boldsymbol{\gamma}^T} \end{bmatrix} = \begin{bmatrix} -\mathcal{A}^2 & \mathbf{0}_{N,N} & \mathbf{0}_{N,\bar{N}L} \\[1mm] \mathcal{A}^2\mathcal{B} & -\mathcal{A} & \mathbf{0}_{N,\bar{N}L} \\[1mm] \dot{\mathbf{G}}^\alpha & \dot{\mathbf{G}}^\beta & \mathbf{G} \end{bmatrix}, \quad (4.82)
\end{aligned}
$$

where $\mathcal{A} = \mathrm{diag}(\boldsymbol{\alpha})^{-1} \in \mathbb{R}^{N\times N}$, $\mathcal{B} = \mathrm{diag}(\boldsymbol{\beta}) \in \mathbb{R}^{N\times N}$, $\mathbf{G}$ is the transformation matrix defined in (4.71). The transformation derivatives $\dot{\mathbf{G}}^{\boldsymbol{\alpha}} \in \mathbb{R}^{\bar{N}L\times\bar{N}L}$, $\dot{\mathbf{G}}^{\boldsymbol{\beta}} \in \mathbb{R}^{\bar{N}L\times\bar{N}L}$ are

$$
\begin{aligned}
\dot{\mathbf{G}}^{\boldsymbol{\alpha}} &\triangleq \frac{\partial \mathbf{P}\mathbf{G}\mathbf{P}^T}{\partial \boldsymbol{\alpha}^T} = \mathbf{P}\left(\frac{\partial \mathbf{G}}{\partial \boldsymbol{\alpha}^T}\right)\mathbf{P}^T \\[1mm]
&= \mathbf{P}\Big(\mathrm{bdiag}\big(\mathbf{I}_{N-1}\otimes \dot{\mathbf{G}}_1^\alpha, \mathbf{I}_{N-2}\otimes \dot{\mathbf{G}}_2^\alpha, \ldots, \mathbf{I}\otimes \dot{\mathbf{G}}_{N-1}^\alpha\big)\Big)\mathbf{P}^T, \quad (4.83) \\[3mm]
\dot{\mathbf{G}}^{\boldsymbol{\beta}} &\triangleq \frac{\partial \mathbf{P}\mathbf{G}\mathbf{P}^T}{\partial \boldsymbol{\beta}^T} = \mathbf{P}\left(\frac{\partial \mathbf{G}}{\partial \boldsymbol{\beta}^T}\right)\mathbf{P}^T \\[1mm]
&= \mathbf{P}\Big(\mathrm{bdiag}\big(\mathbf{I}_{N-1}\otimes \dot{\mathbf{G}}_1^\beta, \mathbf{I}_{N-2}\otimes \dot{\mathbf{G}}_2^\beta, \ldots, \mathbf{I}\otimes \dot{\mathbf{G}}_{N-1}^\beta\big)\Big)\mathbf{P}^T, \quad (4.84)
\end{aligned}
$$

where $\forall\, 1 \leq i \leq N$, $\dot{\mathbf{G}}_i^\alpha \in \mathbb{R}^{L\times L}$ and $\dot{\mathbf{G}}_i^\beta \in \mathbb{R}^{L\times L}$ are

$$
\{\dot{\mathbf{G}}_i^\alpha\}_{l+1,\bar{l}+1} = c \binom{\bar{l}}{l} (-\bar{l})\alpha_i^{-\bar{l}-1}(-\beta_i)^{\bar{l}-l},
$$

$$
\{\dot{\mathbf{G}}_i^\beta\}_{l+1,\bar{l}+1} = \begin{cases} \binom{\bar{l}}{l} (\bar{l}-l)\alpha_i^{-l}(-\beta_i)^{\bar{l}-l-1} & \text{if } \boldsymbol{\beta}_i \neq 0, \\[2mm] \mathbf{0}_{L,L} & \text{if } \boldsymbol{\beta}_i = 0. \end{cases}
$$

Appendix 4.E   CCRB on time-varying distance

Since $\Sigma_\eta = \sigma^2 \mathbf{I}_{K\bar{N}}$ (*See Remark 7*), the Fisher information matrix of $\boldsymbol{\theta}$ (4.41) simplifies to

$$\mathbf{F} = \left[\begin{array}{cc|c} \mathbf{T}^T\mathbf{T} & \mathbf{T}^T\mathbf{H} & \mathbf{T}^T\bar{\mathbf{V}} \\ \mathbf{H}^T\mathbf{T} & \mathbf{H}^T\mathbf{H} & \mathbf{H}^T\bar{\mathbf{V}} \\ \hline \bar{\mathbf{V}}^T\mathbf{T} & \bar{\mathbf{V}}^T\mathbf{H} & \bar{\mathbf{V}}^T\bar{\mathbf{V}} \end{array} \right] = \left[\begin{array}{c|c} \mathbf{F}_{11} & \mathbf{F}_{12}^T \\ \hline \mathbf{F}_{12} & \mathbf{F}_{22} \end{array} \right]$$

and considering all the 3 constraints are levied on the clock parameters, the orthonormal basis for the null space of these constraints are of the form $\mathbf{U} = \mathrm{bdiag}(\tilde{\mathbf{U}}, \mathbf{I}_{\bar{N}})$. Following immediately, the CCRB (4.40) is

$$\begin{aligned} \Sigma_\theta &= \sigma^2 \mathbf{U} \left[\mathbf{U}^T \mathbf{F} \mathbf{U} \right]^{-1} \mathbf{U}^T \\ &= \sigma^2 \mathbf{U} \left[\begin{array}{cc} \tilde{\mathbf{U}}^T\mathbf{F}_{11}\tilde{\mathbf{U}} & \tilde{\mathbf{U}}^T\mathbf{F}_{12}^T \\ \mathbf{F}_{12}\tilde{\mathbf{U}} & \mathbf{F}_{22} \end{array} \right]^{-1} \mathbf{U}^T \\ &= \sigma^2 \left[\begin{array}{cc} * & * \\ * & \mathcal{S}_2^{-1} \end{array} \right] = \left[\begin{array}{cc} * & * \\ * & \Sigma_\gamma \end{array} \right], \end{aligned} \tag{4.85}$$

where Σ_γ is the lower bound on $\boldsymbol{\gamma}$ and

$$\mathcal{S}_2 = \bar{\mathbf{V}}^T\bar{\mathbf{V}} - \mathbf{F}_{12}\tilde{\mathbf{U}} \left[\tilde{\mathbf{U}}^T\mathbf{F}_{11}\tilde{\mathbf{U}} \right]^{-1} \tilde{\mathbf{U}}^T\mathbf{F}_{12}^T, \tag{4.86}$$

is the Schur complement and subsequently, the CCRB on distance $\mathbf{d}$ is given by $\Sigma_d = c^2 \mathbf{V} \Sigma_\gamma \mathbf{V} = c^2 \sigma^2 \mathbf{V} \mathcal{S}_2^{-1} \mathbf{V}^T$. It is observed that contribution of the term $\mathbf{F}_{12}\tilde{\mathbf{U}} \left[\tilde{\mathbf{U}}^T\mathbf{F}_{11}\tilde{\mathbf{U}} \right]^{-1} \tilde{\mathbf{U}}^T\mathbf{F}_{12}^T$ is insignificant (in all 3 constraint cases) for the experimental setup. Hence, the CCRB of distance and the performance of the MGLS solution is observed to be independent of the clock constraints in the simulations.

<div style="text-align: right">

5

</div>

Relative velocity and relative position

Localization is a fundamental challenge for any network of nodes, particularly when the nodes are in motion within a framework where no reference nodes are available. In the previous chapter, we proposed a solution to decouple the time-varying distances and clock errors, where the distance is approximated as a polynomial function in time. In this chapter, we assume the nodes are synchronized and using the coefficients of the distance approximation, propose a novel framework to localize an anchorless network of mobile nodes. The time derivatives of the pairwise distances are used to jointly estimate the initial relative position and relative velocity of the nodes. Under linear velocity assumption for a small time duration, we show that the combination of the initial relative positions and relative velocity beget the relative motion of the nodes at discrete time instances. The proposed approach can be seen as an extension of the classical MDS in scenarios when the nodes are mobile. In addition, the Doppler measurements, if available, can be readily incorporated in the proposed framework. We derive Cramér-Rao bounds and perform simulations to evaluate the performance of the proposed estimators. Furthermore, the computational complexity and the benefits of the proposed algorithms are also presented.

5.1   Introduction

Localization is a key requirement for the deployment of wireless networks in a wide range of applications. There are numerous absolute localization algorithms, such as Time of Arrival (TOA), Time Difference of Arrival (TDOA) and Received Signal Strength (RSS) which cater to anchored networks, where a few node positions are known [Sayed, Tarighat and Khajehnouri 2005a]. Alternatively, when there are no reference anchors, then the relative positions of the nodes, up to a rotation and translation, can still be obtained using Multidimensional scaling (MDS) based solutions [Borg and Groenen 2005; Cheung and So 2005]. Such anchorless networks arise naturally when the nodes are deployed in inaccessible locations or when anchor information is known intermittently. In both anchored or anchorless scenarios, pairwise distances are one of the key inputs for almost all localization techniques. For stationary nodes, these pairwise distances are classically obtained by measuring the propagation delays of multiple time stamp exchanges between the nodes and averaging these measurements over a time period.

A step further, when the nodes are mobile, then conventionally either the nodes are considered relatively stationary within desired accuracies for the complete duration of the measurement interval (i.e., multiple distance measurements) [Rajan and van der Veen 2011] or Doppler measurements are utilized [Wei et al. 2010]. Un-

fortunately, Doppler measurements are not always available and the assumption on the node positional stability for large time periods is simply impractical in many applications. For a mobile network, the application of classical MDS-based relative positioning at every time instant yields a sequence of position matrices with arbitrary rotation, thereby providing no information on the relative velocities of the nodes. We define the term relative velocities as the velocity vectors of the nodes, up to a common rotation, translation and reflection. This has, to the best of the authors' knowledge, not yet been investigated in the literature. Given the relative velocities up to the appropriate rotation, the time-varying positions can be readily obtained for a linear mobility model. Hence, the estimation of relative velocities therefore constitutes a paramount challenge to be solved in next-generation localization technologies.

5.1.1 Contributions

In this article, our quest is to localize an anchorless network of mobile nodes, given time-varying pairwise distance measurements. We propose a two-step approach to solve this problem. Firstly, we approximate the time-varying pairwise propagation delays (and subsequently the distances) between the mobile nodes as a Taylor series in time, which is aptly termed dynamic ranging (Section 5.2). A simple yet efficient time-basis is employed, to estimate the derivatives of the pairwise distances at a given time instant (Section 5.3). Secondly, under the assumption of constant velocity for a short time duration, we show that the relative position of each node is dependent only on the initial relative position, the relative velocity and a unique rotation matrix (Section 5.4). Furthermore, we also show that the solutions to the unknown initial relative position, the relative velocity and the rotation matrix lie in the first three derivatives of the time-varying pairwise distance. Subsequently, we present MDS-like and least squares solutions to estimate the unknown parameters in Section 5.5 and Cramér-Rao Bounds are derived in Section 5.6. Finally, based on the proposed estimators we propose two algorithms, namely linearized MDS (LMDS) and connected MDS (CMDS) to estimate the relative positions of the nodes over discrete time intervals (Section 5.7). Simulations are conducted to evaluate the performance of the proposed estimators in Section 5.8. The novelty of our work lies in the proposed framework and subsequent estimators to estimate time-varying relative motion in Euclidean space.

5.2   Dynamic ranging

5.2.1   Range model

Consider a cluster of N nodes in a P-dimensional Euclidean space. If the nodes are fixed, then the pairwise propagation delay at time t_0 between a given node pair (i, j) is defined as

$$\tau_{ij}(t_0) \equiv \tau_{ji}(t_0) \triangleq c^{-1}d_{ij}(t_0), \tag{5.1}$$

where $d_{ij}(t_0)$ is the fixed distance between the node pair at t_0 and c is the speed of the electromagnetic wave in the medium. However, when the nodes are mobile, the relative distances between the nodes are a non-linear function of time (for $P \geq 2$), even when the nodes are in linear motion. For a small time interval $\Delta t_k = t_k - t_0$, we consider these relative distances as a smoothly varying polynomial in time. The propagation delay $\tau_{ij}(t_k) \equiv \tau_{ji}(t_k)$ between a given node pair (i, j) can be expanded classically as an infinite Taylor series around a time instant t_0 within the neighborhood Δt_k. As an extension of the second-order distance model [Rajan and van der Veen 2013], we have

$$\tau_{ij}(t_0 + \Delta t_k) \triangleq c^{-1}d_{ij}(t_0 + \Delta t_k) \triangleq c^{-1}d_{ij}(t_k), \tag{5.2}$$

where $d_{ij}(t_k)$ is the distance at $t_k = t_0 + \Delta t_k$, given by

$$d_{ij}(t_k) \;\simeq\; r_{ij} + \frac{\dot{r}_{ij}}{1!}\Delta t_k + \frac{\ddot{r}_{ij}}{2!}\Delta t_k^2 + \dots, \tag{5.3}$$

where $[r_{ij}, \dot{r}_{ij}, \ddot{r}_{ij}, \dots]^T \in \mathbb{R}^{L \times 1}$ are the range parameters for the Lth order approximation of the time-varying distance. The first coefficient $r_{ij} \equiv d_{ij}(t_0)$ is the initial pairwise distance and the following $L-1$ coefficients are successive derivatives of r_{ij} at t_0. Without loss of generality, assuming $t_0 = 0$, we have $t_k = \Delta t_k$ and subsequently (5.2) and (5.3) simplify to the Maclaurin series as

$$\tau_{ij}(t_k) = c^{-1}\Big(r_{ij} + \dot{r}_{ij}t_k + \frac{\ddot{r}_{ij}}{2!}t_k^2 + \dots\Big). \tag{5.4}$$

The polynomial range basis is simplified further by introducing

$$\big[\underline{r}_{ij}, \underline{\dot{r}}_{ij}, \underline{\ddot{r}}_{ij}, \dots\big]^T \triangleq \operatorname{diag}(\mathbf{f})^{-1}\big[r_{ij}, \dot{r}_{ij}, \ddot{r}_{ij}, \dots\big]^T, \tag{5.5}$$

where $\mathbf{f} = c[1,\ 1!,\ 2!,\ \dots]^T \in \mathbb{R}^{L \times 1}$, such that (5.4) is

$$\tau_{ij}(t_k) \triangleq c^{-1}d_{ij}(t_k) \;=\; \underline{r}_{ij} + \underline{\dot{r}}_{ij}t_k + \underline{\ddot{r}}_{ij}t_k^2 + \dots. \tag{5.6}$$
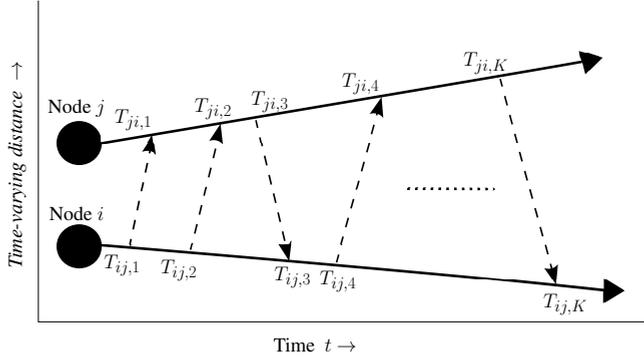
Figure 5.1: *Illustration of a pair of mobile nodes in linear motion:* A generalized Two-Way Ranging (TWR) between a pair of *mobile* nodes, where the solid-skewed lines indicate the linear motion of the nodes. During the linear motion, the nodes transmit and receive K time stamps, which are recorded at the respective nodes. Similar to [Rajan and van der Veen 2011; Rajan and van der Veen 2013; Rajan and van der Veen 2015], we levy no constraints on the sequence, direction or number of communications.

Now, for the entire network of N nodes, the unique pairwise ranges are collected in a vector $\mathbf{r} \in \mathbb{R}^{\bar{N} \times 1}$, where $\bar{N} = \binom{N}{2}$ is the number of unique pairwise baselines. Along similar lines, we define $\dot{\mathbf{r}} \in \mathbb{R}^{\bar{N} \times 1}$, $\ddot{\mathbf{r}} \in \mathbb{R}^{\bar{N} \times 1}$ and corresponding higher-order terms. The unknown range parameters for all pairwise links are collected under the vector $\boldsymbol{\theta} = \left[\mathbf{r}^T, \dot{\mathbf{r}}^T, \ddot{\mathbf{r}}^T, \ldots\right]^T \in \mathbb{R}^{\bar{N}L \times 1}$. Furthermore, similar to the definition of $\boldsymbol{\theta}$, we define $\underline{\boldsymbol{\theta}} = \left[\underline{\mathbf{r}}^T, \underline{\dot{\mathbf{r}}}^T, \underline{\ddot{\mathbf{r}}}^T, \ldots\right]^T \in \mathbb{R}^{\bar{N}L \times 1}$, where $\underline{\mathbf{r}} \in \mathbb{R}^{\bar{N} \times 1}$, $\underline{\dot{\mathbf{r}}} \in \mathbb{R}^{\bar{N} \times 1}$, $\underline{\ddot{\mathbf{r}}} \in \mathbb{R}^{\bar{N} \times 1}$ and corresponding higher-order terms are modified range parameters. The relationship between $\boldsymbol{\theta}$ and $\underline{\boldsymbol{\theta}}$, using (5.5), is then

$$\boldsymbol{\theta} = \left(\text{diag}(\mathbf{f}) \otimes \mathbf{I}_{\bar{N}}\right) \underline{\boldsymbol{\theta}}. \tag{5.7}$$

Remark 8: (**Doppler measurements**): Observe that in essence, $\mathbf{r}$ is the time of arrival (TOA) at t_0, the range rate $\dot{\mathbf{r}}$ is the radial velocity (as obtained from a Doppler shift) and the second order range parameter $\ddot{\mathbf{r}}$ is the rate of radial velocity (as observed from a Doppler spread) between the nodes at $t = t_0$. These range coefficients can be readily incorporated if these measurements are available.

5.2.2   Data model

We now consider a relaxed two-way ranging (TWR) setup for collecting distance information as follows. Let each node pair (i, j) within the network be capable of communicating with each other as shown in Figure 5.1. The nodes communicate K messages back and forth, and the time of transmission and reception is registered independently at the respective nodes. The kth time stamp recorded at node i when communicating with node j is denoted by $T_{ij,k}$ and similarly at node j the time stamp is $T_{ji,k}$. The direction of the communication is indicated by $E_{ij,k}$, where $E_{ij,k} = +1$ for transmission from node i to node j and $E_{ij,k} = -1$ for transmission from node j to node i. Under ideal noiseless conditions, the propagation delay between the node pair at the kth time instant is $\tau_{ij,k} \triangleq E_{ij,k}(T_{ji,k} - T_{ij,k})$, and in conjunction with the polynomial approximation (5.6), we have

$$\tau_{ij,k} \triangleq E_{ij,k}(T_{ji,k} - T_{ij,k}) = \underline{r}_{ij} + \underline{\dot{r}}_{ij}T_{ij,k} + \underline{\ddot{r}}_{ij}T_{ij,k}^2 + \dots, \qquad (5.8)$$

where without loss of generality we have replaced t_k with $T_{ij,k}$.

Remark 10: (**Synchronized nodes**): By replacing true time t_k by $T_{ij,k}$, we assume without loss of generality that $T_{ij,k}$ is in the neighborhood of $t_0 = 0$ and the propagation delay is measured as a function of the local time at node i. Furthermore, we also assume that the clocks of these nodes are synchronized. This is a valid assumption since for an asynchronous network of mobile nodes, the clock parameters (up to first order) can be decoupled from the range parameters and the distances can be estimated efficiently as shown in chapter 4 [Rajan and van der Veen 2011; Rajan and van der Veen 2013; Rajan and van der Veen 2015]. .

In practice, the time measurements are also corrupted with noise and thus (5.8) is

$$\underline{r}_{ij} + \underline{\dot{r}}_{ij}(T_{ij,k} + q_{i,k}) + \underline{\ddot{r}}_{ij}(T_{ij,k} + q_{i,k})^2 + \dots$$
$$= E_{ij,k}\Big((T_{ji,k} + q_{j,k}) - (T_{ij,k} + q_{i,k})\Big), \qquad (5.9)$$

where $q_{i,k} \sim \mathcal{N}(0, \Sigma_i)$, $q_{j,k} \sim \mathcal{N}(0, \Sigma_j)$ are modelled as Gaussian i.i.d. noise variables, plaguing the timing measurements at node i and node j, respectively. Rearranging the terms, we have

$$\underline{r}_{ij} + \underline{\dot{r}}_{ij}T_{ij,k} + \underline{\ddot{r}}_{ij}T_{ij,k}^2 + \dots = E_{ij,k}(T_{ji,k} - T_{ij,k}) + q_{ij,k}, \qquad (5.10)$$

where

$$q_{ij,k} = E_{ij,k}(q_{j,k} - q_{i,k}) - (\underline{\dot{r}}_{ij}q_{i,k} + 2\underline{\ddot{r}}_{ij}T_{ij,k}q_{i,k} + \underline{\ddot{r}}_{ij}q_{i,k}^2 + \dots). \qquad (5.11)$$

For wireless communication with $c = 3 \times 10^8$m/s, note that the modified range parameters are scaled by c^{-1} (5.7). Furthermore, since the dynamic range model is proposed for a small time interval, the term $(\dot{\underline{r}}_{ij}q_{i,k} + 2\ddot{\underline{r}}_{ij}T_{ij,k}q_{i,k} + \ddot{\underline{r}}_{ij}q_{i,k}^2 + \ldots)$ is relatively small and subsequently the noise vector plaguing the measurements can be approximated as $q_{ij,k} \approx E_{ij,k}(q_{j,k} - q_{i,k})$ which begets

$$q_{ij,k} \sim \mathcal{N}(0, \Sigma_{ij}), \tag{5.12}$$

where $\Sigma_{ij} = \Sigma_i + \Sigma_j$. Aggregating all K packets, we have

$$\overbrace{\begin{bmatrix} \mathbf{1}_K & \mathbf{t}_{ij} & \mathbf{t}_{ij}^{\odot 2} & \ldots \end{bmatrix}}^{\mathbf{A}_{ij}} \overbrace{\begin{bmatrix} \underline{r}_{ij} \\ \dot{\underline{r}}_{ij} \\ \ddot{\underline{r}}_{ij} \\ \vdots \end{bmatrix}}^{\boldsymbol{\theta}_{ij}} = \boldsymbol{\tau}_{ij} + \mathbf{q}_{ij}, \tag{5.13}$$

where

$$\boldsymbol{\tau}_{ij} \triangleq \mathbf{e}_{ij} \odot (\mathbf{t}_{ji} - \mathbf{t}_{ij}) \in \mathbb{R}^{K \times 1}, \tag{5.14}$$

$$\mathbf{e}_{ij} = [E_{ij,1}, E_{ij,2}, \ldots, E_{ij,K}]^T \in \mathbb{R}^{K \times 1}, \tag{5.15}$$

$$\mathbf{t}_{ij} = [T_{ij,1}, T_{ij,2}, \ldots, T_{ij,K}]^T \in \mathbb{R}^{K \times 1}. \tag{5.16}$$

The known Vandermonde matrix $\mathbf{A}_{ij} \in \mathbb{R}^{K \times L}$ contains the measured time stamps and is full column rank if $T_{ij,k}$ are unique. The direction vector $\mathbf{e}_{ij}$ is encapsulated in the propagation delay $\boldsymbol{\tau}_{ij}$ and $\underline{\boldsymbol{\theta}}_{ij} \in \mathbb{R}^{L \times 1}$ is a vector containing the unknown range parameters. The noise vector on this linear system is $\mathbf{q}_{ij} = [q_{ij,1}, q_{ij,2}, \ldots q_{ij,K}]^T \in \mathbb{R}^{K \times 1}$, where $q_{ij,k}$ is given by (5.12) and the corresponding covariance matrix is

$$\boldsymbol{\Sigma}_{ij} \triangleq \mathbb{E}\left[\mathbf{q}_{ij}\mathbf{q}_{ij}^T\right] = \Sigma_{ij}\mathbf{I}_K \in \mathbb{R}^{K \times K}. \tag{5.17}$$

For a network of N nodes, the normal equation (5.13) can be extended to the dynamic ranging model

$$\overbrace{\begin{bmatrix} \mathbf{I}_{\bar{N}} \otimes \mathbf{1}_K & \mathbf{T} & \mathbf{T}^{\odot 2} & \ldots \end{bmatrix}}^{\mathbf{A}} \overbrace{\begin{bmatrix} \underline{\mathbf{r}} \\ \dot{\underline{\mathbf{r}}} \\ \ddot{\underline{\mathbf{r}}} \\ \vdots \end{bmatrix}}^{\underline{\boldsymbol{\theta}}} = \boldsymbol{\tau} + \mathbf{q}, \tag{5.18}$$

where

$$\mathbf{T} \quad = \quad \text{bdiag}(\mathbf{t}_{12}, \mathbf{t}_{13}, \dots \mathbf{t}_{1N}, \ \mathbf{t}_{23}, \dots) \in \mathbb{R}^{\bar{N}K \times \bar{N}}, \tag{5.19}$$

$$\boldsymbol{\tau} \quad = \quad [\boldsymbol{\tau}_{12}^T, \boldsymbol{\tau}_{13}^T, \dots \boldsymbol{\tau}_{1N}^T, \ \boldsymbol{\tau}_{23}^T, \dots]^T \in \mathbb{R}^{\bar{N}K \times 1}, \tag{5.20}$$

contain the time stamp exchanges of the $\bar{N}$ unique pairwise links in the network and $\boldsymbol{\theta} \in \mathbb{R}^{\bar{N}L \times 1}$ contains the unknown range parameters for the entire network. The noise vector is $\mathbf{q} = [\mathbf{q}_{12}^T, \mathbf{q}_{13}^T, \dots, \mathbf{q}_{1N}^T, \ \mathbf{q}_{23}^T, \dots]^T \in \mathbb{R}^{\bar{N}K \times 1}$ and the covariance matrix is

$$\boldsymbol{\Sigma} \quad \triangleq \quad \mathbb{E}\left[\mathbf{q}\mathbf{q}^T\right] \in \mathbb{R}^{\bar{N}K \times \bar{N}K}. \tag{5.21}$$

Remark 12: (**Mobility of the nodes**): In (5.8), we implicitly assumed that the nodes are relatively fixed during a time period of $\delta t_k = |T_{ij,k} - T_{ji,k}|$ i.e., the propagation time of the message. This is a much weaker assumption compared to traditional TWR, where for a pair of fixed nodes (i.e., $L = 1$), the pairwise distance is assumed to be invariant for the total measurement period $\Delta T = |T_{ij,K} - T_{ij,1}|$. In reality, when the nodes are mobile, the distance at each kth time instant is dissimilar and this feature is naturally incorporated in the presented dynamic ranging model.

5.3   Dynamic ranging algorithm

Suppose that we have collected all the TWR timing data in $\mathbf{A}$ and $\boldsymbol{\tau}$, then in this section we find an estimate for the unknown $\underline{\boldsymbol{\theta}}$ using the model (5.18). Given an estimate of $\underline{\boldsymbol{\theta}}$, the range coefficients $\boldsymbol{\theta} = [\mathbf{r}^T, \dot{\mathbf{r}}^T, \ddot{\mathbf{r}}^T, \dots]^T$ can be directly obtained from (5.7).

5.3.1   Weighted Least Squares

Under the assumption that the covariance matrix $\boldsymbol{\Sigma}$ is known, a Weighted Least Squares (WLS) solution $\hat{\underline{\boldsymbol{\theta}}}$ is obtained by minimizing the l_2 norm of the linear system (5.18), leading to

$$\hat{\underline{\boldsymbol{\theta}}} \quad = \quad \arg\min_{\underline{\boldsymbol{\theta}}} \ ||\boldsymbol{\Sigma}^{-1/2}(\mathbf{A}\underline{\boldsymbol{\theta}} - \boldsymbol{\tau})||^2 \tag{5.22}$$

$$= \quad (\mathbf{A}^T\boldsymbol{\Sigma}^{-1}\mathbf{A})^{-1}\mathbf{A}^T\boldsymbol{\Sigma}^{-1}\boldsymbol{\tau}, \tag{5.23}$$

which is a valid solution if $K \geq L$ for each of the $\bar{N}$ pairwise links. More generally, when the polynomial model order L is unknown in (5.3), order recursive least squares

algorithms (such as iMGLS [Rajan and van der Veen 2015]) can be employed to obtain the range coefficients for increasing values of L, until an optimal polynomial fit for (5.22) is reached.

5.3.2 Distributed Weighted Least Squares

If we consider independent pairwise communication between all the nodes, with no broadcasting, then the noise in each pairwise link is independent of each other and subsequently the covariance matrix (5.21) simplifies to

$$\boldsymbol{\Sigma} \;=\; \mathrm{bdiag}\left(\boldsymbol{\Sigma}_{12}, \boldsymbol{\Sigma}_{13}, \ldots \boldsymbol{\Sigma}_{1N}, \, \boldsymbol{\Sigma}_{23}, \ldots\right). \tag{5.24}$$

In which case, the centralized system (5.18) is a cascade of pairwise linear systems (5.13) and subsequently (5.23) is a generalized version of solving the distributed pairwise system for estimating the pairwise range parameters $\underline{\boldsymbol{\theta}}_{ij}$ independently as

$$\begin{aligned}
\widehat{\underline{\boldsymbol{\theta}}}_{ij} &= \; \arg\min_{\underline{\boldsymbol{\theta}}_{ij}} \|\boldsymbol{\Sigma}_{ij}^{-1/2}(\mathbf{A}_{ij}\underline{\boldsymbol{\theta}}_{ij} - \boldsymbol{\tau}_{ij})\|^2 \\
&= \; (\mathbf{A}_{ij}^T\boldsymbol{\Sigma}_{ij}^{-1}\mathbf{A}_{ij})^{-1}\mathbf{A}_{ij}^T\boldsymbol{\Sigma}_{ij}^{-1}\boldsymbol{\tau}_{ij},
\end{aligned} \tag{5.25}$$

which, similar to (5.23), has a valid solution for $K \geq L$ for each pairwise link. It is worth noting that when the noise is correlated between pairwise links, the distributed weighted least squares (5.25) may be sub-optimal. In this case, a consensus based distributed least squares algorithm [Bertrand and Moonen 2011] can be employed for improved solutions.

5.3.3 Cramér-Rao bounds

The Cramér-Rao lower Bound (CRB) [Kay 1993] for the linear model (5.18) is

$$\boldsymbol{\Sigma}_{\underline{\theta}} = \; (\mathbf{A}^T\boldsymbol{\Sigma}^{-1}\mathbf{A})^{-1}, \tag{5.26}$$

and in combination with the range scaling (5.7), the CRB on $\boldsymbol{\theta}$ is given by

$$\boldsymbol{\Sigma}_{\theta} = \; (\mathrm{diag}(\mathbf{f}) \otimes \mathbf{I}_{\bar{N}})(\mathbf{A}^T\boldsymbol{\Sigma}^{-1}\mathbf{A})^{-1}(\mathrm{diag}(\mathbf{f}) \otimes \mathbf{I}_{\bar{N}}), \tag{5.27}$$

where

$$\boldsymbol{\Sigma}_{\theta} = \begin{bmatrix} \boldsymbol{\Sigma}_r & * & * & * \\ * & \boldsymbol{\Sigma}_{\dot{r}} & * & * \\ * & * & \boldsymbol{\Sigma}_{\ddot{r}} & * \\ * & * & * & \ddots \end{bmatrix}, \tag{5.28}$$

is the lowest variance achievable by any unbiased estimate of the range parameters $\boldsymbol{\theta} = [\mathbf{r}^T, \dot{\mathbf{r}}^T, \ddot{\mathbf{r}}^T, \ldots]^T$. It is worth noting that (5.23) achieves these lower bounds for an appropriate L.

Remark 14: (**Direction independence**): In general, observe that the proposed solution (5.23) is feasible for any direction marker $E_{ij,k}$, which is incorporated in $\boldsymbol{\tau}$ (5.14). In addition, the lower bounds are unaffected by the choice of direction vector $\mathbf{e}_{ij}$, $\forall\, i, j \leq N$, since all direction vectors are encapsulated in the measurement vector $\boldsymbol{\tau}_{ij}$, which is not a part of the CRB (5.27). Hence communication between the nodes could be arbitrary or one way, and need not be necessarily bi-directional. However, this is not true for an asynchronous network, where two-way communication is pivotal in jointly estimating the clock and range parameters [Rajan and van der Veen 2015]. In addition, we impose no pre-requisite on the number, sequence or direction of the communication links [Rajan and van der Veen 2011; Rajan and van der Veen 2015]. Therefore, the proposed solution is amenable to prevalent TWR protocols, such as classical pairwise communication [IEEE Working Group 802.15.4 2007], passive listening and broadcasting [Wang, Ma and Leus 2011a].

5.4 First-order relative kinematics

In the previous section, we estimated $\underline{\boldsymbol{\theta}}$ which contains the solution to the unknown range derivatives $\boldsymbol{\theta} = \begin{bmatrix} \mathbf{r}^T, \dot{\mathbf{r}}^T, \ddot{\mathbf{r}}^T, \ldots \end{bmatrix}$. Our next motive is to use these range derivatives to estimate the positions of the mobile nodes. When the nodes are in motion, similar to the pairwise range rates, the position vector of each node is also a Taylor series in time. However, exploiting piecewise linearity, we assume that the nodes are in linear motion with no acceleration, which is valid for a sufficiently small measurement period. Note that despite this assumption, the pairwise distance remains a non-linear function of time.

5.4.1 Absolute linear motion

Let the position of N $(N > P)$ nodes in a P-dimensional Euclidean space at the kth time instant be given by $\mathbf{S}_k \in \mathbb{R}^{P \times N}$. Furthermore, the ith node has velocity $\mathbf{y}_i \in \mathbb{R}^{P \times 1}$ and all such velocities are collected in $\mathbf{Y} = [\mathbf{y}_1, \mathbf{y}_2, \ldots \mathbf{y}_N] \in \mathbb{R}^{P \times N}$. Then, under a linear motion assumption, we have

$$\frac{d\mathbf{y}_i}{dt} = \mathbf{0}_P \quad \forall\, i \leq N. \tag{5.29}$$

Now, let $\Delta t_k = t_k - t_0$ where for the sake of notational convenience and without loss of generality, we assume $t_k = T_{ij,k} \ \forall \ k$, then the position matrix at the kth time instant is

$$\boxed{\mathbf{S}_k = \mathbf{X} + \Delta t_k \mathbf{Y}} \tag{5.30}$$

where $\mathbf{X} \triangleq \mathbf{S}_0 = \begin{bmatrix} \mathbf{x}_1, \mathbf{x}_2, \ldots, \mathbf{x}_N \end{bmatrix}$ is the initial position matrix at time instant t_0 and $\mathbf{S}_k$ only depends on the initial Position and Velocity (PV) of the nodes.

5.4.2   Range derivatives

To estimate the position matrix at the kth time instant $\mathbf{S}_k$, we begin by stating explicit expressions for the range derivatives $[\mathbf{r}, \dot{\mathbf{r}}, \ddot{\mathbf{r}}, \ldots]$ in terms of $\mathbf{X}, \mathbf{Y}$ under linear velocity assumption. The pairwise distance $d_{ij}(t)$ between a node pair (i, j) in $P \geq 2$ dimensional Euclidean space is a non-linear function of time, even if the nodes are only in linear motion. As derived in 5.A, the range parameters $[r_{ij}, \dot{r}_{ij}, \ddot{r}_{ij}, \ldots]$ at $t = t_0$ satisfy

$$r_{ij} = \sqrt{\mathbf{x}_i^T \mathbf{x}_i + \mathbf{x}_j^T \mathbf{x}_j - 2\mathbf{x}_i^T \mathbf{x}_j}, \tag{5.31a}$$

$$\dot{r}_{ij} = r_{ij}^{-1}(\mathbf{x}_i - \mathbf{x}_j)^T(\mathbf{y}_i - \mathbf{y}_j), \tag{5.31b}$$

$$\ddot{r}_{ij} = r_{ij}^{-1}\left(\|(\mathbf{y}_i - \mathbf{y}_j)\|^2 - \dot{r}_{ij}^2 \right). \tag{5.31c}$$

Although these range parameters can be estimated up to the $(L-1)$th order (as demonstrated in Section 5.3), in the rest of this article we utilize the information only up to $L = 3$ for estimating the relative PV. Rearranging the equations for $r_{ij}, \dot{r}_{ij}, \ddot{r}_{ij}$, from (5.31) we obtain

$$r_{ij}^2 = (\mathbf{x}_i - \mathbf{x}_j)^T(\mathbf{x}_i - \mathbf{x}_j), \tag{5.32a}$$

$$r_{ij}\dot{r}_{ij} = (\mathbf{x}_i - \mathbf{x}_j)^T(\mathbf{y}_i - \mathbf{y}_j), \tag{5.32b}$$

$$r_{ij}\ddot{r}_{ij} + \dot{r}_{ij}^2 = (\mathbf{y}_i - \mathbf{y}_j)^T(\mathbf{y}_i - \mathbf{y}_j). \tag{5.32c}$$

Extending the above equations for all N nodes and defining N dimensional vectors $\mathbf{g}_{xx} = \text{diag}(\mathbf{X}^T\mathbf{X}), \mathbf{g}_{xy} = \text{diag}(\mathbf{X}^T\mathbf{Y})$ and $\mathbf{g}_{yy} = \text{diag}(\mathbf{Y}^T\mathbf{Y})$, we have

$$\mathbf{R}^{\odot 2} = \mathbf{g}_{xx}\mathbf{1}_N^T + \mathbf{1}_N\mathbf{g}_{xx}^T - 2\mathbf{X}^T\mathbf{X}, \tag{5.33a}$$

$$\mathbf{R} \odot \dot{\mathbf{R}} = \mathbf{g}_{xy}\mathbf{1}_N^T + \mathbf{1}_N\mathbf{g}_{xy}^T - \mathbf{X}^T\mathbf{Y} - \mathbf{Y}^T\mathbf{X}, \tag{5.33b}$$

$$\mathbf{R} \odot \ddot{\mathbf{R}} + \dot{\mathbf{R}}^{\odot 2} = \mathbf{g}_{yy}\mathbf{1}_N^T + \mathbf{1}_N\mathbf{g}_{yy}^T - 2\mathbf{Y}^T\mathbf{Y}, \tag{5.33c}$$

where the square matrices $\mathbf{R} = [r_{ij}] \in \mathbb{R}^{N \times N}$, $\dot{\mathbf{R}} = [\dot{r}_{ij}] \in \mathbb{R}^{N \times N}$ and $\ddot{\mathbf{R}} = [\ddot{r}_{ij}] \in \mathbb{R}^{N \times N}$ contain the initial pairwise ranges, range rates and rate of range rates, respectively.

It is evident from (5.33) that without apriori knowledge of a few known PV, estimating the PVs of the network is an ill-posed problem and hence, we look to find solutions for the relative PV. Applying the centering matrix $\mathbf{P} = \mathbf{I}_N - N^{-1}\mathbf{1}_N\mathbf{1}_N^T \in \mathbb{R}^{N \times N}$ on (5.33), and defining

$$\mathbf{B}_{xx} \triangleq -0.5\mathbf{P}\mathbf{R}^{\odot 2}\mathbf{P}, \tag{5.34a}$$

$$\mathbf{B}_{xy} \triangleq -\mathbf{P}(\mathbf{R} \odot \dot{\mathbf{R}})\mathbf{P}, \tag{5.34b}$$

$$\mathbf{B}_{yy} \triangleq -0.5\mathbf{P}(\mathbf{R} \odot \ddot{\mathbf{R}} + \dot{\mathbf{R}}^{\odot 2})\mathbf{P}, \tag{5.34c}$$

we have,

$$\mathbf{B}_{xx} = \mathbf{P}\mathbf{X}^T\mathbf{X}\mathbf{P}, \tag{5.35a}$$

$$\mathbf{B}_{xy} = \mathbf{P}(\mathbf{X}^T\mathbf{Y} + \mathbf{Y}^T\mathbf{X})\mathbf{P}, \tag{5.35b}$$

$$\mathbf{B}_{yy} = \mathbf{P}\mathbf{Y}^T\mathbf{Y}\mathbf{P}. \tag{5.35c}$$

where we exploit the property $\mathbf{P}\mathbf{1}_N = \mathbf{0}_N$. The equations (5.35a) and (5.35c) can now be used to estimate the initial relative positions and relative velocities of the nodes respectively, which will be addressed in Section 5.5. However, first we present a relative framework of the absolute mobility model discussed in (5.30).

5.4.3   Relative linear motion

We define the relative PV vectors as an affine transformation of the corresponding absolute PV $(\mathbf{S}_k, \mathbf{Y})$ i.e.,

$$\mathbf{S}_k = \mathbf{H}_{x,k}\underline{\tilde{\mathbf{S}}}_k + \mathbf{h}_{x,k}\mathbf{1}_N^T, \tag{5.36}$$

$$\mathbf{Y} = \mathbf{H}_y\underline{\mathbf{Y}} + \mathbf{h}_y\mathbf{1}_N^T, \tag{5.37}$$

where $\underline{\tilde{\mathbf{S}}}_k$ is the relative position matrix of the nodes at t_k up to a rotation $\mathbf{H}_{x,k} \in \mathbb{R}^{P \times P}$ and translation $\mathbf{h}_{x,k} \in \mathbb{R}^{P \times 1}$. Along similar lines, we define relative velocity as $\mathbf{H}_y\underline{\mathbf{Y}}$ and relative velocity up to a rotation as $\underline{\mathbf{Y}}$, where $\mathbf{H}_y \in \mathbb{R}^{P \times P}$ is an unknown rotation matrix. The relative velocity of the nodes $\mathbf{H}_y\underline{\mathbf{Y}}$ is relative to the group velocity of the network, which is $\mathbf{h}_y \in \mathbb{R}^{P \times 1}$. Under a linear velocity assumption (5.29), the group velocity is the rate at which the translation vector varies with time i.e.,

$$\mathbf{h}_y = \Delta t_k^{-1}(\mathbf{h}_{x,k} - \mathbf{h}_{x,0}). \tag{5.38}$$

Furthermore, the rotation matrices $\mathbf{H}_{x,k}, \mathbf{H}_y$ are orthogonal i.e.,

$$\mathbf{H}_{x,k}^T \mathbf{H}_{x,k} = \mathbf{H}_y^T \mathbf{H}_y = \mathbf{I}_p. \tag{5.39}$$

Substituting (5.36) and (5.37) in (5.30), and using the property (5.38) we have

$$\mathbf{H}_{x,k}\tilde{\underline{\mathbf{S}}}_k = \mathbf{H}_{x,0}\underline{\mathbf{X}} + \Delta t_k \mathbf{H}_y \underline{\mathbf{Y}}, \tag{5.40}$$

where we use $\underline{\mathbf{X}} \triangleq \tilde{\underline{\mathbf{S}}}_0$ to denote the relative position matrix at t_0. Note that the translation vectors $\mathbf{h}_{x,k}, \mathbf{h}_y$ are unidentifiable from observations (5.35). Subsequently, we shall also see in the following section, that the solution to the relative PVs are independent of the translation vectors $\mathbf{h}_x, \mathbf{h}_y$ and hence without loss of generality can be considered to be $\mathbf{0}_P$ for notational simplicity. Secondly, in order to have a meaningful interpretation of the relative position at the kth time instant (5.40), we must choose a reference coordinate system e.g., $\mathbf{H}_{x,0} = \mathbf{I}$. To this end, without loss of generality and for notational simplicity, we make the following assumptions

$$\mathbf{H}_{x,0} = \mathbf{I}_P, \tag{5.41a}$$
$$\mathbf{h}_{x,0} = \mathbf{0}_P, \tag{5.41b}$$
$$\mathbf{h}_y = \mathbf{0}_P. \tag{5.41c}$$

Applying these assumptions on (5.40), we have

$$\boxed{\underline{\mathbf{S}}_k = \underline{\mathbf{X}} + \Delta t_k \mathbf{H}_y \underline{\mathbf{Y}}} \tag{5.42}$$

where $\underline{\mathbf{S}}_k \triangleq \mathbf{H}_{x,k}\tilde{\underline{\mathbf{S}}}_k$ is the relative position of the nodes at the kth time instant up to a translation and rotation, under the assumption (5.41). The above is the relative linear counterpart of the absolute linear model presented in (5.30). More significantly, observe that the relative position at each kth time instant is only dependent on the instantaneous relative PV and $\mathbf{H}_y$. In the following sections, we estimate $\underline{\mathbf{X}}, \underline{\mathbf{Y}}$ and $\mathbf{H}_y$ using the range parameters $(\mathbf{R}, \dot{\mathbf{R}}, \ddot{\mathbf{R}})$, which was previously defined in (5.35) and estimated in Section 5.3.

5.4.4   Relative kinematic matrices

Substituting the affine transformation of the absolute PV from (5.36) and (5.37) in (5.35), we have

$$
\begin{aligned}
\mathbf{B}_{xx} &= \mathbf{PX}^T\mathbf{XP} = \mathbf{PX}^T\mathbf{H}_{x,0}^T\mathbf{H}_{x,0}\mathbf{XP} = \underline{\mathbf{X}}^T\underline{\mathbf{X}}, & (5.43a)\\
\mathbf{B}_{xy} &= \mathbf{P}(\mathbf{X}^T\mathbf{Y} + \mathbf{Y}^T\mathbf{X})\mathbf{P} \\
&= \mathbf{P}(\underline{\mathbf{X}}^T\mathbf{H}_{x,0}^T\mathbf{H}_y\underline{\mathbf{Y}} + \underline{\mathbf{Y}}^T\mathbf{H}_y^T\mathbf{H}_{x,0}\underline{\mathbf{X}})\mathbf{P} \\
&= \underline{\mathbf{X}}^T\mathbf{H}_y\underline{\mathbf{Y}} + \underline{\mathbf{Y}}^T\mathbf{H}_y^T\underline{\mathbf{X}}, & (5.43b)\\
\mathbf{B}_{yy} &= \mathbf{PY}^T\mathbf{YP} = \mathbf{PY}^T\mathbf{H}_y^T\mathbf{H}_y\mathbf{YP} = \underline{\mathbf{Y}}^T\underline{\mathbf{Y}}, & (5.43c)
\end{aligned}
$$

where we use the property (5.39) in (5.43a) and (5.43c), and the assumption (5.41a) in (5.43b). $\mathbf{B}_{xx}$ and $\mathbf{B}_{yy}$ are Gramian matrices of the relative PVs and the expression for $\mathbf{B}_{xy}$ is the generalized Lyapunov-like linear matrix equation [Penzl 1998]. It is worth noting that the relative kinematic equations $\mathbf{B}_{xx}, \mathbf{B}_{xy}, \mathbf{B}_{yy}$ are dependent only on the relative PVs and the unique rotation matrix $\mathbf{H}_y$ at time t_0. For an alternative derivation of the relative kinematic matrices, refer to Appendix 5.B.

Given an estimate of the range matrices, i.e., $\hat{\mathbf{R}}, \dot{\hat{\mathbf{R}}}, \ddot{\hat{\mathbf{R}}}$, either using (5.23) or alternative methods, an estimate of the relative kinematic matrices, i.e., $\hat{\mathbf{B}}_{xx}, \hat{\mathbf{B}}_{xy}, \hat{\mathbf{B}}_{yy}$ can be readily obtained using (5.34). Using these relative kinematic matrices, we aim to estimate the relative position $\underline{\mathbf{X}}$, the relative velocity $\underline{\mathbf{Y}}$ and the unknown velocity rotation matrix $\mathbf{H}_y$ from (5.43a), (5.43c) and (5.43b) respectively.

5.5   Estimation of first-order relative kinematics

5.5.1   Relative position and velocity

The relative PV can be directly obtained by the spectral decomposition of the matrices $\mathbf{B}_{xx}, \mathbf{B}_{yy}$. Let

$$
\begin{aligned}
\hat{\mathbf{B}}_{xx} &= \mathbf{U}_x\mathbf{\Lambda}_x\mathbf{U}_x^T, & (5.44)\\
\hat{\mathbf{B}}_{yy} &= \mathbf{U}_y\mathbf{\Lambda}_y\mathbf{U}_y^T, & (5.45)
\end{aligned}
$$

where $\mathbf{U}_x, \mathbf{U}_y \in \mathbb{R}^{N\times N}$ contain the eigenvectors and the diagonal matrices $\mathbf{\Lambda}_x, \mathbf{\Lambda}_y \in \mathbb{R}^{N\times N}$ contain the increasingly ordered eigenvalues of the matrices $\hat{\mathbf{B}}_{xx}, \hat{\mathbf{B}}_{yy}$ respectively. Then, for a P-dimensional setup, an estimate of the relative positions $\underline{\mathbf{X}}$

and relative velocities $\underline{\mathbf{Y}}$ of the nodes up to a rotation is then

$$\hat{\underline{\mathbf{X}}} = \boldsymbol{\Lambda}_x^{1/2} \underline{\mathbf{U}}_x^T, \qquad (5.46)$$

$$\hat{\underline{\mathbf{Y}}} = \boldsymbol{\Lambda}_y^{1/2} \underline{\mathbf{U}}_y^T, \qquad (5.47)$$

where $\underline{\boldsymbol{\Lambda}}_x, \underline{\boldsymbol{\Lambda}}_y \in \mathbb{R}^{P \times P}$ contain the first P nonzero eigenvalues and $\underline{\mathbf{U}}_x, \underline{\mathbf{U}}_y \in \mathbb{R}^{N \times P}$ contain the corresponding eigenvectors.

Relative positioning (5.46) from pairwise distance measurements using MDS is a well known technique [Borg and Groenen 2005]. However, our contribution is the definition and estimation of relative velocities , i.e., (5.37) and (5.47) respectively.

5.5.2 Rotation matrix

The estimate of the relative velocity $\underline{\mathbf{Y}}$ up to an arbitrary rotation gives no information on the direction of node mobility in Euclidean space. Hence, it is important to find the relative velocities w.r.t. the orientation of the initial positions i.e., $\mathbf{H}_y$. Substituting the estimates of $\mathbf{B}_{xy}, \underline{\mathbf{X}}, \underline{\mathbf{Y}}$ from (5.34b), (5.46) and (5.47) respectively in (5.43b), we have

$$\hat{\mathbf{B}}_{xy} = \hat{\underline{\mathbf{X}}}^T \mathbf{H}_y \hat{\underline{\mathbf{Y}}} + \hat{\underline{\mathbf{Y}}}^T \mathbf{H}_y^T \hat{\underline{\mathbf{X}}}, \qquad (5.48)$$

where $\mathbf{H}_y$ is the unknown rotation matrix. Now, vectorizing (5.48) and rearranging the terms, we have

$$\begin{aligned} \hat{\mathbf{b}}_{xy} &= (\hat{\underline{\mathbf{Y}}}^T \otimes \hat{\underline{\mathbf{X}}}^T) \operatorname{vec}(\mathbf{H}_y) + (\hat{\underline{\mathbf{X}}}^T \otimes \hat{\underline{\mathbf{Y}}}^T) \operatorname{vec}(\mathbf{H}_y^T) \\ &= (\mathbf{I}_{N^2} + \mathbf{J})(\hat{\underline{\mathbf{Y}}}^T \otimes \hat{\underline{\mathbf{X}}}^T) \operatorname{vec}(\mathbf{H}_y) \\ &= \hat{\mathbf{G}} \operatorname{vec}(\mathbf{H}_y), \end{aligned} \qquad (5.49)$$

where $\hat{\mathbf{b}}_{xy} = \operatorname{vec}(\hat{\mathbf{B}}_{xy})$ is a vector of the known measurement matrix $\hat{\mathbf{B}}_{xy}$ from (5.35b) and $\mathbf{J} \in \mathbb{R}^{N^2 \times N^2}$ is an orthogonal permutation matrix such that $\mathbf{J} \operatorname{vec}(\mathbf{H}_y) = \operatorname{vec}(\mathbf{H}_y^T)$. Let $\hat{\mathbf{H}}_y$ be an estimate of $\mathbf{H}_y$, the unknown rotation can be obtained by minimizing the cost function

$$\hat{\mathbf{H}}_y = \arg \min_{\mathbf{H}_y} \|\hat{\mathbf{G}} \operatorname{vec}(\mathbf{H}_y) - \hat{\mathbf{b}}_{xy}\|^2. \qquad (5.50)$$

Since both $\hat{\mathbf{G}}$ and $\hat{\mathbf{b}}_{xy}$ are plagued with errors, we propose a Total Least Squares solution. Let the singular value decomposition of the augmented matrix $\begin{bmatrix} \hat{\mathbf{G}} & \mathbf{b}_{xy} \end{bmatrix}$ be

$$\begin{bmatrix} \hat{\mathbf{G}} & \mathbf{b}_{xy} \end{bmatrix} = \begin{bmatrix} \mathbf{U}_{s1} & \mathbf{U}_{s2} \end{bmatrix} \begin{bmatrix} \boldsymbol{\Lambda}_s & \\ & \mathbf{0} \end{bmatrix} \begin{bmatrix} \mathbf{V}_{s11} \mathbf{V}_{s12} \\ \mathbf{V}_{s21} \mathbf{V}_{s22} \end{bmatrix}^T,$$

then the total least squares solution for minimizing the cost function (5.50) is

$$\text{vec}(\hat{\mathbf{H}}_y) = -\mathbf{V}_{s12}\mathbf{V}_{s22}^{-1}, \tag{5.51}$$

which has a feasible solution for $N > P$ [Lawson and Hanson 1974]. The proposed solution does not exploit the orthogonality property of the unknown rotation matrix $\mathbf{H}_y$. Hence, more optimal solutions are feasible by solving the constrained least squares problem on the Stiefel manifold [Viklands 2006], such as solving the following cost function

$$\min_{\mathbf{H}_y} \|\hat{\mathbf{G}}\text{vec}(\mathbf{H}_y) - \hat{\mathbf{b}}_{xy}\|^2 \quad \text{s.t} \quad \mathbf{H}_y^T\mathbf{H}_y = \mathbf{I}_P, \tag{5.52}$$

which is beyond the scope of this article and will be addressed in a follow-up work.

5.6 Cramér-Rao Bounds

The Cramér-Rao Bounds (CRB) for relative positioning were studied in [Ash and Moses 2008; Chang and Sahai 2006], however the Fisher Information Matrix (FIM) for a general P-dimensional anchorless network was not investigated, which we present here. Furthermore, we also derive a lower bound for the proposed relative velocity estimator.

The CRB for any unbiased estimate of the unknown relative PVs

$$
\begin{aligned}
\boldsymbol{\phi}_x \triangleq \text{vec}(\underline{\mathbf{X}}) &= \left[\underline{\mathbf{x}}_1^T, \underline{\mathbf{x}}_2^T, \ldots, \underline{\mathbf{x}}_N^T\right]^T \in \mathbb{R}^{NP \times 1}, & (5.53) \\
\boldsymbol{\phi}_y \triangleq \text{vec}(\underline{\mathbf{Y}}) &= \left[\underline{\mathbf{y}}_1^T, \underline{\mathbf{y}}_2^T, \ldots, \underline{\mathbf{y}}_N^T\right]^T \in \mathbb{R}^{NP \times 1}, & (5.54)
\end{aligned}
$$

are given by the inverse of the respective FIM i.e.,

$$\text{Tr}\left(\mathbb{E}\left\{(\hat{\boldsymbol{\phi}}_x - \boldsymbol{\phi}_x)(\hat{\boldsymbol{\phi}}_x - \boldsymbol{\phi}_x)^T\right\}\right) \triangleq \text{Tr}(\boldsymbol{\Sigma}_x) \geq \text{Tr}(\mathbf{F}_x^\dagger), \tag{5.55}$$

$$\text{Tr}\left(\mathbb{E}\left\{(\hat{\boldsymbol{\phi}}_y - \boldsymbol{\phi}_y)(\hat{\boldsymbol{\phi}}_y - \boldsymbol{\phi}_y)^T\right\}\right) \triangleq \text{Tr}(\boldsymbol{\Sigma}_y) \geq \text{Tr}(\mathbf{F}_y^\dagger), \tag{5.56}$$

where $\{\hat{\boldsymbol{\phi}}_x, \hat{\boldsymbol{\phi}}_y\}$ are estimates of the unknown relative PVs $\{\boldsymbol{\phi}_x, \boldsymbol{\phi}_y\}$ and $\{\boldsymbol{\Sigma}_x, \boldsymbol{\Sigma}_y\}$ are the corresponding lowest achievable covariances. The FIMs for relative PVs $\mathbf{F}_x, \mathbf{F}_y$ are derived in Appendix 5.C and Appendix 5.D respectively.

The derived FIMs are singular in the absence of anchor information. More specifically, for a $2-$dimensional network the FIM for relative positions and relative

velocities are rank deficient by 3. Since the FIM are not invertible, we use the pseudoinverse of the FIM as a lower bound to verify the optimality of the proposed estimators. Such scenarios arise in reference-free clock estimation [Rajan and van der Veen 2015], anchor-deficient localization [Chang and Sahai 2006], blind channel estimation [Carvalho, Cioffi and Slock 2000] and array calibration [Wijnholds and van der Veen 2006] to name a few, where the inverse of the rank-deficient FIM is replaced by the pseudoinverse. This approach can be reasoned by investigating the CRB for a constrained framework.

When the FIM is singular, a set of linearly independent constraints, say $\mathbf{C}$, is required on the unknown parameters to obtain the CRB. Let $\mathbf{U}_c$ be an orthonormal basis for the null space of this constraint matrix $\mathbf{C}$, then the CRB for the constrained scenario is given by $\mathrm{Tr}\left(\mathbf{U}_c\left(\mathbf{U}_c^T\mathbf{U}_c\right)^{-1}\mathbf{U}_c^T\right)$ [Stoica and Ng 1998]. Now, let $\mathbf{F} \triangleq \mathbf{U}_f\boldsymbol{\Lambda}_f\mathbf{U}_f^T$ be the eigenvalue decomposition of the singular FIM. Then, the constrained CRB is lowest when the $\mathbf{U}_c$ spans the range of $\mathbf{F}$ [Carvalho, Cioffi and Slock 2000], which simplifies the CRB to $\mathrm{Tr}\left(\boldsymbol{\Lambda}_f^{\dagger}\right)$, where $\boldsymbol{\Lambda}_f^{\dagger}$ is obtained by taking the reciprocal of each non-zero elements along the diagonal and leaving the zeros in place. Observe that the pseudoinverse of the singular FIM yields exactly the same expression i.e., $\mathrm{Tr}\left(\left(\mathbf{U}_f\boldsymbol{\Lambda}_f\mathbf{U}_f^T\right)^{\dagger}\right) = \mathrm{Tr}\left(\boldsymbol{\Lambda}_f^{\dagger}\right)$. Thus, among the set of all feasible linearly independent constraints, the pseudo-inverse of the unconstrained FIM yields the lowest value for the total variance on all estimated parameters. There exists no unbiased estimator which achieves this bound without apriori knowledge or additional constraints on the system, and hence the bounds (5.55, 5.56) are termed *oracle-bounds*.

5.7 Relative positions over time

We now briefly summarize the steps to find the relative position at discrete time instances using the time stamp measurements discussed in Section 5.2.

5.7.1 Linearized MDS (LMDS)

Given the noisy time stamps $\hat{T}_{ij,k} = T_{ij,k} + q_{i,k}, \forall\,(i,j)$ node pairs in the network and $\forall\,1 \leq k \leq K$ time instances, the relative position of the nodes at the kth time instance can be estimated as follows.

1. Estimate the Range derivatives $\hat{\mathbf{R}}, \hat{\dot{\mathbf{R}}}, \hat{\ddot{\mathbf{R}}}$

    a) using dynamic ranging (5.23) and/or

b) via Doppler measurements and/or by other means.

2. Using these range derivatives, construct the relative kinematic matrices $\hat{\mathbf{B}}_{xx}$, $\hat{\mathbf{B}}_{xy}$, $\hat{\mathbf{B}}_{yy}$ (5.34a).

3. Obtain an estimate of the relative position $\underline{\mathbf{X}}$, relative velocity $\underline{\mathbf{Y}}$ and rotation matrix $\mathbf{H}_y$ from (5.36), (5.37) and (5.51) respectively.

4. Defining $\Delta \hat{t}_k = \hat{T}_{ij,k} - \hat{T}_{ij,0}$ and using (5.42), the relative position at the kth time instant is

$$\hat{\underline{\mathbf{S}}}_{k,lmds} = \hat{\underline{\mathbf{X}}} + \Delta \hat{t}_k \hat{\mathbf{H}}_y \hat{\underline{\mathbf{Y}}}. \tag{5.57}$$

5.7.2   Connected MDS (CMDS)

Alternatively, the relative positions of the nodes can also be estimated using MDS at each time instant. Let $\mathbf{D}_k \triangleq c[\tau_{ij,k}] \in \mathbb{R}^{N \times N}$ be the Euclidean Distance Matrix (EDM) at each discrete time instant k where $\tau_{ij,k} = E_{ij,k}(T_{ij,k} - T_{ji,k})$ (5.8). Furthermore, let $\hat{\mathbf{D}}_k \triangleq c[\tau_{ij,k} + q_{ij,k}]$ be the corresponding noisy distance estimate where $q_{ij,k}$ is the noise plaguing the measurements as shown in (5.12). Let $-0.5\mathbf{P}(\hat{\mathbf{D}}_k^{\odot 2})\mathbf{P} = \bar{\mathbf{U}}_k \bar{\mathbf{\Lambda}}_k \bar{\mathbf{U}}_k^T$ be an eigenvalue decomposition, then the solution to the relative position is

$$\hat{\underline{\mathbf{S}}}_{k,cmds} = \bar{\mathbf{\Lambda}}_k^{1/2} \bar{\underline{\mathbf{U}}}_k^T, \tag{5.58}$$

where $\bar{\mathbf{\Lambda}}_k \in \mathbb{R}^{P \times P}$ contains the first P nonzero eigenvalues and $\bar{\underline{\mathbf{U}}}_k \in \mathbb{R}^{N \times P}$ the corresponding eigenvectors.

The relative position estimate using CMDS i.e., $\hat{\underline{\mathbf{S}}}_{k,cmds}$ is up to an arbitrary rotation and translation, unlike $\hat{\mathbf{S}}_{k,lmds}$ which yields the relative position of the nodes up to a translation alone. Hence to align all the relative position estimates (5.58), a unique rotation matrix at each time instant k must be estimated. Under constant velocity assumption, note that

$$\mathbf{S}_{k-1} - 2\mathbf{S}_k + \mathbf{S}_{k+1} = \mathbf{0}_P,$$

and using (5.36) and multiplying by $\mathbf{H}_k^T$, we have

$$\mathbf{H}_k^T \mathbf{H}_{k-1} \underline{\mathbf{X}}_{k-1} - 2\underline{\mathbf{S}}_k + \mathbf{H}_k^T \mathbf{H}_{k+1}^T \underline{\mathbf{S}}_{k+1} = \mathbf{0}_{P,N}.$$

Now, substituting the relative position estimates from (5.58), we have

$$\overbrace{\left[\hat{\underline{\mathbf{S}}}_{k-1,cmds}^T \quad \hat{\underline{\mathbf{S}}}_{k+1,cmds}^T\right]}^{\hat{\mathbf{A}}_k} \overbrace{\begin{bmatrix} \mathbf{H}_k^T \mathbf{H}_{k-1} \\ \mathbf{H}_k^T \mathbf{H}_{k+1} \end{bmatrix}}^{\mathbf{\Theta}_k} = 2\hat{\underline{\mathbf{S}}}_{k,cmds}^T,$$

Algorithm	DR	MDS	Rotation	FLOPS
CMDS	−	K	K	$K(12N^3 + 4NP^4 + 8P^6)$
LMDS	−	2	1	$24N^3 + 4NP^2 + 8P^3$
LMDS-DR	1	2	1	$2KN^2L^2 + 24N^3 + 4NP^2 + 8P^3$

Table 5.1: Computational complexity of proposed estimators, namely connected multidimensional scaling (CMDS), linear multidimensional scaling (LMDS) and LMDS with dynamic ranging (DR).

where $\mathbf{\Theta}_k$ containing the unknown rotation matrices can be estimated by minimizing the l_2 norm

$$\hat{\mathbf{\Theta}}_k = \arg\min_{\mathbf{\Theta}_k} \|\hat{\mathbf{A}}_k \mathbf{\Theta}_k - 2\hat{\mathbf{S}}_{k,cmds}^T\|^2, \tag{5.59}$$

which similar to (5.50), has a solution for $N > P$. We name the estimation of relative positions (5.58) and the subsequent rotation matrices (5.59) under constant velocity assumption as Connected MDS (CMDS).

5.7.3 Computational complexity

The computational complexity of the proposed estimators are listed in Table. 5.1. We evaluate the computation costs based on floating point operationS (FLOPS), ignoring the negligibly less complex additions and subtractions. The columns indicate the algorithms, the number of executions for various methods and the total number of FLOPS for each algorithm. To implement dynamic ranging i.e., least squares estimator, we assume the Gram-Schmidt method. In case of MDS and Rotation matrix estimation we use the Golub-Reinsch based singular value decomposition [Golub and Van Loan 2012]. Observe that, in contrast to the CMDS which estimates the relative position and corresponding rotation matrices for all K time instances, the proposed LMDS estimator estimates only the relative position, relative velocity and a single rotation matrix. Furthermore, the CMDS estimates 2 rotation matrices at each time instant (5.59) and hence has a factor P^2 more complexity in rotation matrix estimation. Overall, the LMDS shows clear advantage, as it reduces the use of the expensive Eigenvalue decomposition for MDS and total least squares for rotation matrix estimation, in comparison to the CMDS algorithm.
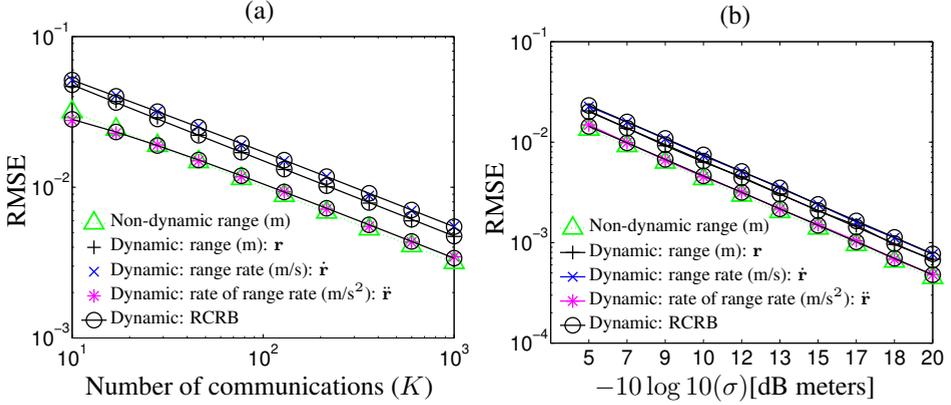
Figure 5.2: ***RMSEs of range parameters*** (a) for varying number of communications (K) between the nodes for $\sigma = 1$ meter and (b) for varying noise (σ) on the time measurements with number of communication $K = 10$.

5.8 Simulations

Simulations are conducted to evaluate the performance of the proposed solutions. We consider a cluster of $N = 5$ nodes in $P = 2$ dimensions, whose coordinates $\mathbf{X}$ and velocities $\mathbf{Y}$ are arbitrarily chosen as

$$\mathbf{X} = \begin{bmatrix} -629 & 311 & 123 & -503 & 297 \\ -812 & 929 & 237 & 490 & -662 \end{bmatrix} \text{meters},$$

$$\mathbf{Y} = \begin{bmatrix} -5 & 5 & 4 & -5 & -2 \\ -8 & -9 & 2 & -5 & 5 \end{bmatrix} \text{meters/second}.$$

Without loss of generality, we assume that all nodes employ one-way communication, i.e., $\mathbf{e}_{ij} = \mathbf{1}_K, \forall\, i, j \leq N$. Furthermore, all nodes communicate with each other within the time interval $\Delta T = [T_{ij,1}, T_{ij,K}] = [-2.5, 2.5]$ seconds and the transmit time markers are chosen to be linearly spaced within this interval. We consider a classical pairwise communication scenario, where all the pairwise communications are independent of each other and thus $\boldsymbol{\Sigma} = \sigma^2 \mathbf{I}_{\bar{N}K}$.

The metric used to evaluate the performance of the distances and range parameters is the Root Mean Square Error (RMSE), given by

$$\text{RMSE}(\mathbf{z}) = \sqrt{N_{exp}^{-1} \sum_{n=1}^{N_{exp}} \|\hat{\mathbf{z}}(n) - \mathbf{z}\|^2}, \tag{5.60}$$

where $\hat{\mathbf{z}}(n)$ is the nth estimate of the unknown vector $\mathbf{z}$ during $N_{exp} = 1000$ Monte Carlo runs. To qualify these estimates, the square Root of the Cramér-Rao Bound (RCRB) is plotted along with the respective RMSE. We also use the same metric for evaluating the rotation $\text{vec}(\mathbf{H}_y)$. In contrast to the range parameters, the relative PVs $(\underline{\mathbf{X}}, \underline{\mathbf{Y}})$ and $\mathbf{X}_k$ are known only up to an arbitrary rotation. Hence, we define the RMSE for these matrices as

$$\text{RMSE}(\mathbf{Z}) = \sqrt{N_{exp}^{-1} \sum_{n=1}^{N_{exp}} \|\text{vec}(\mathbf{H}\hat{\mathbf{Z}}(n) - \mathbf{Z}\mathbf{P})\|^2}, \qquad (5.61)$$

where $\mathbf{P}$ is the centering matrix and $\mathbf{H}$ is the optimal Procrustes rotation, given the matrix $\mathbf{Z}$ and the corresponding estimate $\hat{\mathbf{Z}}(n)$ of the nth Monte Carlo run. *See 5.E.* The RCRBs derived for the relative PVs (Section 5.6) are plotted along with the corresponding RMSEs.

5.8.1   Range parameters

The dynamic ranging algorithm (5.23) is implemented for $L = 4$, where the number of communications K is varied from 10 to 1000. The noise on the propagation delays is $\sigma = 0.1$ meters, which is typical in classical TWR [Patwari et al. 2003] or in conventional anchored MDS-based velocity estimation using Doppler measurements [Wei et al. 2010]. Figure 5.2 shows the RMSE of the first 3 range coefficients (which are relevant for estimating the relative positions and velocities) . A second experiment is carried out by varying σ in the range $[-20, -5]$ dB meters for a fixed number of communications $K = 500$. For the sake of comparison, we also plot the range estimate for the 'non-dynamic' scenario, where the nodes are immobile and the range between the nodes is fixed over the measurement period i.e., for $\mathbf{Y} = \mathbf{0}_{2,N}$. The RMSEs of the range coefficients obtained via the dynamic ranging algorithm (5.23) are plotted in Figure 5.2. In both these experiments, the RMSEs of these range parameters achieve the corresponding RCRBs asymptotically for $L = 4$. Without loss of generality, we assume that the order of approximation is known, since iterative solutions such as iMGLS [Rajan and van der Veen 2015] can be employed to estimate L. For a detailed discussion on the effect of L on the distance estimation, particularly for an unsynchronized network, please refer to the Chapter 4 [Rajan and van der Veen 2015].
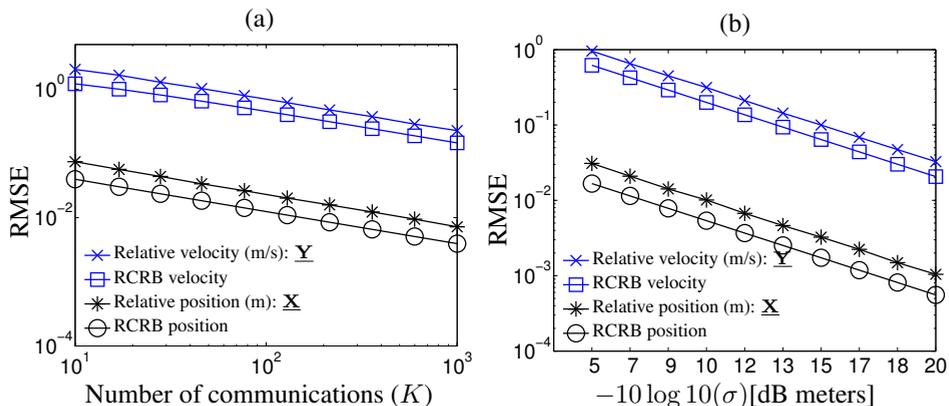
Figure 5.3: ***RMSEs of relative positions and velocities*** (a) for varying number of communications (K) between the nodes for $\sigma = 1$ meter and (b) for varying noise (σ) on the time measurements with number of communication $K = 10$.

5.8.2   Relative positions, velocities and rotation

The range parameters obtained via dynamic ranging are used to estimate the relative PV from (5.46) and (5.47). Figure 5.3(a) shows the RMSEs of the PV plotted along with the respective RCRBs, for varying number of two-way communications K and Figure 5.3(b) shows the RMSE plots for the relative PVs for varying signal-to-noise ratio. For the given experimental setup, the estimates are shown to perform reasonably well against the derived oracle-bounds. Furthermore, it is observed that the performance of the relative velocity is poorer in comparison to the relative positions. This is primarily because the measurement matrix for the relative velocity estimation $\mathbf{B}_{yy}$ is dependent on $\mathbf{R}, \dot{\mathbf{R}}, \ddot{\mathbf{R}}$, whereas the relative position estimation relies only on the EDM $\mathbf{R}$. Hence, we observe that the magnitude of the noise covariance on the velocity model $\mathbf{\Sigma}_{\eta y}$ (5.83) is much larger than that of the position model $\mathbf{\Sigma}_{\eta x}$ (5.75). However, improved solutions can be expected if the Doppler measurements are made available, which is not investigated here and is beyond the scope of this chapter. The RMSEs of the relative rotation matrix $\mathbf{H}_y$ estimate (5.51) are plotted in Figure 5.4, where the relative PV estimates are used.

5.8.3   Relative position over time t_k

To illustrate the benefits of jointly estimating the relative PVs of the network, we simulate the proposed LMDS and CMDS algorithms. The relative PV and the rotation matrix estimates are used to realize the relative position of the nodes across time
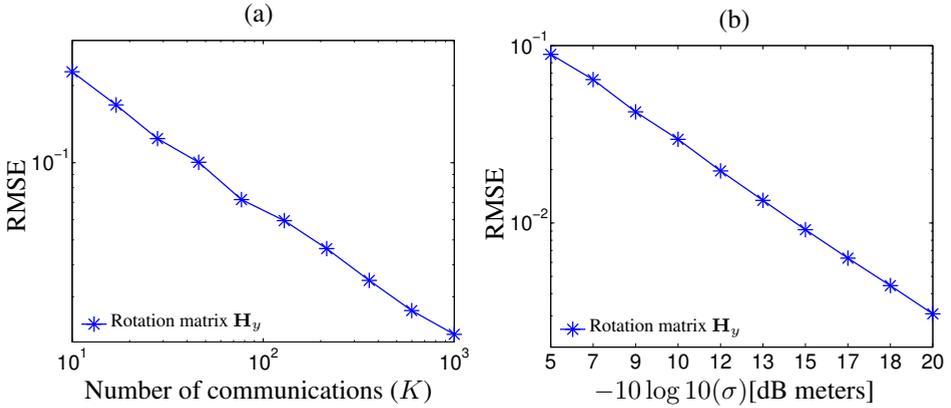
Figure 5.4: ***RMSEs of rotation matrix*** (a) for varying number of communications (K) between the nodes for $\sigma = 1$ meters and (b) for varying noise (σ) on the time measurements with number of communication $K = 10$.

using LMDS (5.57). For the sake of comparison, the CMDS solution is also evaluated by estimating the relative positions using MDS (5.58) and the corresponding rotation matrix (5.59) at each time instant t_k. Figure 5.5(a) shows the RMSE plots for $\underline{\mathbf{X}}_{k,\text{cmds}}$ and $\mathbf{X}_{k,\text{lmds}}$ around the region of interest i.e., $t_0 = 0$ with Gaussian noise of $\sigma = 0.1$ meters and varying communication links $K = [100, 300, 500]$. Secondly, for a fixed $K = 500$, the signal-to-noise ratio is varied $\sigma = [-3\text{dB}, -10\text{dB}, -20\text{dB}]$ and the LMDS is compared against CMDS in Figure 5.5(b). The $\underline{\mathbf{X}}_{k,\text{cmds}}$ estimate steadily achieves a constant RMSE, which is expected since CMDS is independently applied at each kth time instant. On the contrary, the relative position estimation via dynamic ranging betters this estimate around t_0, where the improvement of up to a factor $\sqrt{K}$ is primarily due to averaging over K measurements. However, the error estimate of $\underline{\mathbf{X}}_{k,\text{lmds}}$ increases as we move away from t_0, which is typical of Taylor series approximation. Note that, without loss of generality the range derivatives can be estimated in general for any t_0 along the time interval. Hence, the relative PVs can be jointly estimated along the time-line, yielding improved solutions compared to CMDS at any given time instant.

5.9 Conclusions

We proposed a novel relative localization framework for an anchorless network of mobile nodes, given only the time-varying pairwise distances. Given the inter-nodal
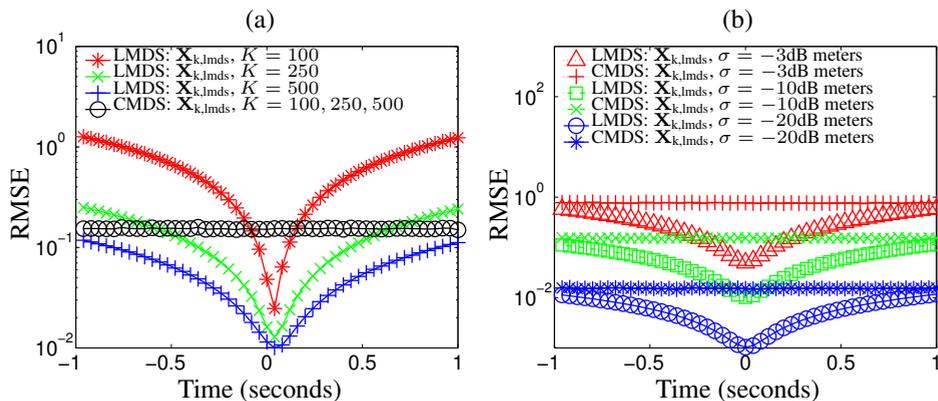
Figure 5.5: **_RMSE of relative positions over time_** t_k around $t_0 = 0$ (a) for $K = [100, 250, 500]$ communication links with noise on time measurements $\sigma = 1$ meters and (b) for varying signal-to-noise ratio $\sigma = [-3, -10, -20]$ dB meter with fixed $K = 500$.

distances over time, the dynamic ranging algorithm employs a classical Taylor series based approximation, which extracts pairwise distance derivatives at any given time instant efficiently. Under linear velocity assumption, these derivatives are used to jointly estimate the initial relative PVs and a unique rotation matrix. We propose the LMDS algorithm, which combines the relative PVs and the rotation matrix to beget the relative motion of the nodes at discrete time instances. The LMDS can be considered as an extension of the well-known MDS. In addition, we also propose the CMDS where the relative node positions and the corresponding rotation matrices are estimated at each time instant. The Cramér-Rao bounds are also derived for the range parameters, and the relative PV and simulations are conducted to verify the performance of the proposed estimators. While the CMDS shows consistent performance over time, the LMDS is computationally cost effective and shows up to a factor $\sqrt{K}$ improvement around the region of interest. Furthermore, the LMDS permits the usage of Doppler measurements if available. The presented solutions are suited for autonomous networks with minimal a priori knowledge, where the positions and velocities need to be estimated at cold start. In practice, over longer durations, the estimated parameters can be readily extended to both relative and absolute tracking, which will be addressed in a follow-up work.

One of the key bottlenecks in the proposed model is the constraint on linear motion of the mobile nodes. In the following chapter, we present a generalized model in search for solutions to higher order kinematics, such as relative acceleration.

Appendix 5.A   Distance non-linearity

Consider an arbitrary pair of of nodes $\{i, j\}$ with initial positions $\{\mathbf{x}_i, \mathbf{x}_j\}$ at $t = t_0$ and constant velocities $\{\mathbf{y}_i, \mathbf{y}_j\}$, then the pairwise distance at $t = t_k$ is

$$
\begin{aligned}
d_{ij,k} &= \|(\mathbf{x}_i - \mathbf{x}_j) - (\mathbf{y}_i - \mathbf{y}_j)t_k\| \\
&= \sqrt{\mathbf{x}_{ij}^T\mathbf{x}_{ij} - \mathbf{y}_{ij}^T\mathbf{y}_{ij}t_k^2 - 2\mathbf{x}_{ij}^T\mathbf{y}_{ij}t_k},
\end{aligned}
\tag{5.62}
$$

where $\mathbf{x}_{ij} = \mathbf{x}_i - \mathbf{x}_j$ and $\mathbf{y}_{ij} = \mathbf{y}_i - \mathbf{y}_j$, which shows the pairwise distance is non-linear in time.

Let $\{\bar{\mathbf{x}}_i(t), \bar{\mathbf{x}}_j(t)\}$ be the time varying positions of the node pair and $d_{ij}(t)$ be the corresponding pairwise distance at time t, then the range parameters are derived as follows. By definition, the pairwise range between the nodes is the Euclidean norm

$$
r_{ij} \triangleq d_{ij}(t_0) = \|\mathbf{x}_i - \mathbf{x}_j\|,
\tag{5.63}
$$

From (5.63), we compute the first-order range parameter as

$$
\begin{aligned}
\dot{r}_{ij} &= \frac{d}{dt}d_{ij}(t) \\
&= \frac{1}{2r_{ij}}\frac{d}{dt}\left((\bar{\mathbf{x}}_i(t) - \bar{\mathbf{x}}_j(t))^T(\bar{\mathbf{x}}_i(t) - \bar{\mathbf{x}}_j(t))\right) \\
&= \frac{1}{r_{ij}}\left(\mathbf{y}_i^T\mathbf{x}_i + \mathbf{y}_j^T\mathbf{x}_j - \mathbf{y}_i^T\mathbf{x}_j - \mathbf{y}_j^T\mathbf{x}_i\right) \\
&= r_{ij}^{-1}(\mathbf{y}_i - \mathbf{y}_j)^T(\mathbf{x}_i - \mathbf{x}_j).
\end{aligned}
\tag{5.64}
$$

Similarly, under the assumption of constant velocities, the second-order range parameter using (5.63) is

$$
\begin{aligned}
\ddot{r}_{ij} &= \frac{d^2}{dt^2}d_{ij}(t) \\
&= -r_{ij}^{-2}\dot{r}_{ij}\left((\mathbf{y}_i - \mathbf{y}_j)^T(\mathbf{x}_i - \mathbf{x}_j)\right) \\
&\quad + r_{ij}^{-1}\frac{d}{dt}\left((\mathbf{y}_i - \mathbf{y}_j)^T(\bar{\mathbf{x}}_i(t) - \bar{\mathbf{x}}_j(t))\right) \\
&= -r_{ij}^{-1}\dot{r}_{ij}^2 + r_{ij}^{-1}(\mathbf{y}_i - \mathbf{y}_j)^T(\mathbf{y}_i - \mathbf{y}_j) \\
&= r_{ij}^{-1}\left(\|\mathbf{y}_i - \mathbf{y}_j\|^2 - \dot{r}_{ij}^2\right).
\end{aligned}
\tag{5.65}
$$

The third-order derivative of the range parameter under linear motion (5.63) yields

$$
\begin{aligned}
\dddot{r}_{ij} &= \frac{d^3}{dt^3} d_{ij}(t) \\
&= -r_{ij}^{-2} \dot{r}_{ij} (\|\mathbf{y}_i - \mathbf{y}_j\|^2 - \dot{r}_{ij}^2) - r_{ij}^{-1} \frac{d^2}{dt^2}(d_{ij}^2(t)) \\
&= -r_{ij}^{-1} \dot{r}_{ij} \ddot{r}_{ij} - 2 r_{ij}^{-1} \dot{r}_{ij} \ddot{r}_{ij} \\
&= -3 r_{ij}^{-1} \dot{r}_{ij} \ddot{r}_{ij}.
\end{aligned}
\tag{5.66}
$$

The higher-order range derivatives can be derived along similar lines.

Appendix 5.B $\quad \mathbf{B}_{xx}, \mathbf{B}_{xy} \, \mathbf{B}_{yy}$

We now present an alternative derivation for $\mathbf{B}_{xx}, \mathbf{B}_{xy} \, \mathbf{B}_{yy}$. With an abuse of notation, let $\mathbf{D}(t) \in \mathbb{R}^{N \times N}$ be the time-varying Euclidean Distance Matrix (EDM) for a network of N nodes in P-dimensional Euclidean space and let

$$
\mathbf{B}(t) = -0.5 \mathbf{P} \mathbf{D}(t)^{\odot 2} \mathbf{P},
\tag{5.67}
$$

where $\mathbf{P} = \mathbf{I}_N - N^{-1} \mathbf{1}_N \mathbf{1}_N^T$ is the centering matrix. Then observe that at $t = t_0$,

$$
\mathbf{B}(t_0) \triangleq \mathbf{B}_{xx} = \underline{\mathbf{X}}^T \underline{\mathbf{X}},
\tag{5.68}
$$

and the subsequent first derivative is

$$
\begin{aligned}
\mathbf{B}_{xy} &\triangleq \frac{d\mathbf{B}(t)}{dt} \triangleq -\mathbf{P} \Big(\mathbf{D}(t) \odot \dot{\mathbf{D}}(t) \Big) \mathbf{P} \Big|_{t=t_0} \\
&= \underline{\mathbf{X}}^T \mathbf{H}_{xy} \underline{\mathbf{Y}} + \underline{\mathbf{Y}}^T \mathbf{H}_{xy}^T \underline{\mathbf{X}}.
\end{aligned}
\tag{5.69}
$$

A step further, differentiating again w.r.t. time and substituting $t = t_0$ we have

$$
\frac{d^2 \mathbf{B}(t)}{dt^2}\Big|_{t=t_0} \triangleq \mathbf{B}_{yy} \triangleq -0.5 \mathbf{P}(\mathbf{R} \odot \ddot{\mathbf{R}} + \dot{\mathbf{R}}^{\odot 2}) \mathbf{P} = \underline{\mathbf{Y}}^T \underline{\mathbf{Y}},
\tag{5.70}
$$

where $\dot{\mathbf{R}} = [\dot{r}_{ij}] \in \mathbb{R}^{N \times N}$ and $\ddot{\mathbf{R}} = [\ddot{r}_{ij}] \in \mathbb{R}_+^{N \times N}$ which, perhaps not surprisingly, concurs with the relations obtained in (5.43) and offers an alternative verification.

Secondly, unlike the time-varying distance function $\mathbf{D}(t)$, which is infinitely differentiable, $\mathbf{B}(t)$ is a second-order function under the linear velocity assumption (5.29). Differentiating (5.70) yet again, we have

$$
\frac{d^3 \mathbf{B}(t)}{dt^3}\Big|_{t=t_0} = -0.5 \mathbf{P}(\mathbf{R} \odot \dddot{\mathbf{R}} + 3 \dot{\mathbf{R}} \odot \ddot{\mathbf{R}}) \mathbf{P} = \mathbf{0}_{N,N},
\tag{5.71}
$$

where

$$\dddot{\mathbf{R}} \triangleq \frac{d^3\mathbf{R}}{dt^3} = -3\mathbf{R}^{-1} \odot \dot{\mathbf{R}} \odot \ddot{\mathbf{R}}. \tag{5.72}$$

Appendix 5.C   FIM of the relative positions

The problem of estimating the unknown positions $\phi_x \triangleq \mathrm{vec}(\underline{\mathbf{X}}) = \left[\underline{\mathbf{x}}_1^T, \underline{\mathbf{x}}_2^T, \ldots, \underline{\mathbf{x}}_N^T\right]^T$ $\in \mathbb{R}^{NP \times 1}$ from the distance measurements is formulated as

$$\mathbf{a}_x(\phi_x) - \mathbf{d}_x = \boldsymbol{\eta}_x, \tag{5.73}$$

where the vector $\mathbf{d}_x = \{r_{ij}\} \forall \, i, j \leq N, \; i \neq j \in \mathbb{R}^{2\bar{N} \times 1}$ is the set of distances between N points, with $\bar{N} = \begin{pmatrix} N \\ 2 \end{pmatrix}$. The distance vector is related to the positions by $\mathbf{a}(\phi_x) = \left[a_x(\underline{\mathbf{x}}_1, \underline{\mathbf{x}}_2), a_x(\underline{\mathbf{x}}_1, \underline{\mathbf{x}}_3), \ldots, a_x(\underline{\mathbf{x}}_{N-1}, \underline{\mathbf{x}}_N)\right]^T \in \mathbb{R}^{2\bar{N} \times 1}$ where,

$$\mathbf{a}_x(\underline{\mathbf{x}}_i, \underline{\mathbf{x}}_j) \triangleq \left(\underline{\mathbf{x}}_i^T \underline{\mathbf{x}}_i + \underline{\mathbf{x}}_j^T \underline{\mathbf{x}}_j - 2\underline{\mathbf{x}}_i^T \underline{\mathbf{x}}_j\right)^{\frac{1}{2}}. \tag{5.74}$$

Furthermore, the noise plaguing the distance vector is

$$\boldsymbol{\eta}_x \sim \mathcal{N}(0, \boldsymbol{\Sigma}_{\eta x}), \quad \text{where} \quad \boldsymbol{\Sigma}_{\eta x} = \mathrm{bdiag}(\boldsymbol{\Sigma}_r, \boldsymbol{\Sigma}_r), \tag{5.75}$$

and $\boldsymbol{\Sigma}_r$ is given by (5.28). For the data model (5.73), the FIM $\mathbf{F}_x \in \mathbb{R}^{NP \times NP}$ is

$$\mathbf{F}_x = \left[\frac{\partial \mathbf{a}_x(\phi_x)}{\partial \phi_x^T}\right]^T \boldsymbol{\Sigma}_{\eta x}^{-1} \left[\frac{\partial \mathbf{a}_x(\phi_x)}{\partial \phi_x^T}\right]. \tag{5.76}$$

where the Jacobian is of the form

$$\frac{\partial \mathbf{a}_x(\phi_x)}{\partial \phi_x^T} = \left[\frac{\partial \mathbf{a}_x(\phi_x)}{\partial \underline{\mathbf{x}}_1^T}, \frac{\partial \mathbf{a}_x(\phi_x)}{\partial \underline{\mathbf{x}}_2^T}, \ldots, \frac{\partial \mathbf{a}_x(\phi_x)}{\partial \underline{\mathbf{x}}_N^T}\right]. \tag{5.77}$$

The ith element of the Jacobian $\left[\frac{\partial \mathbf{a}_x(\phi)}{\partial \underline{\mathbf{x}}_i^T}\right]$ is given by

$$\left[\frac{\partial a(\underline{\mathbf{x}}_1, \underline{\mathbf{x}}_2)^T}{\partial \underline{\mathbf{x}}_i^T}, \frac{\partial a(\underline{\mathbf{x}}_1, \underline{\mathbf{x}}_3)^T}{\partial \underline{\mathbf{x}}_i^T}, \ldots, \frac{\partial a(\underline{\mathbf{x}}_{N-1}, \underline{\mathbf{x}}_N)^T}{\partial \underline{\mathbf{x}}_i^T}\right],$$

where $\forall 1 \leq j, k \leq N, \; j \neq k$, we have

$$\frac{\partial a(\underline{\mathbf{x}}_j, \underline{\mathbf{x}}_k)}{\partial \underline{\mathbf{x}}_i^T} = \begin{cases} r_{jk}^{-1} \left(\underline{\mathbf{x}}_j - \underline{\mathbf{x}}_k\right)^T & \text{if } i = j & (5.78\text{a}) \\ -r_{jk}^{-1} \left(\underline{\mathbf{x}}_j - \underline{\mathbf{x}}_k\right)^T & \text{if } i = k & (5.78\text{b}) \\ \mathbf{0}_P^T & \text{otherwise.} & (5.78\text{c}) \end{cases}$$

Appendix 5.D   FIM of the relative velocities

The estimation of relative velocities $\phi_x \triangleq \text{vec}(\underline{\mathbf{Y}}) = \left[\underline{\mathbf{y}}_1^T, \underline{\mathbf{y}}_2^T, \ldots, \underline{\mathbf{y}}_N^T\right]^T \in \mathbb{R}^{NP \times 1}$
is modeled as

$$\mathbf{a}_y(\phi_y) - \mathbf{d}_y^{\odot 2} = \boldsymbol{\eta}_y, \tag{5.79}$$

where $\mathbf{a}(\phi_y) = \left[a_y(\underline{\mathbf{y}}_1, \underline{\mathbf{y}}_2), a_y(\underline{\mathbf{y}}_1, \underline{\mathbf{y}}_3), \ldots, a_y(\underline{\mathbf{y}}_{N-1}, \underline{\mathbf{y}}_N)\right]^T \in \mathbb{R}^{2\bar{N} \times 1}$ and

$$a_y(\underline{\mathbf{y}}_i, \underline{\mathbf{y}}_j) \triangleq \underline{\mathbf{y}}_i^T \underline{\mathbf{y}}_i + \underline{\mathbf{y}}_j^T \underline{\mathbf{y}}_j - 2\underline{\mathbf{y}}_i^T \underline{\mathbf{y}}_j. \tag{5.80}$$

The distance squared vector $\mathbf{d}_y^{\odot 2} = \{r_{ij}\ddot{r}_{ij} + \dot{r}_{ij}^{\odot 2}\} \forall\, i, j \leq N, i \neq j \in \mathbb{R}^{2\bar{N} \times 1}$, where $r_{ij}, \dot{r}_{ij}, \ddot{r}_{ij}$ are the corresponding range estimates. The noise $\boldsymbol{\eta}_y = \{\eta_{y,ij}\}$ in the data model is

$$\begin{aligned}
\eta_{y,ij} &= r_{ij}q_{\ddot{r},ij} + \ddot{r}_{ij}q_{r,ij} + 2\dot{r}_{ij}q_{\dot{r},ij} + q_{r,ij}q_{\ddot{r},ij} + q_{\dot{r},ij}q_{\dot{r},ij} \\
&\approx r_{ij}q_{\ddot{r},ij} + \ddot{r}_{ij}q_{r,ij} + 2\dot{r}_{ij}q_{\dot{r},ij},
\end{aligned} \tag{5.81}$$

where $q_{r,ij}, q_{\dot{r},ij}, q_{\ddot{r},ij}$ are the noise variables plaguing the range parameters $r_{ij}, \dot{r}_{ij}, \ddot{r}_{ij}$ respectively. The covariance of the noise is subsequently defined as ,

$$\boldsymbol{\Sigma}_{\eta y} = \mathbb{E}\left\{\boldsymbol{\eta}_y \boldsymbol{\eta}_y^T\right\} \approx \text{bdiag}(\underline{\boldsymbol{\Sigma}}_{\eta y}, \underline{\boldsymbol{\Sigma}}_{\eta y}), \tag{5.82}$$

where

$$\underline{\boldsymbol{\Sigma}}_{\eta y} \approx \underline{\mathbf{R}}\boldsymbol{\Sigma}_{\ddot{r}}\underline{\mathbf{R}} + \underline{\ddot{\mathbf{R}}}\boldsymbol{\Sigma}_r\underline{\ddot{\mathbf{R}}} + 4\underline{\dot{\mathbf{R}}}\boldsymbol{\Sigma}_{\dot{r}}\underline{\dot{\mathbf{R}}}, \tag{5.83}$$

$\underline{\mathbf{R}} = \text{diag}(\mathbf{r})$, $\underline{\dot{\mathbf{R}}} = \text{diag}(\dot{\mathbf{r}})$, $\underline{\ddot{\mathbf{R}}} = \text{diag}(\ddot{\mathbf{r}})$ are the range parameters and $\boldsymbol{\Sigma}_r, \boldsymbol{\Sigma}_{\dot{r}}, \boldsymbol{\Sigma}_{\ddot{r}}$ are the corresponding covariances matrices (5.28). The FIM $\mathbf{F}_y \in \mathbb{R}^{NP \times NP}$ is then

$$\mathbf{F}_y = \left[\frac{\partial \mathbf{a}_y(\phi_y)}{\partial \phi_y^T}\right]^T \boldsymbol{\Sigma}_{\eta y}^{-1} \left[\frac{\partial \mathbf{a}_y(\phi_y)}{\partial \phi_y^T}\right], \tag{5.84}$$

where the Jacobian is of the form

$$\frac{\partial \mathbf{a}_y(\phi_y)}{\partial \phi_y^T} = \left[\frac{\partial \mathbf{a}_y(\phi_y)}{\partial \underline{\mathbf{y}}_1^T}, \frac{\partial \mathbf{a}_y(\phi_y)}{\partial \underline{\mathbf{y}}_2^T}, \ldots, \frac{\partial \mathbf{a}_y(\phi_y)}{\partial \underline{\mathbf{y}}_N^T}\right]. \tag{5.85}$$

The ith element of the Jacobian $\left[\dfrac{\partial \mathbf{a}_y(\phi)}{\partial \underline{\mathbf{y}}_i^T}\right]$ is given by

$$\left[\frac{\partial a(\underline{\mathbf{y}}_1, \underline{\mathbf{y}}_2)^T}{\partial \underline{\mathbf{y}}_i^T}, \frac{\partial a(\underline{\mathbf{y}}_1, \underline{\mathbf{y}}_3)^T}{\partial \underline{\mathbf{y}}_i^T}, \ldots, \frac{\partial a(\underline{\mathbf{y}}_{N-1}, \underline{\mathbf{y}}_N)^T}{\partial \underline{\mathbf{y}}_i^T}\right],$$

where $\forall 1 \le j, k \le N, \; j \ne k$, we have

$$\frac{\partial a(\underline{\mathbf{y}}_j, \underline{\mathbf{y}}_k)}{\partial \underline{\mathbf{y}}_i^T} = \begin{cases} 2\left(\underline{\mathbf{y}}_j - \underline{\mathbf{y}}_k\right)^T & \text{if } i = j \qquad\qquad\quad (5.86\text{a}) \\[2mm] -2\left(\underline{\mathbf{y}}_j - \underline{\mathbf{y}}_k\right)^T & \text{if } i = k \qquad\qquad\quad (5.86\text{b}) \\[2mm] \mathbf{0}_P^T & \text{otherwise.} \qquad\qquad (5.86\text{c}) \end{cases}$$

Appendix 5.E Procrustes alignment

Let $\mathbf{Z}, \underline{\mathbf{Z}} \in \mathbb{R}^{P \times N}$ be matrices identical up to a rotation and let $\mathbf{U}_z$ contain the eigenvectors of the matrix product $\underline{\mathbf{Z}}\mathbf{Z}^T$, then there exists a rotation matrix $\mathbf{H}$ which minimizes the following cost function

$$\min_{\mathbf{H}} \|\mathbf{Z} - \mathbf{H}\underline{\mathbf{Z}}\| \quad \text{s.t.} \quad \mathbf{H}^T\mathbf{H} = \mathbf{I}_P, \qquad\qquad (5.87)$$

and the corresponding optimal *Procrustes rotation* [Schönemann 1966] is

$$\hat{\mathbf{H}} = \mathbf{U}_z \mathbf{U}_z^T. \qquad\qquad (5.88)$$

6

Relative kinematics

The estimation of the location of N points in a P dimensional Euclidean space, given the pairwise distance or proximity measurement, is a principal challenge in a wide variety of fields. Conventionally, the multidimensional scaling algorithm is applied on the Euclidean distance matrix to obtain the relative coordinates upto a rotation and translation. In this chapter, we focus on an anchorless network of mobile nodes, where the distance measurements between the mobile nodes are time-varying in nature and there is no absolute information on the network co-ordinates. The data model discussed in the previous chapter, which relates the time-varying distances to the time-varying relative positions of the anchorless network, is now extended for non-linear motion. In particular, the aim is to estimate the relative position, relative velocity and higher order derivatives of the initial node coordinates, which is cumulatively labeled as relative kinematics. The derived data model is inherently ill-posed, however can be solved using certain relative immobility constraints on a few nodes. Elegant constrained closed form solutions are proposed, to recursively estimate the relative kinematics of the network. For the sake of completeness, we also estimate the absolute kinematics of the nodes given these time-varying distance measurements in the presence of known reference anchors. Cramér-Rao bounds are derived for the new data model and simulations are performed to analyze the performance of the proposed estimators.

6.1 Introduction

Estimating the relative coordinates of N points (or nodes) in a P dimensional Euclidean space using proximity measurements is a fundamental problem spanning a broad range of applications. These applications include, but are not limited to, psychometric analysis [Koehler et al. 2005], perceptual mapping [Ho, MacDorman and Pramono 2008], range-based anchorless localization [Dil, Dulman and Havinga 2006], combinatorial-chemistry [Agrafiotis, Rassokhin and Lobanov 2001], polar-based navigation [Rehm, Klawonn and Kruse 2005], sensor array calibration [Jenkins and Matarić 2004] and in general exploratory data analysis [Borg and Groenen 2005]. In anchorless localization scenarios for instance, nodes heavily rely on co-operative estimation of relative coordinates. Such anchorless networks naturally arise when nodes are inaccessible or only intermittently monitored, as is the case in space-based satellite arrays [Rajan et al. 2016], underwater networks [Chandrasekhar et al. 2006] or indoor wireless sensor networks [Yang, Wu and Liu 2012]. In such reference-free scenarios, the proximity information which is often measured as pairwise distances between the nodes, form a key input to estimating the relative coordinates of nodes.

Multidimensional scaling (MDS) like algorithms are typically employed to estimate the relative coordinates of the cluster, which have been studied rigorously over the past decades [Borg and Groenen 2005; Forero and Giannakis 2012; Young 2013]. However, considerably less attention has been directed towards anchorless mobile scenarios.

Our primary focus in this chapter is on an anchorless network of mobile nodes, where the term anchorless is to indicate no absolute knowledge of the node positions, motion or reference frame. Furthermore, since the nodes are mobile, both the node positions and the pairwise distance measurements between the nodes are time-varying in nature. Our motive is to relate the time-varying pairwise distance measurements to time-derivatives of the node coordinates. For an anchorless network, these include the relative position, relative velocity, relative acceleration and higher-order derivatives which are cumulatively referred to as relative kinematics in this chapter. It is worth noting that the universal definition of relative kinematics inherently relies on the information in the absolute reference frame. For example, the non-relativistic relative velocity between two objects is (rightly) defined as the difference between their respective absolute velocity vectors [Halliday, Resnick and Walker 2010]. In an anchorless framework however, a natural question arises on whether the relative kinematics can be estimated, given only time-varying distance measurements. Ergo, the aim is to understand the relationship between the time-varying distance measurements and the relative kinematics of mobile nodes, which is the goal of this chapter.

6.1.1 Previous work

A key challenge in our pursuit is that both the time-varying distance and the time-varying relative positions are non-linear in nature. In particular, the Euclidean distance between a pair of mobile nodes is almost always a non-linear function of time, even if the nodes are in linear independent motion. Therefore, it is perhaps not surprising that traditional methods to solving such a problem have been state-space based approaches with the assistance of known anchors [Kay 1993]. The initial position of the nodes is estimated using MDS like algorithms, which use the Euclidean distance matrix (EDM) at a single time-instant to estimate the relative node positions. Given this initial estimate, the relative positions are tracked over a period of time with Doppler measurements and known anchors [Wei et al. 2010], or via subspace tracking methods [Jamali-Rad and Leus 2012]. Unfortunately, Doppler measurements and anchor information are not always available. Secondly, subspace tracking is applicable only for small perturbations in motion and offers little insights on the kinematics of motion itself.

In our previous chapter, a two-step solution was proposed to estimate the relative velocities of the nodes from time-varying distance measurements [Rajan, Leus and van der Veen 2015]. Firstly, the derivatives of the time-varying distances were estimated by solving a Vandermonde-like system of linear equations. The estimated regression coefficients (called range parameters) jointly yield the relative velocities and the relative positions, using MDS-like algorithms. However, the proposed solution is valid only for linear motion, which is not always practical. Furthermore, the previously proposed MDS-based relative velocity estimator heavily relies on the second-order time-derivative of distance, and under Gaussian noise assumptions, the proposed estimator performs worse than the well known MDS-based relative position estimator. Thus, more optimal estimators for relative velocity is one of the key motivations for the pursuit of a generalized framework presented in this chapter. Moreover, understanding the higher order relative kinematics of motion in Euclidean space via time-varying distance measurements is crucial for next-generation localization solutions, particularly mobile networks which are only intermittently accessible.

6.1.2   Overview

A novel data model is proposed, which relates the time-varying distances to the kinematics of the mobile nodes in Section 6.2. More specifically, this relationship is established via the derivatives of the time-varying distance, which is estimated using dynamic ranging as discussed in Chapter 5. In Section 6.3 we show that the relationship between the range parameters and the relative kinematics is of the form of a Lyapunov-like set of equations, which is inherently ill-posed. In pursuit of unique solutions, we propose elegant least squares algorithms, which can be solved under certain assumptions. For the sake of completion in Section 6.4, we also propose similar algorithms for estimating the absolute kinematics of the nodes, given known reference parameters in the cluster. To compare the performance of our estimators, we derive constrained Cramér-Rao bounds (CRBs), under Gaussian noise assumption on the data. A optimal choice of the weighting matrix ensures the proposed estimator is the best linear unbiased estimator (BLUE) for the given data model. In addition, unconstrained oracle bounds are also derived in Section 6.5, as a benchmark for next generation estimators. In Section 6.6, we conduct experiments to validate the performance of the proposed estimators.

6.2 Data model

6.2.1 Absolute kinematics

Consider a cluster of N mobile nodes in a P dimensional Euclidean space ($N > P$), whose positions at time t are given by $\mathbf{S}(t) \in \mathbb{R}^{P \times N}$. For a time interval t close to $t_0 = 0$, we assume the time-varying position is continuously differentiable M times and that the Mth derivative exists in the interior of this interval[1]. Therefore, the position vectors of the respective nodes can be expanded using a classical Taylor series as

$$\begin{aligned}
\mathbf{S}(t) &= \mathbf{X} + \mathbf{Y}_1 t + 0.5 \mathbf{Y}_2 t^2 + \dots \\
&= \mathbf{X} + \sum_{m=1}^{M} (m!)^{-1} \mathbf{Y}_m t^{\odot m},
\end{aligned} \tag{6.1}$$

where $\mathbf{X}$ contains the initial co-ordinates of the mobile nodes at time t_0. The instantaneous velocities of the nodes i.e., the first-order derivatives of the position vectors are collected in $\mathbf{Y}_1 \in \mathbb{R}^{P \times N}$. Similarly, we define acceleration as $\mathbf{Y}_2 \in \mathbb{R}^{P \times N}$ and other higher-order derivatives as $\mathbf{Y}_m \; \forall \; 1 \leq m \leq M$.

6.2.2 Relative kinematics

The absolute positions at t_0 are an affine transformation of the relative positions, i.e.,

$$\mathbf{X} = \mathbf{H}_0 \underline{\mathbf{X}} + \mathbf{h}_0 \mathbf{1}_N^T, \tag{6.2}$$

where $\underline{\mathbf{X}} \in \mathbb{R}^{P \times N}$ is the relative position matrix upto a rotation and translation, $\mathbf{H}_0 \in \mathbb{R}^{P \times P}$ is the unknown rotation and $\mathbf{h}_0 \in \mathbb{R}^{P \times 1}$ is the unkown translation of the network at t_0 [Borg and Groenen 2005]. Now, we extend this well-known relative position definition to the higher order derivatives. For instance, the velocity of the nodes can be written as

$$\mathbf{Y}_1 = \mathbf{H}_1 \underline{\tilde{\mathbf{Y}}}_1 + \mathbf{h}_1 \mathbf{1}_N^T, \tag{6.3}$$

where $\underline{\tilde{\mathbf{Y}}}_1$ represents the instantaneous relative velocities of the network at t_0. The translational vector $\mathbf{h}_1$ is the group velocity and $\mathbf{H}_1$ is the unique rotation matrix of

---

[1]Throughout this article, we assume $t_0 = 0$ without loss of generality. The presented model, bounds and corresponding solutions can be readily extended for any $t_0 \in \mathbb{R}$ in general.

the relative velocities [Rajan, Leus and van der Veen 2015]. More generally, the mth order derivative is an affine model defined as

$$\mathbf{Y}_m = \mathbf{H}_m \tilde{\mathbf{Y}}_m + \mathbf{h}_m \mathbf{1}_N^T. \tag{6.4}$$

Now substituting (6.2) and (6.4) in (6.1), multiplying both sides by the centering matrix $\mathbf{P} = \mathbf{I}_N - N^{-1} \mathbf{1}_N \mathbf{1}_N^T$ on the right and $\mathbf{H}_0^T$ on the left, we can write the relative position at time t as

$$\mathbf{H}_0^T \mathbf{S}(t) \mathbf{P} \;=\; \underline{\mathbf{X}} + \sum_{m=1}^{M} (m!)^{-1} \mathbf{H}_0^T \mathbf{H}_m \tilde{\mathbf{Y}}_m t^m, \tag{6.5}$$

where we exploit the property $\mathbf{P} \mathbf{1}_N = \mathbf{0}_N$ to eliminate the translational vectors and enforce the orthonormality of the rotation matrix, i.e., $\mathbf{H}_0^T \mathbf{H}_0 = \mathbf{I}_N$. Furthermore, by introducing

$$\underline{\mathbf{Y}}_m = \mathbf{H}_0^T \mathbf{H}_m \tilde{\mathbf{Y}}_m, \tag{6.6}$$

for all $1 \leq m \leq M$, (6.5) simplifies to

$$\boxed{\underline{\mathbf{S}}(t) = \underline{\mathbf{X}} + \sum_{m=1}^{M} (m!)^{-1} \underline{\mathbf{Y}}_m t^m,} \tag{6.7}$$

where we define the relative time varying position as

$$\underline{\mathbf{S}}(t) = \mathbf{H}_0^T \mathbf{S}(t) \mathbf{P}. \tag{6.8}$$

The above equation represents the relative counterpart of the absolute Taylor expansion (6.1), where the matrices $\big(\underline{\mathbf{X}}, \underline{\mathbf{Y}}_1, \underline{\mathbf{Y}}_2, \ldots, \underline{\mathbf{Y}}_M\big)$ denote the relative kinematics of the corresponding absolute kinematics $\big(\mathbf{X}, \mathbf{Y}_1, \mathbf{Y}_2, \ldots, \mathbf{Y}_M\big)$. Our quest in this article is to estimate the relative (and absolute) kinematic matrices, given time-varying pairwise distance measurements between the nodes. Consequently, the relative (and absolute) position $\underline{\mathbf{S}}(t)$ (and $\mathbf{S}(t)$) at any time t can then be estimated using (6.7).

6.2.3 Time-varying distances

Similar to the node positions, the pairwise distances are also time-varying which we denote by the time-varying EDM $\mathbf{D}(t) \triangleq [d_{ij}(t)] \in \mathbb{R}^{N \times N}$ where $d_{ij}(t)$ is

the pairwise Euclidean distance between the node pair (i, j) at time instant t. More explicitly

$$\big(\mathbf{D}(t)\big)^{\odot 2} = \mathbf{g}(t)\mathbf{1}_N^T + \mathbf{1}_N\mathbf{g}^T(t) - 2\mathbf{S}^T(t)\mathbf{S}(t), \tag{6.9}$$

where $\mathbf{g}(t) = \text{diag}\big(\mathbf{S}^T(t)\mathbf{S}(t)\big)$. Observe that $\mathbf{D}(t)$ is a non-linear function of time t, even when the nodes are in independent linear motion and hence $\mathbf{D}(t)$ is a continuously differentiable function in time. Now, based on the time-varying EDM $\mathbf{D}(t)$, we define the double centered matrix $\underline{\mathbf{B}}(t)$ and its time derivatives as

$$\underline{\mathbf{B}}(t) \triangleq -0.5\mathbf{P}\big(\mathbf{D}(t)\big)^{\odot 2}\mathbf{P}, \tag{6.10a}$$

$$\underline{\dot{\mathbf{B}}}(t) \triangleq -\mathbf{P}\big(\mathbf{D}(t) \odot \dot{\mathbf{D}}(t)\big)\mathbf{P}, \tag{6.10b}$$

$$\underline{\ddot{\mathbf{B}}}(t) \triangleq -\mathbf{P}\big(\mathbf{D}(t) \odot \ddot{\mathbf{D}}(t) + (\dot{\mathbf{D}}(t))^{\odot 2}\big)\mathbf{P}, \tag{6.10c}$$

where $\big(\dot{\mathbf{D}}(t), \ddot{\mathbf{D}}(t), \dots\big)$ are the derivatives of the time-varying EDM, which indicate the radial velocity and other higher order derivatives. Now, let the EDM and the corresponding derivatives at t_0 be denoted by $\mathbf{D}(t_0) \triangleq \mathbf{R} = [r_{ij}]$, $\dot{\mathbf{D}}(t_0) \triangleq \dot{\mathbf{R}} = [\dot{r}_{ij}]$, $\ddot{\mathbf{D}}(t_0) \triangleq \ddot{\mathbf{R}} = [\ddot{r}_{ij}], \forall\{i, j\} \leq N$, then with an abuse of notation (6.10) becomes

$$\underline{\mathbf{B}}^{(0)} \triangleq \underline{\mathbf{B}}(t)|_{t_0} = -0.5\mathbf{P}\mathbf{R}^{\odot 2}\mathbf{P}, \tag{6.11a}$$

$$\underline{\mathbf{B}}^{(1)} \triangleq \underline{\dot{\mathbf{B}}}(t)|_{t_0} = -\mathbf{P}\Big[\mathbf{R} \odot \dot{\mathbf{R}}\Big]\mathbf{P}, \tag{6.11b}$$

$$\underline{\mathbf{B}}^{(2)} \triangleq \underline{\ddot{\mathbf{B}}}(t)|_{t_0} = -\mathbf{P}\Big[\mathbf{R} \odot \ddot{\mathbf{R}} + \dot{\mathbf{R}}^{\odot 2}\Big]\mathbf{P}. \tag{6.11c}$$

In general, given the distance derivatives at t_0, i.e., the range parameters ($\mathbf{R}$, $\dot{\mathbf{R}}$, $\ddot{\mathbf{R}}$, ...), the double centered matrix $\underline{\mathbf{B}}^{(0)}$ and the corresponding higher-order derivatives ($\underline{\mathbf{B}}^{(1)}$, $\underline{\mathbf{B}}^{(2)}$, ...) can be readily obtained.

6.2.4 Data model

To understand the relationship between the time-varying distances and the relative kinematics of the nodes, we substitue the definition of the EDM from (6.9) in (6.10a) and differentiate recursively, to obtain

$$\underline{\mathbf{B}}(t) = \underline{\mathbf{S}}^T(t)\underline{\mathbf{S}}(t), \tag{6.12a}$$

$$\underline{\dot{\mathbf{B}}}(t) = \underline{\dot{\mathbf{S}}}^T(t)\underline{\mathbf{S}}(t) + \underline{\mathbf{S}}^T(t)\underline{\dot{\mathbf{S}}}(t), \tag{6.12b}$$

$$\underline{\ddot{\mathbf{B}}}(t) = \underline{\mathbf{S}}^T(t)\underline{\ddot{\mathbf{S}}}(t) + \underline{\ddot{\mathbf{S}}}^T(t)\underline{\mathbf{S}}(t) + 2\underline{\dot{\mathbf{S}}}^T(t)\underline{\dot{\mathbf{S}}}(t), \tag{6.12c}$$

where we use the definition (6.8) and introduce $(\dot{\underline{\mathbf{S}}}(t), \ddot{\underline{\mathbf{S}}}(t), \ldots)$ as the derivatives of $\underline{\mathbf{S}}(t)$. Now, rearranging the terms and substituting the definition of $\underline{\mathbf{S}}(t)$ at t_0 from (6.7), we have

$$
\begin{aligned}
\mathbf{B}_0 \;&\triangleq\; \underline{\mathbf{B}}^{(0)} & &= \underline{\mathbf{X}}^T \underline{\mathbf{X}}, & (6.13a)\\
\mathbf{B}_1 \;&\triangleq\; \underline{\mathbf{B}}^{(1)} & &= \underline{\mathbf{X}}^T \underline{\mathbf{Y}}_1 + \underline{\mathbf{Y}}_1^T \underline{\mathbf{X}}, & (6.13b)\\
\mathbf{B}_2 \;&\triangleq\; \underline{\mathbf{B}}^{(2)} - 2\underline{\mathbf{Y}}_1^T \underline{\mathbf{Y}}_1 & &= \underline{\mathbf{X}}^T \underline{\mathbf{Y}}_2 + \underline{\mathbf{Y}}_2^T \underline{\mathbf{X}}, & (6.13c)
\end{aligned}
$$

where we introduce the matrices $(\mathbf{B}_0, \mathbf{B}_1, \mathbf{B}_2, \ldots)$. The joint left and right centering using the centering matrix $\mathbf{P}$ in (6.10) ensures that the phase center of the relative kinematic matrices $(\underline{\mathbf{Y}}_1, \underline{\mathbf{Y}}_2, \ldots)$ are at $\mathbf{0}_P$, similar to the relative position $\underline{\mathbf{X}}$.

Combining (6.11a) and (6.13a) for $M = 0$, we have

$$
\mathbf{B}_0 \;=\; \underline{\mathbf{X}}^T \underline{\mathbf{X}} = -0.5 \mathbf{P} \mathbf{R}^{\odot 2} \mathbf{P}, \tag{6.14}
$$

and more generally for a given $M \geq 1$, (6.11) and (6.13) can be generalized to

$$
\begin{aligned}
\mathbf{B}_M \;&\triangleq\; \underline{\mathbf{B}}^{(M)} - \sum_{m=1}^{M-1} \binom{M-1}{m} \underline{\mathbf{Y}}_{M-m}^T \underline{\mathbf{Y}}_m & (6.15a)\\
\;&=\; \underline{\mathbf{X}}^T \underline{\mathbf{Y}}_M + \underline{\mathbf{Y}}_M^T \underline{\mathbf{X}}, & (6.15b)
\end{aligned}
$$

where $\underline{\mathbf{B}}^{(M)}$ is the Mth derivative of the double centered matrix and $\underline{\mathbf{Y}}_M$ is the Mth order relative kinematic matrix.

Remark 16: (**Measurement matrix $\mathbf{B}_M$**): We make two critical observations on $\mathbf{B}_M$ in (6.15a). Firstly, note that $\mathbf{B}_M$ is dependent on the range parameters $\mathbf{R}, \dot{\mathbf{R}}, \ddot{\mathbf{R}}, \ldots$ via the definition of $\underline{\mathbf{B}}^{(M)}$ from (6.11). Secondly, $\mathbf{B}_M$ also relies on the relative kinematic matrices of order less than M. Thus given all the necessary range parameters and the kinematic matrices of order less than M, the measurement matrix $\mathbf{B}_M$ can be reconstructed. Finally, (6.15b) is a bilinear system containing the unknown $\underline{\mathbf{Y}}_M$ as a function of the initial relative position $\underline{\mathbf{X}}$.

6.2.5   Problem Statement

Problem: Given the time-varying pairwise distances $\mathbf{D}(t)$ between the N nodes in a P dimensional Euclidean space, estimate the relative kinematics $(\underline{\mathbf{X}}, \underline{\mathbf{Y}}_1, \underline{\mathbf{Y}}_2 \ldots)$ and absolute kinematics $(\mathbf{Y}_1, \mathbf{Y}_2 \ldots)$ of the mobile network. These estimates subsequently yield the relative (and absolute) time-varying positions.

Solution: We propose a two-step approach to estimate the relative (and absolute) kinematic matrices, from the time-varying distances.
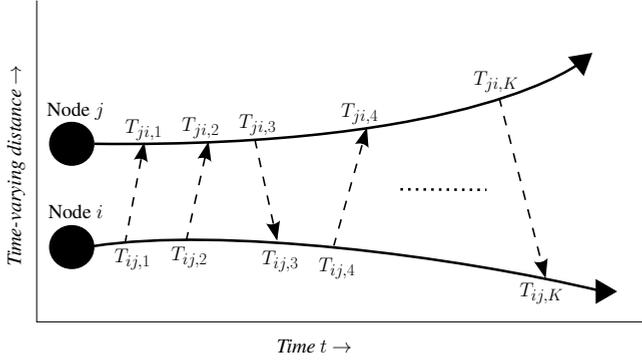
Figure 6.1: *Illustration of a pair of mobile nodes in non-linear motion:* A generalized two-way ranging (TWR) scenario between a pair of mobile nodes, where the nodes exchange K time stamps asymmetrically with each other. The curved lines symbolize the non-linear motion of the mobile nodes with time. Unlike our previous model in Chapter 5, which considered only linear independent velocities of the nodes, in this chapter we consider non-linear motion of the nodes.

(a) *Dynamic ranging* : Given distance measurements $\mathbf{D}(t)$, estimate the range parameters $(\mathbf{R}, \dot{\mathbf{R}}, \ddot{\mathbf{R}}, \ldots)$.

(b) *Kinematics*: Using the range parameters, estimate the unknown 1) relative kinematics (Section 6.3), and 2) absolute kinematics (Section 6.4).

The range parameters $(\mathbf{R}, \dot{\mathbf{R}}, \ddot{\mathbf{R}}, \ldots)$ can be estimated using the dynamic ranging algorithm discussed in the previous chapter (see Section 5.3). Given an estimate of $\boldsymbol{\theta}$ using (5.23), an estimate of the range parameter matrices $(\hat{\mathbf{R}}, \hat{\dot{\mathbf{R}}}, \hat{\ddot{\mathbf{R}}}, \ldots)$ can be constructed and subsequently, from (6.11) we have the following estimates

$$\hat{\underline{\mathbf{B}}}^{(0)} = -0.5\mathbf{P}\hat{\mathbf{R}}^{\odot 2}\mathbf{P}, \tag{6.16a}$$

$$\hat{\underline{\mathbf{B}}}^{(1)} = -\mathbf{P}\left[\hat{\mathbf{R}} \odot \hat{\dot{\mathbf{R}}}\right]\mathbf{P}, \tag{6.16b}$$

$$\hat{\underline{\mathbf{B}}}^{(2)} = -\mathbf{P}\left[\hat{\mathbf{R}} \odot \hat{\ddot{\mathbf{R}}} + \hat{\dot{\mathbf{R}}}^{\odot 2}\right]\mathbf{P}. \tag{6.16c}$$

The relative position $\mathbf{X}$ can now be estimated from $\hat{\mathbf{B}}^{(0)}$ using classical multidimensional scaling as shown in Section 5.5.1 of the previous chapter.

6.3 Relative kinematics

Given the estimates $\left(\hat{\underline{\mathbf{B}}}^{(0)}, \hat{\underline{\mathbf{B}}}^{(1)}, \hat{\underline{\mathbf{B}}}^{(2)}, \dots \right)$ and the relative position estimate $\hat{\mathbf{X}}$ from (6.16) and (5.46) respectively, we aim to find the unknown relative kinematic matrices $\underline{\mathbf{Y}}_M$ using (6.15b).

6.3.1 Lyapunov-like equations

For any $M \geq 1$, the model (6.15b)

$$\mathbf{B}_M = \underline{\mathbf{X}}^T \underline{\mathbf{Y}}_M + \underline{\mathbf{Y}}_M^T \underline{\mathbf{X}}, \qquad (6.17)$$

is the relative *Lyapunov-like equation* [Hodges 1957; Chiang, Chu and Lin 2012], where $\mathbf{B}_M$ is a $N \times N$ measurement matrix and $\mathbf{Y}_M$ is the Mth order kinematics to be estimated. Our equation is very similar, but not the same as the following equations,

$$
\begin{aligned}
\mathbf{A}^H \mathbf{Y} + \mathbf{Y} \mathbf{A} &= \mathbf{B}, \\
\mathbf{A} \mathbf{Y} + \mathbf{Y} \mathbf{A} &= \mathbf{0}, \\
\mathbf{A} \mathbf{Y} + \mathbf{Y} \mathbf{C} &= \mathbf{E},
\end{aligned}
$$

which are the (continuous) *Lyapunov equation*, *commutativity equation* [Horn and Johnson 1991, chapter 4] and *Slyvester equation* [Bartels and G.W.Stewart 1972; Golub, Nash and Van Loan 1979] respectively, where the unknown matrix $\mathbf{Y}$ has to be estimated, given $\mathbf{A}, \mathbf{B}, \mathbf{C}, \mathbf{E}$. The solutions to these equations exist and are extensively investigated in control theory literature [Bhatia and Rosenthal 1997]. However, the Lyapunov-like equation has received relatively less attention. The Lyapunov-like equation has a straight forward solution for $P = 1$. But, for $P \geq 2$, although a general solution was proposed by Braden [Braden 1998], a unique solution to (6.17) does not exist. See Appendix 6.A.

Now, vectorizing (6.15b), the cost function we intend to minimize is

$$
\begin{aligned}
\hat{\underline{\mathbf{y}}}_M &= \arg \min_{\underline{\mathbf{y}}_M} \| (\mathbf{I}_{N^2} + \mathbf{J})(\mathbf{I}_N \otimes \underline{\mathbf{X}}^T) \underline{\mathbf{y}}_M - \mathbf{b}_M \|^2 \\
&= \arg \min_{\underline{\mathbf{y}}_M} \| \underline{\mathbf{A}} \underline{\mathbf{y}}_M - \mathbf{b}_M \|^2, \qquad (6.18)
\end{aligned}
$$

where

$$
\begin{aligned}
\underline{\mathbf{A}} &= (\mathbf{I}_{N^2} + \mathbf{J})(\mathbf{I}_N \otimes \underline{\mathbf{X}}^T) \in \mathbb{R}^{N^2 \times NP}, & (6.19a) \\
\underline{\mathbf{y}}_M &= \operatorname{vec}(\underline{\mathbf{Y}}_M) \in \mathbb{R}^{NP \times 1}, & (6.19b) \\
\mathbf{b}_M &= \operatorname{vec}(\mathbf{B}_M) \in \mathbb{R}^{NP \times 1}, & (6.19c)
\end{aligned}
$$

and $\mathbf{J}$ is an orthogonal permutation matrix. The matrix $(\mathbf{I}_N \otimes \underline{\mathbf{X}}^T) \in \mathbb{R}^{N^2 \times NP}$ is full column rank, since $\mathbf{X}$ is typically non-singular. However, the sum of permutation matrices $(\mathbf{I}_{N^2} + \mathbf{J}) \in \mathbb{R}^{N^2 \times N^2}$ is always rank deficient by at least $\binom{N}{2}$. Hence, the matrix primary objective function $\underline{\mathbf{A}}$ is not full column rank, but is rank deficient by at least $\bar{P} \triangleq 0.5P(P-1)$. In (6.17), since the translational vectors of both $\mathbf{X}$ and $\mathbf{Y}_M$ are projected out using the centering matrix $\mathbf{P}$, the $\bar{P}$ dependent columns in $\underline{\mathbf{A}}$ indicate the rotational degrees of freedom in a P-dimensional Euclidean space.

6.3.2 Lyapunov-like least squares (LLS)

A unique solution to the Lyapunov-like equation is not feasible without sufficient constraints on the linear system (6.18). Let $\hat{\mathbf{A}}$ be an estimate of the matrix $\mathbf{A}$, obtained by substituting the estimated relative position $\hat{\underline{\mathbf{X}}}$ (5.46). Similarly, let $\hat{\mathbf{b}}_M$ be an estimate of $\mathbf{b}_M$ obtained by substituting the range parameters and appropriate relative kinematic matrices upto order $M - 1$. Then the constrained Lyapunov-like least squares (LLS) solution to estimating the relative kinematic matrices is given by minimizing the cost function

$$\hat{\underline{\mathbf{y}}}_{M,lls} = \arg \min_{\underline{\mathbf{y}}_M} \|\hat{\underline{\mathbf{A}}}\underline{\mathbf{y}}_M - \hat{\mathbf{b}}_M\|^2 \quad \text{s.t.} \ \bar{\mathbf{C}}\underline{\mathbf{y}}_M = \bar{\mathbf{d}}, \tag{6.20}$$

where $\bar{\mathbf{C}}$ is a set of non-redundant constraints. The above optimization problem has a closed-form solution, given by solving the KKT equations (Appendix 6.B).

6.3.3 Weighted Lyapunov-like LS (WLLS)

In reality, both $\mathbf{A}$ and $\mathbf{b}$ are plagued with errors and hence the solution to the cost function (6.20) is sub-optimal. Let $\bar{\mathbf{W}}_M$ be an appropriate weighting matrix on the Lyapunov-like equation, then the weighted lyapunov-like least squares (WLLS) solution is obtained by minimizing the cost function

$$\hat{\underline{\mathbf{y}}}_{M,wlls} = \arg \min_{\underline{\mathbf{y}}_M} \|\bar{\mathbf{W}}_M^{1/2}(\hat{\underline{\mathbf{A}}}\underline{\mathbf{y}}_M - \hat{\mathbf{b}}_M)\|^2 \quad \text{s.t.} \ \bar{\mathbf{C}}\underline{\mathbf{y}}_M = \bar{\mathbf{d}}, \tag{6.21}$$

which, similar to (6.20), can be solved using the constrained KKT solutions (See Appendix 6.B). An appropriate choice of the weighting matrix $\bar{\mathbf{W}}_M$ will be discussed in Section 6.5.2.

6.3.4 Choice of constraints: Relative immobility

In the absence of absolute location information, a unique solution is feasible if the relative motion of at least P nodes or features are invariant (or known) over a small time duration ΔT. In an anchorless framework, a set of given nodes would have equivalent relative kinematics, if they are identical in motion upto a translation or if they are immobile for the small measurement time ΔT. Such situations could arise, for example, in underwater localization, when a few immobile nodes could be deployed in fixed but unknown absolute locations, which in turn could assist the relative localization of the other nodes. For $P = 2$, if the first P nodes are relatively immobile for the small measurement time, a valid constraint for (6.20) and (6.21) is

$$\bar{\mathbf{C}}_1 = \begin{bmatrix} \mathbf{I}_2 & -\mathbf{I}_2 & \mathbf{0} \end{bmatrix}, \qquad \bar{\mathbf{d}}_1 = \mathbf{0}, \tag{6.22}$$

which can be readily extended for $P > 2$ and if required, for a larger number of immobile nodes. In essence, the relative immobility constraint reduces the parameter space in pursuit of a unique solution for the ill-posed Lyapunov-like equation. '

6.4   Absolute kinematics

In addition to relative kinematics, (6.17) can also be reformulated to estimate the absolute kinematics of the network. For the sake of completion, we propose an estimate of the absolute kinematics $\mathbf{Y}_M$ using our data model.

Note that the initial rotation $\mathbf{H}_0$ and translation $\mathbf{h}_0$ do not affect the model, as observed in (6.17). Thus, without the loss of generality, we assume

$$\mathbf{H}_0 = \mathbf{I}_P \quad \text{and} \quad \mathbf{h}_0 = \mathbf{0}_P. \tag{6.23}$$

Under this assumption, the relative position is identical to the absolute position $\underline{\mathbf{X}} = \mathbf{X}$, which we use to estimate the higher order kinematics.

6.4.1   Generalized Lyapunov-like equation

Recall that $\mathbf{Y}_M$ is the absolute kinematic matrix of the Mth order, such that $\mathbf{Y}_M \mathbf{P} = \mathbf{H}_M \tilde{\underline{\mathbf{Y}}}$ holds (6.4). Then, under the assumption (6.23), the relative kinematic model (6.17) is

$$\underline{\mathbf{X}}^T \mathbf{Y}_M \mathbf{P} + \mathbf{P} \mathbf{Y}_M^T \underline{\mathbf{X}} = \mathbf{B}_M. \tag{6.24}$$

The above equation is similar, but not the same, to the generalized (continuous-time) Lyapunov equation

$$\mathbf{A}^T \mathbf{Y} \mathbf{C} + \mathbf{C}^T \mathbf{Y} \mathbf{A} = \mathbf{B},$$

where $\mathbf{A}, \mathbf{B}, \mathbf{C}$ are known square matrices [Penzl 1998]. We now vectorize (6.24) and aim to minimize the following cost function

$$\hat{\mathbf{y}}_M = \arg\min_{\mathbf{y}_M} \|\mathbf{A}\mathbf{y}_M - \mathbf{b}_M\|^2, \tag{6.25}$$

where

$$\mathbf{A} = (\mathbf{I}_{N^2} + \mathbf{J})(\mathbf{P} \otimes \underline{\mathbf{X}}^T) \in \mathbb{R}^{N^2 \times NP}, \tag{6.26a}$$

$$\mathbf{y}_M = \text{vec}(\mathbf{Y}_M) \in \mathbb{R}^{NP \times 1}, \tag{6.26b}$$

and $\mathbf{b}_M$ is given by (6.19c). In comparison to (6.18), the matrix $(\mathbf{I}_N \otimes \underline{\mathbf{X}}^T)$ is replaced with $(\mathbf{P} \otimes \underline{\mathbf{X}}^T)$ in (6.26a). The rank of the centering matrix P is $N - 1$ and since $\underline{\mathbf{X}}$ is typically full row rank, the Kronecker product is utmost of rank $NP - P$. This rank-deficiency of P is also reflected in the matrix $\mathbf{A}$. Unlike $\underline{\mathbf{A}}$ which has $\bar{P}$ dependent colomns, $\mathbf{A}$ is rank-deficient by $\binom{P+1}{2} = \bar{P} + P$. The additional P dependent columns are perhaps not surprising, as they indicate the lack of information on the translational vector, i.e., the group center of the Mth order kinematic matrix.

6.4.2 Generalized Lyapunov-like Least Squares (GLLS)

In pursuit of a unique solution to the rank-deficient system (6.25), we propose a constrained generalized Lyapunov-like least squares (GLLS) to estimate the absolute kinematic matrices which is obtained by minimizing the cost function

$$\hat{\mathbf{y}}_{M,glls} = \arg\min_{\mathbf{y}_M} \|\hat{\mathbf{A}}\mathbf{y}_M - \hat{\mathbf{b}}_M\|^2 \quad \text{s.t. } \mathbf{C}\mathbf{y}_M = \mathbf{d}, \tag{6.27}$$

where $\hat{\mathbf{A}}$ and $\hat{\mathbf{b}}_M$ are estimates of $\mathbf{A}$ and $\mathbf{b}_M$ respectively. The matrix $\mathbf{C}$ is a set of non-redundant constraints, which will be discussed in Section 6.4.4.

6.4.3 Weighted generalized lyapunov-like LS (WGLLS)

The performance of the estimator can be improved by weighting the cost function (6.27), i.e.,

$$\hat{\mathbf{y}}_{M,wglls} = \arg\min_{\mathbf{y}_M} \|\mathbf{W}_M^{1/2}(\hat{\mathbf{A}}\mathbf{y}_M - \hat{\mathbf{b}}_M)\|^2 \quad \text{s.t. } \mathbf{C}\mathbf{y}_M = \mathbf{d}, \tag{6.28}$$

which yields the weighted generalized lyapunov-like least squares (WGLLS) solution (See Appendix 6.B), where $\mathbf{W}_M$ is an appropriate weighting matrix (See Section 6.5.2).

6.4.4 Choice of constraints: Anchor-aware network

For an anchored scenario, if the Mth order absolute kinematics of a few nodes are known, then the absolute velocity, acceleration and higher order derivatives can be estimated. A straightforward minimal constraint for the feasible solution is then

$$\mathbf{C}_1 = \begin{bmatrix} \mathbf{I}_{\bar{P}+P}, & \mathbf{0} \end{bmatrix}, \tag{6.29}$$

where without loss of generality, we assume the first $\bar{P} + P$ parameters are known.

6.5 Cramér-Rao bounds

6.5.1 Kinematics

We now derive the lower bounds on the variance of the estimates of relative kinematics $\underline{\mathbf{y}}_M = \mathrm{vec}(\underline{\mathbf{Y}}_M)$ and absolute kinematics $\mathbf{y}_M = \mathrm{vec}(\mathbf{Y}_M)$. The Gaussian noise vectors plaguing the respective cost functions (6.18) and (6.25) are modelled as

$$\underline{\boldsymbol{\rho}}_M \sim \mathcal{N}(\underline{\mathbf{A}}\underline{\mathbf{y}}_M - \mathbf{b}_M, \underline{\boldsymbol{\Sigma}}_{\rho,M}), \tag{6.30}$$

$$\boldsymbol{\rho}_M \sim \mathcal{N}(\mathbf{A}\underline{\mathbf{y}}_M - \mathbf{b}_M, \boldsymbol{\Sigma}_{\rho,M}), \tag{6.31}$$

where $\boldsymbol{\rho}_M, \underline{\boldsymbol{\rho}}_M$ are N^2 dimensional noise vectors, and the corresponding covariance matrices are of the form

$$\underline{\boldsymbol{\Sigma}}_{\rho,M} \triangleq \mathbb{E}\{\underline{\boldsymbol{\rho}}_M \underline{\boldsymbol{\rho}}_M^T\} \approx \underline{\mathbf{A}}_{y,M} \bar{\boldsymbol{\Sigma}}_x \underline{\mathbf{A}}_{y,M}^T + \boldsymbol{\Sigma}_{b,M}, \tag{6.32a}$$

$$\boldsymbol{\Sigma}_{\rho,M} \triangleq \mathbb{E}\{\boldsymbol{\rho}_M \boldsymbol{\rho}_M^T\} \approx \mathbf{A}_{y,M} \bar{\boldsymbol{\Sigma}}_x \mathbf{A}_{y,M}^T + \boldsymbol{\Sigma}_{b,M}, \tag{6.32b}$$

where

$$\underline{\mathbf{A}}_{y,M} = (\mathbf{I}_{N^2} + \mathbf{J})(\mathbf{I}_N \otimes \underline{\mathbf{Y}}_M^T) \in \mathbb{R}^{N^2 \times NP}, \tag{6.33a}$$

$$\mathbf{A}_{y,M} = (\mathbf{I}_{N^2} + \mathbf{J})(\mathbf{P} \otimes \mathbf{Y}_M^T) \in \mathbb{R}^{N^2 \times NP}, \tag{6.33b}$$

and an expression for $\boldsymbol{\Sigma}_{b,M}$ is derived in Appendix 6.C.

Unconstrained CRBs

The lowest achievable variance by an unbiased estimator is given by

$$\underline{\boldsymbol{\Sigma}}_{y,M} \triangleq \mathbb{E}\left\{(\hat{\underline{\mathbf{y}}}_M - \underline{\mathbf{y}}_M)(\hat{\underline{\mathbf{y}}}_M - \underline{\mathbf{y}}_M)^T\right\} \geq \mathbf{F}_{y,M}^\dagger, \tag{6.34a}$$

$$\boldsymbol{\Sigma}_{y,M} \triangleq \mathbb{E}\left\{(\hat{\mathbf{y}}_M - \mathbf{y}_M)(\hat{\mathbf{y}}_M - \mathbf{y}_M)^T\right\} \geq \mathbf{F}_{y,M}^\dagger, \tag{6.34b}$$

where the corresponding FIMs are given by

$$\underline{\mathbf{F}}_{y,M} = \left(\underline{\mathbf{A}}^T \boldsymbol{\Sigma}_{\rho,M}^\dagger \underline{\mathbf{A}}\right), \tag{6.35a}$$

$$\mathbf{F}_{y,M} = \left(\mathbf{A}^T \boldsymbol{\Sigma}_{\rho,M}^\dagger \mathbf{A}\right). \tag{6.35b}$$

It is worth noting that the Moore-Penrose pseudoinverse is employed since the FIM is rank-deficient, and consequently the derived bounds (6.34) are *oracle-bounds*.

Constrained CRBs

When the FIM is rank-deficient, a constrained CRB can be derived given differentiable and deterministic constraints on the parameters [Stoica and Ng 1998]. Let $\bar{\mathbf{U}}, \mathbf{U}$ be an orthonormal basis for the null space of the constraint matrices $\bar{\mathbf{C}}, \mathbf{C}$, then the constrained Cramér-Rao bound (CCRB) on the Mth order kinematic matrices is given by

$$\underline{\boldsymbol{\Sigma}}_{y,M}^C \triangleq \mathbb{E}\left\{(\hat{\underline{\mathbf{y}}}_M - \underline{\mathbf{y}}_M)(\hat{\underline{\mathbf{y}}}_M - \underline{\mathbf{y}}_M)^T\right\}$$
$$\geq \bar{\mathbf{U}}\left(\bar{\mathbf{U}}^T \underline{\mathbf{F}}_{y,M} \bar{\mathbf{U}}\right)^{-1} \bar{\mathbf{U}}^T, \tag{6.36a}$$

$$\boldsymbol{\Sigma}_{y,M}^C \triangleq \mathbb{E}\left\{(\hat{\mathbf{y}}_M - \mathbf{y}_M)(\hat{\mathbf{y}}_M - \mathbf{y}_M)^T\right\}$$
$$\geq \mathbf{U}\left(\mathbf{U}^T \mathbf{F}_{y,M} \mathbf{U}\right)^{-1} \mathbf{U}^T, \tag{6.36b}$$

where the FIMs are given by (6.35).

6.5.2   Choice of weighting matrices $\bar{\mathbf{W}}_M, \mathbf{W}_M$

To admit a BLUE solution, we use the inverse of the covariance matrices $\underline{\boldsymbol{\Sigma}}_{\rho,M}, \boldsymbol{\Sigma}_{\rho,M}$ as weights to solve the regression problems (6.21) and (6.28), i.e.,

$$\bar{\mathbf{W}}_M \triangleq \hat{\underline{\boldsymbol{\Sigma}}}_{\rho,M}^\dagger = \left(\hat{\underline{\mathbf{A}}}_y \hat{\bar{\boldsymbol{\Sigma}}}_x \hat{\underline{\mathbf{A}}}_y^T + \hat{\bar{\boldsymbol{\Sigma}}}_{b,M}\right)^\dagger, \tag{6.37a}$$

$$\mathbf{W}_M \triangleq \hat{\boldsymbol{\Sigma}}_{\rho,M}^\dagger = \left(\hat{\mathbf{A}}_y \hat{\bar{\boldsymbol{\Sigma}}}_x \hat{\mathbf{A}}_y^T + \hat{\boldsymbol{\Sigma}}_{b,M}\right)^\dagger, \tag{6.37b}$$
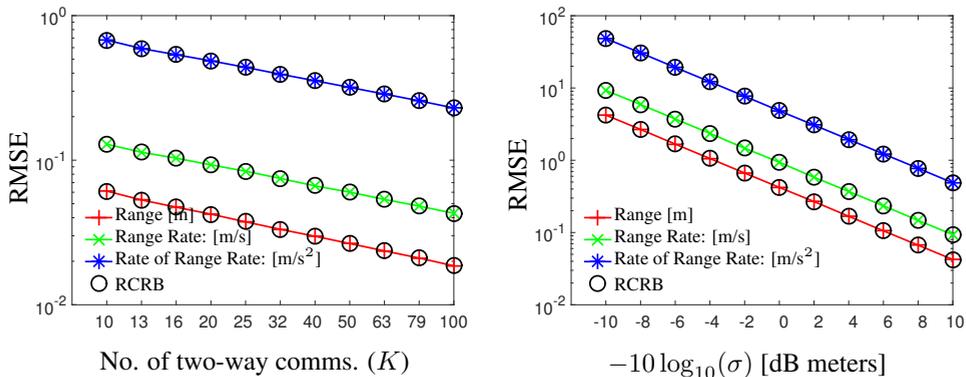
Figure 6.2: *Range parameters:* **(Left) Varying** K **:** RMSEs (and RCRBs) of relative range parameters $(\mathbf{r}, \dot{\mathbf{r}}, \ddot{\mathbf{r}})$ for varying number of communications (K) between the $N = 10$ *mobile* nodes for $\sigma = 0.1$ meters. **(Right) Varying** σ **:** RMSEs (and RCRBs) of relative range parameters $(\mathbf{r}, \dot{\mathbf{r}}, \ddot{\mathbf{r}})$ for a network of $N = 10$ exchanging $K = 10$ timestamps, where the noise on the time markers (σ) is varied. Unlike our previous experiments [Rajan, Leus and van der Veen 2015; Rajan and van der Veen 2015] (See Chapter 4 and Chapter 5), we consider acceleration in the current setup.

where the estimates $\hat{\underline{\mathbf{A}}}_y, \hat{\mathbf{A}}_y$ are obtained by substituting $\hat{\underline{\mathbf{Y}}}_M$ from LLS [(6.20) and (6.27)], in (6.33), $\hat{\bar{\boldsymbol{\Sigma}}}_x$ is an estimate of (5.55) and $\hat{\boldsymbol{\Sigma}}_{b,M}$ is derived in Appendix 6.C from appropriate range parameter estimates.

6.6   Simulations

In this section, we conduct experiments to validate the proposed data model, and the solutions against their respective derived lower bounds. A network of $N = 10$ nodes is considered in $P = 2$-dimensional space, with instantaneous position, velocity and acceleration values arbitrarily chosen as in (6.38), such that the constraint (6.22) holds. All the nodes communicate with each other within a small time-interval of $\Delta T = [T_{ij,k}, T_{ji,k}] = [-1, 1]$ seconds , wherein the transmit time markers are chosen to be linearly spaced. Furthermore, we assume that all the pairwise communications are independent of each other, i.e., $\boldsymbol{\Sigma} = \sigma^2 \mathbf{I}_{\bar{N}K}$. The metric used to evaluate the performance of the range parameters, absolute velocity and absolute acceleration is

$$\mathbf{X} = \begin{bmatrix} -244 & 385 & 81 & -19 & -792 & -554 & -965 & -985 & -49 & -503 \\ -588 & -456 & -992 & -730 & 879 & 970 & 155 & 318 & -858 & 419 \end{bmatrix},$$

$$\mathbf{Y}_1 = \begin{bmatrix} -5 & -5 & -6 & 6 & -1 & 2 & 1 & -5 & 9 & -5 \\ -8 & -8 & -7 & -9 & -3 & -2 & -2 & -10 & 2 & -1 \end{bmatrix},$$

$$\mathbf{Y}_2 = \begin{bmatrix} -0.2 & -0.2 & 0.2 & -0.1 & 0.2 & -0.2 & 0.5 & -0.7 & -0.5 & -0.3 \\ 0.4 & 0.4 & 1 & 0.7 & 0.5 & 0.1 & -0.4 & -0.1 & 0.5 & 0.9 \end{bmatrix} \qquad (6.38)$$

the root mean square error (RMSE), given by

$$\mathrm{RMSE}(\mathbf{z}) = \sqrt{N_{exp}^{-1} \sum_{n=1}^{N_{exp}} \|\hat{\mathbf{z}}(n) - \mathbf{z}\|^2},$$

where $\hat{\mathbf{z}}(n) \in \mathbb{R}^{NP \times 1}$ is the nth estimate of the unknown vector $\mathbf{z}$ during $N_{exp} = 500$ Monte Carlo runs. To qualify these estimates, the square root of the Cramér-Rao bound (RCRB) is plotted along with the respective RMSE. For all proposed estimators, we conduct two types of experiments, for (a) varying number of pairwise communications K from 0 to 100, with constant noise of $\sigma = 0.1$m and (b) varying SNR from $[-10, 10]$ dB meter with a fixed $K = 10$ time-stamp exchanges. The noise on the time-markers is typical for classical TWR based fixed localization [Patwari et al. 2003].

6.6.1 Range parameters

We employ the dynamic ranging algorithm (5.23) for $L = 3$, to extract the desired range coefficients. Figure 6.2 shows the RMSE of the first 3 range coefficients, for both varying K and varying SNR. In both experiments, not surprisingly, the RMSEs of the estimated range coefficients achieve the corresponding RCRBs asymptotically. It is worth noting, that unlike previous experiments in Chapter 4 and Chapter 5, which considered only linear motion, we now consider acceleration in the current simulation. Without loss of generality, we assume that the order of approximation L is known. Alternatively, iterative solutions such as iMGLS can be employed to estimate L. For a detailed discussion on the effect of L on the distance estimation, particularly for an asynchronous network, see Chapter 4.
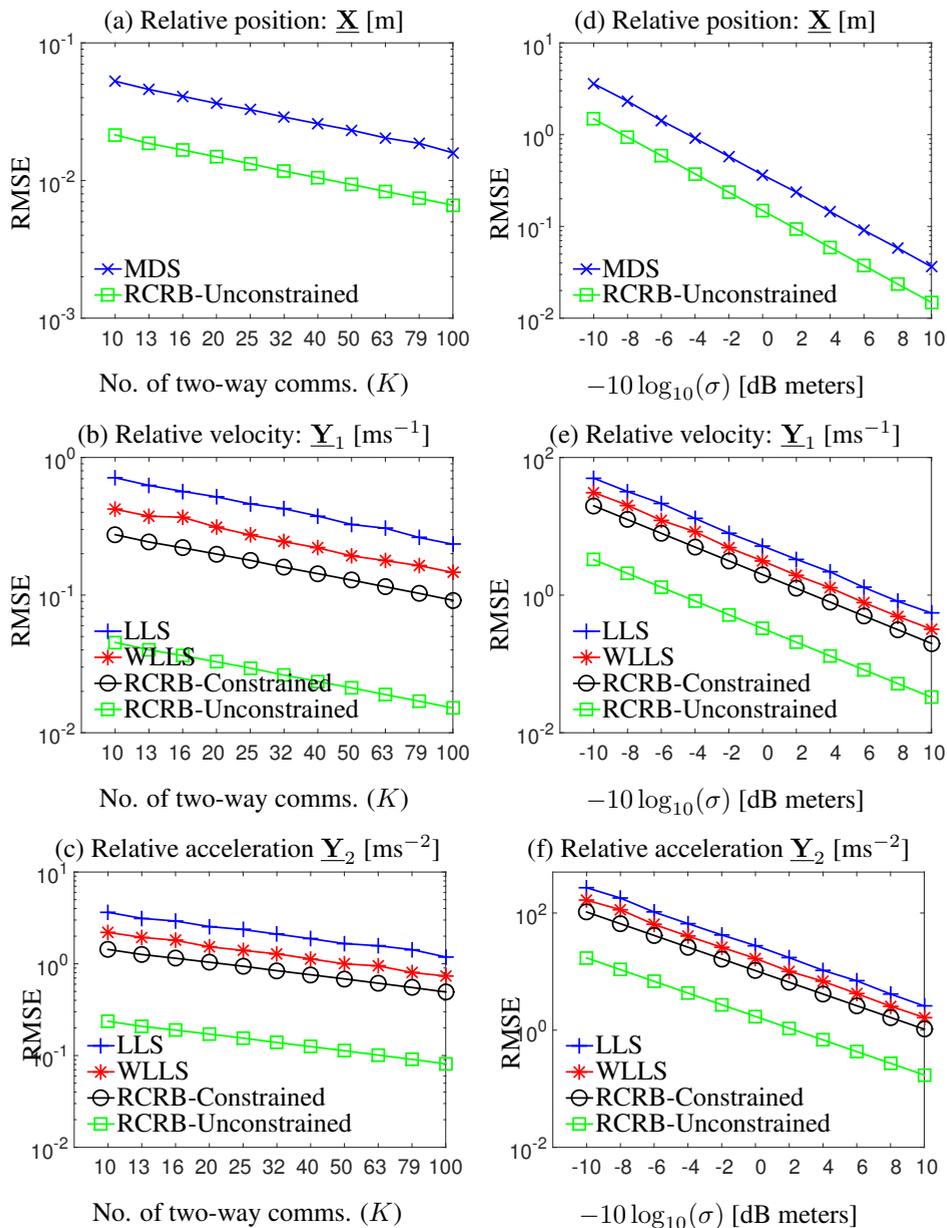
Figure 6.3: *Relative Kinematics:* **Varying** K**:** RMSEs (and RCRBs) of (a) Relative position ($\underline{\mathbf{X}}$), (b) Relative velocity ($\underline{\mathbf{Y}}_1$) and (c) Relative acceleration ($\underline{\mathbf{Y}}_2$) for varying number of communications (K) for $\sigma = 0.1$ meters. **Varying** σ**:** RMSEs (and RCRBs) of (d) Relative position ($\underline{\mathbf{X}}$), (e) Relative velocity ($\underline{\mathbf{Y}}_1$) and (f) Relative acceleration ($\underline{\mathbf{Y}}_2$) for $K = 10$, and where the noise on the time markers (σ) is varied.
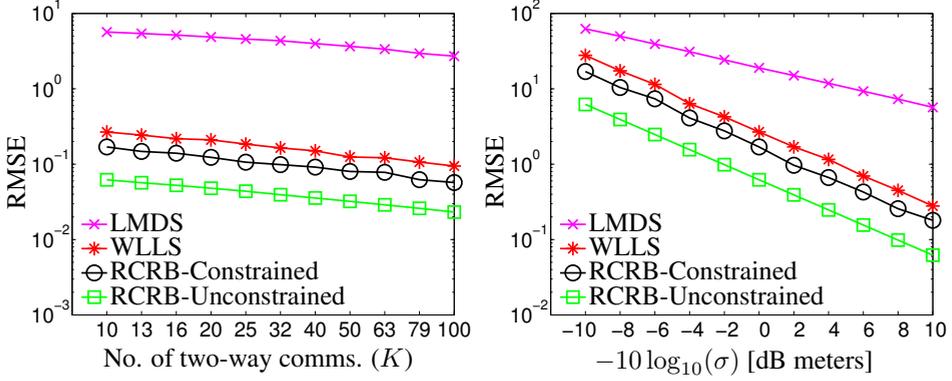
Figure 6.4: ***Comparison of relative velocity estimators:*** RMSEs (and RCRBs) of relative range parameters $\mathbf{Y}_1$ for (left) varying number of communications (K) for $\sigma = 0.1$ meters and (right) varying σ between the $N = 10$ *mobile* nodes.

6.6.2   Relative kinematics

The estimated relative range parameters yield the desired relative kinematics matrices. Figure 6.3 shows the RMSEs (and RCRBs) of all the relative kinematic estimates. The MDS-based relative position estimates presented in Figure 6.3(a) and in Figure 6.3(d), perform well against the derived *orcale-bound*, which was also observed in [Rajan and van der Veen 2015]. In case of the relative velocity and acceleration, we assume the minimal constraint $\bar{\mathbf{C}}_1$ for analysis. Note that the unconstrained *oracle-bounds* are lower as compared to the CCRB, for a fixed SNR and increasing K. The WLLS solution outperforms the LLS solutions for both velocity and acceleration estimation, and asymptotically achieve the derived respective CCRBs.

To compare the performance of the proposed relative velocity estimator against the MDS-based relative velocity estimation (5.47), we perform another experiment. The MDS-based algorithm for relative velocity estimation assumes the nodes are in linear motion. Hence, we set $\mathbf{Y}_2 = \mathbf{0}_{P,N}$ in (6.38), and re-implement the dynamic ranging algorithm for $L = 2$ and plot the standard deviation of the relative velocity estimators in Figure 6.4. Under the constant velocity assumption, the CCRB is comparable to the *oracle-bound*. The proposed WLLS solution outperforms the MDS-based estimator, especially for higher SNR and lower number of pair-wise communications. This is perhaps not surprising, since the previously proposed MDS-based relative velocity estimator is based on $\ddot{\mathbf{R}}$, where the estimated noise on these regression coefficients typically increases with range-order for a Taylor basis (see Figure 6.2). In comparison, the WLLS solution proposed in this chapter is dependent

only on range $\mathbf{R}$ and range rates $\dot{\mathbf{R}}$.

6.6.3   Absolute kinematics

Figure 6.5 shows the RMSEs and the corresponding RCRBs of the absolute velocity $\mathbf{Y}_1$ and acceleration $\mathbf{Y}_2$. We assume constraint (6.29) to solve the proposed GLLS (6.27) and WGLLS (6.28) algorithms. The proposed estimators are seen to converge asymptotically to the derived CCRBs, while the CCRB itself is an order higher than the theoretical *oracle-bound*. The performance of the absolute kinematics is very similar to the that of the relative kinematics (see Figure 6.3), which is due to the fact the FIMs in both scenarios are dominated by the singular values of the relative position matrix.

6.6.4   Relative positions over time

The primary objective of this chapter is to estimate the relative (and absolute) kinematics of motion. However, for the sake of completeness, we discuss the use of these estimates in reconstructing the relative and absolute time-varying positions i.e., $\underline{\mathbf{S}}(t)$ and $\mathbf{S}(t)$. Substituting the proposed constrained solutions in (6.1) and (6.7), the time-varying position estimates are

$$\hat{\underline{\mathbf{S}}}(t) = \hat{\underline{\mathbf{X}}} + \hat{\underline{\mathbf{Y}}}_1 t + 0.5\hat{\underline{\mathbf{Y}}}_2 t^2, \tag{6.39}$$

$$\hat{\mathbf{S}}(t) = \hat{\mathbf{X}} + \hat{\mathbf{Y}}_1 t + 0.5\hat{\mathbf{Y}}_2 t^2, \tag{6.40}$$

where $\hat{\mathbf{X}} = \hat{\underline{\mathbf{X}}}$ is the relative position estimated from (5.46), and $\{\hat{\underline{\mathbf{Y}}}_1, \hat{\underline{\mathbf{Y}}}_2\}$ and $\{\hat{\mathbf{Y}}_1, \hat{\mathbf{Y}}_2\}$ are the relative and absolute kinematic estimates from (6.21) and (6.28) respectively. The RMSE plot for the absolute and relative time-varying positions around the region of interest at $t_0 = 0$ are shown in Figure 6.6, where the number of communications is varied as $K = [50, 100, 500]$ with a Gaussian noise on the distance of $\sigma = 1$ meter. For $K = 500$, the RMSE estimate of both the relative and absolute position around t_0 shows an improvement by an order magnitude in comparison to the noise on the distance measurement, for the given experimental setup. This gain is primarily contributed during dynamic ranging, where K data points are averaged using the Taylor basis which yields a factor $\sqrt{K}$ improvement on the estimate of the range parameters. Secondly, the performance deteriorates as we move away from t_0, which is a typical characteristic of the Taylor approximation. However, if Doppler measurements are available for radial velocities and other higher order derivatives, then the standard deviation of the estimators can be further reduced.

6.7 Conclusions

Understanding the relative kinematics of an anchorless network of mobile nodes is paramount for reference-free localization technologies of the future. We presented a novel data model which relates the time-varying distance measurements to the Mth order relative kinematics for an anchorless network of mobile nodes. The derived data model takes the form of a Lyapunov-like equations, which under certain constraints, can be recursively solved for estimating the relative velocity, acceleration and higher order derivatives. Closed form constrained estimators, such as the LS and WLS are proposed, which are also the BLUE for the given data model. Cramér-Rao lower bounds are derived for the new data model and the performance of the proposed algorithms are validated using simulations. Although our focus is on relative localization, the proposed model and solutions can be broadly applied to understand feature variation in Euclidean space.

In our future work, we are keen in addressing two research challenges. Firstly, our focus in this chapter has been on finding unique solutions to time-derivatives of the relative position matrix. To this end, unbiased constrained estimators are proposed to solve the under-determined Lyapunov-like equation. However, more generally, regularized algorithms can be employed, such as Ridge regression [Golub, Hansen and O'Leary 1999], subset selection [Lawson and Hanson 1974] or Lasso [Tibshirani 1996], without the need for equality constraints on the cost function. The estimates of such unconstrained algorithms can be corroborated against the unconstrained Cramér-Rao bound derived in this chapter. Furthermore, the algorithms are inherently centralized in nature, which could be distributed for resource constrained implementation. Finally, the proposed framework is particularly helpful for cold-start scenarios when there is no apriori information on the position or higher order kinematics. In practice, given the cold-start solution on relative velocity and higher order kinematics, a state-space model readily emerges for dynamic tracking of the relative positions over time, which can be elegantly solved using a Kalman filter.

Appendix 6.A   Lyapunov-like equation

Theorem 1. *Given* $\mathbf{X} \in \mathbb{R}^{P \times N}$ *and* $\mathbf{B} \in \mathbb{R}^{N \times N}$ *for* $N > P$, *the Lyapunov-like equation*

$$\mathbf{X}^T\mathbf{Y} + \mathbf{Y}^T\mathbf{X} = \mathbf{B}, \tag{6.41}$$

is rank-deficient by at least $\bar{P} = \binom{P}{2}$.

(a) Absolute velocity: $\mathbf{Y}_1$ [ms^{-1}]

(c) Absolute velocity: $\mathbf{Y}_1$ [ms^{-1}]

No. of two-way comms. (K)

$-10\log_{10}(\sigma)$ [dB meters]

(b) Absolute acceleration $\mathbf{Y}_2$ [ms^{-2}]

(d) Absolute acceleration $\mathbf{Y}_2$ [ms^{-2}]

No. of two-way comms. (K)

$-10\log_{10}(\sigma)$ [dB meters]
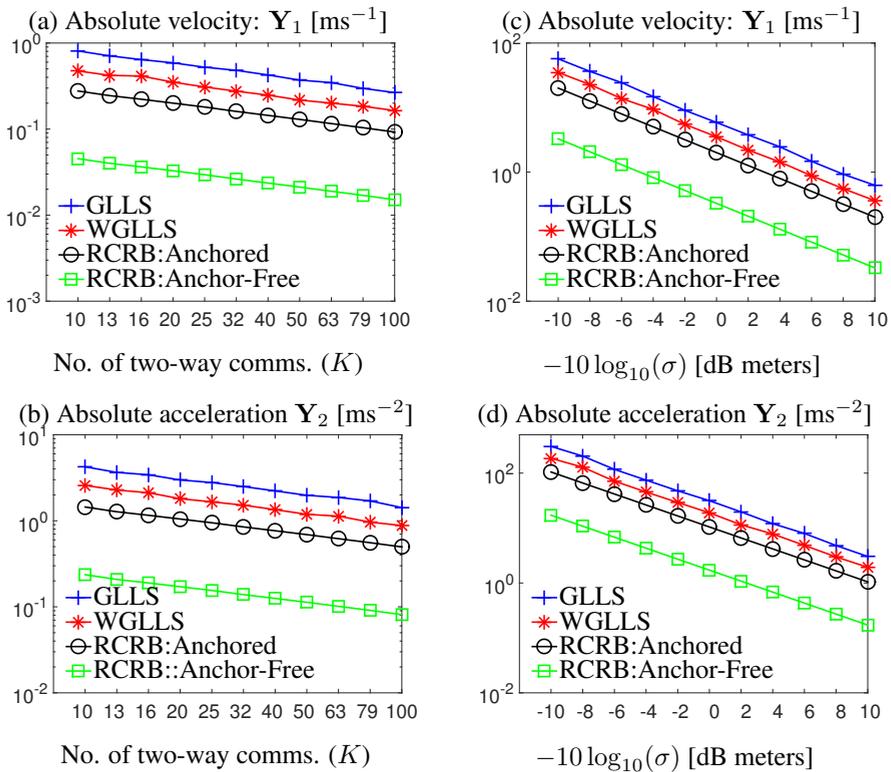
Figure 6.5: *Absolute kinematics:* **Varying** K**:** RMSEs (and RCRBs) of (a) Absolute velocity ($\mathbf{Y}_1$) and (b) Absolute acceleration ($\mathbf{Y}_2$) for varying number of communications (K) between the $N = 10$ *mobile* nodes for $\sigma = 0.1$ meters. **Varying** σ**:** RMSEs (and RCRBs) of (c) Absolute velocity ($\mathbf{Y}_1$) and (d) Absolute acceleration ($\mathbf{Y}_2$), for a network of $N = 10$ exchanging $K = 10$ timestamps, where the Noise on the time markers (σ) is varied.
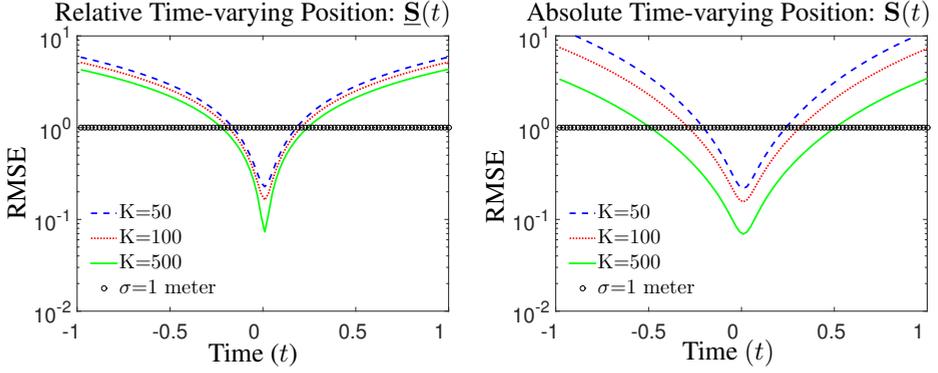
Figure 6.6: *Error on position over time:* RMSEs of (left) relative position $\underline{\mathbf{S}}(t)$ and (right) absolute position $\mathbf{S}(t)$ over time for $K = [50, 100, 500]$ communications between a cluster of $N = 10$ *mobile* nodes, with $\sigma = 1$ meter.

Proof. Let the singular value decomposition of $\mathbf{X}$ be

$$\mathbf{X} = \mathbf{U}_x \begin{bmatrix} \mathbf{\Lambda}_x & \mathbf{0} \end{bmatrix} \mathbf{V}_x^T, \tag{6.42}$$

where $\mathbf{\Lambda}_x \in \mathbb{R}^{P \times P}$ is a diagonal matrix containing the singular values and $\mathbf{U}_x \in \mathbb{R}^{P \times P}$, and $\mathbf{V}_x \in \mathbb{R}^{N \times N}$ are the corresponding singular vectors. Then, (6.41) is

$$\begin{bmatrix} \mathbf{\Lambda}_x & \mathbf{0} \end{bmatrix}^T \tilde{\mathbf{Y}} + \tilde{\mathbf{Y}}^T \begin{bmatrix} \mathbf{\Lambda}_x & \mathbf{0} \end{bmatrix} = \tilde{\mathbf{B}}, \tag{6.43}$$

where

$$\tilde{\mathbf{B}} = \begin{bmatrix} \tilde{\mathbf{B}}_{11} & \tilde{\mathbf{B}}_{12} \\ \tilde{\mathbf{B}}_{12}^T & \tilde{\mathbf{B}}_{22} \end{bmatrix} = \mathbf{V}_x^T \mathbf{B}_x \mathbf{V}_x, \tag{6.44}$$

$$\tilde{\mathbf{Y}} = \begin{bmatrix} \tilde{\mathbf{Y}}_1 & \tilde{\mathbf{Y}}_2 \end{bmatrix} = \mathbf{U}_x^T \mathbf{Y} \mathbf{V}_x, \tag{6.45}$$

where $\tilde{\mathbf{Y}}_1 \in \mathbb{R}^{P \times P}$, $\tilde{\mathbf{Y}}_2 \in \mathbb{R}^{P \times N - P}$ and $\tilde{\mathbf{B}}_{22} = \mathbf{0}$ for the equation to be consistent. A solution to the system (6.41) is obtained by solving for $\tilde{\mathbf{Y}}$ the set of equations,

$$\mathbf{\Lambda}_x \tilde{\mathbf{Y}}_1 + \tilde{\mathbf{Y}}_1^T \mathbf{\Lambda}_x = \tilde{\mathbf{B}}_{11}, \tag{6.46}$$

$$\mathbf{\Lambda}_x \tilde{\mathbf{Y}}_2 = \tilde{\mathbf{B}}_{12}. \tag{6.47}$$

An estimate for $\tilde{\mathbf{Y}}_2$ is straightforward and is given by $\hat{\tilde{\mathbf{Y}}}_2 = \mathbf{\Lambda}_x^{-1} \tilde{\mathbf{B}}_{12}$. Let $\tilde{\mathbf{\Lambda}}_x, \tilde{\mathbf{Y}}_1$ and $\tilde{\mathbf{B}}_{11}$ be partitioned into

$$\begin{bmatrix} \sigma_1 & 0 \\ 0 & \mathbf{\Lambda}_{x,1} \end{bmatrix}, \quad \begin{bmatrix} y_{11} & \tilde{\mathbf{y}}_{12} \\ \tilde{\mathbf{y}}_{21} & \tilde{\mathbf{Y}}_{1,1} \end{bmatrix}, \quad \begin{bmatrix} \tilde{b}_{11} & \tilde{\mathbf{b}}_{12} \\ \tilde{\mathbf{b}}_{12}^T & \tilde{\mathbf{B}}_{11,1} \end{bmatrix}, \tag{6.48}$$

then (6.46) is equivalent to solving

$$y_{11} = \tilde{b}_{11}/2\sigma_1, \tag{6.49}$$
$$\sigma_1 \tilde{\mathbf{y}}_{12} + \tilde{\mathbf{y}}_{21}^T \mathbf{\Lambda}_{x,1} = \tilde{\mathbf{b}}_{12}, \tag{6.50}$$
$$\mathbf{\Lambda}_{x,1} \tilde{\mathbf{Y}}_{1,1} + \tilde{\mathbf{Y}}_{1,1}^T \mathbf{\Lambda}_{x,1} = \tilde{\mathbf{B}}_{11,1}. \tag{6.51}$$

Note that the solution to y_{11} in (6.49) is straightforward, however the solution to off-diagonal terms $\tilde{\mathbf{y}}_{12}, \tilde{\mathbf{y}}_{21}$ is underdetermined. Furthermore, since (6.51) is in form similar to (6.46), $\tilde{\mathbf{Y}}_{1,1}$ can be estimated recursively [Chu 1989]. Thus, the diagonal terms of the $P-$dimensional matrix $\tilde{\mathbf{Y}}_{1,1}$ can be estimated, however to resolve the ambiguity of the off-diagonal terms at least $\bar{P} = \binom{P}{2}$ constraints are required. $\square$

Appendix 6.B Karush-Kuhn-Tucker (KKT) system

A solution to minimize the equality constrained l_2 norm

$$\min_{\mathbf{y}} \|\mathbf{A}\mathbf{y} - \mathbf{b}\|^2 \quad \text{s.t.} \quad \mathbf{C}\mathbf{y} = \mathbf{d}, \tag{6.52}$$

is obtained by solving the Karush-Kuhn-Tucker system (KKT) equations [Boyd and Vandenberghe 2004],

$$\begin{bmatrix} \hat{\mathbf{y}} \\ \hat{\boldsymbol{\lambda}} \end{bmatrix} = \begin{bmatrix} 2\mathbf{A}^T\mathbf{A} & \mathbf{C}^T \\ \mathbf{C} & \mathbf{0}_{N_2,N_2} \end{bmatrix}^{-1} \begin{bmatrix} 2\mathbf{A}^T\mathbf{b} \\ \mathbf{d} \end{bmatrix}, \tag{6.53}$$

where $\hat{\mathbf{y}}$ is an estimate of the unknown parameter $\mathbf{y}$ and $\hat{\boldsymbol{\lambda}}$ collects the corresponding Lagrange multipliers. The problem has a feasible solution provided $\begin{bmatrix} \mathbf{A} \\ \mathbf{C} \end{bmatrix}$ is full column rank [Lawson and Hanson 1974].

Appendix 6.C Expression for $\mathbf{\Sigma}_{b,M}$

We present an explicit expression for the covariance matrix $\mathbf{\Sigma}_{b,M}$, which is obtained by ignoring higher order noise terms i.e., for sufficiently large SNR. For $M = 1$, i.e., relative velocity, we have

$$\mathbf{\Sigma}_{b,1} \approx \tilde{\mathbf{P}} \left(\mathbf{\Psi}_r \bar{\mathbf{\Sigma}}_{\dot{r}} \mathbf{\Psi}_r + \mathbf{\Psi}_{\dot{r}} \bar{\mathbf{\Sigma}}_r \mathbf{\Psi}_{\dot{r}} \right) \tilde{\mathbf{P}}, \tag{6.54}$$

and for $M = 2$, i.e., relative acceleration, we have

$$\Sigma_{b,2} \approx \tilde{\mathbf{P}}\Big(\mathbf{\Psi}_r\bar{\mathbf{\Sigma}}_{\ddot{r}}\mathbf{\Psi}_r + \mathbf{\Psi}_{\ddot{r}}\bar{\mathbf{\Sigma}}_r\mathbf{\Psi}_{\ddot{r}} + 4\mathbf{\Psi}_{\dot{r}}\bar{\mathbf{\Sigma}}_{\dot{r}}\mathbf{\Psi}_{\dot{r}}\Big)\tilde{\mathbf{P}} + 4\mathbf{\Psi}_y\bar{\mathbf{\Sigma}}_{\dot{x}}\mathbf{\Psi}_y, \quad (6.55)$$

where we $\tilde{\mathbf{P}} \triangleq \mathbf{P} \otimes \mathbf{P}$, $\mathbf{\Psi}_r \triangleq \text{diag}\big(\text{vec}(\mathbf{R})\big)$, $\mathbf{\Psi}_{\dot{r}} \triangleq \text{diag}\big(\text{vec}(\dot{\mathbf{R}})\big)$ and $\mathbf{\Psi}_{\ddot{r}} \triangleq$ $\text{diag}\big(\text{vec}(\ddot{\mathbf{R}})\big)$. The matrix $\mathbf{\Psi}_y = \mathbf{A}_{y,1}$ for absolute kinematics and $\mathbf{\Psi}_y = \underline{\mathbf{A}}_{y,1}$ for relative kinematics. Observe that the diagonal elements of the range paramet-ers $\mathbf{R}, \dot{\mathbf{R}}, \ddot{\mathbf{R}}, \ldots$ contain zeros and consequentially the matrices $\mathbf{\Psi}_r, \mathbf{\Psi}_{\dot{r}}, \mathbf{\Psi}_{\ddot{r}}, \ldots$ are singular. Hence the covariance matrix $\Sigma_{b,M}$ is in general rank deficient. Further-more, $\mathbf{A}_y$ in (6.33b) is rank deficient by definition and subsequently Σ_ρ (6.32) is ill-conditioned and therefore, we use the Moore-Penrose pseudo-inverse in (6.35) and (6.37). An expression for higher order $M > 2$ can be similarly derived.

7

Conclusions

In this chapter, the conclusions of this dissertation are summarized. In addition, suggestions to improve the proposed solutions are enlisted, along with directions for future work.

7.1   Summary and conclusions

The primary goal of this dissertation has been to estimate the time-varying positions and clock discrepancies of an anchorless mobile network, with no apriori absolute reference information of position or time. In particular, the quest has been to understand the relative space-time kinematics in Euclidean space, as formulated in Section 1.6.3. This research problem was further broken down into 4 key research questions, which were addressed in the various chapters of this dissertation, as laid out in Section 1.6.5. In Chapters 3-6, novel models and algorithms are proposed, to estimate the derivatives of relative position (i.e., relative kinematics) and the first-order clock model, given only two-way communication. One of the key motivations behind this dissertation topic is space-based radio astronomy at 0.3- 30MHz, which remains one of the last unexplored spectrum in radio astronomy (Chapter 2).

7.1.1   Space-based radio astronomy

Space-based ultra-long wavelength radio astronomy has come of age. In the past, studies were primarily limited by technology, as discussed in Chapter 2. However, recently completed studies such as DARIS and SURO-LC have shown the feasibility of a small satellite-array using off the shelf components. A satellite cluster of greater than 10 satellites equipped with dipole antennas and observing at $0.3 - 30$MHz for over a year is scientifically interesting, and meets the requirements for the extragalactic survey science cases in terms of resolution and sensitivity. The ultra-long wavelengths will be observed by all the satellites, each equipped with dipole antenna(s) and pre-processing block for signal conditioning and RFI mitigation. To minimize downlink data rate, all the satellites must communicate the observed data with each other and process the data on-board. In view of next generation arrays consisting of larger number of satellites, to avoid single point of failure, both centralized and distributed architectures are presented for communication and processing. The on-board processing for a cluster of 10 satellites can be easily performed using present day technology. However, the intra satellite communication and downlink of the processed data to Earth based communication appears to be the fundamental bottleneck.

The potential deployment location must be chosen to ensure, minimal RFI during radio astronomy observations, offer maximum downlink data rate and provide sufficient positional stability. Among all deployment locations discussed in this dissertation, the Lunar orbiting scenario emerges as the most favorable, since it meets almost all the requirements. There are numerous research areas which were identified during these feasibility studies, which include intra-satellite and downlink communication for larger arrays [Budianu 2015], antenna design for $0.3 - 30$MHz observational frequencies, efficient imaging techniques for ultra-long wavelength radio astronomy and investigating control and reliability of large satellite arrays [Engelen, Gill and Verhoeven 2014]. In addition, co-operative localization and synchronization of anchorless network of mobile nodes was recognized as a fundamental challenge during these studies, which is addressed in this dissertation.

7.1.2   Synchronization and ranging

The choice of clocks for ultra-long wavelength radio astronomy was discussed in Chapter 3. In particular, it was shown that if the Allan deviation of a given clock is sufficiently low, then the inherently non-linear clock model can be approximated up to the first order. Furthermore, a few commercially available clocks which meet these requirements were discussed.

In Chapter 4, the joint time-range basis is proposed, which combines the aforementioned linear clock model along with a $(L - 1)$th order Taylor approximation of the time-varying distance for a pair of mobile nodes. This joint time-range model is applied to the proposed GTWR framework, which is an extension of the classical TWR for a pair of fixed nodes. Least squares based solutions are proposed for network wide synchronization, namely MPLS and MGLS. Furthermore, when the order of distance approximation L is unknown, iterative solutions (iMPLS, iMGLS) are proposed for estimating the distance derivatives i.e., range parameters. A novel constrained Cramér-Rao bound is derived for the model, and simulation results show that the proposed estimators asymptotically achieve this bound.

The proposed estimators are part of a constrained framework, which allow additional knowledge of clock or distance to be incorporated. The solutions are for a full mesh network with two-way communication capability, however a robust synchronization is still feasible despite missing links. Furthermore, in search of an optimal choice of clock reference, two virtual clocks references are suggested. The Null constraint based clock reference is a data dependent reference, which is the most optimal reference in the l_2 sense. In comparison, the data independent sum constraint yields a near-optimal performance and does not need additional processing.

7.1.3   Relative kinematics in Euclidean space

The Chapters 5 and 6 exclusively focus on relative kinematics of N nodes in P dimensional Euclidean space where $N > P$. A novel relative localization framework is proposed for an anchorless network of mobile nodes, given only the time-varying pairwise distances. The Dynamic ranging algorithm employs a Taylor approximation of time-varying distance to obtain its derivatives. The proposed framework is similar to the joint time-range model proposed in the previous chapter, however is applicable to a synchronized network. Relative velocities (and higher order relative kinematics) are defined as an affine model of the absolute velocities (and corresponding higher order absolute kinematics).

In Chapter 5, under linear velocity assumption, the first 3 derivatives of time-varying distances are used to jointly estimate the relative positions, relative velocities and a unique rotation matrix. MDS-based algorithms are proposed to estimate the relative positions and velocities of the nodes, and total Least squares algorithm is proposed for the rotation matrix estimation. The LMDS algorithm, which is an extension of the MDS algorithm for mobile scenario, combines these estimates to provide the time-varying relative positions of the nodes. In addition, the CMDS algorithm is also proposed which yields the relative position and unique rotation matrices at each time instant. Simulation results show that the CMDS algorithm performs consistently over time, however in comparison, the LMDS algorithm shows improvement up to a factor $\sqrt{K}$. In addition, the LMDS algorithm and dynamic ranging allows incorporation of the Doppler measurements if available. For the generalized scenario of N mobile nodes in P dimensions, novel Cramér-Rao lower bounds are derived for the relative positions and relative velocities.

The LMDS and the CMDS algorithms are applicable only to mobile nodes under linear independent velocities. In search of higher order kinematics e.g., relative acceleration, a more generalized framework is proposed in Chapter 6 which relates the L derivatives of the time-varying distance to a Mth order relative kinematic of the mobile nodes. This relationship is bi-linear in form and is a Lyapunov-like equation, which is inherently ill posed. However, in the presence of some relative immobility constraints, the relative kinematics can be uniquely estimated. Constrained Least squares and Weighted Least squares solutions are proposed, and the estimated kinematics naturally yield the relative time-varying positions of the mobile nodes in non-linear motion. Cramér-Rao bounds are derived for the relative kinematic estimates, given the novel data model. The proposed algorithms in this chapter show significant improvement over the MDS based relative velocity algorithms in Chapter 5, despite the disadvantage of enforcing relative immobility constraints.

7.2 Directions for future work

The focus of this dissertation, particularly in Chapters 3-6, has been to "model" the problem of relative space-time estimation of an anchorless network. Therefore, there is a significant scope to improve the proposed estimators, and there are numerous directions for extending these solutions. A few possible extensions and other suggestions for future work are listed below.

1. **Improved joint synchronization and ranging:** The Least squares based solutions proposed for joint ranging and synchronization are suboptimal for heteroscedastic models, or when the noise between the various time markers are correlated. In such scenarios, a Weighted Least Squares algorithm with an appropriate weighting matrix would yield an optimal estimate (see Remark 3). Furthermore, throughout this dissertation we have considered Gaussian noise plaguing the data model for dynamic ranging, which may not always be valid. For instance, some experimental results have favored the use of exponential delay models [Moon, Skelly and Towsley 1999], for which Maximum-likelihood estimators (MLE) have been proposed [Abdel-Ghaffar 2002; Jeske 2005]. Along similar lines, optimal estimators in the presence of exponential (and other) noise distributions should be investigated for the proposed joint ranging and synchronization model.

2. **Joint relative space-time kinematics:** In Chapters 5-6, to estimate the relative kinematics, we assume the clocks in the nodes to be synchronized. Although this assumption is without loss of generality, for all practical purposes the nodes will be asynchronous. The clock errors would adversely affect the accuracy of the range parameters and subsequently the relative kinematic estimates. This can be resolved by jointly estimating the first-order clock coefficients, range parameters and the relative kinematics.

3. **On the choice of basis:** In Chapter 4, a Taylor basis is employed to estimate the clock discrepancies and time-varying distances. This is feasible since, both clock and distance are assumed to be continuous functions of time, and their respective derivatives exist up to the appropriate order. The advantage is that this approximation is exact at the given point and the estimated derivatives give physical insights the space-time variations. However, the approximation error in this representation gradually worsens when going away as observed in the simulations. The bottleneck can be overcome by employing an orthonormal basis; such as Legendre, splines or wavelets; for approximating the clock

model, or time-varying distance model or both [Vetterli, Kovačević and Goyal 2014, Chap. 4].

4. **Extension to other communication protocols:** The generalized two-way ranging is an extension of the pairwise TWR, which has been employed in this dissertation to estimate the relative space-time kinematics. More generally, the proposed framework can be extended towards broadcasting and passive listening protocols, which can possibly further improve the clock parameter estimates (see [Serpedin and Chaudhari 2009] and references therein). In particular, passive listening exploits more number of communication measurements in contrast to a full-mesh network employing TWR, and consequentially can offer better performance.

5. **Tracking the coefficients over time:** The proposed algorithms for estimating relative space-time kinematics of the mobile network are designed for *cold-start* scenarios, when there is no apriori information available. In practice, for longer time scales, a state-space based recursive Bayesian filter naturally emerges from the proposed framework, where in the predicted state equation can be readily constructed using the first-order derivative estimates i.e., clock offset and relative velocity. These filters include, for instance, the Kalman filter, unscented Kalman filter and particle filters [Särkkä 2013].

6. **Optimal relative kinematics:** In Chapter 5, for obtaining the relative position and relative velocity, the classical MDS algorithm is employed, which minimizes the Strain criterion and fits the double center semi-definite matrix by applying an eigenvalue decomposition. This approach is identical to kernel Principal component analysis (PCA), where the kernel is isotropic [Williams 2002]. The classic metric multidimensional scaling can be improved using Nyström methods, FastMDS or Isomap. Alternatively, estimators can also be designed using nonmetric MDS techniques which minimize the Stress function, or other numerous variants of Stress, for e.g., a majorization approach such as SMACOF. [Borg and Groenen 2005]. In Chapter 6, unbiased constrained Least squares solutions are proposed for estimating the relative kinematics of the Mth order. More generally, regularized solutions e.g., Tikhonov regularization can be investigated, for solving the rank-deficient Lyapunov-like equations[Boyd and Vandenberghe 2004].

7. **Distributed algorithms:** All the algorithms in this dissertation are inherently centralized, which in reality must be distributed to minimize the computation

overhead. The objective and the constraint functions of the proposed equality constrained least squares systems can be split, to employ distributed proximal algorithms such as the alternating direction method of multipliers (ADMM) [Parikh and Boyd 2014]. Similarly, the MDS based solutions can be solved frugally, for instance using the distributed variants of the SMACOF algorithm, such as Distributed weighted multidimensional scaling (DWMDS) [Costa, Patwari and Hero III 2006].

8. **Beyond the l_2 norm:** For a sufficiently large network exhibiting mobility sparsely, one can reconstruct the relative kinematics of the mobile nodes using compressive sensing (CS) techniques. This typically entails the minimization of the proposed estimator for joint synchronization and ranging, and relative kinematic estimation using l_1 minimization norm. For e.g., the joint ranging and synchronization Least squares algorithms can be solved in the l_1 sense, by using a greedy approach such as the Orthogonal Matching Pursuit (OMP).

9. **Beyond localization:** The spatial kinematic estimators in this dissertation are discussed in the context of relative localization, where time-varying distances are input measurements. However, more generally, these algorithms can also be applied to predict trends of mobile features in Euclidean space, given only time-varying proximity measurements. Such solutions can possibly find applications in time-varying scenarios of data reduction, manifold learning, data visualization, data pre-processing and in general exploratory multivariate analysis.

10. **Beyond Euclidean distance:** In the context of localization, throughout this dissertation the focus is on the study of kinematics of mobile nodes, where the metric used is Euclidean distances between the nodes i.e., l_2. More generally, time-varying systems with l_p distance metrics for $p \neq 2$ can also be investigated. These may lead to possible extensions of the Kruskals' original MDSCAL algorithm, which only exploits the proximity information between all the nodes at a single time frame [Cox and Cox 2000].

Glossary

Abbreviations and acronyms

ADC   analog to digital converter

AOCS   attitude and orbit control system

CRB   Cramér-Rao bound

CCRB   constrained Cramér-Rao bound

CSAC   chip scale atomic clock

DARIS   distributed aperture array for radio astronomy in space

DFT   discrete Fourier transform

DOA   direction of arrival

EDM   Euclidean distance matrix

ENOB   effective number of bits

ESA   European space agency

FFT   fast Fourier transform

FIM   Fisher information matrix

FLOPS   floating point operations

FX   Fourier transform followed by correlation

GTWR   generalized two-way ranging

Glossary

ISL	inter-satellite link
KKT	Karush-Kuhn-Tucker
LOFAR	low frequency array
MDS	multidimensional scaling
OBC	on-board computer
OCXO	oven-controlled crystal oscillator
OLFAR	orbiting low frequency antennas for radio astronomy
PFB	poly-phase filterbank
PSF	point spread function
RAFS	rubidium atomic frequency standard
RF	radio frequency
RFIM	radio frequency interference mitigation
S/H	sample and hold
SNR	signal to noise ratio
SPOF	single point of failure
SURO	space-based ultra-long wavelength radio observatory
TDOA	time difference of arrival
TOA	time of arrival
TWR	two-way ranging
ULW	ultra-long wavelength
VCSEL	vertical cavity surface emitting laser
WLS	weighted least squares
WSN	wireless sensor networks
XF	correlation followed by Fourier transform

Notations

Symbols

a, A	lower or uppercase characters denote scalars
$\mathbf{a}$	bold lower case characters denote column vectors
$\mathbf{A}$	bold upper case characters denote matrices
$\mathbb{R}$	space of real numbers
σ^2	variance
$\mathbf{I}_N$	$N \times N$ identity matrix
$\mathbf{1}_N$	$N \times 1$ column vector of ones
$\mathbf{0}_N$	$N \times 1$ column vector of zeros
$\mathbf{0}_{M,N}$	$M \times N$ matrix of zeros
j	square root of -1

Operators

$(\cdot)^T$	transpose
$\hat{(\cdot)}$	estimated value
$(\cdot)^\dagger$	Moore-penrose pseudo-inverse
$(\cdot)^{\odot N}$	element-wise matrix exponent
$\exp(\cdot)$	exponential function
$\mathrm{vec}(\cdot)$	vectorize matrix argument
$\mathrm{diag}(\cdot)$	diagonalize vector argument
$\mathrm{bdiag}(\cdot)$	block diagonal matrix from input arguments
$\mathrm{Tr}(\cdot)$	trace of a matrix

$\text{var}(\cdot)$	variance of the argument
$\|\cdot\|$	Euclidean norm
$\odot$	Hadamard or element-wise product of two matrices or vectors
$\oslash$	element-wise division of two matrices or vectors
$\otimes$	Kronecker product of two matrices or vectors
$\mathcal{N}(\mu, \sigma)$	normal distribution with mean μ and variance σ
$\mathcal{N}(\boldsymbol{\mu}, \boldsymbol{\Sigma})$	multivariate normal distribution with mean $\boldsymbol{\mu}$ and covariance $\boldsymbol{\Sigma}$

Matrix relations

In this dissertation, various matrix operators and properties are exploited, e.g., Kronecker and Hadamard products. Here is an overview of their definitions and some of the key properties.

Definition 1: Let $\mathbf{A}$ and $\mathbf{B}$ be matrices of dimensions $M \times N$ and $K \times L$ respectively, then the Kronecker product is a $MK \times NL$ block matrix defined as

$$\mathbf{A} \otimes \mathbf{B} = \begin{bmatrix} a_{11}\mathbf{B} & \dots & a_{1N}\mathbf{B} \\ \vdots & \ddots & \vdots \\ a_{M1}\mathbf{B} & \dots & a_{MN}\mathbf{B} \end{bmatrix}.$$

Definition 2: Let $\mathbf{A}$ and $\mathbf{B}$ be matrices of dimension $M \times N$, then the Hadmard product or element-wise product is a $M \times N$ matrix defined as

$$\mathbf{A} \odot \mathbf{B} = \begin{bmatrix} a_{11}b_{11} & \dots & a_{1N}b_{1N} \\ \vdots & \ddots & \vdots \\ a_{M1}b_{M1} & \dots & a_{MN}b_{MN} \end{bmatrix}.$$

Key properties: Let $\mathbf{A}, \mathbf{B}$ and $\mathbf{C}$ be matrices of compatible dimensions, then

$$\begin{aligned} (\mathbf{A} \otimes \mathbf{B})^T &= \mathbf{A}^T \otimes \mathbf{B}^T \\ \text{vec}(\mathbf{ABC}) &= (\mathbf{C}^T \otimes \mathbf{A})\text{vec}(\mathbf{B}) \\ \text{vec}(\mathbf{A}) &= \mathbf{J}\text{vec}(\mathbf{A}^T) \end{aligned}$$

where $\mathbf{J}$ is an orthogonal permutation matrix.

References

Abdel-Ghaffar, H. (2002). "Analysis of synchronization algorithms with time-out control over networks with exponentially symmetric delays". In: *Communications, IEEE Transactions on* 50.10, pp. 1652–1661.

Agrafiotis, D. K., D. N. Rassokhin and V. S. Lobanov (2001). "Multidimensional scaling and visualization of large molecular similarity tables". In: *Journal of Computational Chemistry* 22.5, pp. 488–500.

Ahmad, A. et al. (2013). "Joint node localization and time-varying clock synchronization in wireless sensor networks". In: *Wireless Communications, IEEE Transactions on* 12.10, pp. 5322–5333.

Airbus Defense and Space (2012). *Quartz crystal oscillators OCXO-F*. Tech. rep. Airbus Defense and Space.

— (2015). *Quartz crystal oscillators OCXO-H*. Tech. rep. Airbus Defense and Space.

Akyildiz, I. F., D. Pompili and T. Melodia (2005). "Underwater acoustic sensor networks: research challenges". In: *Ad hoc networks* 3.3, pp. 257–279.

Alexander, J. et al. (1974). "Scientific instrumentation of the Radio Astronomy Explorer 2 satellite". In: *NASA STI/Recon Technical Report N* 75, p. 18284.

Allan, D. W., N. Ashby and C. C. Hodge (1997). *The science of timekeeping*. Hewlett-Packard.

Allan, D. (1987). "Time and Frequency (Time-Domain) Characterization, Estimation, and Prediction of Precision Clocks and Oscillators". In: *IEEE Transactions on Ultrasonics, Ferroelectrics and Frequency Control* 34.6, pp. 647 –654.

Altunin, V. (2001). "Protecting Space-Based Radio Astronomy". In: *Preserving the Astronomical Sky*. Ed. by R. J. Cohen and W. T. Sullivan. Vol. 196. IAU Symposium, p. 324.

Aminaei, A. et al. (2014). "Basic radio interferometry for future lunar missions". In: *2014 IEEE Aerospace Conference*. IEEE, pp. 1–19.

References

Arnold, S. (2014). "The History of Radio Astronomy". In: *Getting Started in Radio Astronomy*. Springer, pp. 1–32.

Arts, M., E. van der Wal and A.-J. Boonstra (2010). "Antenna concepts for a space-based low-frequency radio telescope". In: *ESA Antenna Workshop on Antennas for Space Applications, Noordwijk*, pp. 5–8.

Ash, J. and R. Moses (2008). "On the Relative and Absolute Positioning Errors in Self-Localization Systems". In: *IEEE Transactions on Signal Processing* 56.11, pp. 5668 –5679.

Atwood, W. et al. (2009). "The Large Area Telescope on the Fermi gamma-ray space telescope mission". In: *The Astrophysical Journal* 697.2, p. 1071.

Baan, W (2012). "SURO-LC: A space-based ultra-long wavelength radio observatory". In: *Proceedings of the meeting 'From Antikythera to the Square Kilometre Array: Lessons from the Ancients' (Antikythera & SKA). 12-15 June 2012. Kerastari, Greece.* Vol. 1, p. 45.

Barnes, J. A. et al. (1971). "Characterization of Frequency Stability". In: *Instrumentation and Measurement, IEEE Transactions on* IM-20.2, pp. 105 –120.

Bartels, R. H. and G.W.Stewart (1972). "Solution of the matrix equation $AX+XB = C$". In: *Communications of the ACM* 15.9, pp. 820–826.

Basart, J. et al. (1997a). "Directions for space-based low frequency radio astronomy: 1. System considerations". In: *Radio Science* 32.1, pp. 251–263.

— (1997b). "Directions for Space-Based Low-Frequency Radio Astronomy: 2. Telescopes". In: *Radio Science* 32.1, pp. 265–275.

Bellusci, G. et al. (2008). "Low complexity ultra-wideband ranging in indoor multipath environments". In: *Position, Location and Navigation Symposium, 2008 IEEE/ION*, pp. 394–401.

Bentum, M. et al. (2009). "A novel astronomical application for formation flying small satellites". In: *60th International Astronautical Congress: IAC 2009, 12-16 October 2009, Daejeon, Republic of Korea.*

Bentum, M. and A. Boonstra (2011). "Low frequency astronomy - The challenge in a crowded RFI environment". In: *General Assembly and Scientific Symposium, 2011 XXXth URSI*. IEEE, pp. 1–4.

Bergman, J. E. S. et al. (2009). "FIRST Explorer – An innovative low-cost passive formation-flying system". In: *arXiv* arXiv:0911.0991. arXiv: `0911.0991 [astro-ph.IM]`.

Bertrand, A. and M. Moonen (2011). "Consensus-Based Distributed Total Least Squares Estimation in Ad Hoc Wireless Sensor Networks". In: *IEEE Transactions on Signal Processing* 59.5, pp. 2320 –2330.

Bhatia, R. and P. Rosenthal (1997). "How and why to solve the operator equation $AX - XB = Y$". In: *Bulletin of the London Mathematical Society* 29.1, pp. 1–21.

Bik, J., P. Visser and O Jennrich (2007). "LISA satellite formation control". In: *Advances in Space Research* 40.1, pp. 25–34.

Boonstra, A.-J. et al. (2010). "DARIS, A low-frequency distributed aperture array for radio astronomy in space". In: *61st International Astronautical Congress*. IAC.

Boonstra, A.-J. et al. (2011). *DARIS: Distributed aperture array for radio astronomy in space*. Report ESA-ESTEC Contract Number 22109/08/NL/ST. ASTRON, Dwingeloo.

Borg, I. and P. J. F. Groenen (2005). *Modern Multidimensional Scaling: Theory and Applications (Springer Series in Statistics)*. 2nd. Springer.

Boyd, S. and L. Vandenberghe (2004). *Convex Optimization*. Cambridge University Press.

Braden, H. (1998). "The equations $A^T X \pm X^T A = B$". In: *SIAM Journal on Matrix Analysis and Applications* 20.2, pp. 295–302.

Budianu, A., A. Meijerink and M. Bentum (2015). "Swarm-to-Earth communication in {OLFAR}". In: *Acta Astronautica* 107.0, pp. 14 –19.

Budianu, A. et al. (2011). "OLFAR: Adaptive topology for satellite swarms". In: *International Astronautical Congress, Cape Town*, pp. 3–7.

Budianu, A. (2015). "Echoes from the past: the communication layer of a nanosatellite swarm". PhD thesis.

Budianu, A. et al. (2013). "Inter-satellite links for cubesats". In: *IEEE Aerospace Conference*, pp. 1–10.

Bunton, J. (2004). "SKA Correlator Advances". In: *Experimental Astronomy* 17 (1), pp. 251–259.

Burke, B. F. (1990). "Astrophysics from the Moon". In: *Science* 250.4986, pp. 1365–1370.

Bürkle, A., F. Segor and M. Kollmann (2011). "Towards autonomous micro UAV swarms". In: *Journal of intelligent & robotic systems* 61.1-4, pp. 339–353.

Burns, J. (1990). "The Lunar Observer radio astronomy experiment (LORAE)". In: *Low frequency astrophysics from space*, pp. 19–28.

Burns, J. O. et al. (1990). "Observatories on the Moon". In: *Scientific American* 262, pp. 42–49.

Burns, J. O. et al. (2012). "Probing the first stars and black holes in the early Universe with the Dark Ages Radio Explorer (DARE)". In: *Advances in Space Research* 49.3, pp. 433–450.

References

Čapkun, S., M. Hamdi and J.-P. Hubaux (2002). "GPS-free positioning in mobile ad hoc networks". In: *Cluster Computing* 5.2, pp. 157–167.

Carvalho, E. de, J. Cioffi and D. Slock (2000). "Cramér-Rao bounds for blind multichannel estimation". In: *IEEE Global Telecommunications Conference* 2, pp. 1036–1040.

Chan, Y. and K. Ho (1994). "A simple and efficient estimator for hyperbolic location". In: *Signal Processing, IEEE Transactions on* 42.8, pp. 1905–1915.

Chandrasekhar, V. et al. (2006). "Localization in underwater sensor networks: survey and challenges". In: *Proceedings of the 1st ACM international workshop on Underwater networks*. ACM, pp. 33–40.

Chang, C. and A. Sahai (2006). "Cramér-Rao-Type Bounds for Localization". In: *EURASIP Journal on Applied Signal Processing*, pp. 1–14.

Cheung, K. and H. So (2005). "A multidimensional scaling framework for mobile location using time-of-arrival measurements". In: *IEEE Transactions on Signal Processing* 53.2, pp. 460–470.

Cheung, K. et al. (2004). "Least squares algorithms for time-of-arrival-based mobile location". In: *Signal Processing, IEEE Transactions on* 52.4, pp. 1121–1130.

Chiang, C.-Y., E. K.-W. Chu and W.-W. Lin (2012). "On the $\star-$Sylvester equation $AX \pm X^\star B^\star = C$". In: *Applied Mathematics and Computation* 218.17, pp. 8393–8407.

Chikada, Y. et al. (1987). "A 6 x 320-MHz 1024-channel FFT cross-spectrum analyzer for radio astronomy". In: *Proceedings of the IEEE* 75.9, pp. 1203–1210.

Chu, K.-w. E. (1989). "Symmetric solutions of linear matrix equations by matrix decompositions". In: *Linear Algebra and its Applications* 119, pp. 35–50.

Cohen, A. (2004). *Estimates of the classical confusion limit for the LWA*. Long Wavelength Array Memo Series 17. Washington, DC 20375: Naval Research Laboratory.

Costa, J. A., N. Patwari and A. O. Hero III (2006). "Distributed weighted multidimensional scaling for node localization in sensor networks". In: *ACM Transactions on Sensor Networks (TOSN)* 2.1, pp. 39–64.

Cox, T. F. and M. A. Cox (2000). *Multidimensional scaling*. CRC press.

De Vos, M., A. Gunst and R. Nijboer (2009). "The LOFAR Telescope: System Architecture and Signal Processing". In: *Proceedings of the IEEE* 97.8, pp. 1431–1437.

Dil, B., S. Dulman and P. Havinga (2006). "d". In: *Wireless Sensor Networks*. Springer, pp. 164–179.

Droz, F. et al. (2007). "Galileo Rubidium Standard - Lifetime data and GIOVE-A related telemetries". In: *21st European Frequency and Time Forum*. IEEE, pp. 1122–1126.

"Dynamics of Multibody Systems" (2008). In: Berlin, Heidelberg: Springer Berlin Heidelberg. Chap. Rigid Body Kinematics, pp. 9–36.

Ellingson, S. et al. (2009). "The Long Wavelength Array". In: *Proceedings of the IEEE* 97.8, pp. 1421 –1430.

Elson, J. and K. Römer (2003). "Wireless sensor networks: A new regime for time synchronization". In: *ACM SIGCOMM Computer Communication Review* 33.1, pp. 149–154.

Elson, J. E. and D. Estrin (2003). "Time synchronization in wireless sensor networks". PhD thesis. University of California, Los Angeles.

Engelen, S., E. Gill and C. Verhoeven (2014). "On the reliability, availability, and throughput of satellite swarms". In: *IEEE Transactions on Aerospace and Electronic Systems* 50.2, pp. 1027–1037.

Etzlinger, B., H. Wymeersch and A Springer (2014). "Cooperative Synchronization in Wireless Networks". In: *Signal Processing, IEEE Transactions on* 62.11, pp. 2837–2849.

Etzlinger, B. et al. (2013). "Cooperative simultaneous localization and synchronization: A distributed hybrid message passing algorithm". In: *Signals, Systems and Computers, 2013 Asilomar Conference on*. IEEE, pp. 1978–1982.

Falcke, H et al. (2005). "Detection and imaging of atmospheric radio flashes from cosmic ray air showers". In: *Nature* 435.7040, pp. 313–316.

Forero, P. A. and G. B. Giannakis (2012). "Sparsity-Exploiting Robust Multidimensional Scaling". In: *IEEE Transactions on Signal Processing* 60.8, pp. 4118–4134.

Freris, N., S. Graham and P. Kumar (2010). "Fundamental limits on synchronizing clocks over networks". In: *Automatic Control, IEEE Transactions on*.

Golub, G. H., P. C. Hansen and D. P. O'Leary (1999). "Tikhonov regularization and total least squares". In: *SIAM Journal on Matrix Analysis and Applications* 21.1, pp. 185–194.

Golub, G. H. and C. F. Van Loan (2012). *Matrix computations*. JHU Press.

Golub, G. H., S. Nash and C. Van Loan (1979). "A Hessenberg-Schur method for the problem AX+ XB= C". In: *IEEE Transactions on Automatic Control* 24.6, pp. 909–913.

Gorgolewski, S (1965). "The Advantages of a Lunar Radio Astronomy Observatory". In: *Astronautica Acta, New New Series* 11.2, pp. 130–131.

References

Goujon, D et al. (2010). "Development of the Space active Hydrogen Maser for the ACES Mission". In: *EFTF-2010 24th European Frequency and Time Forum*. IEEE, pp. 1–6.

Gunst, A. W. and G. Schoonderbeek (2007). *LOFAR Station Architecture document*. Tech. rep. LOFAR-ASTRON-ADD-013. ASTRON.

Gurvits, L (2012). "Space radio astronomy in the next 1000001 (binary) years". In: *Resolving The Sky-Radio Interferometry: Past, Present and Future*. Vol. 1, p. 45.

Halliday, D., R. Resnick and J. Walker (2010). *Fundamentals of physics extended*. Vol. 1. John Wiley & Sons.

Haslam, C. et al. (1982). "A 408 MHz all-sky continuum survey. II-The atlas of contour maps". In: *Astronomy and Astrophysics Supplement Series* 47, p. 1.

Hirabayashi, H. et al. (2000). "The VLBI space observatory programme and the radio-astronomical satellite HALCA". In: *Publications of the Astronomical Society of Japan* 52.6, pp. 955–965.

Ho, C.-C., K. F. MacDorman and Z. D. Pramono (2008). "Human emotion and the uncanny valley: a GLM, MDS, and Isomap analysis of robot video ratings". In: *Proceedings of the 3rd ACM/IEEE international conference on Human robot interaction*. ACM, pp. 169–176.

Hodges, J. H. (1957). "Some matrix equations over a finite field". In: *Annali di Matematica Pura ed Applicata* 44.1, pp. 245–250.

Horn, R. and C. R. Johnson (1991). *Topics in matrix analysis*. Cambridge University Press.

IEEE Working Group 802.15.4 (2007). *Part 15.4: Wireless medium access control (MAC) and physical layer (PHY) specifications for low-rate wireless personal area networks (WPANs)*. Tech. rep. IEEE.

Jamali-Rad, H. and G. Leus (2012). "Dynamic multidimensional scaling for low-complexity mobile network tracking". In: *Signal Processing, IEEE Transactions on* 60.8, pp. 4485–4491.

Jansen, F et al. (2001). "Xmm-newton observatory-i. the spacecraft and operations". In: *Astronomy & Astrophysics* 365.1, pp. L1–L6.

Jenkins, O. C. and M. J. Matarić (2004). "A spatio-temporal extension to isomap nonlinear dimension reduction". In: *Proceedings of the twenty-first international conference on Machine learning*. ACM, p. 56.

Jeske, D. R. (2005). "On maximum-likelihood estimation of clock offset". In: *Communications, IEEE Transactions on* 53.1, pp. 53–54.

Jester, S. and H. Falcke (2009). "Science with a lunar low-frequency array: From the dark ages of the Universe to nearby exoplanets". In: *New Astronomy Reviews* 53, pp. 1–26. arXiv: 0902.0493 [astro-ph.CO].

Jia, T. and R. Buehrer (2008). "A new Cramer-Rao lower bound for TOA-based localization". In: *Military Communications Conference, 2008. MILCOM 2008. IEEE*, pp. 1 –5.

Jones, D. L. et al. (2007). "Towards a lunar epoch of reionization telescope". In: *Bulletin of the American Astronomical Society*. Vol. 39, p. 196.

Jones, D. et al. (2000). "The ALFA medium explorer mission". In: *Advances in Space Research* 26.4, pp. 743–746.

Kaiser, M. L. and K. W. Weiler (2000). "The Current Status of Low Frequency Radio Astronomy from Space". In: *Geophysical monograph* 119, pp. 1–11.

Kaplan, E. D. and C. J. Hegarty (2006). *Understanding GPS: principles and applications*. Artech House Publishers.

Kardashev, N. et al. (2013). ""RadioAstron"-A telescope with a size of 300 000 km: Main parameters and first observational results". In: *Astronomy Reports* 57.3, pp. 153–194.

Kassim, N. E. et al. (1993). "Subarcminute resolution imaging of radio sources at 74 MHz with the Very Large Array". In: *The Astronomical Journal* 106, pp. 2218–2228.

Kay, S. M. (1993). *Fundamentals of statistical signal processing: estimation theory*. Upper Saddle River, NJ, USA: Prentice-Hall, Inc.

Kester, W. (2004). *Analog-Digital Conversion*. Tech. rep. Analog Devices.

Klein-Wolt M. et al. (2013). "Dark ages EXplorer, DEX, A white paper for a low frequency radio interferometer mission to explore the cosmological Dark Ages for the L2". L3 ESA Cosmic Vision Program.

Knappe, S et al. (2004). "A microfabricated atomic clock". In: *Applied Physics Letters* 85.9, pp. 1460–1462.

Koehler, M. et al. (2005). "Measuring depression in nursing home residents with the MDS and GDS: an observational psychometric study". In: *BMC geriatrics* 5.1, p. 1.

Kruskal, J. B. (1964). "Multidimensional scaling by optimizing goodness of fit to a nonmetric hypothesis". In: *Psychometrika* 29.1, pp. 1–27.

Kuiper, T. and D Jones (2000). "Lunar surface arrays". In: *Radio Astronomy at Long Wavelengths*, pp. 351–357.

Lawson, C. L. and R. J. Hanson (1974). *Solving least squares problems*. Vol. 161. SIAM.

Leng, M. and Y.-C. Wu (2010). "On Clock Synchronization Algorithms for Wireless Sensor Networks Under Unknown Delay". In: *IEEE Transactions on Vehicular Technology* 59.1, pp. 182 –190.

References

Lindsey, W. et al. (1985). "Network synchronization". In: *Proceedings of the IEEE* 73.10, pp. 1445–1467.

Linfield, R. et al. (1996). "A test of water vapor radiometer-based troposphere calibration using very long baseline interferometry observations on a 21-km baseline". In: *Radio Science* 31.1, pp. 129–146.

Liu, H. et al. (2007). "Survey of wireless indoor positioning techniques and systems". In: *Systems, Man, and Cybernetics, Part C: IEEE Transactions on Applications and Reviews* 37.6, pp. 1067–1080.

Lombardi, M. A. et al. (2001). "Time and Frequency Measurements Using the Global Positioning System". In: *Cal Lab*, pp. 26–33.

Lonsdale, C. et al. (2009). "The Murchison Widefield Array: Design Overview". In: *Proceedings of the IEEE* 97.8, pp. 1497–1506.

Maccone, C. (2005). "NASA gateways at L1 and L2 and the radio-quiet Moon Farside imperative". In: *Acta Astronautica* 57. Selected Proceedings of the 55th International Astronautical Federation Congress, Vancouver, Canada, 4-8 October 2004, pp. 145 –155.

Manning, R. (2000). "Instrumentation for space-based low frequency radio astronomy". In: *Geophysical Monograph Series* 119, pp. 329–337.

Mao, G., B. Fidan and B. D. Anderson (2007). "Wireless sensor network localization techniques". In: *Computer Networks* 51.10, pp. 2529 –2553.

Markley, F. L. and J. L. Crassidis (2014). *Fundamentals of Spacecraft Attitude Determination and Control*. Vol. 33. Springer.

Mautz, R. (2012). "Indoor positioning technologies". PhD thesis. Habilitationsschrift ETH Zürich, 2012.

Moon, S. B., P. Skelly and D. Towsley (1999). "Estimation and removal of clock skew from network delay measurements". In: *INFOCOM'99. Eighteenth Annual Joint Conference of the IEEE Computer and Communications Societies. Proceedings. IEEE*. Vol. 1. IEEE, pp. 227–234.

Naghshvar, M., H. Zhuang and T. Javidi (2012). "A general class of throughput optimal routing policies in multi-hop wireless networks". In: *IEEE Transactions on Information Theory* 58.4, pp. 2175–2193.

Nee, R. v. and R. Prasad (2000). *OFDM for wireless multimedia communications*. Artech House, Inc.

Noh, K.-L. et al. (2007). "Novel Clock Phase Offset and Skew Estimation Using Two-Way Timing Message Exchanges for Wireless Sensor Networks". In: *IEEE Transactions on Communications* 55.4, pp. 766 –777.

Novaco, J. C. and L. W. Brown (1978). "Nonthermal galactic emission below 10 megahertz". In: *The Astrophysical Journal* 221, pp. 114–123.

Oberoi, D. and J.-L. Pincon (2005). "A new design for a very low frequency space-borne radio interferometer". In: *Radio science* 40.4.

Parikh, N. and S. P. Boyd (2014). "Proximal Algorithms." In: *Foundations and Trends in optimization* 1.3, pp. 127–239.

Patwari, N. et al. (2003). "Relative location estimation in wireless sensor networks". In: *IEEE Transactions on Signal Processing* 51.8, pp. 2137–2148.

Patwari, N. et al. (2005). "Locating the nodes: Cooperative localization in wireless sensor networks". In: *IEEE Signal Processing Magazine* 22.4, pp. 54 –69.

Penzl, T. (1998). "Numerical solution of generalized Lyapunov equations". In: *Advances in Computational Mathematics* 8.1-2, pp. 33–48.

Priyantha, N. B. et al. (2003). "Anchor-free distributed localization in sensor networks". In: *Proceedings of the 1st international conference on Embedded networked sensor systems*. ACM, pp. 340–341.

Quillien, K. et al. (2013). "Astronomical Antenna for a Space Based Low Frequency Radio Telescope". In: *27th Conference on Small Satellites*, pp. 1–4.

Rajan, R. T., M. Bentum and A.-J. Boonstra (2013). "Synchronization for space based ultra low frequency interferometry". In: *2013 IEEE Aerospace Conference*, pp. 1–8.

Rajan, R. T., G. Leus and A.-J. van der Veen (2015). "Joint relative position and velocity estimation for an anchorless network of mobile nodes". In: *Signal Processing* 115.0, pp. 66 –78.

Rajan, R. T. and A.-J. van der Veen (2011). "Joint ranging and clock synchronization for a wireless network". In: *2011 4th IEEE International Workshop on Computational Advances in Multi-Sensor Adaptive Processing (CAMSAP)*, pp. 297 –300.

— (2012). "Joint motion estimation and clock synchronization for a wireless network of mobile nodes". In: *IEEE International Workshop on Acoustics, Speech, and Signal Processing (ICASSP)*, pp. 2845–2848.

— (2013). "Joint non-linear ranging and affine synchronization basis for a network of mobile nodes". In: *21st European Signal Processing Conference (EUSPICO)*, pp. 1–5.

— (2015). "Joint Ranging and Synchronization for an Anchorless Network of Mobile Nodes". In: *IEEE Transactions on Signal Processing,* 63.8, pp. 1925–1940.

Rajan, R. T. et al. (2011). "Orbiting Low Frequency Array for Radio astronomy". In: *IEEE Aerospace Conference*, pp. 1 –11.

Rajan, R. T. et al. (2013). "Distributed correlators for interferometry in space". In: *2013 IEEE Aerospace Conference*, pp. 1–9.

References

Rajan, R. T. et al. (2016). "Space-based aperture array for ultra-long wavelength radio astronomy". In: *Experimental Astronomy* 41.1, pp. 271–306.

Rehm, F., F. Klawonn and R. Kruse (2005). "MDS polar: a new approach for dimension reduction to visualize high dimensional data". In: *Advances in Intelligent Data Analysis VI*. Springer, pp. 316–327.

Richard Thompson.A James M. Moran, G. W. S. J. (1994). *Interferometry and Synthesis in Radio astronomy*. KRIENGER.

Riess, A. G. et al. (1998). "Observational evidence from supernovae for an accelerating universe and a cosmological constant". In: *The Astronomical Journal* 116.3, p. 1009.

Riley, W. (2008). *Handbook of Frequency*. Special Publication 1065. NIST.

Romney.J.D (1999). "Cross Correlators". In: *Synthesis Imaging in Radio Astronomy*.

Röttgering, H. et al. (2011). "LOFAR and APERTIF surveys of the radio sky: probing shocks and magnetic fields in galaxy clusters". In: *Journal of Astrophysics and Astronomy* 32.4, pp. 557–566.

Saks, N. et al. (2010). "DARIS, A Fleet of Passive Formation Flying Small Satellites for Low Frequency Radio Astronomy". In: *The 4S Symposium (Small Satellites Systems & Services Symposium), Madeira, Portugal, 31 May - 4 June 2010 (ESA and CNES conference)*.

Samama, N. (2007). "A Brief History of Navigation and Positioning". In: *Global Positioning*. John Wiley & Sons, Inc., pp. 1–27.

Särkkä, S. (2013). *Bayesian filtering and smoothing*. Vol. 3. Cambridge University Press.

Sayed, A., A Tarighat and N. Khajehnouri (2005a). "Network-based wireless location: challenges faced in developing techniques for accurate wireless location information". In: *IEEE Signal Processing Magazine* 22.4, pp. 24–40.

Sayed, A. H., A. Tarighat and N. Khajehnouri (2005b). "Network-based wireless location: challenges faced in developing techniques for accurate wireless location information". In: *Signal Processing Magazine, IEEE* 22.4, pp. 24–40.

Schönemann, P. (1966). "A generalized solution of the orthogonal Procrustes problem". English. In: *Psychometrika* 31.1, pp. 1–10.

Serkland, D. K. et al. (2006). "VCSELs for atomic clocks". In: *Integrated Optoelectronic Devices 2006*. International Society for Optics and Photonics, pp. 613208–613208.

Serpedin, E. and Q. M. Chaudhari (2009). *Synchronization in Wireless Sensor Networks: Parameter Estimation, Peformance Benchmarks, and Protocols*. 1st. New York, NY, USA: Cambridge University Press.

Shang, Y. and W. Ruml (2004). "Improved MDS-based localization". In: *INFOCOM 2004. Twenty-third AnnualJoint Conference of the IEEE Computer and Communications Societies*. Vol. 4. IEEE, pp. 2640–2651.

Smith, D. and M. Arts (2013). "Characterization of Astronomical Antenna for Space based low frequency radio telescope". In: *IEEE Aerospace Conference, March 2-9, 2013, Big Sky, Montana US*.

Smith, H. J. (1990). "Very low frequency radio astronomy from the moon". In: *Low Frequency Astrophysics from Space*. Springer, pp. 29–33.

Sodnik, Z., B. Furch and H. Lutz (2006). "Free-Space Laser Communication Activities in Europe: SILEX and beyond". In: *19th Annual Meeting of the IEEE Lasers and Electro-Optics Society (LEOS)*, pp. 78–79.

Stanford (2006). *PRS10-Rubidium frequency standard*. Tech. rep. Stanford.

Stappers, B. et al. (2011). "Observing pulsars and fast transients with LOFAR". In: *Astronomy & Astrophysics* 530, A80.

Stoica, P. and B. C. Ng (1998). "On the Cramer-Rao Bound under parametric constraints". In: *IEEE Signal Processing Letters* 5.7, pp. 177–179.

Sundararaman, B., U. Buy and A. D. Kshemkalyani (2005). "Clock synchronization for wireless sensor networks: a survey". In: *Ad Hoc Networks* 3.3, pp. 281 –323.

Takahashi, Y. D. (2003). "A concept for a simple radio observatory at the lunar south pole". In: *Advances in Space Research* 31.11, pp. 2473–2478.

Taylor, G. B., C. L. Carilli and R. A. Perley, eds. (1999). *Synthesis Imaging in Radio Astronomy II*. Vol. 180. Astronomical Society of the Pacific Conference Series. Socorro, New Mexico: Astronomical Society of the Pacific.

Thompson, A. R., James.M.Moran and G. W. Swenson (1994). "Interferometry and Synthesis in Radio Astronomy". In: Krieger publishing company. Chap. Phase stability and Atomic frequency standards, pp. 269–291.

Thompson, A. R., J. M. Moran and G. W. Swenson Jr (2008). *Interferometry and synthesis in radio astronomy*. John Wiley & Sons.

Tibshirani, R. (1996). "Regression shrinkage and selection via the lasso". In: *Journal of the Royal Statistical Society. Series B (Methodological)*, pp. 267–288.

Toyoshima, M. (2005). "Trends in satellite communications and the role of optical free-space communications". In: *Journal of Optical Networking* 4.6, pp. 300–311.

Ulvestad, J. S., C. D. Edwards and R. P. Linfield (1986). *Very Long baseline Interferometry using a radio telescope in Earth orbit*. Tech. rep. 42-88. JPL.

van Haarlem, M. P et al. (2013). "LOFAR: The LOw-Frequency ARray". In: *Astronomy & Astrophysics* 556, A2, A2. arXiv: 1305.3550 [astro-ph.IM].

References

Vassallo, E. et al. (2007). "The European Space Agency's Deep-Space Antennas". In: *Proceedings of the IEEE* 95.11, pp. 2111–2131.

Vetterli, M., J. Kovačević and V. K. Goyal (2014). *Foundations of signal processing*. Cambridge University Press.

Viklands, T. (2006). "Algorithms for the weighted orthogonal Procrustes problem and other least squares problems". PhD thesis. Umeå University, Umeå, Sweden.

Wang, J., R. K. Ghosh and S. K. Das (2010). "A survey on sensor localization". In: *Journal of Control Theory and Applications* 8.1, pp. 2–11.

Wang, Y., X. Ma and G. Leus (2011a). "Robust Time-Based Localization for Asynchronous Networks". In: *IEEE Transactions on Signal Processing* 59.9, pp. 4397 –4410.

Wang, Y., X. Ma and G. Leus (2011b). "Robust time-based localization for asynchronous networks". In: *Signal Processing, IEEE Transactions on* 59.9, pp. 4397– 4410.

Weber, R., J. Alexander and R. Stone (1971). "The Radio Astronomy Explorer Satellite, a Low-Frequency Observatory". In: *Radio Science* 6.12, pp. 1085–1097.

Wei, H.-W. et al. (2010). "Multidimensional Scaling Analysis for Passive Moving Target Localization With TDOA and FDOA Measurements". In: *IEEE Transactions on Signal Processing* 58.3, pp. 1677 –1688.

Weiler, K. W. (2000). *The promise of long wavelength radio astronomy*. Vol. 119. AGU AMERICAN GEOPHYSICAL UNION, pp. 243–256.

Weiler, K. et al. (1988). "A low frequency radio array for space". In: *Astronomy and Astrophysics* 195, pp. 372–379.

Weisskopf, M. C. et al. (2000). "Chandra X-ray Observatory (CXO): overview". In: *Astronomical Telescopes and Instrumentation*. International Society for Optics and Photonics, pp. 2–16.

Wijnholds, S. and A. J. van der Veen (2006). "Effects of Parametric Constraints on the CRLB in Gain and Phase Estimation Problems". In: *IEEE Signal Processing Letters* 13.10, pp. 620 –623.

Wijnholds, S. J. et al. (2010). "Calibration challenges for future radio telescopes". In: *IEEE Signal Processing Magazine* 27.1, pp. 30–42.

Wikipedia (2008). *Atmospheric electromagnetic transmittance or opacity*. Tech. rep. Wikipedia.

Williams, C. K. (2002). "On a connection between kernel PCA and metric multidimensional scaling". In: *Machine Learning* 46.1-3, pp. 11–19.

Wilson, T. L., K. Rohlfs and S. Hüttemeister (2009). *Tools of radio astronomy*. Vol. 86. Springer.

Woan, G (1999). "A very low frequency radio telescope on the far side of the moon". In: *Measuring the Size of Things in the Universe: HBT Interferometry and Heavy Ion Physics*. Vol. 1, p. 347.

Wu, Y.-C., Q. Chaudhari and E. Serpedin (2011). "Clock Synchronization of Wireless Sensor Networks". In: *Signal Processing Magazine, IEEE* 28.1, pp. 124 –138.

Xie, Y., G. J. Janssen and A.-J. van der Veen (2016). "A practical clock synchronization algorithm for UWB positioning systems". In: *2016 IEEE International Conference on Acoustics, Speech and Signal Processing (ICASSP)*. IEEE, pp. 3891–3895.

Yang, Z., C. Wu and Y. Liu (2012). "Locating in fingerprint space: wireless indoor localization with little human intervention". In: *Proceedings of the 18th annual international conference on Mobile computing and networking*. ACM, pp. 269–280.

Young, F. W. (2013). *Multidimensional scaling: History, theory, and applications*. Psychology Press.

Zaroubi, S et al. (2012). "Imaging neutral hydrogen on large scales during the Epoch of Reionization with LOFAR". In: *Monthly Notices of the Royal Astronomical Society* 425.4, pp. 2964–2973.

Zhang, L., Z. Liu and C. Honghui Xia (2002). "Clock synchronization algorithms for network measurements". In: *INFOCOM 2002. Twenty-First Annual Joint Conference of the IEEE Computer and Communications Societies. Proceedings. IEEE*. Vol. 1, 160–169 vol.1.

Zheng, J. and Y.-C. Wu (2010). "Joint Time Synchronization and Localization of an Unknown Node in Wireless Sensor Networks". In: *IEEE Transactions on Signal Processing* 58.3, pp. 1309 –1320.

Zhu, S. and Z. Ding (2010). "Joint synchronization and localization using TOAs: A linearization based WLS solution". In: *Selected Areas in Communications, IEEE Journal on* 28.7, pp. 1017 –1025.

References

Propositions

1. In an era of cheaper, lighter and more accurate clocks, the first-order model is a sufficient representation of the clock discrepancies for a certain coherence time (*this thesis, Chapter 3*)

2. For a cluster of asynchronous mobile nodes, both the clock discrepancies and the time-varying pairwise distance in Euclidean space can be jointly estimated under non-relativistic conditions (*this thesis, Chapter 4*)

3. Under independent linear-velocity assumptions, the relative velocities of an anchorless network of mobile nodes can be estimated via time-varying pairwise distance measurements (*this thesis, Chapter 5*)

4. The generalized Mth order relative kinematic motion of an anchorless network of mobile nodes can be estimated under certain relative immobility constraints, although common sense dictates this assumption is not needed (*this thesis, Chapter 6*)

5. Space-based radio astronomy for ultra-long wavelength observations has come of age, but lacks political will and therefore funding for a launch

6. All models are approximations, some approximately better than the rest –an ode to *George E. P. Box*

7. The failure to value life and respect natural resources is the most expensive crime of man kind

8. Every person is an embodiment of the opportunities presented to them, the choices they made and the courage they have shown to live by them

9. Valorization based research funding likely turns aspiring scientists into glorified engineers

10. A publication delayed, is a publication denied

These propositions are regarded as opposable and defendable, and have been approved as such by the promotor, Prof. dr. ir. A. -J. van der Veen.

Acknowledgments

Acknowledgments

I am indebted to you all, for your consistent support, advice and guidance, which has led to the fruitful culmination of this dissertation, and I look forward to many more years of our collaboration.

I am honored to have *Prof. dr. ir. P. Visser*, *Prof. dr. ir. E. Gill*, *Prof. dr. A. Leshem*, *Prof. dr. ir. M. Moonen* and my advisors in the PhD committee. Thank you all for reviewing the first draft of this dissertation and providing me with valuable inputs, which helped improve the quality of this book.

I would like to thank the team members of DARIS, OLFAR and various other space-based astronomy projects, with whom I have enjoyed numerous discussions. *Albert-Jan*, *Mark Bentum*, *Marc Klein-Wolt*, *Noah Saks*, *Kees van't Klooster*, *Willem Baan*, *Heino Falcke*, *Jan Noordam*, *Chris Verhoeven*, *Andre Gunst*, *Wim van Cappellen* and *Stefan Wijnholds*. Thank you for spending your valuable time in teaching me the nuances of terrestrial radio astronomy arrays and the potential challenges of futuristic space-based arrays. The Chapter 2 of this dissertation is an ode to you all.

Special thanks to *Steven*, *Alex*, *Frederik*, *Hamid*, *Maneesh* and *Prem* for the many brainstorming sessions, which gave rise to ~~ludicrous~~ insightful ideas to counter the challenges of space-based arrays. Cheers to our conference visits, pool table conversations, deliberations over coffee, endless email threads, and the never-ending project meetings.

My doctoral journey began while I was an integral part of ASTRON. I am grateful to *Arnold van Ardenne* and *Ananthakrishnan sir* for believing in me. Thank you *Albert-Jan*, for entrusting me with various work packages in diverse projects at ASTRON, and later encouraging me to focus on statistical signal processing. I would like to extend my gratitude to all ASTRON colleagues for their support and encouragement, and in particular to my office mates *Parisa* and *Gregory*.

I am thankful to all my colleagues and friends at the ever-evolving-CAS group, for their ardent support and good times. *Nihan*, *Milad*, *Yongchang*, *Yan*, *Yiyin*, *Yu*, *Dony*, *Shahrzad*, *Venkat*, *Sumeet*, *Hadi*, *Shahzad*, *Sina*, *Sundeep*, *Hamid*, *George*, *Adib*, *Seyran* and many more. I will forever cherish our numerous technical brainstorms, coffee corner discussions, signal processing seminars, and the pleasant outings in The Netherlands and around the globe. In particular, I would like to acknowledge our post-docs *Jorge Abraham Martínez Castañeda*, *Andrea Simonetto* and *Rocío Arroyo Valles*, who raised the bar for us promovendi; professionally, socially and intellectually. The smooth functioning of my doctoral program was due to a strong technical and bureaucratic support. Thanks to *Patricia* for managing my numerous trips between ASTRON and Delft, *Antoon* for energetically responding to all ICT requests and supporting my simulations, *Rosario* for managing the finances, and finally to *Minaksie* for her liveliness, and for handling all official matters.

Acknowledgments

Biography

Raj Thilak Rajan was born in Madurai, India, and grew up in the Indian cities of Chennai, Bangalore, Delhi, Mumbai and Pune. He received his M.Sc (with highest honors) and B.Sc (with honors) in Electronic science from University of Pune, India, in 2006 and 2004 respectively.

In the past decade, he has worked at various research organizations across Europe and India, in the diverse fields of nuclear physics, radio astronomy and signal processing. During 2006-2007, he was a software trainee at Whirlpool Labs in Pune, India, where he worked on embedded programming of the next-generation consumer electronic products. In the period from 2007-2008, he was a MIUR Fellow at INFN, Politecnico di Bari, Italy, and was a visiting researcher at CERN, Switzerland for the large hadron collider (LHC) project. In this term, he contributed to the cosmic muon tracking algorithm for the cosmic muon solenoid experiment (CMS), which was successfully employed as a technical trigger for detecting muons.

His interest in signal processing implementation urged him to join ASTRON, Netherlands institute for radio astronomy, where he was a digital signal processing engineer from 2008 until 2014. During this tenure, he was part of a research team which was involved in the development of novel radio astronomy backends. In particular, he focused on the design of resource-constrained implementation of fundamental signal processing blocks, such as FFT and poly-phase filter banks. In addition, he was also an intrinsic part of many space-based aperture array feasibility studies, and subsequently collaborated with various space science organizations.

In 2010, he started his PhD under the supervision of Prof. dr. ir. Alle-Jan van der Veen at the CAS group in TU Delft. During his doctoral program, he addressed different system and signal processing challenges of the STW-sponsored OLFAR project. In particular, he worked on the topic of joint localization and synchronization for an

anchorless network of asynchronous mobile nodes. He was nominated for the best paper award at the *IEEE* CAMSAP 2013 conference for the paper titled "Relative velocity estimation using Multidimensional scaling". He is a graduate student member of IEEE and EURASIP, and his research interests broadly lie in data modeling and statistical inference.

Since August 2015, he is an Algorithm researcher with the IoT team at IMEC, Holst center in Eindhoven, The Netherlands.